7-23-2018

Thermal, Electrical, and Electrochemical Characterizations of Advanced Nanomaterials for Energy Conversion and Storage Applications

Sajad Yazdani
University of Connecticut - Storrs, sajad.yazdani@uconn.edu

Thermal, Electrical, and Electrochemical Characterizations of Advanced Nanomaterials for Energy Conversion and Storage Applications

Sajad Yazdani, PhD

University of Connecticut, 2018

This work is concerned with the leading methods of bottom-up material synthesis and characterization for electrochemical storage as well as thermal-to-electrical energy interconversion. Among various metal oxides, manganese oxide-based materials are very attractive for electrochemical applications due to being abundant, especially anode applications in lithium ion batteries. The main issues hindering the effective use of manganese oxides are their ultra-high electrical resistivity, and phase instability during cycling. These issues are addressed by a purposeful use of controlled growth on multiwalled carbon nanotubes and Co-alloying.

The presence of oxygen vacancy sites fundamentally affects physical and chemical properties of materials. It is reported that a thermochemical interaction between poly(diallyldimethylammonium chloride) PDDA and α-MoO_3 enables formation of high-concentrations of oxygen vacancies. A proposed mechanism suggests that the vacancy sites are created through absorption of terminal site oxygen (O_t) upon decomposition of the N─C bond in the pentagonal ring of PDDA during the thermal treatment. O_t atoms are absorbed as ionic O^- and neutral O^{2-}, creating Mo^{5+}-$v_O^{\cdot}$ and Mo^{4+}-$v_O^{\cdot\cdot}$ vacancy bipolarons and polarons, respectively. Samples with higher concentrations of oxygen vacancies are found to be more active for oxygen reduction reaction.

Furthermore, high temperature energy conversion materials, such as PbS, are very attractive for waste heat recovery from a thermodynamic stand point. However, chemistry of bottom-up methods can be quite complicated and introduce vacancies sites and defects leading to uncontrolled chemical potentials and charged interfaces altering the electronic transport properties of PbS. It is shown that the electronic transport is dominated by the existence of trap states and dramatic effects of highly charged interfaces on electro-thermal properties of PbS_{1-x} have been investigated.

Finally, thermal, electrical and electrochemical materials property measurements can be quite challenging especially at high temperatures introducing significant uncertainty. In this thesis, an instrument design for consecutive and accurate measurements of thermal conductivity, electrical conductivity, and ionic conductivity as well as Seebeck coefficient within a wide range of temperatures is presented by eliminating potential sources of error.

Thermal, Electrical, and Electrochemical Characterizations of Advanced Nanomaterials for Energy Conversion and Storage Applications

Sajad Yazdani

B.Sc., Razi University, 2007

M.Sc., University of Tehran, 2009

A Dissertation

Submitted in Partial Fulfillment of the

Requirements for the Degree of

Doctor of Philosophy

at the

University of Connecticut

2018

APPROVAL PAGE

Doctor of Philosophy Dissertation

Thermal, Electrical, and Electrochemical Characterizations of Advanced Nanomaterials for Energy Conversion and Storage Applications

Presented by

Sajad Yazdani, B.Sc., M.Sc.,

Major Advisor

_____

Michael T. Pettes

Associate Advisor

_____

Ugur Pasaogullari

Associate Advisor

_____

Wilson K.S. Chiu

Associate Advisor

_____

Niloy Dutta

Associate Advisor

_____

Jason Lee

University of Connecticut

2018

AKNOWLEDGMENTS

First and foremost, my greatest gratitude goes to my advisor Prof. Michael Pettes whom I could not have imagined performing this work without his supervision, insights, and support. His mentorship guided me throughout my study and research at the University of Connecticut. During my journey, I have learned many valuable lessons from him. Priceless lessons that will help me to grow, both in my academic career and non-academic life. I am forever in debt for his great mentorship, expertise and encouragement.

I would like to thank my advisory committee, Prof. Ugur Pasaogullari, Prof. Wilson K.S. Chiu, Prof. Niloy Dutta and Jason Lee for their support, guidance and valuable comments and time.

Throughout my journey, I have been blessed and had the privilege of collaborating with fantastic colleagues and friends. My special thank goes to Raana Kashfi-Sadabad whom I learned the very basics and advanced chemical processes. She has been the greatest help and a source of inspiration to me and my research since the very beginning of journey at UConn. Raana, I cannot thank you enough! Second, I am most grateful to Dr. Huan Tran for performing all the density functional theory calculations in the present work. Huan, I am very thankful to have the opportunity of working with you and learning from your valuable expertise. I would like to thank Dr. Alessandro Palmieri and Prof. William Mustain for their collaborations on battery research. Alessandro, I am grateful for our collaborations and I wish you all the best in your future endeavors. I would like to sincerely thank Prof. Jian He, and my friends and colleagues Yufei Liu, and Ms. Menghan Zhou for their help and sharing their expertise during my experiments at Clemson University.

Additionally, I would like to thank all of my fellow lab members for their collaborations, insights and help with my research. I am grateful to Hyun-Young Kim for his collaboration and help with the finite element analysis, and Raul Montaño for his help with the chemical syntheses during his NSF REU summer programs in our lab. Also, my gratitude goes to Mr. Zhao Cai for his collaborations on the ORR measurements.

Furthermore, I would like to thank all the faculty and staff of the department of Mechanical Engineering Department at the University of Connecticut as well as Prof. Helena Silva and my friend Lhacene Adnane at the Nanoelectronics Laboratory. I am thankful to the technical staff at the Institute of Materials Science, especially Dr. Daniela Morales, Dr. Laura Pinatti, Dr. Roger Ristau, and Dr. Lichun Zhang for all the training and help that they patiently provided.

I am thankful to National Science Foundation for supporting the present work through my advisor's NSF CAREER award (NSF Award #1553987, PI: Dr. Michael Pettes) and NSF I-Corps award (NSF Award #1811480, PI: Dr. Michael Pettes, Entrepreneurial Lead: Sajad Yazdani). I am also grateful to General Electric and the School of Engineering at the University of Connecticut for receiving Graduate Fellowship for Innovation in 2016 and supporting my research.

Last but not least, there is no word that can express my deep gratitude to my family for all their support in achieving my goals.

TABLE OF CONTENTS

LIST OF TABLES

LIST OF FIGURES

CHAPTER 1: Introduction

1.1 Background: Transition metal oxides for lithium ion battery anodes

Despite having high capacities, Li alloying anodes such as Si, usually lack the stability upon clinging due to dramatic expansions and contractions during alloying or de-alloying[1]. In comparison, transition metal oxides are very appealing for anode applications in lithium ion batteries due to their high specific capacity and reversible reactions with Li ions preventing metal-Li alloy formation[1-3]. The reversible reaction can be written as

$$MO + xLi^{+} + xe^{-} \leftrightarrow LiO_2 + M, (M = Fe, Co, Ni, Cu, Mn) \quad (1.1)$$

The forward reaction is thermodynamically favorable but the backward reaction leading to Li^{+} formation from LiO_2 is not thermodynamically favorable[4]. It has been reported that nanostructuring can significantly facilitate the reversibility of the redox reaction[4-6]. Other main challenges in anode materials design and fabrication include having low electrical conductivity and Li ion diffusion coefficient[4].

Among various metal oxides, Mn_xO_y materials are particularly interesting for large-scale applications due to their abundance. The high theoretical capacity of MnO (755 $mAhg^{-1}$), Mn_3O_4 (936 $mAhg^{-1}$) and MnO_2 (1230 $mAhg^{-1}$) make them very promising. However, having extremely low electrical conductivity (e.g. 10^{-9} S cm^{-1} for MnO)[4, 7, 8] hindering the potential applications. The other challenge is related to poor reversibility and phase stability of manganese oxides. Phase transformation to higher oxidation degree from MnO to Mn_2O_4 which is thermodynamically

favorable can also lead to poor cyclability of the anodes. Thus, despite being a very attractive candidate, any effort to fabricate high performance Mn_xO_y anodes, need be focused on solving the insulating behavior and phase transitions of Mn_xO_y while cycling.

1.2 Background: Molybdenum oxides for electrochemical applications: The importance of oxygen vacancies in MoO_{3-x}.

The unique properties of molybdenum-based oxides such as relatively high electrical conductivity and mechanical and thermal durability make them ideal candidates for development of efficient electrochemical energy storage systems [9, 10]. Among different Mo-based electrocatalysts, layered orthorhombic MoO_3 and conductive monoclinic MoO_2 are the most promising[9, 11]. The majority of previous studies on these materials have been carried out in the fields of Li-ion batteries[12], oxygen reduction reaction[13, 14], supercapacitors and pseudocapacitors[9, 15] and the hydrogen evolution reaction[11] (Figure 1.1).

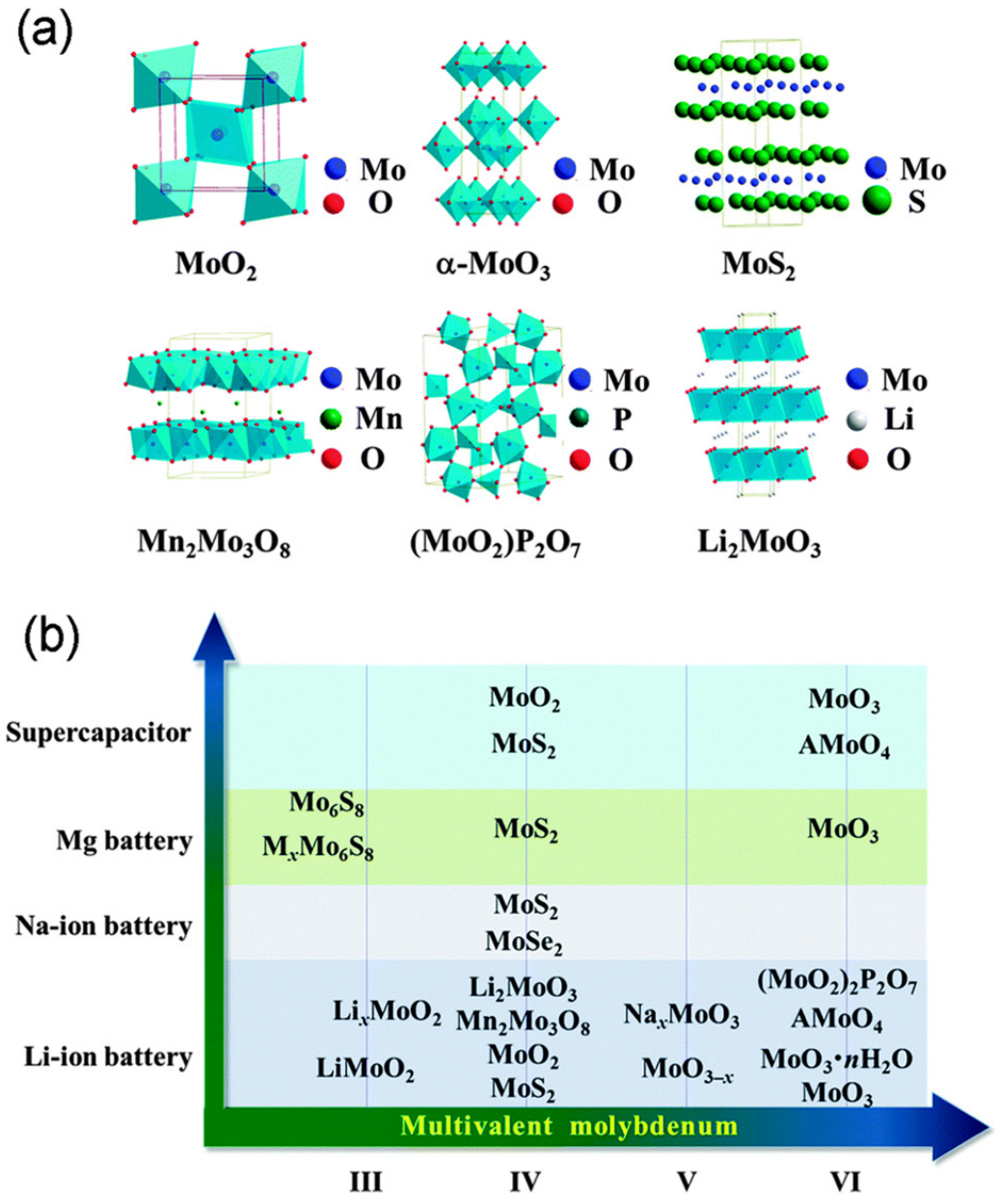

Figure 1.1. Mo-based materials for electrochemical applications. (a) Crystal structures of various Mo-based compounds. (b) Rich chemistry of multivalent Mo-based materials for electrochemical applications such as lithium ion, sodium ion and magnesium batteries, as well as supercapacitors. Reprinted with permission from ref.[9]. Copyright 2015 Royal Society of Chemistry.

Molybdenum oxidizes exist in a wide variety of structures and stoichiometries (Figure 1.1 a). Among these, α-MoO_3 is layered with an orthorhombic structure and monoclinic MoO_2 is known for high electrical conductivity. Depending on the synthesis methods, oxygen vacancies can be formed which essentially dictate many physical and electrochemical properties of metal oxides. An oxygen vacancy is a shallow donor in MoO_3 making MoO_{3-x} a degenerate *n*-type semiconductor. The presence of oxygen vacancies has been shown to substantially alter physiochemical properties of MoO_3 such as optical properties and electrical conductivity. Additionally, oxygen vacancy formation can increase interlayer distances[16], which can potentially lead to improvement of electrochemical performance[15]. This necessitates exploring and discovering effective approaches for creation of high concentrations of oxygen vacancies in important and commonly used metal oxides such as molybdenum and manganese oxides.

1.3 Waste heat thermal energy conversion using bottom-up synthesized materials

1.3.1 Background

The increasing global demand for energy production requires developing more efficient and reliable alternative power generation technologies as well as energy harvesting devices, especially thermal-to-electrical energy conversion and electrochemical energy storage. Thermoelectric energy generation is one of the most promising solutions to convert heat to useful electricity considering the fact that the majority of produced energy is lost as waste heat[17].

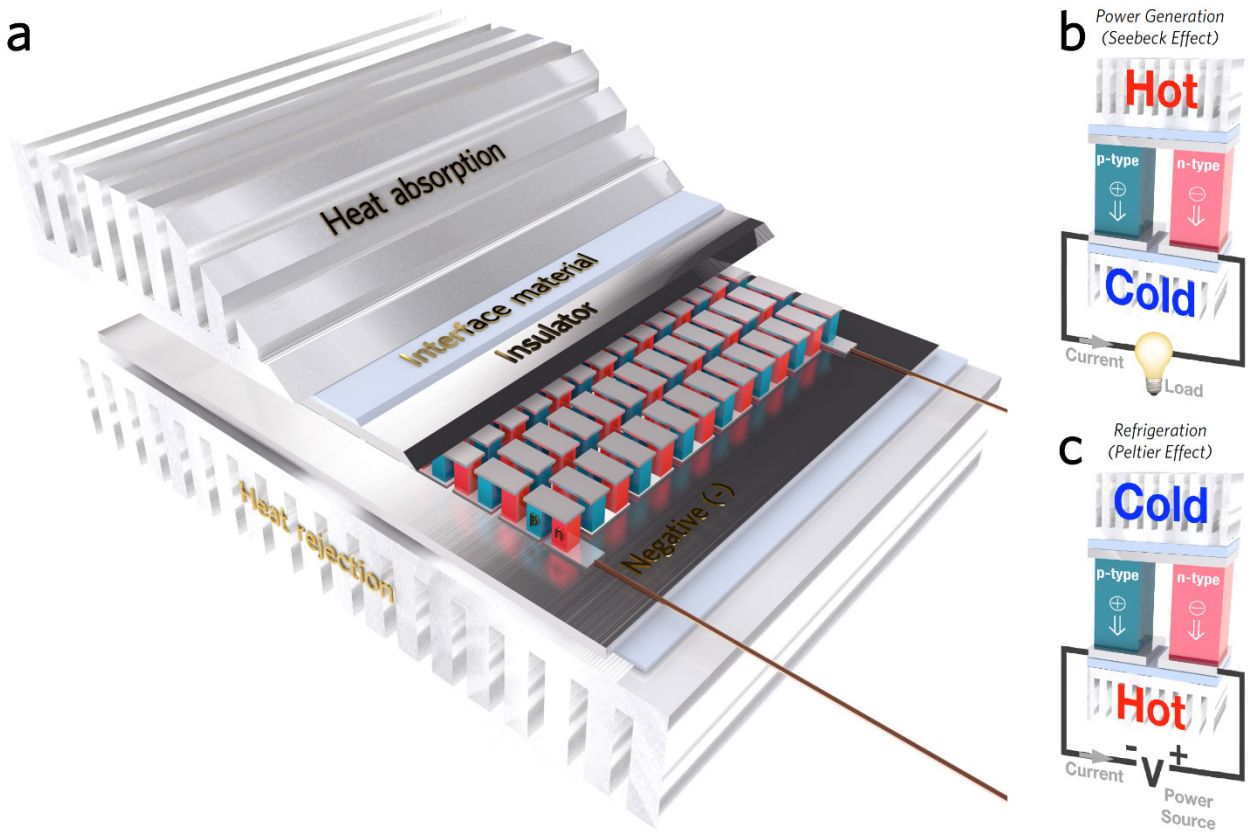

Figure 1.2. Thermal to electrical energy interconversion. (a) Schematic of the device structure of a thermoelectric energy conversion device. (b) Seebeck effect: temperature difference across a thermoelectric can cause the charge carries to be drawn towards the cold junction resulting in a formation of an electromotive force which can be used for power generation when connected to a load in an electrical circuit. (c) Peltier effect: when a TE material is subjected to an electrical current, a temperature difference due to the charge carries diffusion is formed which can be used for the refrigeration applications.

Thermoelectric energy conversion holds the potential to augment current cooling and energy production technologies, offering improved reliability, smaller size, operational lifetime on the order of decades, and no moving parts. In thermoelectric (TE) energy conversion, waste heat is

directly converted into electricity. When a thermoelectric material is exposed to a temperature gradient, the charge carriers – electrons in *n*-type and holes in *p*-type materials – diffuse from one side of the solid material to the other. In a power generation mode taking advantage of the Seebeck effect, a temperature gradient is used to generate electrical current as the diffusion of electrons is from the hot side towards the cold side and vice versa for holes. The opposite effect (using an electrical current to force a temperature gradient) can be used in a refrigeration mode and takes advantage of the Peltier effect (Figure 1.2).

The design of high performance thermoelectric materials can have a sizeable impact on the commercial industry as a sustainable energy recycler for the constant losses demonstrated by the excess waste provided by current manufacturing processes[18]. The performance of a thermoelectric material can be described by a non-dimensional quantity zT, defined as

$$zT \equiv \frac{S^2\sigma}{\kappa}T = \frac{S^2}{L}\cdot\left(1+\frac{\kappa_l}{\kappa_e}\right)^{-1} \tag{1.2}$$

where σ is the electrical conductivity, S is the Seebeck coefficient, L is the Lorenz number, T is the absolute temperature, and $\kappa = \kappa_e + \kappa_l$ is the thermal conductivity comprised of electronic (κ_e) and lattice (κ_l) components. The energy conversion efficiency at optimum efficiency is related to the Carnot efficiency, η_{Carnot}, and figure of merit, zT, as indicated by the following equation[19]

$$\eta = \eta_{Carnot}\cdot\left(\frac{\sqrt{1+zT_{device}}-1}{\sqrt{1+zT_{device}}+T_{cold}/T_{hot}}\right);\ \eta_{Carnot} = \frac{T_{hot}-T_{cold}}{T_{hot}}, \tag{1.3}$$

where T_{hot} and T_{cold} are the temperatures at the hot and cold side of the device, respectively, and where the properties we are concerned with are taken across the range of temperatures over which the device operates, zT_{device}. A more detailed discussion of the relationship between temperature-dependent material properties and device efficiency is given in ref.[20]. Reported values for state-of-the-art chemically synthesized thermoelectric materials is given in Figure 1.3.

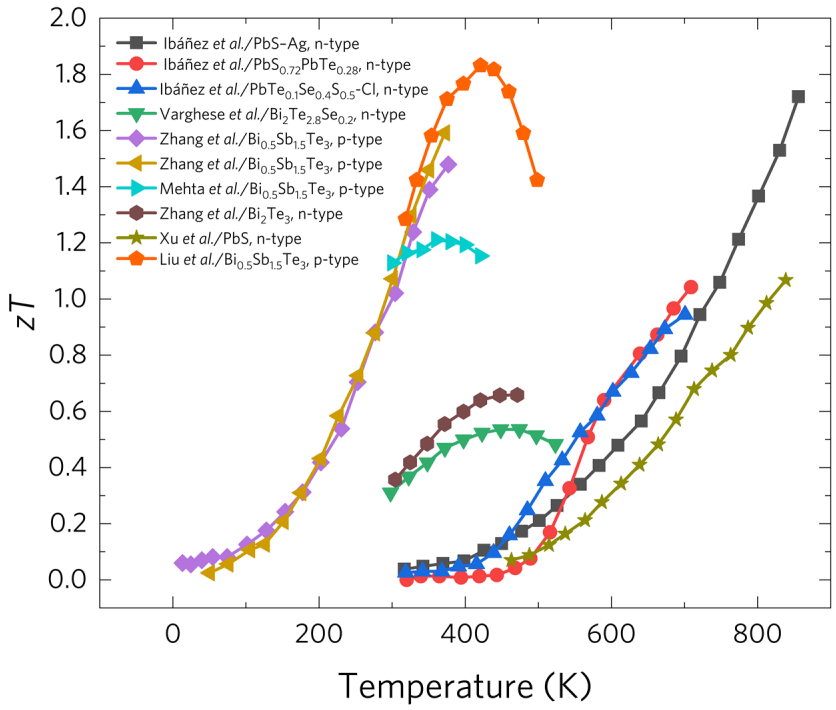

Figure 1.3. The reported high-performance figure of merit zT for bottom-up synthesized thermoelectrics at various temperatures for PbS-Ag (Ibáñez *et al.*[21], *n*-type), $PbS_{0.72}Te_{0.28}$ (Ibáñez *et al.*[22], *n*-type), $PbTe_{0.1}Se_{0.4}S_{0.5}$-Cl (Ibáñez *et al.*[23], *n*-type), $Bi_2Te_{2.8}Se_{0.2}$ (Varghese *et al.*[24], *n*-type), $Bi_{0.5}Sb_{1.5}Te_3$ (Zhang *et al.*[25], *p*-type), $Bi_{0.5}Sb_{1.5}Te_3$ (Zhang *et al.*[24], *p*-type), $Bi_{0.5}Sb_{1.5}Te_3$ (Mehta *et al.*[26], *p*-type), Bi_2Te_3 (Zhang *et al.*[27], *n*-type), PbS (Xu *et al.*[28], *n*-type), $Bi_{0.5}Sb_{1.5}Te_3$ (Liu *et al.*[29], *p*-type).

A graphical representation of the efficiency as a function of zT_{device} is shown in Figure 1.4 using a hot side temperature of 773 K and a cold side temperature of 300 K, where the predicted energy conversion efficiency for these materials according to their zT_{device} over the 300-773K temperature range is also plotted as a demonstration of the promise of this technology. Note that as an upper limit, this temperature difference correlates to a Carnot efficiency of 61.2%. For an energy conversion technology to be considered practical, the efficiency should be greater than one third of the Carnot efficiency[18], hence the zT_{device} required for practical energy conversion over the temperature range T_{hot} to T_{cold} can be expressed as

$$zT_{device,practical} = \frac{\left(T_{cold} + T_{hot}\right)\cdot\left(T_{cold} + 5T_{hot}\right)}{4T_{hot}^2}. \tag{1.4}$$

Comparison with state-of-the-art reports of zT_{device} over this temperature, which is highest for top-down synthesized materials[30-33], demonstrates that while progress has been made to increase efficiency, materials performance is still the realm in which improvements must be made before thermoelectric energy conversion can become a practical technology.

According to equation 1.2, emphasis in materials engineering should be placed on enhancing the power factor ($S^2\sigma$) while suppressing the thermal conductivity (κ). However, in reality, these properties are related to each other and act in opposite trends with respect to carrier concentration. As all three of the transport properties (S, σ, and κ) change interdependently, the carrier concentration can be adjusted to the value that leads to the maximum zT, which is carried out by deliberate *p*-type or *n*-type doping.

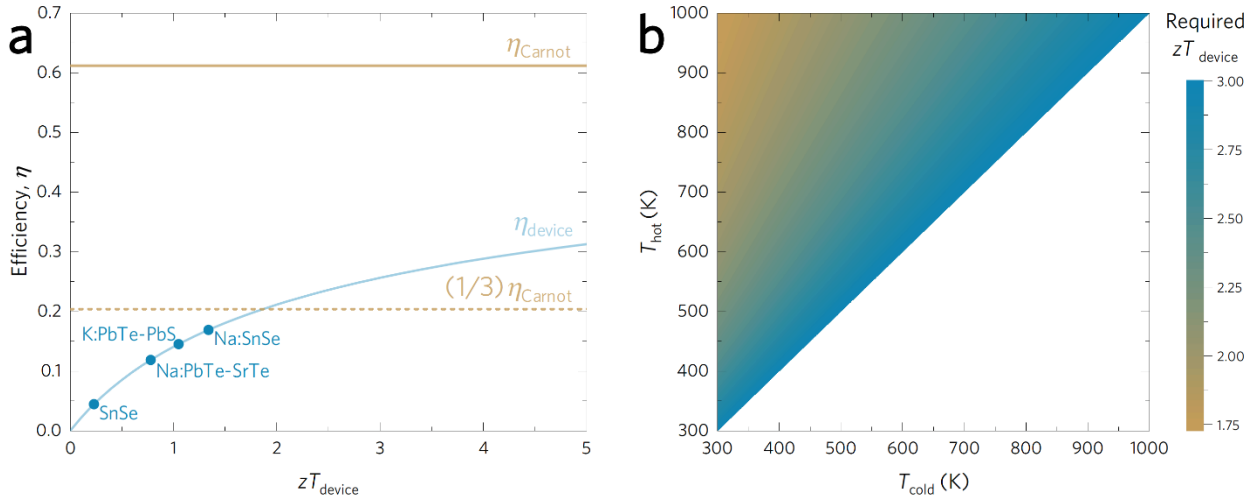

Figure 1.4. Materials performance parameters required for practical thermal-to-electrical energy interconversion. (a) Power generation efficiency as a function of device figure-of-merit (zT_{device}) at hot- and cold-side temperatures of 773 and 300 K, respectively, shown in comparison with values of zT_{device} for state-of-the-art bulk materials for energy generation over the same temperature range: SnSe [32], Na-doped PbTe-SrTe [30], K-doped PbTe-PbS [31], and Na-doped SnSe [33]. The maximum efficiency is limited by the Carnot efficiency, and practical energy conversion technologies [18] are defined as having $\eta \geq \eta_{Carnot}/3$, which will require $zT_{Device} \geq 1.87$ for the given operating temperatures. (b) For hot- and cold-side temperatures over the range of 300 to 1000 K, a zT_{device} ranging from 1.75 to 3 is required to demonstrate an efficiency of one third the Carnot efficiency.

For most cases, the optimum carrier concentration[34] is ~ 10^{18}–10^{20} cm^{-3}. The carrier concentration needs to be optimized regardless of the material fabrication process (top-down or bottom-up). The carrier concentration needs to be optimized regardless of the material fabrication process (top-down or bottom-up) which can be dominated by presence of defects and vacancies[35].

Other than possessing a high *zT*, any developed synthesis approach should be capable of the mass production of thermally and mechanically stable materials at low cost. Developing these production techniques is crucial especially for potential operations in large industries such as petroleum refining and primary metals manufacturing. A majority of previous investigations are based on top-down (solid-state) methods for material preparation, and currently most of high *zT* thermoelectrics have been obtained using solid-state synthesis processes[31-33, 35]. Each approach – solid-state or bottom-up – has its own advantages and limitations. Compared to the solid-state methods, bottom-up synthesis has been relatively overlooked and we argue that the highest potential for impact lays in investigations utilizing chemistry-based approaches. In contrast to thermoelectrics, solution-based approaches have long been utilized for various applications such as energy storage (batteries [36], supercapacitors [37], solar cells [38-40] and catalysis [41]). There are many well-developed synthesis methods in these fields that can potentially be adapted to modify the electronic or thermal performance of nanostructured materials[42-44]. For instance, chemical routes have been discovered to control the shape, morphology, and dimensionality of inorganic materials that enable manipulation of their physico-chemical proprties[45-48]. Ligand exchange techniques have been introduced for improvements of electrical properties in nanocrystals[49]. These are unique capabilities of bottom-up methods that have rarely been exploited for thermoelectric purposes. Bottom-up techniques such as microwave rapid synthesis also have inherent potential for mass-production.

1.3.2. Hydro/solvothermal and microwave synthesis of thermoelectric nanomaterials

In a hydro/solvothermal process, the synthesis constituents such as precursors, solvents, surfactants, and reduction agents are allowed to react under a high-pressure and temperature,

usually in a sealed Teflon autoclave. In microwave synthesis, the reaction is sealed and heated by microwave radiation allowing for faster processing on the order of minutes. Several studies have reported the use of hydro/solvothermal synthesis of materials for thermoelectric applications such as PbTe[50], Bi_2Te_3[51-54], $La_{0.2}Bi_{1.8}Te_3$[55], $CoSb_3$[56], PbTe nanowires[57], nanoboxes[58], and nanocubes[59], Sb_2Te_3[60-63], Sb_2Te_3–Te[64], $(Bi_{1-x}Sb_x)_2Te_3$[65], S-doped Ag_2Te[66], $Sn_xSb_2Te_{3+x}$[67], and *p*-type Sb_2Te_3/poly(3,4-ethylenedioxythiophene) [68]. The hydro/solvothermal thermal method can also be used as a post-synthesis treatment to modify already made materials via grain boundary engineering. Ji and Tritt *et al.,*[52] reported modification of commercial *p*-type $(Bi_{0.2}Sb_{0.8})_2Te_3$ powders by a hydrothermal treatment in a solution of AOH, and ABH_4, where A = Na, K, and Rb. The untreated and treated x-ray diffraction data showed no extra peaks and suggested no intercalations or formation of a new crystalline phase. However, a hump feature was observed which was attributed to an amorphous constituent of a new phase which dramatically changed thermoelectric properties. Selected area electron diffraction (SAED) patterns of the treated samples showed cubic symmetry against the hexagonal symmetry of the un-treated samples, suggesting the existence of a secondary crystallinity from the bare materials along with a non-crystalline phase. An interesting observation was that this coating layer could be easily removed by a short ultrasonication, suggesting that the coating layer is loosely bound to the parent material which also introduces an elastic mismatch at the boundaries. Transport measurements indicated that the power factor was retained upon post-synthesis hydrothermal surface treatment, and even increased for Rb treatment. The electrical conductivity was improved due to an enhancement of carrier concentrations resulting in overall improvement of the thermoelectric power factor, σS^2. All surface-treated samples exhibited lower thermal conductivities compared to those of the bare

$(Bi_{0.2}Sb_{0.8})_2Te_3$. In the case of Na treatment, a 15% reduction in room temperature thermal conductivity was reported.

1.3.3. High-temperature bottom-up materals: The importance of charged-interfaces

High temperature thermoelectrics, such as PbS, are more attractive for large-scale waste heat recovery from a thermodynamic stand point. Solution chemistry-based, or bottom up, approaches for material syntheses are ideal for large-scale applications and in general produce products with low values of thermal conductivities as an abundance of grain boundaries can suppress the lattice thermal conductivity. However, the chemistry of bottom-up methods can be quite complicated and introduce vacancies sites leading to uncontrolled chemical potentials. Existence of chalcogen vacancies, such as sulfur in PbS, can completely alter electronic transport properties. Other than changing chemical potential, the vacancy or impurities can charge solution processed interface-rich materials creating potential barriers against charge transport. Thus, it is crucial to investigate the effects of charged-interfaces on electrical and thermal properties.

1.4 Background: Thermal, electrical, and ionic conductivity and Seebeck coefficient measurements: Challenges and accuracy of high-temperature measurements

Accurate measurement of materials properties is essential in successful material design for thermal energy conversion and electrochemical energy storage applications. This becomes more critical especially at high temperatures where obtaining accurate measurements of thermal properties becomes more complicated. Experimental investigations of solid materials at elevated temperatures rely on optimized thermal design of the measurement system, as radiation becomes

a predominant source of heat loss which can lead to large uncertainty in measured temperature and related physical properties of a test sample. In most cases, high temperature thermal transport measurements are conducted using transient flash diffusivity technologies. This means that thermal conductivities are not obtained directly, and additional specific heat measurements are required, usually conducted by differential scanning calorimetry. Measuring specific heat, however, introduces large uncertainties in the overall thermal conductivity data. Quantification of such errors is challenging and depends on the conditions of the equipment, pans, contamination, and temperatures. High-thermal conductivity samples need to be thick because of the slow signal detection and low thermal conductivity materials are required to be thin in order to detect acceptable signals. Beside the large uncertainty and skepticism associated with obtaining thermal conductivity through diffusivity and specific heat measurements, the current methods are cumbersome, time consuming and expensive. On the other hand, the current steady state methods for direct thermal conductivity measurements are not rigorous enough to be employed for high-temperature accurate applications.

Moreover, quantitative temperature-dependent electrochemical validation and the surface temperature of the material must be measured under operation at fast charging rates (e.g., about 350 kW to about 400 kW), where Joule heating is expected to contribute to up to about 90% of the volumetric heating rate, and ionic conductivity may influence the temperature asymmetry across the material. Lack of such accurate measurements can lead to performance failures and catastrophic safety issues such as ignition in batteries. As no instrument exists for this purpose, we aimed to design an instrument for accurate and consecutive measurements of thermal conductivity, electrical conductivity, ionic conductivity, and Seebeck coefficient as well as surface temperature

while maintaining a vacuum or inert gas environment. Our design overcomes prior technological barriers as none of the current technologies provide consecutive measurements for these materials properties.

1.5 Motivation and scope

The objectives of the present work include: (i) Improving the electrical conductivity and phase stability of MnO nanomaterials for high performance lithium ion battery anode applications. (ii) Defect engineering in MoO_{3-x} materials for electrochemical applications. (iii) Understanding the role of highly charged interfaces on the thermal and electrical transport properties of PbS_{1-x}. (iv) Identifying the uncertainty sources associated with high-temperature thermal, electrical, ionic conductivity and Seebeck coefficient measurements. (v) developing a new design for consecutive and accurate measurements of the electrical, ionic conductivity and Seebeck coefficient with a main focus on high-temperature applications.

Chapter 2. It is demonstrated that the electrochemical performance of MnO can be greatly improved by using oxygen-functional groups created on the outer walls of multiwalled carbon nanotubes (MWCNTs) as nucleation sites for metal oxide nanoparticles. Based on the mass of the active material used in the preparation of electrodes, the composite conversion-reaction anode material $Mn_{1-x}Co_xO$/MWCNT with $x = 0.2$ exhibited the highest reversible specific capacity, 790 and 553 $mAhg^{-1}$ at current densities of 40 and 1600 mAg^{-1}, respectively. This is 3.1 times higher than that of MnO/MWCNT at a charge rate of 1600 mAg^{-1}. Phase segregation in the $Mn_{1-x}Co_xO$ nanoparticles was not observed for $x \leq 0.15$. Capacity retention in $x = 0$, 0.2 and 1 electrodes showed that the corresponding specific capacities were stabilized at 478, 709 and 602 $mAhg^{-1}$ respectively, after 55 cycles at a current density of 400 mAg^{-1}. As both MnO and CoO exhibit

similar theoretical capacities and MnO/MWCNT ($x = 0$) and CoO/MWCNT ($x = 1$) anodes showed lower performances than that of $x = 0.2$, the improved performance of $Mn_{1-x}Co_xO$/MWCNT alloy can be due to possible interactions in the bimetallic system.

Chapter 3. It is shown that that the presence of oxygen vacancy sites fundamentally affects physical and chemical properties of materials. A dipole-containing interaction between poly(diallyldimethylammonium chloride) PDDA and α-MoO_3 is found to enable high-concentrations of surface oxygen vacancies. Thermal annealing under Ar resulted in negligible reduction of MoO_3 to MoO_{3-x} with $x = 0.03$ at 600°C. In contrast, we show that thermochemical reaction with PDDA polyelectrolyte under Ar can significantly reduce MoO_3 to MoO_{3-x} with $x = 0.36$ ($MoO_{2.64}$) at 600°C. Thermal annealing under H_2 gas enhanced the sub-stoichiometry of MoO_{3-x} from $x = 0.62$ to 0.98 by using PDDA at the same conditions. Density functional theory calculations, supported by experimental analysis, suggest that the vacancy sites are created through absorption of terminal site oxygen (O_t) upon decomposition of the N─C bond in the pentagonal ring of PDDA during the thermal treatment. O_t atoms are absorbed as ionic O^- and neutral O^{2-}, creating Mo^{5+}-$v_O^{\cdot}$ and Mo^{4+}-$v_O^{\cdot\cdot}$ vacancy bipolarons and polarons, respectively. X-ray photoemission spectroscopy peak analysis indicates the ratio of charged to neutral molybdenum ions in the PDDA-processed samples increased from $Mo^{4+}/Mo^{6+} = 1.0$ and $Mo^{5+}/Mo^{6+} = 3.3$ when reduced at 400°C to $Mo^{4+}/Mo^{6+} = 3.7$ and $Mo^{5+}/Mo^{6+} = 2.6$ when reduced at 600°C. This is consistent with our *ab initio* calculation where the Mo^{4+}-$v_O^{\cdot\cdot}$ formation energy is 0.22 eV higher than that for Mo^{5+}-$v_O^{\cdot}$ in the bulk of the material and 0.02 eV higher on the surface. The results presented in chapter 3 reveal a new paradigm for effective enhancement of surface oxygen vacancy

concentrations essential for a variety of technologies including advanced energy conversion applications such as low-temperature thermochemical water splitting.

Chapter 4. The role of interfaces on the electro-thermal properties of PbS_{1-x} is investigated. Sulfur vacancy ($v_S^{\cdot\cdot}$) formation is monitored by TGA analysis. The majority of the sulfur vacancy sites are formed at temperature ~ 266.4 ℃. By a combination of experiment and DFT, it is proposed that the formation of $v_S^{\cdot\cdot}$ is more favorable on the surface as opposed to the bulk of the material. At this temperature a weight loss of 1.97 % is measured. As the temperature increases a small and continues weight loss is observed with a maximum of only 0.3% weight loss at 600 ℃. This smaller weight loss is attributed to the $v_S^{\cdot\cdot}$ formations at layers closer to the outer surfaces where the majority of $v_S^{\cdot\cdot}$ vacancy formation occurs. A potential barrier against the carrier transport, attributed to charged interfaces, is observed and analyzed. The effects of these charged interfaces on the electro-thermal transport properties of PbS_{1-x} materials is discussed in detail.

Chapter 5. Advancements in surface temperature measurements by reducing thermal losses arising from the cold-finger effect using axially inserted thermocouples, and from radiation using shields or other thermal guards are discussed in detail. The leading technology for temperature sensing at temperatures up to ~900°C makes use of these design features for measuring thermopower, yet uncertainty analysis estimation of this technique is not known. The report presented in this chapter makes use of finite element modeling to determine spatial temperature distributions to obtain the upper limit of confidence expected for the axially inserted thermocouple approach when a heated radiation shield is incorporated into the design. Using an axially inserted thermocouple to measure the sample surface temperature, the temperature variations across the sample hot and cold surfaces at 900°C for a temperature drop of 0, 5, and

10°C are calculated to be as low as 0.02, 0.21, and 0.41°C, respectively when a heated radiation shield is employed. Uniform temperature distribution on the thermocouple cross-wire geometry indicates that the axial thermocouple measurement design is indeed effective for suppressing the cold-finger effect. Using a heated radiation shield is found to significantly reduce the temperature gradient across the thermocouples. In addition, a new design of an instrument for accurate measurements of thermal, electrical and ionic conductivity as well as Seebeck coefficient is introduced and analyzed.

Chapter 6. In this chapter a summary of the findings and impact of the present work is discussed.

CHAPTER 2: Improving the Electrochemical Performance of Manganese Oxide Nanoparticles Nucleated on Multiwalled Carbon Nanotubes by Cobalt Alloying*

2.1 Background

Manganese oxide based materials are attractive for lithium ion batteries due to their high abundance and low environmental impact [69]. Among different classes of these materials, MnO has a relatively high theoretical capacity of 755 $mAhg^{-1}$ and low hysteresis voltage (< 0.7 V). However, extremely high electrical resistivity and rapid capacity degradation are the limiting factors in reaching the theoretical capacity and achieving long service life [3, 4, 70]. Thus, it is highly desirable to improve the electrochemical performance of MnO-based materials by increasing their ultra-low electrical conductivity, on the order of 10^{-9} S cm^{-1} [7]. In pioneering reports, the electrochemical performance of MnO indicated a low-potential reaction with Li, although capacity was not promising [71]. Through microstructuring, an initial capacity of 650 $mAhg^{-1}$ was obtained in inverse micelle-templated $MnCO_3$ [72]. However, this capacity degraded to 390 $mAhg^{-1}$ after only 25 cycles. Capacity and stability were improved using a mixture of MnO and Mn_3O_4 nanoparticles confined to carbonized polyacrylonitrile (PAN) nanofibers with mesoporous features using electrospinning [73]. First cycle specific charge and discharge capacities of 1155 and 785 $mAhg^{-1}$ were reported at a current rate of 50 mAg^{-1}, as well as a reversible capacity of 597 $mAhg^{-1}$ after 50 cycles (23.6 % decay with respect to the initial reversible capacity). Higher electrical conductivity of the carbon used in the preparation process and nanoscale electrochemically active materials were proposed to

* Reproduced in part with permission from Sajad Yazdani, Raana Kashfi-Sadabad, Alessandro Palmieri, William E. Mustain and Michael Thompson Pettes, "Effect of cobalt alloying on the electrochemical performance of manganese oxide nanoparticles nucleated on multiwalled carbon nanotubes" *Nanotechnology* **28**(15), 155403 (2017), https://doi.org/10.1088/1361-6528/aa6329. Copyright 2017 IOP PUBLISHING, LTD.

be responsible for the improved performance of their materials, as in other reports[74, 75]. A detailed review of MnO/carbon as well as MnO/reduced graphene oxide (rGO) composites is given in refs. [3] and [76]. As an alternative strategy to increasing conductivity, porous structures of pure MnO, MnO/CoO solid solutions and a nanocomposite of MnO and metallic cobalt (MnO/Co) were prepared by reduction of solid solutions of their corresponding carbonate precursors[77]. The MnO/Co structure exhibited improved reversible charge–discharge stability and it was concluded that deposition of the Co nanocrystals and the formation of a CoO surface layer were responsible for the enhanced performance. In addition, a significant number of previous reports on MnO-based materials show a dramatic increase in the capacity retention during cycling[78-88] which is most likely due to the formation of phases with higher oxidation states and correspondingly higher theoretical capacities [such as Mn_3O_4 (936 $mAhg^{-1}$), Mn_2O_3 (1019 $mAhg^{-1}$)[76], MnO_2 (1230 $mAhg^{-1}$)[4]]. However, in most cases even these materials exhibit poor high rate charge-discharge performance. Although the exact mechanism is still unclear, it has been reported that defect formations in MnO particles, arising from volume changes during cycling, can facilitate the oxidation [81, 89]. One feature common to previous investigations is that MnO, when used as an anode material, exhibits poor performance unless structural or chemical modifications are introduced. A summary is given in Table 2.1. It should be noted that in most studies promising specific capacities are obtained only at very low current densities (50-100 mAg^{-1}) which greatly restricts their use in practical applications.

Table 2.1. Summary of performance of state-of-the-art MnO-based materials. The theoretical capacities of MnO[4], CoO[90], and MWCNTs[3] are 755, 716, and 372 $mAhg^{-1}$, respectively.

Material	Number of cycles reported (#)	Current density used in stability test (mAg^{-1})	Final reversible capacity ($mAhg^{-1}$)	High rate capacity ($mAhg^{-1}$) at current density (mAg^{-1}) [a]	
Carbon-coated MnO[75]	2-150	50	650	213	(1600 mAg^{-1})
MnO/graphene nanosheets[85]	2-60	100	691 [b]	390	(1000 mAg^{-1})
Nitrogen-doped MnO/graphene nanosheets[86]	2-90	100	772 [b]	267	(1000 mAg^{-1})
MnO coated with N-doped carbon[87]	2-100	100	626 [b]	314	(800 mAg^{-1})
MnO/reduced graphene oxide[91]	2-50	100	670 [b]	331	(800 mAg^{-1})
MnO/C composites[92]	2-50	100	730	562	(1000 mAg^{-1})
MnO nanoparticle@mesoporous carbon composites[93]	2-80	100	784	609	(1000 mAg^{-1})
MnO coated with N-doped carbon[94]	2-400	200	640	451	(1000 mAg^{-1})

Hollow porous MnO/C microspheres[95]	2-50	100	700	260	(1000 mAg^{-1})
MnO/Carbon nanopeapods[96]	2-100	500	1047	551	(1500 mAg^{-1})
Porous MnO/N-doped carbon[97]	2-600	500	693	658	(1000 mA g^{-1})
MnO/MWCNT (present study)	2-55	400	478	177	(1600 mAg^{-1})
$Mn_{0.8}Co_{0.2}O$/MWCNT (present study)	5-55	400	709	642	(800 mAg^{-1})
				553	(1600 mAg^{-1})

[a] The reported higher current density rates up to 1600 mAg^{-1} were chosen as these are both more relevant to technological applications and can be more easily compared with the results of the current study; [b] The reported specific capacity increased versus cycling most likely due to the formation of materials with higher oxidation states[98-100].

Here, a chemical route to nucleate $Mn_{1-x}Co_xO$ nanoparticles on the outer walls of multiwalled carbon nanotubes and obtain a capacity among the highest reported at application-relevant charge discharge rates is demonstrated. The structure-electrochemical performance relationship of $Mn_{1-x}Co_xO$ composites with $x = 0$ and 0.2 grown directly on MWCNTs is found to strongly influence the electrochemical performance.

2.2. Methods

2.2.1 Chemicals

Manganese(II) acetate tetrahydrate $Mn(CH_3COO)_2 \cdot 4H_2O$, cobalt(II) acetate tetrahydrate $Co(CH_3COO)_2 \cdot 4H_2O$, ethyl alcohol ($CH_3CH_2OH$), multiwall carbon nanotubes (MWCNTs 724769), potassium permanganate ($KMnO_4$), hydrogen peroxide (H_2O_2, 30%), and sodium nitrate ($NaNO_3$), sulfuric acid (H_2SO_4) 98% and ammonium hydroxide solution (NH_4OH) (with 28.0–30.0% NH_3) basis were obtained from Sigma-Aldrich and used without further purification.

2.2.2 Synthesis of oxidized multiwall carbon nanotubes

Oxidized multiwall carbon nanotubes were prepared according to a procedure reported in ref. [101], which is similar to the Hummer's method for preparation of graphene oxide[102]. In a typical synthesis, 1 g MWCNT was transferred into a round-bottom flask (250 mL) and 60 mL of concentrated sulfuric acid was added and stirred at room temperature for~ 24 h. The flask was then heated in an oil bath, kept at 45 °C for 10 min, after which 0.1 g of sodium nitrate ($NaNO_3$) was added to the mixture. After 10 min while retaining the reaction temperature under 20 °C in an ice bath, 1 g of potassium permanganate ($KMnO_4$) was slowly added to the reaction. It should be noted that the addition of $KMnO_4$ should be slow and all the required safety precautions related to working with concentrated acids should be met. After 30 min, the solution was removed from the iced bath and after 5 min was transferred to an oil bath at 45 °C. After 30 min, 3 mL of deionized (DI) water was slowly added to the flask, and the reaction was proceeded by adding 5 and 40 mL of DI water after 5 and 10 min, respectively. After allowing the reaction to continue for another 15 min, the heat source was removed, and 140 mL of DI water followed by 10 mL of 30% hydrogen peroxide (H_2O_2) solution were poured into the solution in order to stop the reaction. The mixture

was then kept stirring at room temperature for 15 min. The obtained sample was washed with 5% HCl in DI water and centrifuged twice to remove any unreacted cations. The mixture was then continuously washed and centrifuged with DI water until a pH of ~5 was measured. Then the collected sample was dispersed in 100 mL of DI water and sonicated for 30 min. The final product was obtained by centrifugation and room temperature vacuum drying.

2.2.3 Synthesis of $Mn_{1-x}Co_xO$/MWCNT

Similar to refs. [101] and [103], 90 mg of the oxidized MWCNTs was ultrasonically dispersed in a 122.5 ml of 50:1 ethanol:DI water solution for 1 h. The mixture was transferred to a round-bottom flask (250 ml) to which 3 ml of $Mn(CH_3COO)_2 \cdot 4H_2O$ solution (0.6 M) in DI-water was added. A certain amount of Mn solution, x, was replaced by $Co(CH_3COO)_2 \cdot 4H_2O$ solution (0.6 M in DI water) for $x = 0.05$, 0.10, 0.15 and 0.20 samples. Afterwards, 2.5 ml of ammonium hydroxide was added to the mixture and the flask was transferred to an oil bath at 90 °C and re-fluxed for 24 hours. The samples were collected by centrifugation at 7000 rpm and dried in vacuum at room temperature for 72 hours. The dried samples were subsequently annealed in argon at 600 °C for 3 hours with ramp 1 °C min^{-1} in order to crystalize the metal oxides and thermally reduce the partially oxidized MWCNTs.

2.2.4 Synthesis of $Mn_{1-x}Co_xO$ without MWCNTs

The samples without MWCNTs ($x = 0$, 0.2) were prepared by dissolving the stochiometric amounts of precursors in 122.5 ml of 50:1 ethanol:DI water solution. Similar to the synthesis described above, the mixture was transferred to a round-bottom flask (250 ml) and re-fluxed in an oil bath at 90 °C for 24 hours. Specific to these samples without MWCNTs, the solution was poured in a Petri dish and placed in an oven at 60 °C in air until the solvent evaporated. The

obtained powder was collected and annealed under argon at 600 °C for 3 hours with ramp 1 °C min^{-1}.

2.2.5 Cell fabrication

Inks containing 70 wt.% active materials, 20 wt.% conductive carbon black (CNERGY Super C65, Imerys), and 10 wt.% polyvinylidene fluoride (PVDF, Kynar blend) as the binder were prepared for fabrication of the half-cell "cathode". First, by repeated sonication and mechanical stirring of all ingredients overnight, a homogenous ink in N-methylpyrrolidone (NMP, Acros, 99.5% Extra Dry) was obtained. Copper foil (Alfa Aesar, 99.999%, thickness 0.002 in) as the current collector was roughened and cleaned by isopropanol. The prepared ink was sprayed onto copper foil to form a coating with a uniform thickness subsequently heated at 100 °C for 24 hours under vacuum. The coated foil was pressed at 1500 lbs and weighed in order to obtain its mass loading. The active loadings were kept between 1.0–1.5 mg cm^{-2}. Coin cells were assembled in a half-cell configuration with lithium metal as the counter negative electrode (Alfa Aesar, 99.9%) and Celgard 2320 tri-layer PP/PE/PP as the separator in a 2.0 cm diameter coin cell (Hohsen Corp). Lithium hexafluorophosphate ($LiPF_6$, Acros 98%) (1M) solution in ethylene carbonate (EC, Acros 99+%): dimethyl carbonate (DMC, Acros 98+%):diethyl carbonate (DEC, Acros 99%) with a ratio of (1:1:1) was used as the electrolyte on both sides of the separator (15 μL). The prepared cathode and counter negative electrode were cut into circles of 1.5 cm in diameter and were used with a 1.9 cm separator. All the battery components were pressed and sealed into the coin cell prior to removal from the glove box.

2.2.6 Electrochemical measurements

All the reported capacities were obtained based on the mass of the active materials. All electrochemical experiments were performed using an Arbin MSTAT battery test system.

2.3 Characterization

Powder X-ray diffraction (XRD) analyses were performed on a Bruker D2 Phaser with Cu K_α radiation ($\lambda = 1.54184$ Å) with an operating voltage and current of 30 kV and 10 mA. Transmission electron microscopy (TEM) analysis was conducted using a FEI Talos F200X TEM/STEM at an accelerating voltage of 200 kV, and chemical analyses were collected using STEM and energy dispersive X-ray spectroscopy (EDS) with HAADAF/BF detectors. Samples were first dispersed in ethanol and then collected using copper grids covered with thin carbon films. X-ray photoelectron spectroscopy (XPS) was performed on a PHI model 590 spectrometer with multipoles (Φ Physical Electronics Industries Inc.), using Al K_α radiation ($\lambda = 1486.6$ eV). Electrochemical impedance spectroscopy (EIS) was conducted using an Autolab PGSTAT302 N Potentiostat (Eco Chemie) from 1000 kHz to 50 mHz with a 5 mV amplitude and a coin-cell open circuit voltage (2.2 V).

2.4 Results and discussion

The $Mn_{1-x}Co_xO$ nanoparticles were grown on oxidized MWCNTs which were prepared by a modified Hummers method with a lower concentration of $KMnO_4$[101, 102]. The mass ratio of $Mn_{1-x}Co_xO$ to MWCNT was kept at 10:1. $Mn(CH_3COO)_2 \cdot 4H_2O$ and $Co(CH_3COO)_2 \cdot 4H_2O$ were used as the Mn and Co sources precursors. In order to reduce the hydrolysis rate and avoid formation or grouping of free particles, 0.5 ml of ammonium hydroxide solution was added to the mixture

before heating. The samples were centrifuged and subsequently annealed in argon at 600 °C in order to crystalize the metal oxides and thermally reduce the partially oxidized MWCNTs[101]. In preparation of a working electrode, the $Mn_{1-x}Co_xO$/MWCNT materials were combined with carbon black and polyvinyldifluoride (PVDF) in a weight ratio of 70:20:10. Coin cells in half-cell configuration were used to perform the electrochemical measurements with lithium metal as the counter electrode. For a detailed explanation of the chemical synthesis and electrochemical measurements refer to the methods section.

X-ray powder diffraction measurements for the obtained products as shown in Figure 2.1(a). At $x = 0$, all diffraction peaks can be indexed to a pure cubic crystal structure of MnO with the space group of $Fm\bar{3}m$ (225) according to JCPDS No. 01-077-2929. At $x = 1$, all peaks were assigned to CoO with the space group of $Fm\bar{3}m$ (225) according to JCPDS No. 48-1719. Cobalt substitution did not result in phase decomposition for $x \leq 0.15$. For $x \leq 0.15$ the results revealed small shifts in the peaks as shown in the inset of Figure 2.1(a) implying slight changes in lattice d-spacing due to formation of a MnO-CoO solid solution obeying Vegard's law[104]. At $x = 0.2$, formation of a secondary phase is observed, where both the primary and secondary phases have d-spacings smaller than MnO and larger than CoO. This indicates the primary phase is closer in stoichiometry to MnO and the secondary phase is closer to CoO, but both phases are $Mn_{1-x}Co_xO$ solid solutions. Raman spectroscopy indicated expected peaks for MWCNTs[105, 106], where D peaks at 1351.73 and 1350.31 cm^{-1} and G peaks at 1585.13 and 1583.75 cm^{-1} were observed for $x = 0$ and 0.2 samples, respectively (Figure 2.1b). The D-to-G-peak intensity ratio was ~1.3 for both samples, indicating the high degree of disorder remaining in the MWCNTs arising from the surface oxidation process used in the synthesis of the composites. In addition, second order G' peaks at 2700 and 2701.62 and the D+G peaks at 2935.05 and 2940.17 cm^{-1} were detected for $x = 0$ and 0.2,

respectively. The peaks located at 309.97, 358.39 and 650.20 cm^{-1} for $x = 0$ are characteristic of MnO[107, 108]. Peaks located at 297.95, 353.35 and 640.31 cm^{-1} for $x = 0.2$ are red shifted compared to those of the un-doped material, due to the alloying of CoO with the MnO host structure. The small peaks located at 172.04 and 461.42 cm^{-1} were assigned to CoO[109] in the $x = 0.2$ sample. High-resolution transmission electron microscopy (HRTEM) analysis (Figure 2.1c,d and Figure 2.2) confirms the nucleation and growth of MnO and $Mn_{0.8}Co_{0.2}O$ nanoparticles onto the outer walls of the MWCNTs. Nanoparticle sizes were observed to be less than 100 nm for $x = 0$ and 0.2 (diameters ~7–85 nm, Figure 2.3).

The high-resolution X-ray photoelectron spectroscopy (XPS) analysis of the C 1s peak for $x = 0$ and 0.2 samples at 284.7 eV (Figure 2.4a), indicated the existence of C—C, C—O, C═O and COOH functional groups[110] at 284.6, 286.8, 287.3 and 299.93 eV respectively, with percentage area ratios of 10.21:3.93:1.55:1 for both samples. The oxygen bands at 529, 530.5, 531.8 eV were assigned to MnO, C—O and H—O bonds[110], respectively, as shown in Figure 2.4. The band corresponding to absorbed water at ~533.5 eV was almost negligible (3.58 and 3.24% for $x = 0$ and 0.2, respectively). The Mn $2p_{3/2}$ and Mn $2p_{1/2}$ peaks at 640.5 and 652.1 eV, respectively, with peak-to-peak separation of 11.6 eV were well referenced to the Mn(II) oxidation state[98, 111] (Figure 2.4c). Furthermore, Co—O species were detected in the XPS spectra of the $x = 0.2$ sample as shown in Figure 2.4(d), and the XPS survey (Figure 2.5). The XPS spectra of Co $2p_{3/2}$ and $2p_{1/2}$ revealed characteristic peaks of CoO at 780 and 795.8 eV and their corresponding satellite peaks with binding energies of 785.3 and 801.8 eV are in agreement with the literature data[112-114]. It should be mentioned that the intense satellite peaks associated with high-spin Co(II) are due to multiple electron excitations, so-called shake-up[115, 116].

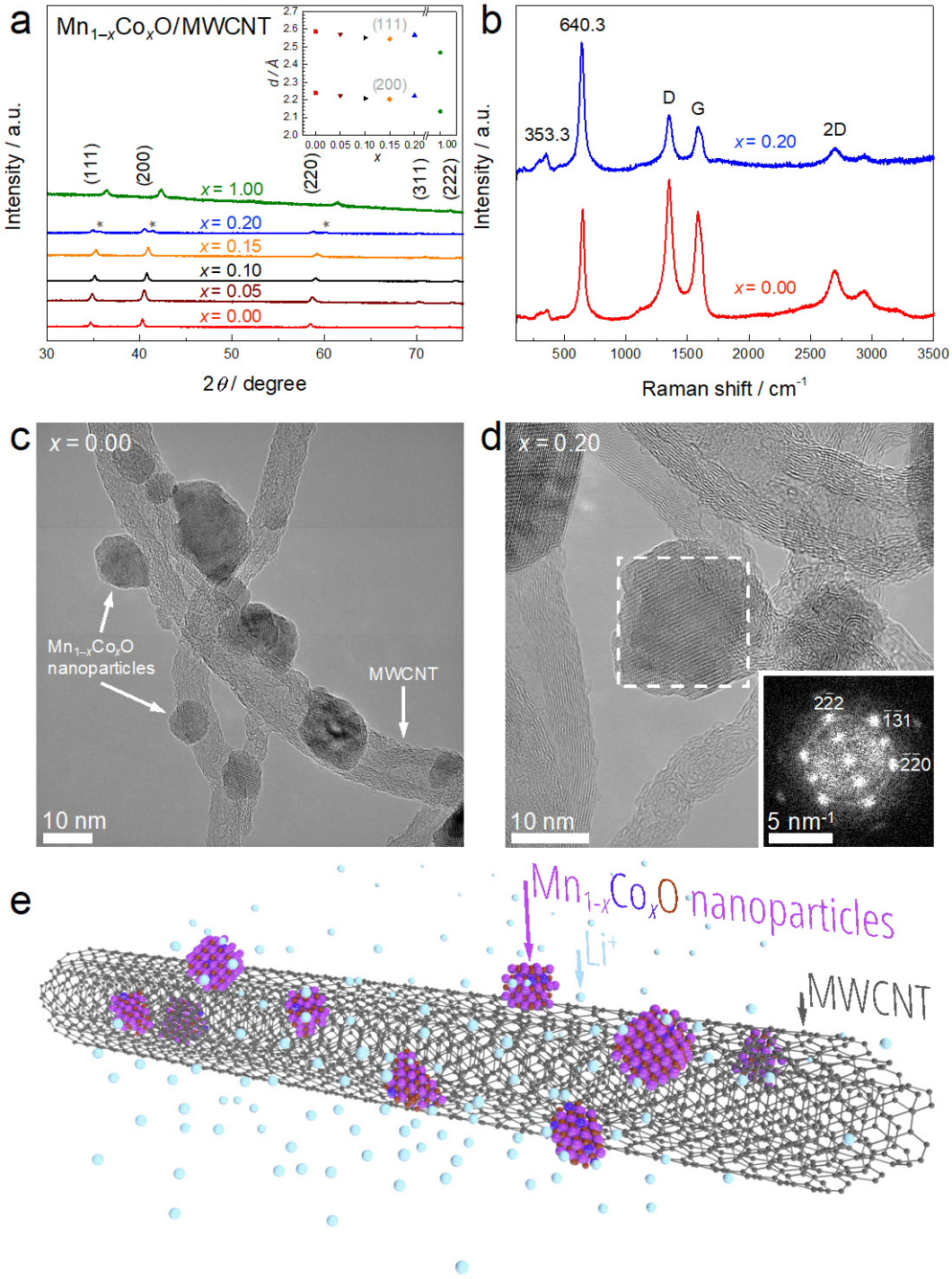

Figure 2.1. (a) XRD patterns for $Mn_{1-x}Co_xO$/MWCNT powders, the inset shows the lattice d-spacing variations versus the Co at.% substitution, *x*. Phase segregation into primary Mn-rich

and secondary Co-rich (asterisks) $Mn_{1-x}Co_xO$ phases is observed for x = 0.2. (b) Raman spectra for $Mn_{1-x}Co_xO$/MWCNT, x = 0 and 0.2. Transmission electron micrographs of (c) MnO and (d) $Mn_{0.8}Co_{0.2}O$ nanoparticles attached to MWCNTs. (d, inset) Fast fourier transform (FFT) pattern along the $[\bar{1}12]$ zone axis. The lattice spacings of d_{111}, $d_{\bar{1}\bar{3}1}$, and $d_{\bar{2}\bar{2}0}$ were within 0.77, 0.12 and 0.39% of those obtained from the XRD data, respectively. (e) Schematic of the $Mn_{1-x}Co_xO$/MWCNT composite nanomaterial.

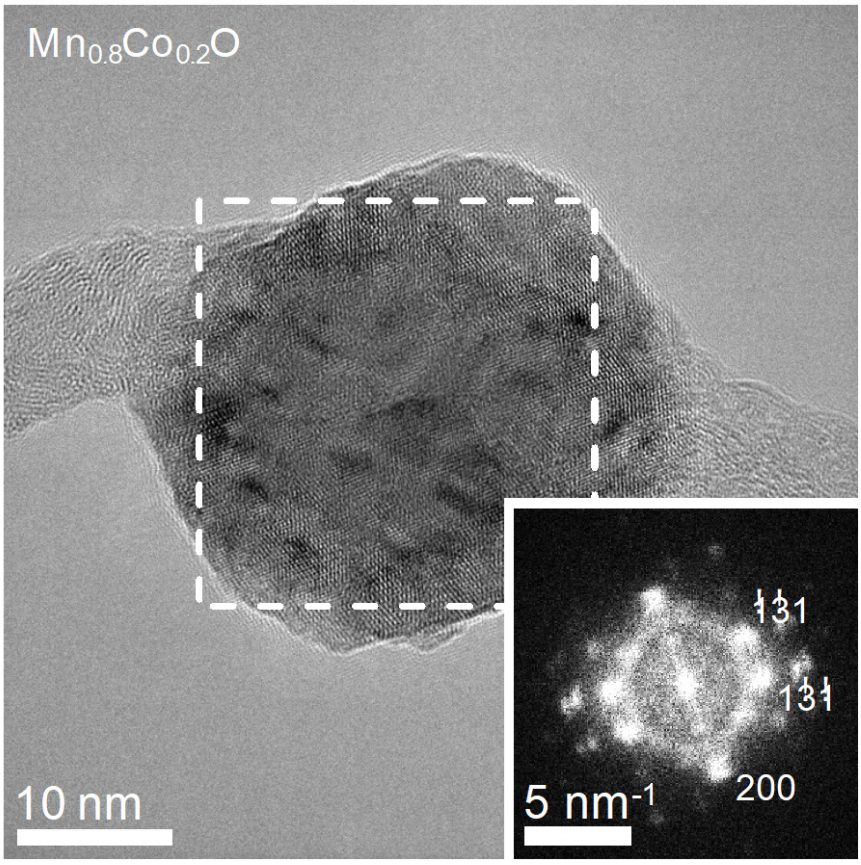

Figure 2.2. High resolution transmission electron microscopy (HRTEM) of a $Mn_{0.8}Co_{0.2}O$ nanoparticle attached to a MWCNT. The the attachtment of the nanoparticle and high oxidation degree of the MWCNT can be observed. (inset) Fast fourier transform (FFT) of the nanoparticle oriented close to the [013] zone axis.

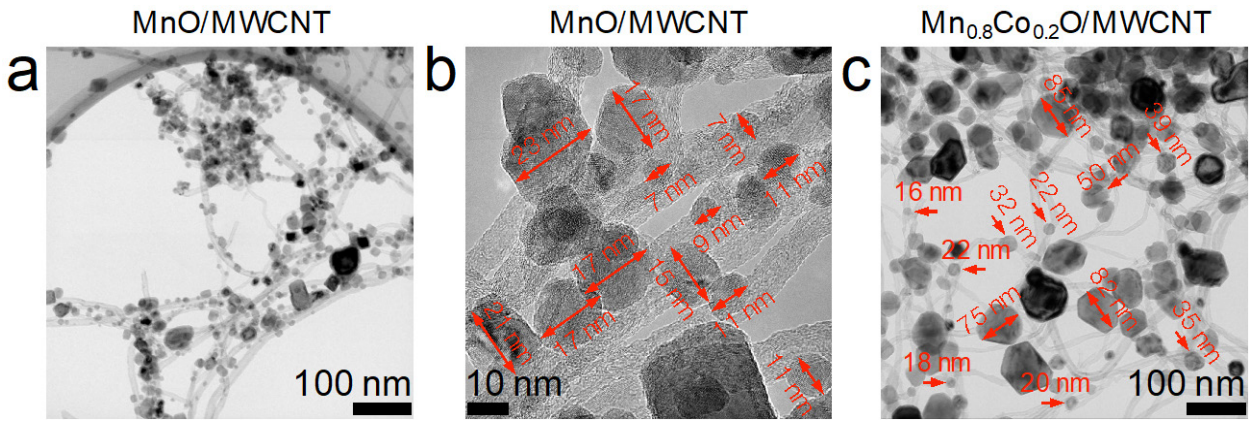

Figure 2.3. TEM images indicating the morphology for: (a–b) MnO/MWCNT and (c) $Mn_{0.8}Co_{0.2}O$/MWCNT samples.

For $x = 0.2$, the Co XPS spectra show that the surface contains CoO, while the XRD results indicate the bulk of the material contains two phases of $Mn_{1-x}Co_xO$, the primary phase being Co poor and the secondary phase being Co rich, likely due to Co segregation towards the surface of the nanoparticles. Because of their rock salt structures and the comparable sizes of Mn^{2+} and Co^{2+} cations, MnO and CoO are known to be soluble over the entire $Mn_{1-x}Co_xO$ ($0 \leq x \leq 1$) composition[117, 118] with a complete solubility at room temperature and a maximum of the miscibility gap in the calculated phase diagram occurring at a very low temperature (242 K) [119]. Despite the calculated complete solubility, phase separation and deviation from the solid solution composition can occur, especially at the surface as has been observed previously by XPS[117] and is observed in the present investigation.

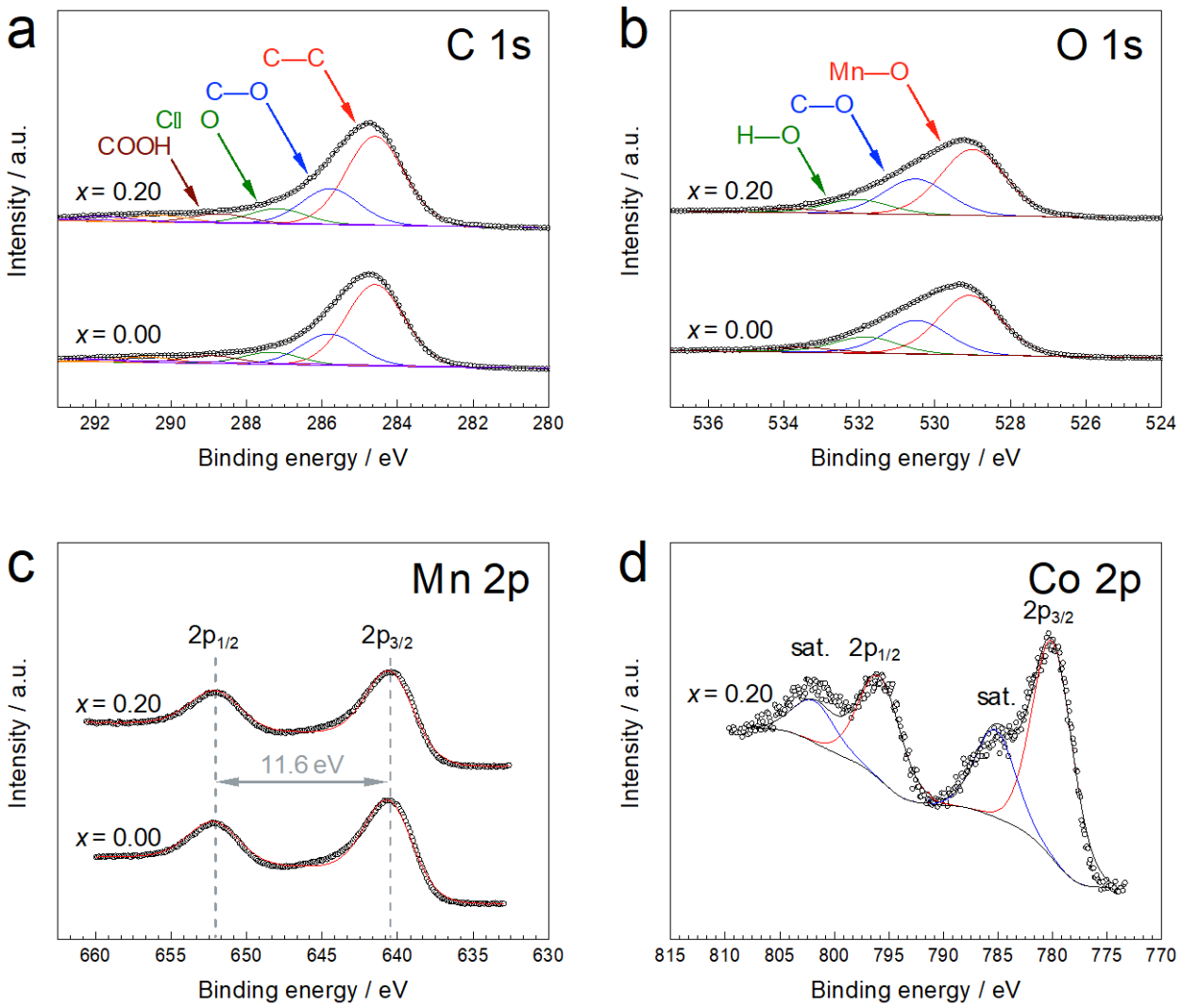

Figure 2.4. High resolution x-ray photoelectron spectroscopy (XPS) spectra of $Mn_{1-x}Co_xO$/MWCNT, $x = 0$ and 0.2, samples at a pass energy of 50 eV and sweep resolution of 0.1 eV for (a) C 1s, (b) O 1s, (c) Mn 2p and (d) Co 2p. Peaks centered at 785.3 and 801.8 eV denoted "sat." are assigned to the satellite peaks of Co(II) in CoO.

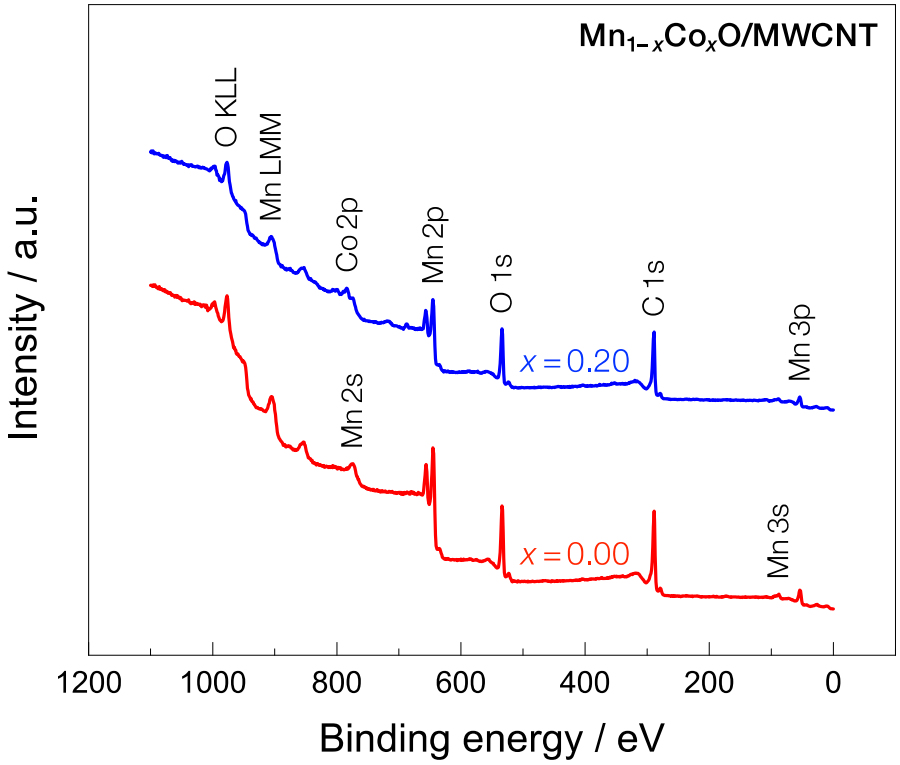

Figure 2.5. X-ray photoelectron spectroscopy (XPS) survey of $Mn_{1-x}Co_xO$/MWCNT for $x = 0$ and 0.2, obtained using Al K_α irradiation at a pass energy of 100 eV and sweeping resolution of 1 eV.

In order to gain more information about the chemical composition of the $Mn_{1-x}Co_xO$/MWCNT, high resolution STEM-EDS analysis was performed as shown in Figure 2.6a-e [Figure 2.6(f-j) for high resolution images] and Figure 2.7. The chemical maps showed spatially uniform dispersion of constituent elements throughout the nanoparticles. No detectable oxygen was found on the MWCNTs (Figure 2.6b,c), although we note that Raman indicates a significant concentration of defects, and XPS indicates C—O, C═O and COOH functional groups.

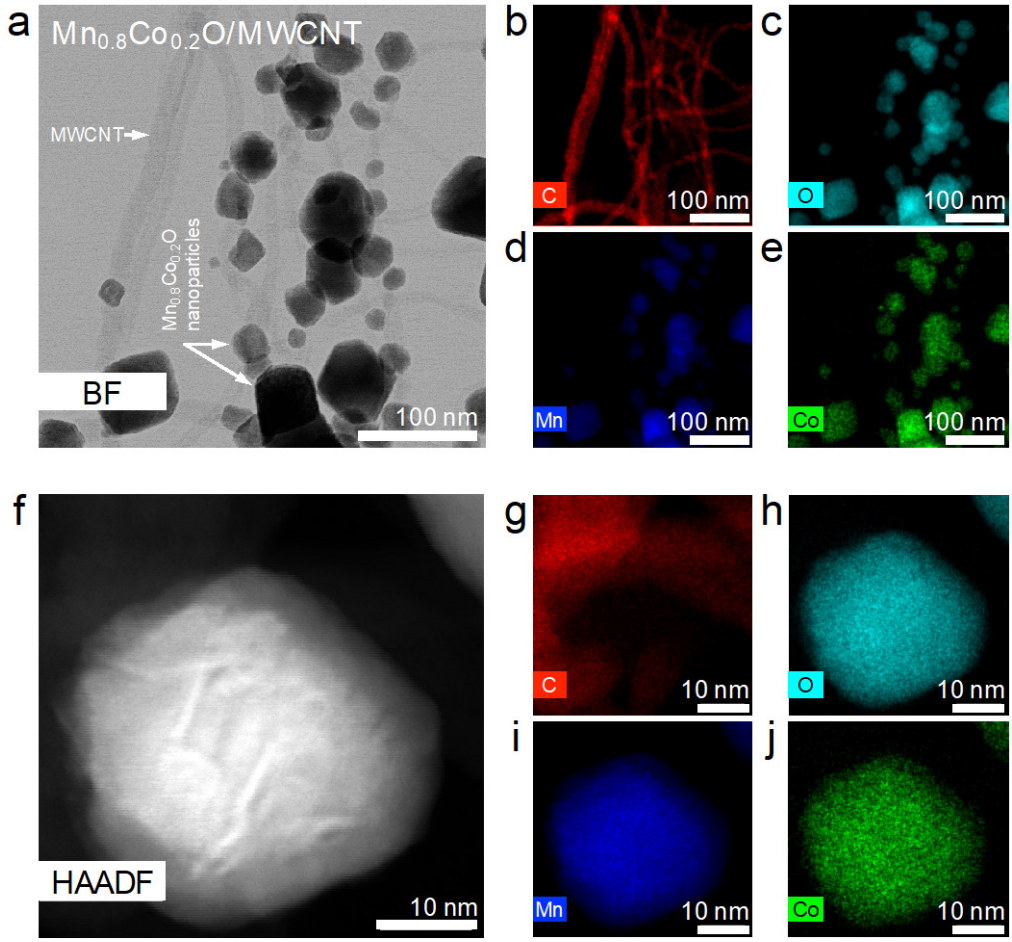

Figure 2.6. Scanning transmission electron microscopy–energy dispersive x-ray spectroscopy (STEM-EDS) analysis of the $Mn_{0.8}Co_{0.2}O$/MWCNT composite. (a) Bright field (BF) STEM image and (b–e) corresponding STEM-EDS intensity maps of the (b) C, (c) O, (d) Mn, and (e) Co K-edge peaks. (f) High-resolution high-angle annular dark-field (HAADF) image and (g–j) corresponding STEM-EDS intensity maps of the (g) C, (h) O, (i) Mn, and (j) Co K-edge peaks.

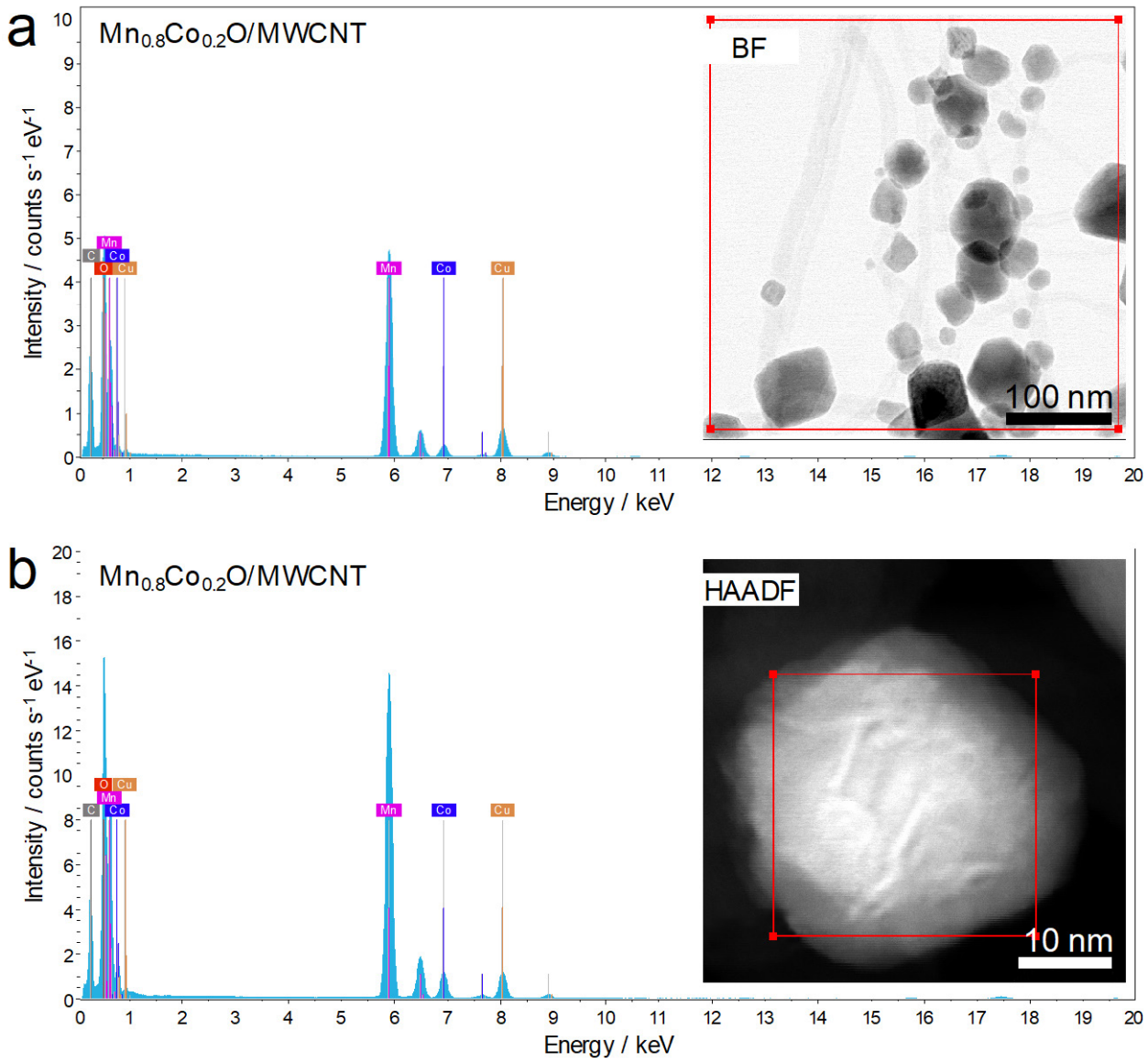

Figure 2.7. Scanning transmission electron microscopy–energy dispersive x-ray spectroscopy (STEM-EDS) spectra of $Mn_{0.8}Co_{0.2}O$/MWCNT nanoparticles exhibiting O, Mn and Co K-edge peaks. Cu peaks originated from the support grid. Insets display the (a) bright field and (b) high-angle annular dark-field (HAADF) images of the nanoparticles.

The $Mn_{1-x}Co_xO$/MWCNT (x = 0, 0.2) nanocomposites were then used as the cathode material in a Li-ion half-cell as described in the methods section. The first cycle charge and

discharge curves of the $x = 0.0$ and 0.2 samples are shown in Figure 2.8(a) and were obtained at a current density of 40 mAg^{-1}. The samples showed initial charge capacities of 474 and 1044 $mAhg^{-1}$ for $x = 0$ and 0.2, respectively at a current density of 40 mAg^{-1}. The features observed in the charge data were correlated with the reduction reaction of Mn^{2+} based on the reaction $MnO + 2Li^{+} + 2e^{-} \rightarrow Mn + Li_2O$, and the formation of the solid electrolyte interphase (SEI) [74]. The re-oxidation (Mn to Mn^{2+}) feature can be found in the slope of the discharge curves from 1 to 1.5 V versus Li/Li^{+} (Figure 2.8(a)). In addition, capacity fades of 25 and 23% from the first cycle to the second cycle were measured for $x = 0$ and 0.2 respectively (at a current density of 40 mAg^{-1}), due to SEI formation.

The charge–discharge behavior of the $x = 0.2$ sample at various current densities are demonstrated in Figure 2.8(b). As expected, the achievable capacities decreased with increasing rates, though the results showed promising trends for high rate capacities. For example, 91% of the discharge capacity at a low current density of 40 mAg^{-1} was still achieved at a higher application-relevant rate of 400 mAg^{-1}. The rate performance of the nanocomposite materials is shown in Figure 2.8(c). Both samples exhibited good high rate capacity performances. For instance, for $x = 0.2$, capacities of 790 and 642 $mAhg^{-1}$ were obtained at current densities of 40 and 800 mAg^{-1}, respectively. At the highest rate we tested, 1600 mAg^{-1}, the $x = 0.2$ sample exhibited a capacity of 553 $mAhg^{-1}$ which is still superior to the theoretical capacity of graphite (372 $mAhg^{-1}$) [3]. This value is higher than that of the reported state-of-the-art Mn-based materials with a higher degree of oxidation (therefore a higher theoretical capacity) at the same current density (390 $mAhg^{-1}$ for Mn_3O_4/reduced graphene oxide composites[120]). After cycling at 1600 mAg^{-1}, excellent reversibility was observed for $x = 0$, 0.2 samples, with measured capacities of 928 and 669 $mAhg^{-1}$ for $x = 0.2$ and 372 and 236 $mAhg^{-1}$ for $x = 0$ at current densities of 40 and 800 mAg^{-1}, respectively.

The remarkable performance of the x = 0.2 composite at high rates is more striking when compared with the state-of-the-art literature data reported in Table 2.1 (high capacity rate column). Figure 2.8(d) illustrates the capacity retention of both samples after 50 cycles from 0 to 3 V versus Li/Li^+ at a current density of 400 mAg^{-1}. After the first five formation cycles, specific capacities of 473 and 740 $mAhg^{-1}$ were maintained at 478 and 709 $mAhg^{-1}$ after 55 cycles at 400 mAg^{-1} for $x = 0$ and 0.2, respectively. A comparison between x = 0, 0.5, 0.15, 0.2, 1 samples is given in the Figure 2.9. As can be seen, the cycling performances of x = 0.15 and 0.2 are close to each other indicating saturation of beneficial charge storage effects in the alloy. Both anodes (x = 0.15, 0.2) show higher capacity retentions than those of MnO/MWCNT and CoO/MWCNT, indicating the improved performance of alloys than their non-alloyed counterparts (x = 0, 1). For instance, the x = 0.2 anode exhibits a capacity 50 and 18 % higher than those of x = 0 and 1 respectively, at the same current rate of 400 mAg^{-1} and after 55 cycles. This is despite the fact that the capacity of the CoO/MWCNT (x = 1) anode increases upon cycling which is attributed to formation of a material with a higher degree of oxidation and a higher theoretical capacity[3, 121]. The excellent stability of a similar preliminary nanocomposite was also demonstrated in a previous study[103].

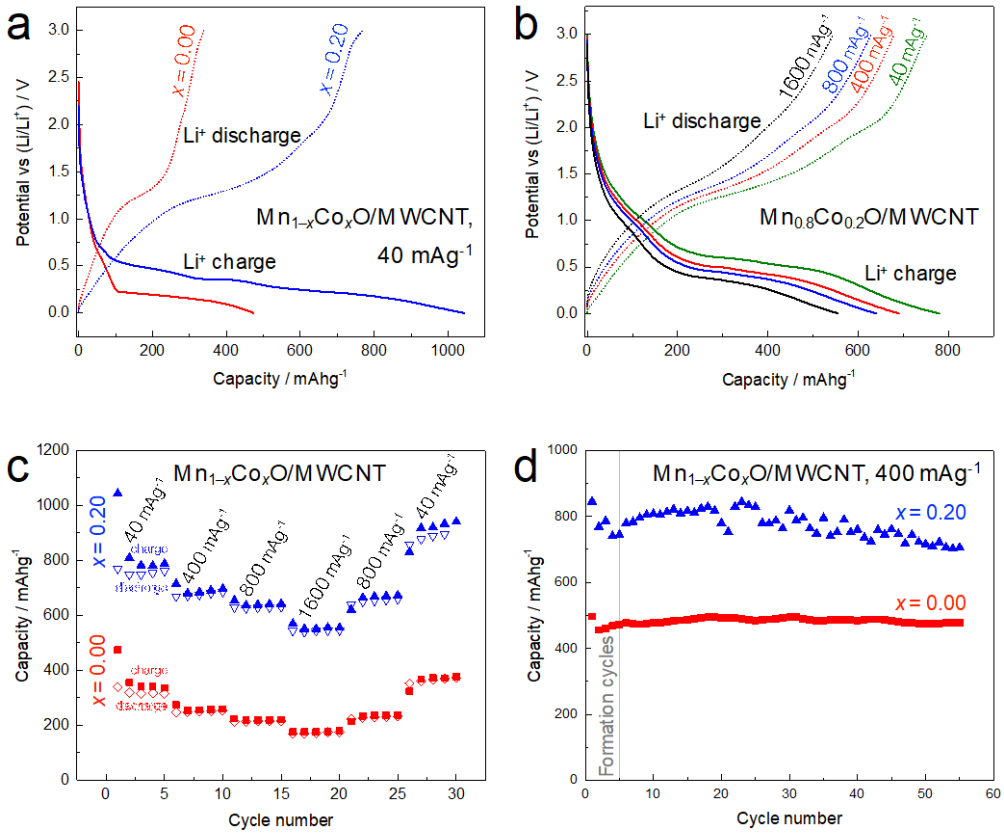

Figure 2.8. (a) First cycle charge–discharge profile of $Mn_{1-x}Co_xO$/MWCNT composites for $x = 0$ and 0.2. (b) Voltage versus specific capacity of $Mn_{0.8}Co_{0.2}O$/MWCNT at different charge–discharge current densities. (c) Current density dependence of the rate capability with cycling initiated at 40 mAg^{-1}. (d) Cycling performance for $x = 0$ and 0.2 initiated and maintained at 400 mAg^{-1} over a voltage range of 0–3 V. The first 5 cycles were considered as formation cycles.

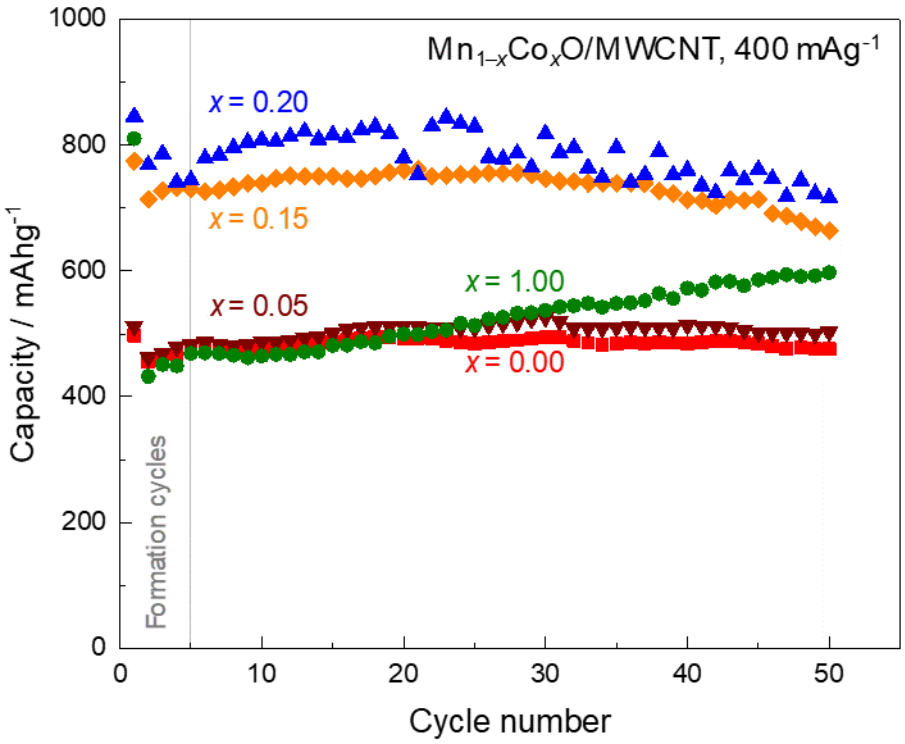

Figure 2.9. Cycling performance of $Mn_{1-x}Co_xO$/MWCNT composites with x = 0, 0.05, 0.15, 0.2 and 1. Cycling was initiated and maintained at 400 mAg^{-1} over a voltage range of 0−3 V.

In order to gain more insights into the role of MWCNTs in the observed high rate-capability of our materials, the electrical resistivities of MnO/MWCNT and pristine MnO were measured using a van der Pauw technique[122, 123] at room temperature. Pellets were fabricated from dried powders using a hydraulic press under 10,000 lb in a 12 mm diameter die. Electrical resistivities of 1.9×10^{7} and 3.9×10^{-1} Ω-cm were obtained from the averaged slopes of multiple current-voltage curves for MnO and MnO/MWCNT samples, respectively. The 8 orders of magnitude reduction in electrical resistivity of the MnO/MWCNT sample at a MWCNT loading of 40 wt% compared to our pure MnO indicated that nucleating electrochemically active nanomaterials onto MWCNTs is an effective strategy to boost electrical conductivity of conversion-reaction anode materials. The

measured electrical resistivity of our pristine MnO is in close agreement with the bulk value (1×10^9 Ω-cm) [7]. The improvement due to MWCNTs is further illustrated by comparison with the cycling performance of MnO and $Mn_{0.8}Co_{0.2}O$ without MWCNTs, where inferior capacities of 273 and 176 $mAhg^{-1}$ are retained after 50 cycles at a current rate of 400 mAg^{-1} (Figure 2.10). Thus, the addition of MWCNTs increases the capacity retention at an application-relevant charge discharge rate of 400 mAg^{-1} by 1.75 and 2 times for $x = 0$ and 0.2 anodes, respectively.

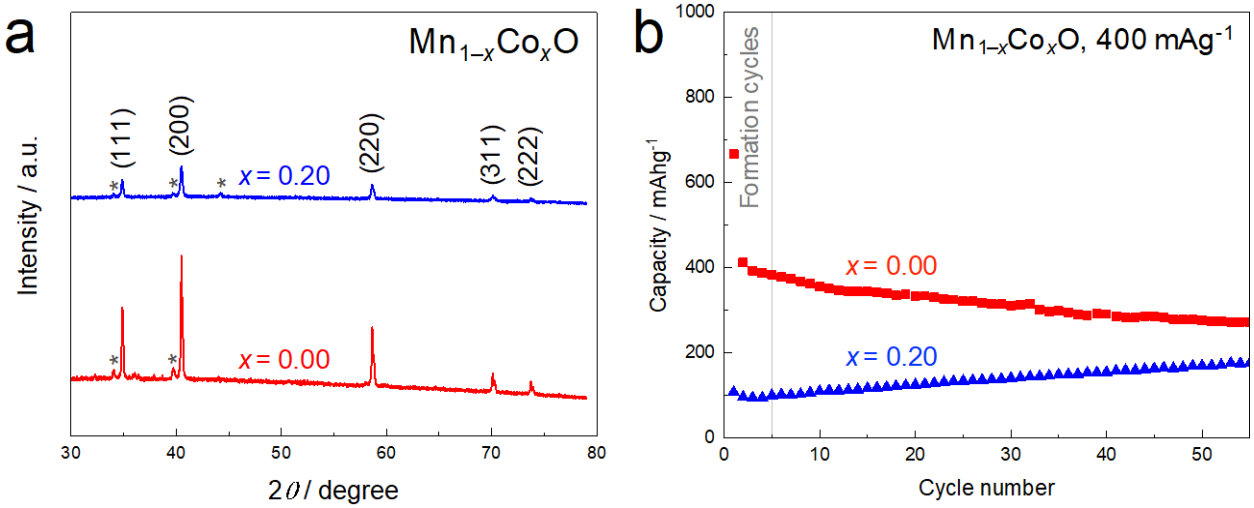

Figure 2.10. (a) XRD patterns and (b) cycling performance of MnO and $Mn_{0.8}Co_{0.2}O$ samples without MWCNTs. (a) The XRD peaks were assigned to cubic MnO according to JCPDS No. 01-077-2929 with a space group of $Fm\bar{3}m$ (225). Small peaks indicated by asterisks do not readily index as MnO_2 or Mn_3O_4, and likely result from unidentified complex manganese oxide phases formed during the synthesis. We note that MnO has a lower theoretical capacity (755 $mAhg^{-1}$) than Mn_3O4 (936 $mAhg^{-1}$) and MnO_2 (1230 $mAhg^{-1}$), therefore these minor phases do not alter our conclusions based on comparison of these samples with our $Mn_{1-x}Co_xO$/MWCNT composite anodes. Cycling was initiated and maintained at 400 mAg^{-1} over a voltage range of 0−3 V. The

low performances of the samples without MWCNTs demonstrates the beneficial role that MWCNTs play in the improvement of these materials by increasing the electrical conductivity.

It should be noted that because the MWCNT weight ratio and oxidation degree play important roles in determining the electrical conductivities of the samples, obtaining a correlation between these variables requires further study. In addition, the effectiveness of the Co substitution can be clearly observed by comparing the electrochemical performance of $x = 0$ and 0.2 samples as the specific capacity of the Co-alloyed sample is 3.1 times higher than that of the sample without Co at the highest measured current density of 1600 mAg^{-1}. This improved performance of the Co-containing samples likely arises due to possible synergistic interactions between Mn and Co in the structure because both MnO[7] and CoO[4] have similar theoretical capacities of 755 and 716 $mAhg^{-1}$, respectively.

The mechanism responsible for improvement through Co-alloying can be better understood through electrochemical impedance spectroscopy (EIS) analysis. The EIS results reveal that Co-alloying facilitates the charge transfer in the composite electrode, as a smaller charge transfer resistance of 315 Ω was obtained for the sample with $x = 0.2$ compared to 700 Ω for $x = 0$ (Figure 2.11 and Table 2.2). To the best of our knowledge, there is no reported computational study describing the physical mechanism responsible for the experimentally observed synergistic effect of Co-alloying on the electrical properties of MnO. However, several experimental studies[124-129] have reported improved electrochemical performances of other phases of manganese oxides by Co-alloying due to enhanced charged transport in the electrode and electrical conductivity of the material. The results of these studies including the present work stress the need for a

comprehensive computational investigation in order to identify fundamental changes in the electronic properties of manganese oxides due to Co-incorporation.

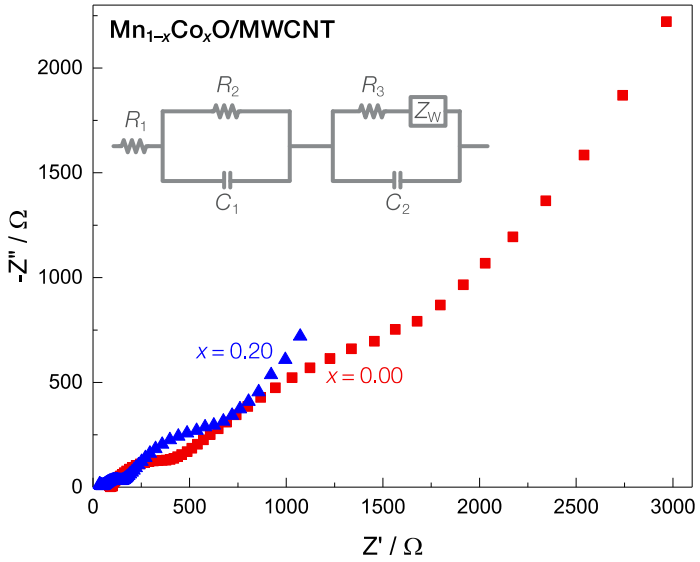

Figure 2.11. Nyquist plot for MnO/MWCNT (red square) and $Mn_{0.8}Co_{0.2}O$/MWCNT (blue triangle). The inset indicates the equivalent circuit.

Table 2.2. Electrochemical impedance spectroscopy analysis of $Mn_{1-x}Co_xO$/MWCNT for $x = 0$, 0.2. The equivalent circuit used to obtain these adjustable parameters is given in Figure 2.11. The smaller value of charge transfer resistance (R_3) observed for $x = 0.2$ is attributed to charge transport facilitation arising from cobalt alloying.

Adjustable Parameters Obtained from EIS	MnO/MWCNT	$Mn_{0.8}Co_{0.2}O$/MWCNT
R_1, electrolyte resistance	95 Ω	40 Ω
R_2, solid electrolyte interphase (SEI) resistance	440 Ω	150 Ω
R_3, charge transfer resistance	700 Ω	315 Ω

Z_W, Warburg diffusion impedance	2.014 mΩ	6.083 mΩ
C_1, SEI capacitance	0.020 mF	0.075 mF
C_2, cell capacitance	0.50 mF	1.50 mF

2.5. Conclusion

In summary, $Mn_{1-x}Co_xO$ nanoparticles were synthesized directly on oxidized multiwalled carbon nanotubes which were subsequently reduced thermally. Structural characterization suggested that the Co incorporated into the MnO structure and no secondary phases were observed up to $x = 0.15$. The improvement in the specific capacity of the composite electrode at charge–discharge rates up to 1600 mAg^{-1} suggests that the method used here can be crucial in the modification of highly insulating earth-abundant materials such as MnO, making them promising candidates for battery applications[3, 130]. In addition to the experimental work described in refs.[8, 103, 131, 132], further detailed investigations are still needed to clear the pathway for the (Mn,Co)O-based materials to reach their optimum potential in practical applications. For instance, the electrochemical contribution of each individual metal oxide and their interactions as an alloy are yet to be understood. The obtained results suggest future computational investigations are necessary to fully understand the role of Co-alloying in improving the charge transport. Identifying the effects of synthesis parameters such as the degree of oxidation of the MWCNTs, the active material to MWCNT weight ratio, and the annealing temperature can optimize the performance of the composite anode. Alloying with other transition metal oxides or alkali and alkaline earth metals will offer the possibility to further increase the electrochemical performance of MnO-based nanocomposite anode materials.

CHAPTER 3: Defect Engineering in MoO_{3-x}: Investigations of Formation Mechanism and Oxygen Reduction Reaction Application[*,†]

3.1 Background

The unique properties of Mo-based oxides including high electrochemical activity and mechanical and thermal durability make them ideal materials for development of many applications including efficient electrochemical energy storage systems[9]. Molybdenum oxidizes exist in a wide variety of structures and stoichiometries[133]. Among these, α-MoO_3 is layered with an orthorhombic structure[15] and monoclinic MoO_2 is known for high electrical conductivity[134]. Previous studies on these materials have been carried out in the fields of Li-ion batteries[12], supercapacitors[9, 15], hydrogen evolution reaction[11], and catalysis[14]. The layered orthorhombic α-MoO_3 with multiple oxidation states is particularly attractive because of its potential for ion intercalation[135], and its high work function (6.6 eV)[136] useful for organic light emitting diode (OLED)[137-140] applications.

MoO_3 is a highly redox-active material as multiple valence states (Mo^{6+}, Mo^{5+} and Mo^{4+}) have been reported to exist as a function of electrochemical potential[135, 141-143], or by oxidation catalysis through interactions with methyl radicals[144]. Further reduction of Mo^{5+} to Mo^{4+} has been reported to occur through formation of a not fully-described intermediate specie by electrochemical electron transfer coupled with a chemical reaction[135, 143]. It has been reported that upon heating α-MoO_3 under vacuum for a long period of times (100 h at 700°C) a series of

[*] Reproduced in part with permission from Sajad Yazdani, Raana Kashfi-Sadabad, Tran Doan Huan, Mayra Daniela Morales-Acosta and Michael Thompson Pettes, "Polyelectrolyte-assisted oxygen vacancies: A new route to defect engineering in molybdenum oxide" *Langmuir* **34**(21), 6296–6306 (2018), https://doi.org/10.1021/acs.langmuir.8b00539. Copyright 2018 American Chemical Society.
[†] Density functional theory calculations was performed by Dr. Huan Tran at the University of Connecticut.

intermediate reduced M_nO_{3n-1} stoichiometries such as Mo_4O_{11}[145], $Mo_{17}O_{47}$, and Mo_8O_{23} are feasible with the most reduced form being MoO_2[133]. Formation of these reduced species involves a lattice rearrangement from corner-shared octahedra to an edge-shared octahedra with a shear structure[133, 146]. Spevack and McIntyre[146] reported that temperatures near 730°C were required in order to reduce MoO_3 thin films, originally synthesized at a low temperature (250°C), to MoO_2. Inzani and co-workers[147] investigated reduction of MoO_3 powders and solution-processed films under dilute (5%) hydrogen gas. Shear defects, nucleation and growth of reduced phases within the MoO_3 matrix were investigated. They reported that extended planar defects within the films acted as nucleation sites for Mo_4O_{11}. Restructuring of the films upon reduction, in order to accommodate oxygen vacancies, was observed.

α-MoO_3 becomes an *n*-type semiconductor by presence of oxygen vacancies as an oxygen vacancy is a shallow donor in MoO_3 making MoO_{3-x} a degenerate *n*-type semiconductor[136]. Furthermore, the presence of oxygen vacancies has been shown to substantially alter physiochemical properties of MoO_3 such as optical properties[16, 148] and electrical conductivity[149-151]. Additionally, oxygen vacancy formation can increase interlayer distances[16], which can potentially lead to improvement of electrochemical performance. Upon reduction of Mo^{6+} to Mo^{5+}, an additional conduction band above the valence band is formed through Mo^{5+}─Mo^{6+} interactions[152]. An additional charge carrier inserted into this conduction band causes a coupled lattice-electron distortion called polaron[152, 153]. A systematic shift of this polaron intervalence band in optical absorption spectra from 2.48 to 2.11 eV has been correlated to a decrease of the metal to oxygen ratio[152, 154].

The layered structure of α-MoO_3 consists of corner-sharing MoO_6 octahedra. This structure includes three oxygen atoms: symmetric (O_s), asymmetric (O_a), and terminal or bridging (O_t). O_a forms a long (2.25 Å) and a short (1.73 Å) asymmetric bond with two Mo atoms in the same sublayer and has 2-fold symmetry, whereas O_s contains 3-fold rotational symmetry with two equal bonds (1.95 Å) to Mo atoms in the same sublayer and a longer (2.33 Å) bond with a Mo atom in an adjacent sublayer. The shortest bond (1.67 Å) is Mo-O_t with only one Mo atom which is perpendicular to the stacking direction[15, 155-158]. Kim and Dunn *et al.* [15] investigated the effects of oxygen vacancies on the structure, chemistry, and charge storage properties of MoO_{3-x}. Using density functional theory (DFT) calculations, they found that a vacancy at oxygen terminal O_t site with two Mo^{5+} ions (bipolaron) near the defect center has the lowest formation enthalpy, and that formation of a Mo^{4+} polaron at the O_t site required slightly (0.19 eV) higher energy than bipolaron Mo^{5+}. Their calculations indicated that vacancy formation at asymmetric O_a and symmetric sites O_s were less favorable with energies of 1.17 eV (for O_a, Mo^{4+} polaron) and 2.09 eV (for O_s, Mo^{5+} bipolaron) higher than that of the O_t site with two Mo^{5+} ions (bipolaron). The reduced MoO_{3-x} retained the original structure during lithiation and delithiation, where incorporation of oxygen vacancies caused a larger interlayer spacing and led to faster charge transfer kinetics and higher specific capacity compared to the fully oxidized MoO_3[15]. In addition, O_t vacancies have been shown to be the catalytic active sites for various reactions including methane oxidation[159], H_2O and CO adsorption[160], hydrogen adsorption[158, 161], methyl adsorption[161], and reduction of NO[162]. Therefore, oxygen vacancies essentially determine physical properties as well as chemical activities of molybdenum oxides which is critical for many applications. This necessitates exploring and discovering effective approaches for the creation of high concentrations of oxygen vacancies in molybdenum oxides.

Oxygen reduction reaction (ORR) is central to the development of various electrochemical systems for energy conversion applications[163, 164]. Developing highly efficient catalysts for ORR is of particular significance in the fabrication of commercial fuel cell devices and metal–air batteries[165]. One of the main challenges in the development of such devices with acceptable cost-effective and energy-efficient characteristics is to find an ideal electrocatalyst for oxygen reduction at the cathode[166]. Nevertheless, electrocatalytic control of the reduction process for gas-phase oxygen is still limited due to slow ORR kinetics which, in turn, is caused by difficult absorption, bond activation, bond cleavage, and removal of oxygen at the solid-gas interface[165]. The slow kinetics of ORR can be overcome through the use of precious noble metal-based catalysts, particularly Pt, which increases the cost significantly. Numerous studies have been conducted on Pt-free catalysts such as transition metal oxides, chalcogenides, nitrides, and oxynitrides[165, 167]. However, the catalytic activity and durability of the existing 'beyond platinum' ORR catalysts are not adequate to an extent that would allow them to replace Pt-based catalysts.

ORR is a reaction that mainly occurs on the surface of the catalyst due to limited oxygen diffusion into the bulk material. As a result, any effort for an improvement should be achievable by modification of the surface chemistry. Liang and Müllen *et al.*[168] reported a collection of mesoporous metal-based ORR catalysts including cobalt/iron–nitrogen-doped carbon by employing vitamin B_{12} and polyaniline–Fe complexes as precursors. The high ORR activity of the mesoporous catalysts was attributed to their high surface area, and uniform distribution of metal and nitrogen active spots. To have the maximum effectiveness, the samples in our work were made mesoporous with surface areas greater than 50 m^2g^{-1}. A high surface area ensures the maximum oxygen accessibility to the catalyst. The electrical conductivity is another factor that plays a crucial role in the ORR activity of catalysts. Graphene supported metal-based catalysts are one of the most

effective means to significantly improve the mechanical and electrical properties as well as surface area[169-171]. In the present work, we report that the interaction between poly(diallyldimethylammonium chloride) (PDDA) and α-MoO_3 is capable of inducing these vacancies. Additionally, a new mechanism is proposed in order to explain the reduction reaction pathway between the charged polymer and the metal oxide surface using experiments and DFT calculations.

Furthermore, reduced graphene oxide (rGO) was used as the conductive support and current collector for the mesoporous catalysts. We combine mesoporous MoO_3 with rGO into a single composite without spoiling the porous mesostructure. Poly(diallyldimethylammonium chloride) (PDDA) was used to create a strong interaction between the rGO support and mesoporous catalysts, as it induces positive charges on rGO[172] causing a strong electrostatic attraction towards mesoporous MoO_3 samples with negative charges.

The results of the DFT calculations supported by experimental observations indicated that the presence of oxygen vacancy sites can greatly enhance the activity by lowering the dissociation energy of ORR intermediate species which are otherwise restricted by stiff Mo─O bonding.

3.2 Methods

3.2.1 Chemicals

Pluronic P123 triblock poly(ethylene oxide)-*b*-poly(propylene oxide)-*b*-poly(ethylene oxide) copolymer (M_w = 5800, $EO_{20}PO_{70}EO_{20}$), 1-butanol (anhydrous, 99.8%), tetraethyl orthosilicate (TEOS), hydrochloric acid (HCl, 37%), ethyl alcohol (CH_3CH_2OH), phosphomolybdic acid (PMA, $H_3PMo_{12}O_{40}{\cdot}xH_2O$), poly(diallyldimethylammonium chloride)

(PDDA) were purchased from Sigma-Aldrich Co. LLC. Hydrofluoric acid (HF, 49%) was purchased from Fischer Scientific Co. LLC. All chemicals were used as received.

3.2.2 Synthesis of mesoporous MoO_3

Based on a previously described procedure[173], mesoporous silica SBA-15 was produced by hydrothermal synthesis a temperature of 100°C for 24 h. 4.4 g of PMA, as the Mo precursor, was impregnated into the channels of SBA-15 (1 g) already dispersed in 25 g of ethanol. The mixture was vigorously stirred for 3 h at room temperature. The nanocasting process was utilized through solvent evaporation[173, 174] of ethanol inside a petri dish placed at 60°C for 12 h. The obtained PMA/mesoporous silica nanocomposite (PMA@SBA-15) was calcined in air at 550°C with a rate of 1 °Cmin^{-1} for 4 h. The silica template in the obtained nanocomposite was removed through etching in a 4% HF aqueous solution.

3.2.3 Synthesis of MoO_{3-x}

200 mg of mesoporous MoO_3 was dispersed in a solution of 200 mL of water:ethanol vol% 1:1. Then 100 µL of PDDA was added to the above solution. The mixture was intensely stirred for 24 hours at room temperature. The PDDA/MoO_3 product was obtained by centrifugation and dried. The final samples were obtained by annealing at 400 and 600°C under Ar (100 sccm) and 5% H_2/95% Ar (20 sccm) for 3 hours with a ramp of 1 °Cmin^{-1}.

3.2.4 Synthesis of mesoporous MoO_3 electrocatalysts

In accordance with established procedures[173, 175], mesoporous silica SBA-15 and KIT-6 hard templates were prepared over the period of 24 hours under hydrothermal conditions at a temperature of 100 °C. A solvent evaporation induced impregnation process[174, 176] was used to

incorporate the PMA precursor into the channels of mesoporous silica similar to the common practice in nanocasting processes. 4.4 g of PMA powder were dispersed in 25g of ethanol followed by the addition of 1 g of SBA-15 template to the solution. The mixture was then stirred intensively at room temperature (20–30°C) for 3 h, before transferring it to a petri dish to be dried at 60°C for 12 h until all of the ethanol evaporated. The obtained PMA/mesoporous silica powder (denoted as PMA@SBA-15) was then transferred into a crucible, heated to 550°C at the rate of 1°C/min, and kept in those conditions for 4 h, producing a MoO_3/mesoporous silica powder (denoted as MoO_3@SBA-15). The silica SBA-15 template in the MoO_3@SBA-15 composite was removed by etching in hydrofluoric acid (4%, aqueous solution). While it may be possible that a small quantity of molybdenum oxide is dissolved in HF, our observation was that MoO_3 was stable in 4% HF aqueous solutions for a period of more than 6 hours. A similar procedure was used to prepare ordered mesoporous MoO_3@KIT-6 samples, except that the SBA-15 template was replaced with an equal amount of KIT-6. The resultant silica template-free powders of MoO_3 nanocast from KIT-6 and SBA-15 are denoted as MoO_3–KIT-6 and MoO_3–SBA-15, respectively.

3.2.5. Synthesis of graphene-wrapped MoO_3–SBA-15

A modified Hummers' method[102, 120] with a lower concentration of oxidizing agent was used to synthesize graphene oxide. The rGO/MoO_3–SBA-15 composite (denoted rGMS) was obtained via an electrostatic interaction between poly (diallyldimethylammonium chloride) (PDDA)-modified graphene oxide and metal oxides in aqueous solutions. In accordance with the procedure described by Chang *et al.,*[177] 0.1 mL of a 20 wt% PDDA solution was first mixed into 40 mL of graphene oxide solution with concentration of 0.5 mL/mg and the mixture was sonicated for 1 h until a transparent solution was obtained. After diluting the solution to 100 mL, 200 mg of mesoporous MoO_3–SBA-15 was sonicated into 100 mL of ethanol. Then, the mesoporous MoO_3–

SBA-15 solution (negatively charged) was mixed with 100 mL of graphene oxide solution (positively charged) and stirred for 12 h. After filtering and drying, the as-prepared GO/MoO_3–SBA-15 composite was thermally reduced at 400°C and 600°C with a rate of 1 °C/min and kept for 2 h at these temperatures in an Ar. Finally, the black-colored products of the reduced samples were obtained. Because MoO_3 is partially reduced during the annealing process, the abbreviation MoO_{3-x} is used to refer to the mixed-phase composites. The products rGO/MoO_{3-x}–SBA15-400°C and rGO/MoO_{3-x}–SBA15-600°C are subsequently denoted as rGMS-400 and rGMS-600.

3.3 Characterization

A Bruker D2 Phaser with Cu Kα radiation (λ = 1.54184 Å) with an operating voltage and current of 30 kV and 10 mA at room temperature was used in order to perform powder X-ray diffraction (XRD) analysis. Quantitative determination of the phase composition was obtained through Rietveld refinement of the XRD patterns using MDI Jade software. The peak profile and background were fitted using a pseudo-Voigt and polynomial functions, respectively. Nitrogen adsorption-desorption isotherms were obtained at -196°C on a Quantachrome Instruments NOVA 2000e®. The degassing process was performed at 150°C under vacuum for a period of 6 h and the Brunauer–Emmett–Teller (BET) method was used in order to calculate the specific surface areas. The pore-size distributions of the samples were obtained by using the Barrett–Joyner–Halenda (BJH) method. Phase contrast transmission electron microscopy (TEM), selected area electron diffraction (SAED), and energy dispersive X-ray spectroscopy (EDS) were performed using a JEOL 2010 FasTEM at 200 kV. X-ray photoelectron spectroscopy (XPS) analysis was conducted on a PHI Model 590 spectrometer with multipoles (Φ Physical Electronics Industries Inc.), with Al Kα radiation (E_{photon} = 1486.6 eV). A TA Instruments Hi-Res TGA Q500 thermogravimetric

analyzer was used to perform thermal gravimetric analysis (TGA) from 25 to 800°C at a heating rate of 10 °Cmin^{-1} and a flow rate of 60 mLmin^{-1} under air and nitrogen. TGA analysis on copper(II) oxalate hemihydrate (98%, Alfa Aesar No. A15365) under N_2 in order to make sure there was no leakage in the TGA furnace. This was confirmed by observing no oxidation in the TGA analysis as shown in Figure 3.1. In addition, the error due to weight loss measurements was obtained by performing the TGA analysis of Pt under Air and N_2. The maximum error corresponding to the weight difference at 600°C was calculated as $x = \pm 0.005$. A TA Instruments SDT Q600 was used in order to perform differential scanning calorimetry (DSC) analysis on the samples from room temperature to 1200°C at a rate of 10 °Cmin^{-1} under Ar with a flow rate of 100 mLmin^{-1}. Zeta potential measurements were conducted on a Malvern Instruments Ltd Zetasizer Nano ZS.

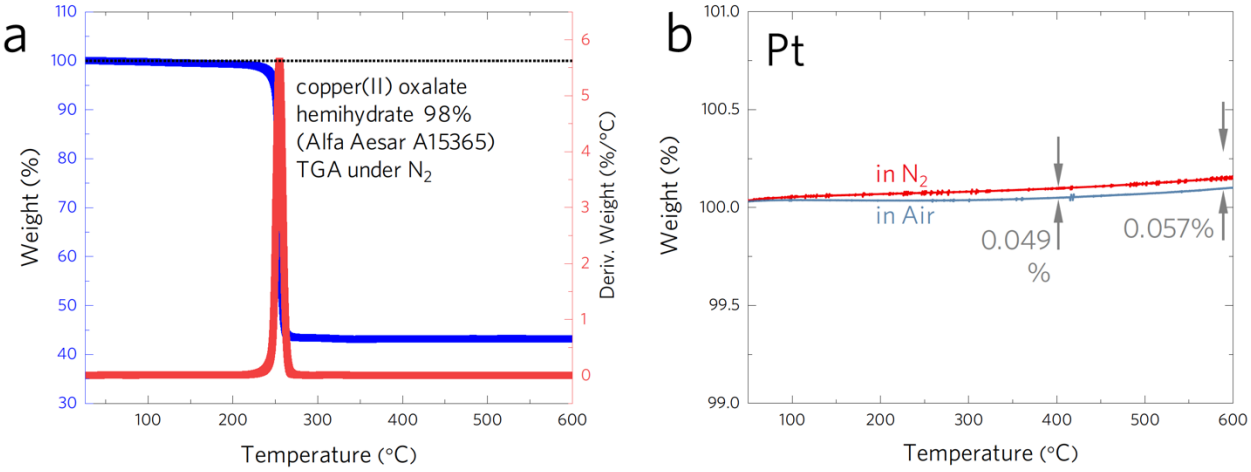

Figure 3.1. (a) Thermogravimetric analysis (TGA) of copper(II) oxalate hemihydrate 98%, Alfa Aesar No. A15365 under N_2. (b) TGA analysis of Pt under air and N_2. The TGA analysis of Copper(II) oxalate hemihydrate with no oxidation confirms there is no leakage in the TGA instrument. The weight difference between Pt analysis in air and N_2 was used as the error in the MoO_{3-x} weight loss measurements by TGA, where we obtain a confidence value in x of ±0.005.

3.4 Electrochemical measurements

The electrochemical measurements were carried out at room temperature in a three-electrode glass cell connected to a CH Instruments 760E electrochemistry workstation. A graphite rod was used as the counter electrode and a saturated calomel electrode (SCE) was used as the reference electrode. The potential was calibrated with respect to a reversible hydrogen electrode (RHE) by experimental measurements using two Pt electrodes and working and counter electrodes in a hydrogen-saturated solution. To prepare the working electrode, 4 mg catalyst, 1 mg carbon black, 200 uL ethanol, 800 uL DI-water and 50 uL nafion solutions were mixed and ultrasonicated for at least 1 h to form a homogeneous catalyst ink. Afterward, 10 μL of this ink was drop-cast onto the 5 mm-diameter glassy carbon rotating disk electrode (RDE, Pine Instruments) and dried under an infrared lamp for 30 min, yielding a catalyst loading of ~0.255 mg/cm^2. Before the test measurements, O_2 was bubbled through the electrolyte solution to supply enough O_2 reactant. Cyclic voltammetry was firstly conducted for tens of scans with a scan rate of 50 mV/s to reach a stable state, and linear sweep voltammetry (polarization curve) with a scan rate of 5 mV/s was measured in 0.1 M KOH electrolyte. AC impedance measurements were carried out in the same configuration at the potential of 1.71 versus RHE from 0.1–10^5 Hz with an AC voltage of 5 mV.

3.5 Density functional theory calculations [*]

The Vienna Ab initio Simulation Package (VASP) [178], was employed for conducting the density functional theory (DFT) calculations by adopting a basis set of plane waves with kinetic energies up to 500 eV. Exchange-correlation energies were obtained by using Perdew-Burke-Ernzerhof functional[179] for all calculations. When the atomic forces calculated during the

[*] DFT calculations was performed by Dr. Huan Tran at the University of Connecticut.

optimization fall below 0.01 eV/Å equilibrium structures were assumed. According to the method established by ref. [179], Dudarev's approach[180] was used to describe the *d* electrons of Mo. $U = 6.0$ eV was adopted for the onsite Coulomb term. The U value may be different across materials. For MoO_3, there are a number of values used by different researchers, who adopted different numerical details. These values include 5 eV[181], 6.3 eV[156, 182], 3eV and 7eV[183]. Here, U = 6 eV was chosen which, when combining with other details of the numerical scheme, produces reasonable geometry with respect to the experimental data. Using the optB88-vdW functional[184, 185], the dispersion van der Waals interaction was calculated. Rozzi and co-workers[186] used a different approach with tight binding LMTO-ASA program with LDA.

For the polaron (Mo^{4+}) and bipolaron ($2 \times Mo^{5+}$) configurations, we adopted the procedure described in ref. [187], i.e. intentionally localizing/delocalizing the electron density at the interest Mo sites. Bulk MoO_3 models were constructed based on a 3×1×3 supercell of MoO_3. In order to model MoO_3 slabs, a vacuum layer in 10 Å thickness was appended to the bulk models, which uncovered O_t atoms on the (010) surface, and to suppress the interactions along the *y*-direction. This is the most stable surface of MoO_3 because of its layered structure. PDDA-MoO_3 interaction was assumed to be on this surface. The relaxed lattice parameters of a = 3.930 Å, b = 13.951 Å, and c = 3.711 Å were consistent with those reported in Ding *et al.* [184] Based on the performed Bader charge analysis, the charge for Mo^{6+}, Mo^{5+}, Mo^{4+}were obtained as 2.11e, 2.66e, and 3.12e, respectively. For these results, we note that we used 6 valence electrons for Mo.

3.6. Oxygen vacancy formation due to the PDDA polyelectrolyte interaction

Mesoporous samples offer higher surface areas accessible for introduction of oxygen vacancies suitable for surface-chemistry related applications[188]. Thus, the nanocasting method

using a SBA-15 silica hard template[173] was adopted in this work in order to effectively enhance the surface area of the samples. Figure 3.2 shows TEM analysis of the templated sample after calcination at 550°C in air and removal of silica SBA-15 template – subsequently denoted as fully oxidized O-MoO_3. A comparison between the TEM images of SBA-15 and O-MoO_3, indicate that the hexagonally aligned nanowire structure of the parent template has been replicated, as shown in Figure 3.2a,b. The BET surface areas were obtained as 529 and 50 m^2g^{-1} for the SBA-15 silica hard template and O-MoO_3, respectively. The BJH pore size distributions of the SBA-15 and O-MoO_3 were focused at 5.4 and 7.2 nm, respectively.

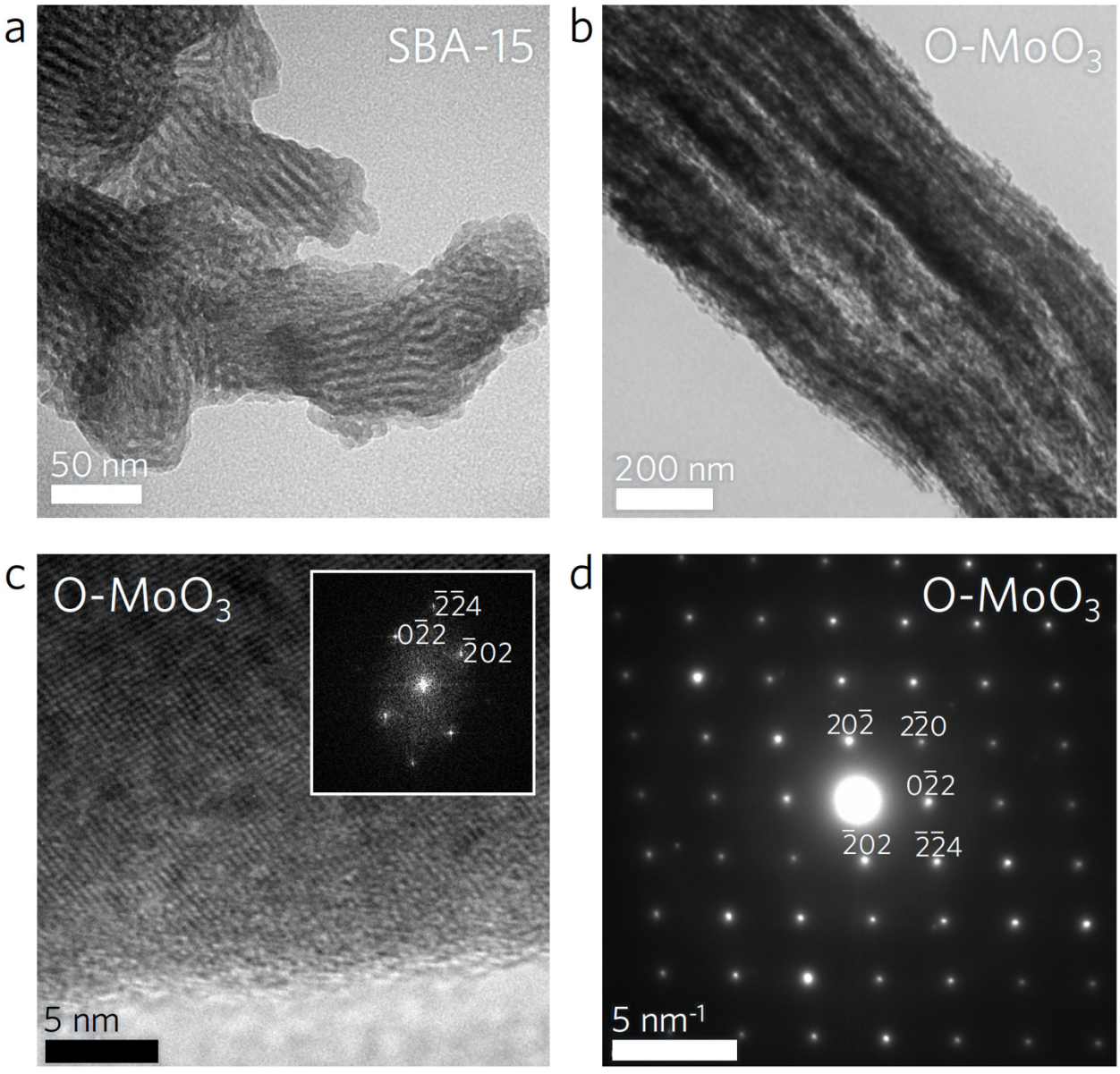

Figure 3.2. Transmission electron microscopy (TEM) analysis of SBA-15 silica hard template and mesoporous fully oxidized O-MoO_3. TEM images of mesoporous (a) SBA-15 and (b) O-MoO_3. (c) High resolution TEM of O-MoO_3 and (c, inset) fast Fourier transform (FFT). (d) Selected area electron diffraction (SAED) pattern along the $[1\bar{1}2]$ zone axis for O-MoO_3.

The selected area electron diffraction (SAED) patterns and high resolution TEM of O-MoO_3 are shown in Figure 3.2c,d. SAED patterns were assigned to the orthorhombic phase of MoO_3 along the [1$\bar{1}$2] zone axis, and the phase contrast image revealed that the sample was well crystallized. The EDS spectra of the mesoporous sample (Figure 3.3) displays strong signals from elemental Mo and O with no signals from silicon, or other detectable impurities indicating the complete removal of the SBA-15 silica template after the HF etching process.

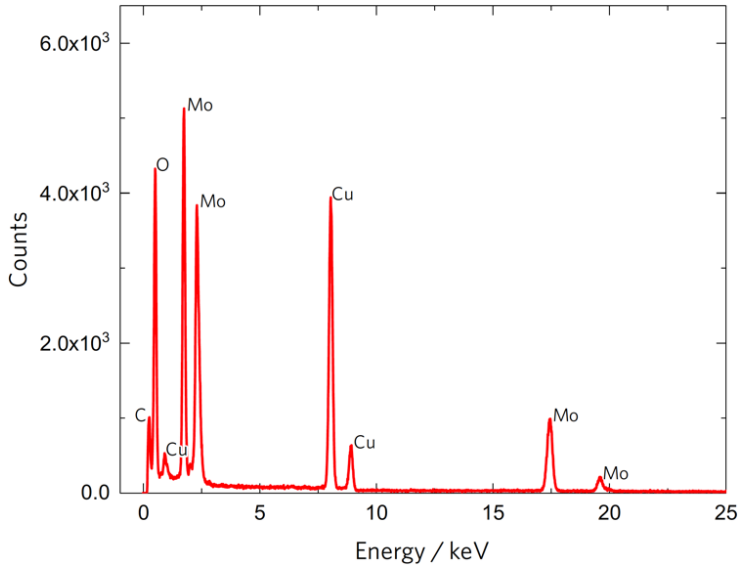

Figure 3.3. Energy dispersive X-ray spectroscopy (EDS) spectrum of O-MoO_3. The C and Cu peaks arise from beam interactions with the grid and sample holder. No peak from Si was detected, indicating the complete removal of the SBA-15 silica hard template.

Figure 3.4 demonstrates the high angle XRD patterns for all samples. O-MoO_3 refers to the fully oxidized mesoporous sample templated by SBA-15, calcined at 550°C in air, and released by HF etching. By annealing the fully oxidized O-MoO_3 sample at 400 and 600°C under Ar or 5%H_2/95%Ar, MoO_{3-x}–400 and MoO_{3-x}–600 samples are obtained, respectively. The XRD

patterns of the samples annealed under Ar (Figure 3.4a) were referenced to an orthorhombic α-MoO_3 with a space group Pbnm (space group 62) according to powder diffraction file #05-0508. From a comparison between the XRD patterns of MoO_{3-x}–400 and O-MoO_3 it can be found that annealing under Ar (400 and 600°C, 3 h) did not result in a full conversion of oxidized MoO_3 to other stoichiometries of the metal oxide. The weak peaks for MoO_{3-x}–600 are indexed to an orthorhombic phase of Mo_4O_{11} ($Pna2_1$, space group 33, powder diffraction file #84-0687) and to a triclinic phase of $Mo_{18}O_{52}$ (P-1, space group 2, powder diffraction file #74-1664), indicating weak reduction at 600°C – and negligible reduction at 400°C – occurs by thermal annealing. The Rietveld quantitative phase analysis indicates that the MoO_{3-x}–600 sample contains 55.8, 33.1 and 11.1 wt% of MoO_3, $Mo_{18}O_{52}$ and Mo_4O_{11}, respectively. In contrast, the XRD patterns of the oxidized O-MoO_3 sample indicate significant reductions of MoO_3 to MoO_{3-x} when thermally reacted with PDDA polyelectrolyte. These samples are denoted as MoO_{3-x}–PDDA-400 and MoO_{3-x}–PDDA-600 where Ar annealing was performed at 400 and 600°C, respectively. MoO_{3-x}–PDDA-400 pattern corresponds to the orthorhombic phase of MoO_3 (84 wt%) and the monoclinic phase of MoO_2 (16 wt%). MoO_{3-x}–PDDA-400 shows changes in the orientation of crystal planes along [020], [040] and [131] directions. Peak intensity ratios $I_{[040]}/I_{[110]}$ = 1.9, $I_{[020]}/I_{[110]}$ = 1.3, and $I_{[131]}/I_{[110]}$ = 0.9 were measured for the MoO_3–PDDA-400 whereas values $I_{[040]}/I_{[110]}$ = 1.0, $I_{[020]}/I_{[110]}$ = 1.0 and $I_{[131]}/I_{[110]}$ = 0.4 were obtained for the O-MoO_3 sample. However, by increasing the annealing temperature to 600°C (sample MoO_{3-x}–PDDA-600), the XRD pattern indicates the presence of Mo_4O_{11} (61.4 wt%), MoO_2 (28.3 wt%) and $Mo_{18}O_{52}$ (2.21 wt%), as indicated in Figure 2. The results of XRD analysis demonstrate the strong oxygen reduction of the oxidized sample triggered by using a PDDA polyelectrolyte to enhance the thermal reduction reaction rate.

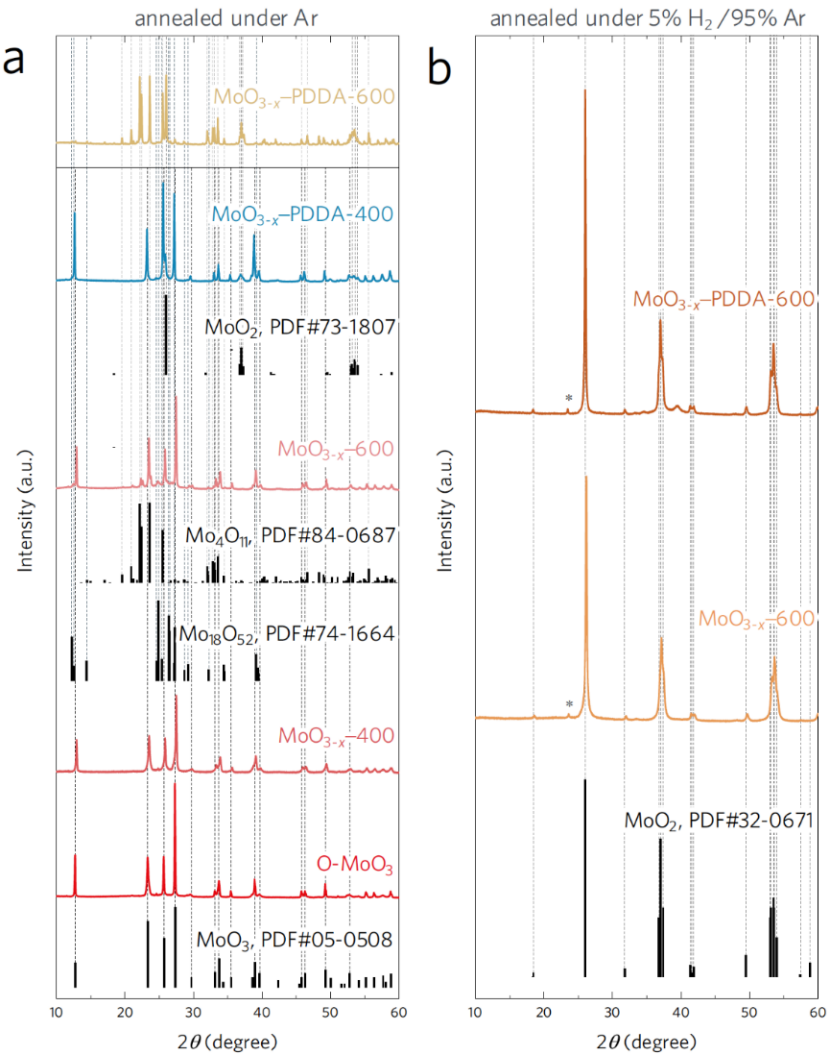

Figure 3.4. X-ray diffraction (XRD) analysis reveals routes to creating sub-stoichiometric MoO_3. XRD patterns for the mesoporous fully oxidized O-MoO_3, oxidized samples annealed under Ar without PDDA polymer (MoO_{3-x}–400 and MoO_{3-x}–600) at 400 and 600°C under Ar respectively, and oxidized samples annealed under Ar with PDDA polymer (MoO_{3-x}–PDDA-400 and MoO_{3-x}–PDDA-600) at 400 and 600°C under Ar respectively. (b) XRD patterns of MoO_{3-x}–600 (sample with no PDDA) and MoO_{3-x}–PDDA-600 (sample with PDDA) annealed under 5% H_2/95% Ar at 600°C. The weak peak at $2\theta = 23.4°$ (asterisks) is due to K-beta emission from the copper anode of the X-ray diffractometer.

Exhibiting more intense reduction compared to the samples annealed under Ar at the same conditions, the XRD patterns of the samples annealed under H_2-containing gas (5% H_2/95% Ar) indicated that both samples without and with PDDA were fully reduced to MoO_2 at 600°C for 3 h (Figure 3.4b).

The degree of reduction of the samples were calculated based on TGA analysis. The difference between the weight loss under air (assuming saturation to the fully oxidized O-MoO_3) and nitrogen (representing the reduced form, MoO_{3-x}) atmospheres were used to calculate the amount of vacancies, as illustrated in Figure 3.5. The sub-stoichiometry concentration x is calculated from the balance equation

$$M_w(MoO_3) = (1+[(\%\ mass\ loss\ or\ gain\ in\ air)–(\%\ mass\ loss\ in\ N_2)]/100)\times M_w(MoO_{3-x}), \quad (3.1)$$

where M_w refers to the molecular weight. Table 3.1 contains the detailed information on thermal treatment conditions, Rietveld quantitative phase analysis and the sub-stoichiometry parameter x of the samples. For the oxidized samples reduced without the use of PDDA polymer, MoO_{3-x}–400 and MoO_{3-x}–600, the degrees of vacancies were calculated as $x = 0.01$, 0.03, respectively. This demonstrates negligible reduction of MoO_3 in the absence of PDDA. In contrast, degree of reduction of $x = 0.14$ ($MoO_{2.86}$) and 0.36 ($MoO_{2.64}$) were obtained for the reduction of oxidized samples with the use of PDDA after thermal annealing at 400°C (MoO_{3-x}–PDDA-400) and 600°C (MoO_{3-x}–PDDA-600), respectively. The weight loss due to PDDA decomposition is not observed as it was previously removed during the annealing process confirmed by TGA analysis of PDDA shown in Figure 3.6.

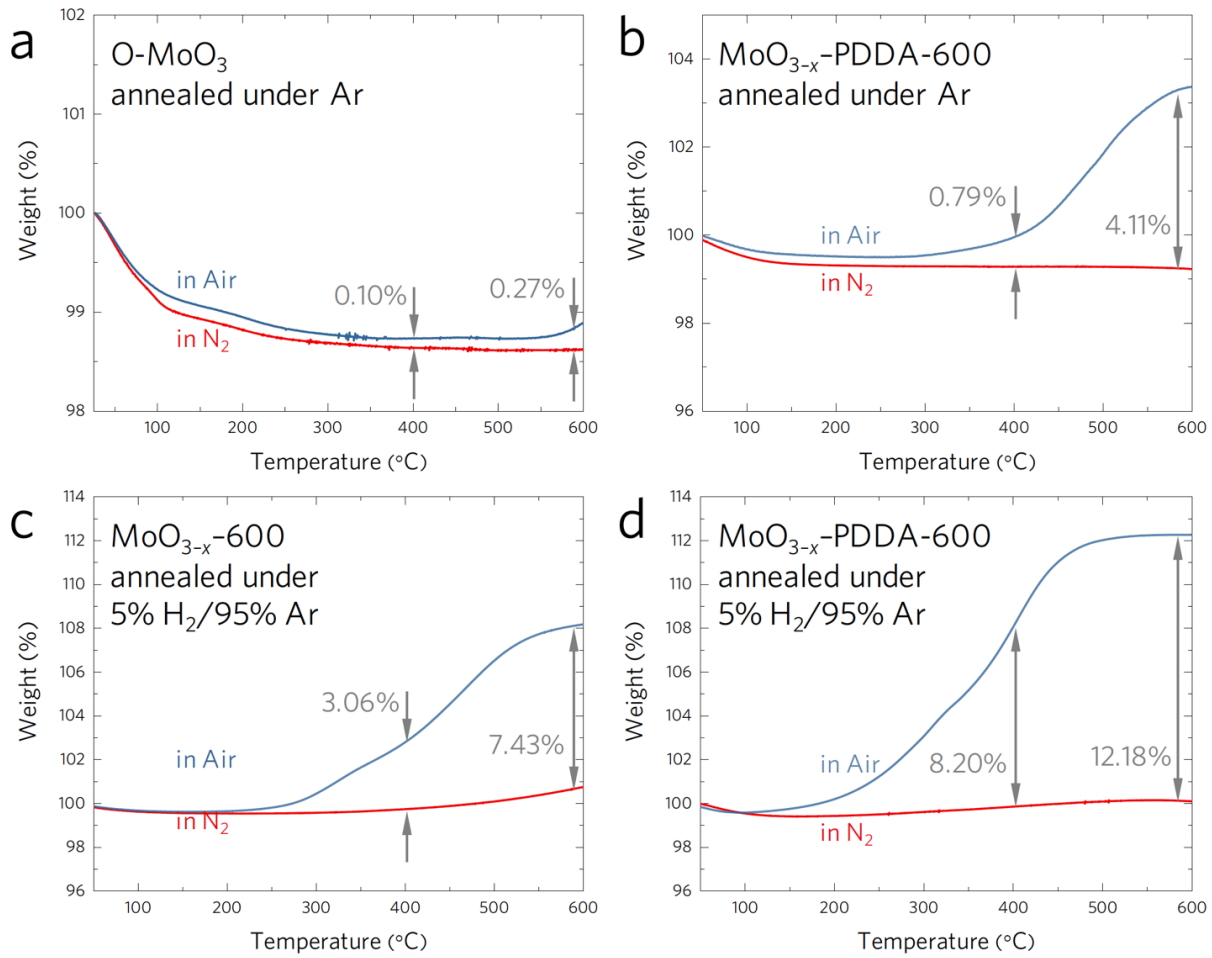

Figure 3.5. Thermogravimetric analysis (TGA) indicates PDDA treatment is effective reduction of MoO_3. Air and nitrogen TGA analysis of: (a) O-MoO_3 (sample without PDDA), (b) MoO_{3-x}–PDDA-600 (sample with PDDA) annealed under Ar at 600°C, (c) MoO_{3-x}–600 (sample without PDDA) annealed under 5%H2/95%Ar at 600°C, and (d) MoO_{3-x}–PDDA-600 (sample with PDDA) annealed under 5% H_2/95% Ar at 600°C. Using the comparison between the weight loss/gain in air and nitrogen, the value of x is quantified according to equation (3.1). Prior to TGA characterization, both samples were annealed under the specified gas at 600°C for 3 hours. For this reason, weight loss due to PDDA decomposition did not appear in the obtained data as the polyelectrolyte was removed during the annealing process. Therefore, any weight loss/gain can be ascribed to oxygen sub-stoichiometry.

The TGA analyses indicated the PDDA interaction significantly enhanced the oxygen sub-stoichiometry concentrations under both Ar and 5% H_2/95% Ar atmospheres. Figure3.5c and 3.5d compare the TGA analysis of the samples without and with PDDA, respectively, both pre-annealed under the H_2-containing gas. It was observed that using PDDA polyelectrolyte enhanced the weight difference between the oxidized and the reduces samples from 7.43 to 12.18% under 5% H_2/95% Ar at 600°C. Similar enhancement was seen from 3.06 to 8.2 at 400°C.

As calculated in Table 3.1, the sub-stoichiometry parameter x in MoO_{3-x} increased from 0.03 to 0.36 by using PDDA under Ar, and from 0.62 to 0.98 by using PDDA under 5% H_2/95% Ar gas. The results of TGA analysis are in agreement with our conclusions based on the XRD data. The reduction of samples with PDDA was further witnessed by differential scanning calorimetry (DSC) analysis showing a disappearance of the endothermic peak corresponding to the MoO_3 melting point at 798.6°C (Figure 3.6a).

Table 3.1. Detailed annealing conditions, Rietveld refinement phase analysis and oxygen sub-stoichiometry concentration "*x*" in MoO_{3-x} determined by thermogravimetric analysis as given by equation 3.1.

Sample ID	Annealing conditions			Annealing gas	Rietveld refinement				x (±0.005) based on TGA
	Temperature (°C)	Rate (°C min^{-1})	Time (h)		MoO_3	$Mo_{18}O_{52}$	$Mo_{18}O_{52}$	MoO_2	
O-MoO_3	550	1	4	Air	100%	--	--	--	0.00
MoO_{3-x}–400	400	1	3	Ar	100%	--	--	--	--
MoO_{3-x}–600	600	1	3	Ar	55.8%	33.1%	11.1%	--	0.03
MoO_{3-x}–PDDA-400	400	1	3	Ar	84.0%	--	--	16.0%	--
MoO_{3-x}–PDDA-600	600	1	3	Ar	--	61.4%	10.3%	28.3%	0.36
MoO_{3-x}–600	600	1	3	5%H_2/95% Ar	--	--	--	100%	0.62
MoO_{3-x}–PDDA-600	600	1	3	5%H_2/95% Ar	--	--	--	100%	0.98

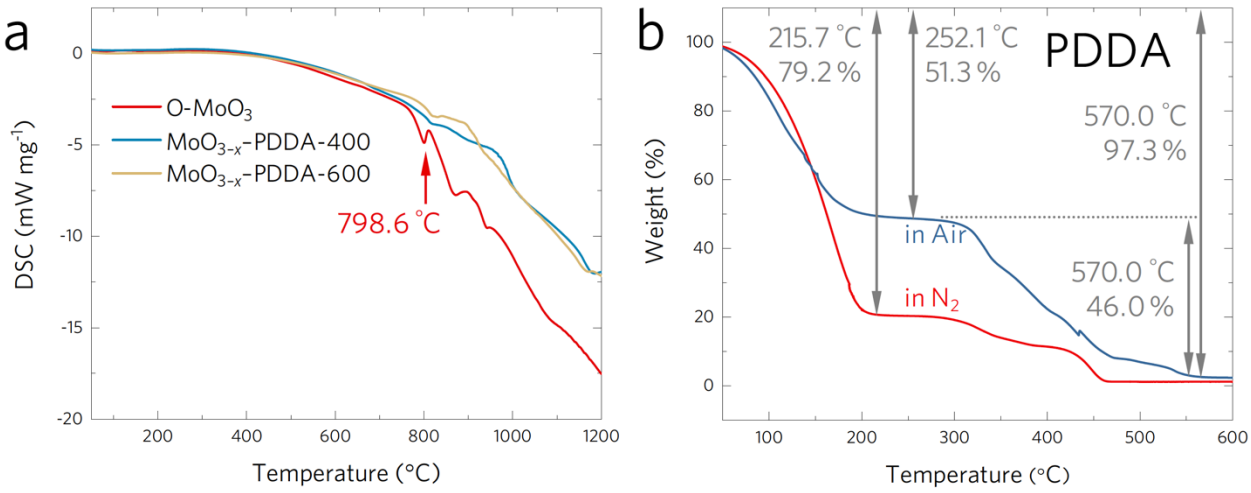

Figure 3.6. (a) Differential scanning calorimetry (DSC) analysis under argon showing the disappearance of the endothermic phase transition corresponding to melting point of MoO_3 towards higher temperatures in reduced samples MoO_{3-x}–PDDA-400 and MoO_{3-x}–PDDA-600 as compared to the fully oxidized O-MoO_3. This disappearance is due to higher melting points of MoO_{3-x} and MoO_2 compared to MoO_3 (measured at 798.6°C for O-MoO_3). (b) Thermal gravimetric analysis (TGA) of the PDDA polyelectrolyte indicating its decompositions under air and nitrogen atmospheres.

X-ray photoelectron spectroscopy (XPS) was employed in order to quantify the oxidation states in O-MoO_3, MoO_{3-x}–PDDA-400, and MoO_{3-x}–PDDA-600 samples (Figure 3.7). The survey XPS is shown in Figure 3.8. The results indicated that MoO_3 involved only peaks assigned to Mo^{6+} in accordance to the XRD analysis. The high-resolution XPS analysis of MoO_{3-x}–PDDA-400 and MoO_{3-x}–PDDA-600 exhibited peaks assigned to both Mo^{4+} and Mo^{5+} which is a clear sign of reduction in these samples. The XPS surface area ratios of molybdenum oxidation states were calculated as $Mo^{4+}/Mo^{6+} = 1.0$ and $Mo^{5+}/Mo^{6+} = 3.3$ for the MoO_{3-x}–PDDA-400 sample reduced at 400°C, showing that its surface consisted primarily of $v_O^{\cdot}$ vacancy sites ($v_O^{\cdot}$ refers to an oxygen

vacancy with a single positive charge according to Kröger-Vink notation). Area ratios of $Mo^{4+}/Mo^{6+} = 3.7$ and $Mo^{5+}/Mo^{6+} = 2.6$ were obtained for the MoO_{3-x}–PDDA-600 sample reduced at 600°C suggesting that $v_O^{\cdot\cdot}$ sites form the majority of the vacancy species when higher annealing temperatures are used ($v_O^{\cdot\cdot}$ refers to an oxygen vacancy with two positive charges according to Kröger-Vink notation). The area ratio of Mo^{4+} in MoO_{3-x}–PDDA-600 to Mo^{4+} in MoO_{3-x}–PDDA-400 was calculated as 2.7. Thus, as annealing temperature increases from 400 to 600°C, the ratio of Mo^{4+} increases significantly. This indicates that creation of Mo^{4+}-$v_O^{\cdot\cdot}$ vacancy complexes likely requires higher thermal energies. The fitting parameters for XPS Mo^{6+}, Mo^{5+}, and Mo^{4+} $3d_{3/2}$ and $3d_{5/2}$ spectral data and peak area ratios were compared with previous studies[173, 189] as presented in Table 3.2.

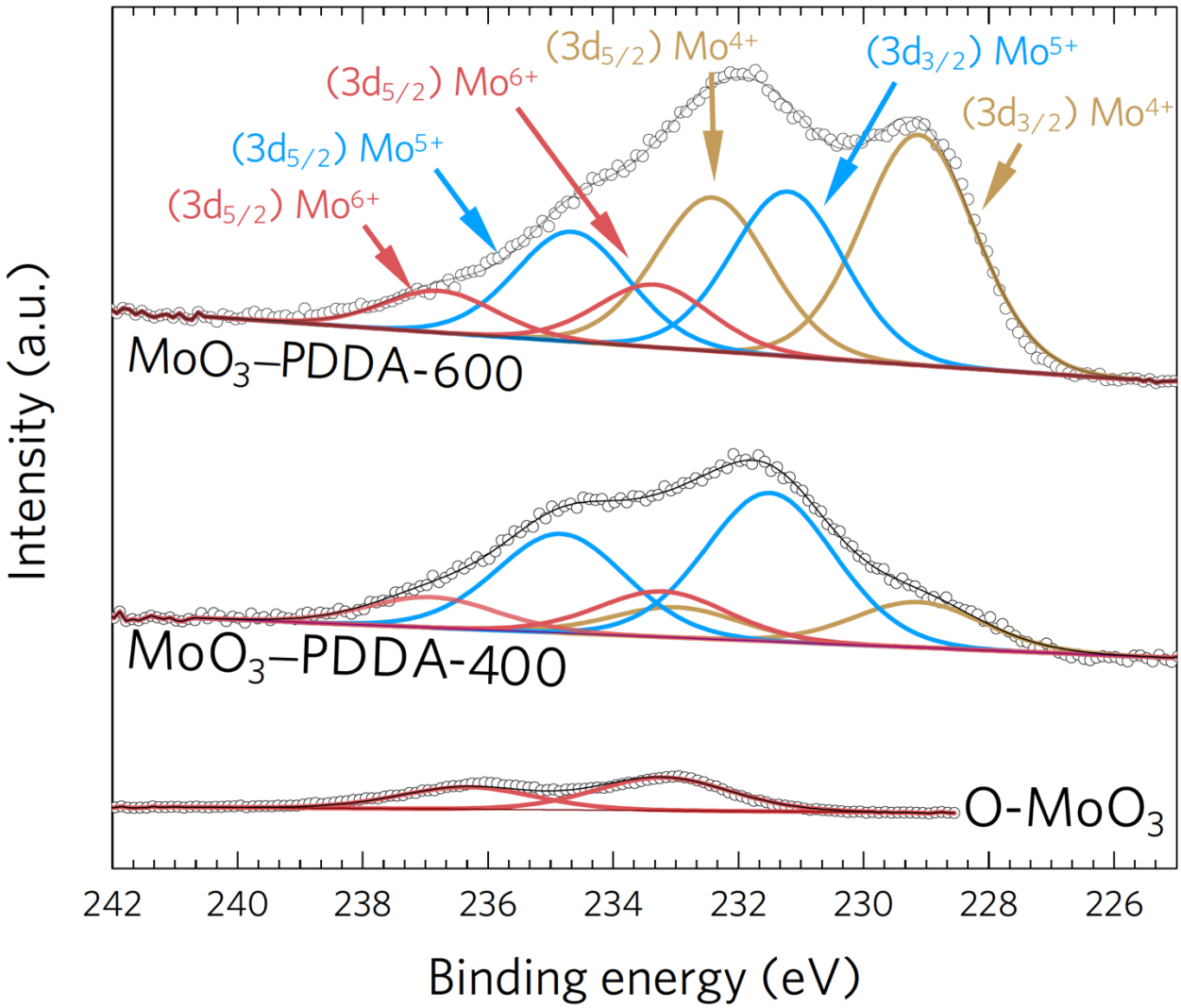

Figure 3.7. X-ray photoelectron spectroscopy (XPS) indicates valence state of oxygen vacancy defects created by metal oxide/PDDA interaction. Deconvolved Mo 3d XPS spectra of pure mesoporous fully oxidized O-MoO_3 and of reduced MoO_{3-x}–PDDA-400 and MoO_{3-x}–PDDA-600 samples.

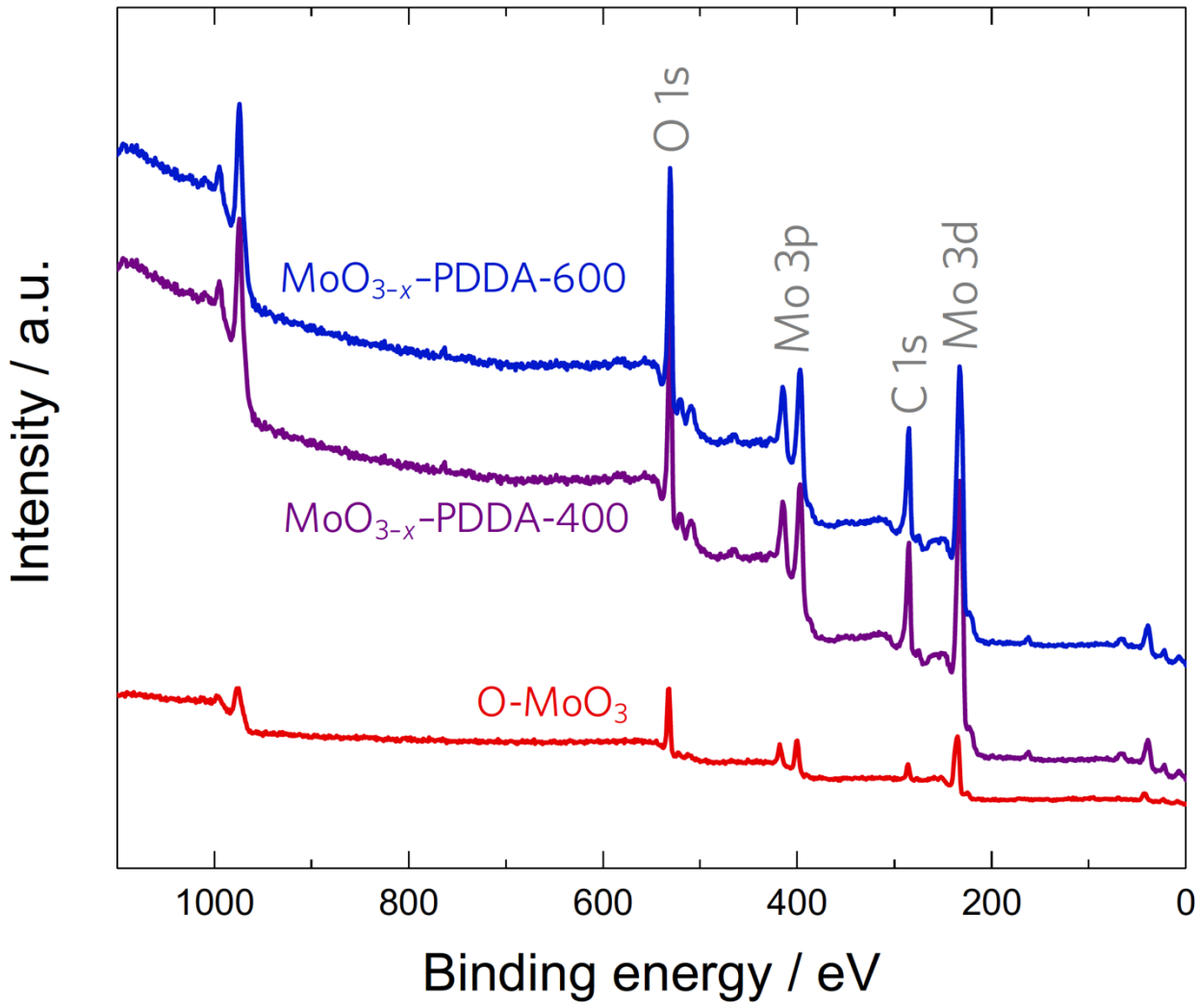

Figure 3.8. Survey X-ray photoelectron spectroscopy (XPS) spectra of the fully oxidized O-MoO_3, reduced MoO_{3-x}–PDDA-400, and reduced MoO_{3-x}–PDDA-600 samples.

Table 3.2. Fitting parameters for XPS Mo^{6+}, Mo^{5+}, and Mo^{4+} $3d_{3/2}$ and $3d_{5/2}$ spectral data and peak area ratios.

Sample	Mo^{6+} $3d_{3/2}$		Mo^{6+} $3d_{5/2}$		Mo^{5+} $3d_{3/2}$		Mo^{5+} $3d_{5/2}$		Mo^{4+} $3d_{3/2}$		Mo^{4+} $3d_{5/2}$	
	binding energy (eV)	area (%)	binding energy (eV)	area (%)	binding energy (eV)	area (%)	binding energy (eV)	area (%)	binding energy (eV)	area (%)	binding energy (eV)	area (%)
O-MoO_3	236.34	40.0	233.20	60.0	--	--	--	--	--	--	--	--
MoO_{3-x}–PDDA-400	236.89	7.62	233.20	11.4	234.84	24.8	231.50	37.2	232.99	7.58	229.13	11.4
MoO_{3-x}–PDDA-600	236.77	5.47	233.35	8.2	234.66	14.4	231.21	21.6	232.41	20.1	229.12	30.2
MoO_{3-x}, Inzani *et al.*[190]	--	--	233.42 233.25	60.1 86.2	--	--	232.22 232.01	39.4 13.8	--	--	229.82	0.5
MoO_{3-x}, Scanlon *et al.*[189]	235.63	--	232.48	--	--	--	--	--	231.49 (MoO_2)	--	228.29 (MoO_2)	--

In order to explain the strong reduction of MoO_3 by the PDDA polyelectrolyte, we propose the following mechanism obtained through theoretical modeling. The interface between the polymer and α-MoO_3 is illustrated in Figure 3.9a. PDDA is attracted to the surface of MoO_3 by strong electrostatic forces that originate from its electrolyte group. We have confirmed the electrostatic interaction experimentally by a zeta potential measurement where we observed a positive shift from -53.3 mV for O-MoO_3 to -7.02 mV for MoO_{3-x}–PDDA-400 and -8.27 mV for MoO_{3-x}–PDDA-600. Based on the TGA analysis of PDDA shown in Figure 3.6b, the oxygen vacancy sites are created by absorption of O_t through decomposition of PDDA upon thermal

annealing at temperatures above ~215°C. As a result, O_t atoms are absorbed as ionic O^- and neutral O^{2-}, causing the creation of Mo^{5+}-$v_O^{\cdot}$ and Mo^{4+}-$v_O^{\cdot\cdot}$ vacancy complexes, respectively. N─C and N─CH_3 bonds were investigated as the most possible bonds to break and absorb O_t. The energy associate with the absorption of O_t through breaking of these bonds are shown in Figure 3.9. The energy between the interface of PDDA and MoO_3 is defined as the reference. According to our calculations, O_t absorption through N─C bond in the pentagonal ring is the most plausible reaction for formation of both the $v_O^{\cdot\cdot}$ vacancy (3.37 eV) and the $v_O^{\cdot}$ vacancy (3.30 eV).

The formation energy of oxygen vacancy polarons in the bulk and surface MoO_{3-x} structures have been calculated and is shown in Figure 3.10. The DFT calculations were conducted based on the vacancy creations at O_t sites as this site advocates the lowest vacancy energy formation compared to asymmetric O_a and symmetric O_s oxygen[15]. O_t bonds with only one Mo site perpendicular to the layers in the structure, whereas O_a and O_s bond with two and three Mo atoms, respectively. Our DFT calculations suggest Mo^{4+} and Mo^{5+} as the most stable defect sites in both the surface and bulk of α-MoO_{3-x}. The formation energy of a Mo^{4+}-$v_O^{\cdot\cdot}$ vacancy complex was calculated as 0.22 and 0.02 eV higher than those of Mo^{5+}-$v_O^{\cdot\cdot}$ in the bulk and on the surface, respectively. Direct comparison between the Mo^{4+} and Mo^{5+} cases is allowed as we have used a bipolaron of Mo^{5+} to maintain an equal total number of electrons. The Mo^{5+} bipolaron configuration is taken as the lowest energy configuration from ref. [15]. This indicates that the formation of Mo^{4+} vacancies is more favorable on the surface of the material compared to within the bulk. In addition, the slightly higher formation energy of Mo^{4+} compared to Mo^{5+} is in agreement with our XPS analysis which indicated the formation of Mo^{4+} required higher thermal

energy. The creation of oxygen vacancies on the surface is essential for metal oxide catalytic activity where the surface is directly involved in the reaction[191].

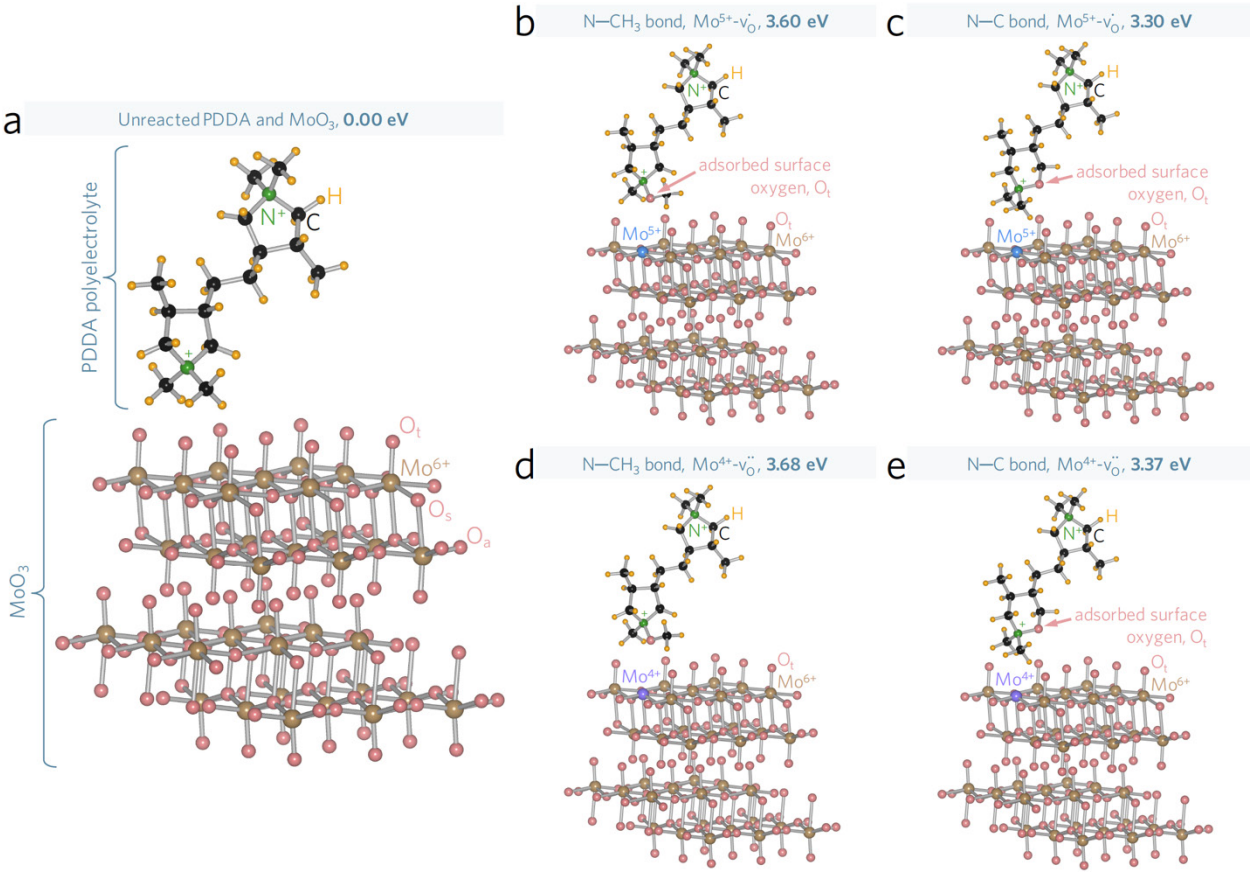

Figure 3.9. Density functional theory (DFT) calculations elucidate a pathway for PDDA-assisted reduction of α-MoO_3 to α-MoO_{3-x}. (a) Interface between the PDDA polyelectrolyte (positively charged molecule) and the surface of α-MoO_3 is used as the reference state for DFT calculations, where two monomers are modeled as the repeating unit of PDDA to minimize the dipole-dipole interaction. (b-e) DFT calculations of the energy required for bond-breaking and insertion of a surface oxygen atom, O_t, by a PDDA polyelectrolyte molecule in order to create (b, c) Mo^{5+}-$v_O^{\cdot}$ and (d, e) Mo^{4+}-$v_O^{\cdot\cdot}$ vacancy complexes through the breaking of (b, d) a N─CH_3 bond and (c, e) a N─C bond in the pentagonal ring of PDDA.

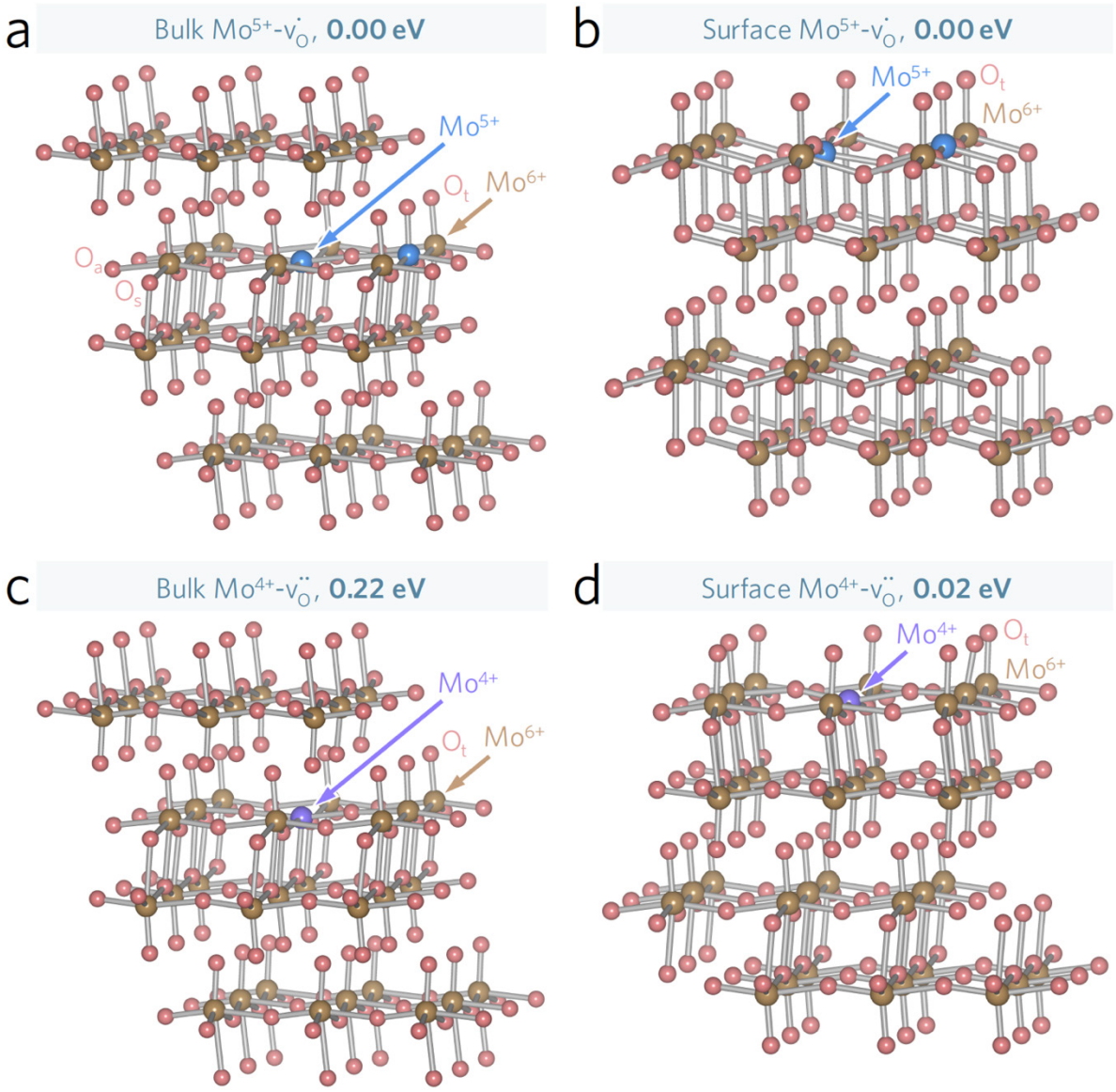

Figure 3.10. DFT calculations of the internal energy of formation for oxygen vacancies in α-MoO_{3-x}. (a) Bulk and (b) surface bipolaron of Mo^{5+} and (c) bulk and (d) surface polaron of Mo^{4+}. The bipolaron configuration in (a,b) is based on the lowest energy configuration given in ref. [15]. The internal energy in (c,d) is referenced to that of (a,b) respectively to highlight the difference

between Mo^{4+} and Mo^{5+} oxidation state formation, where a bipolaron of Mo^{5+} is used to enable direct comparison as the total number of electrons is equal in all panels.

Furthermore, MoO_3 work function was calculated 6.83 eV above the Fermi energy, which was consistent with the results reported by Guo *et al.* [136] The calculated band gap of bulk MoO_3 was obtained as 1.70 eV, being consistent with 1.62 eV calculated by Huang *et al.* [185] Both of these results are significantly lower than the true band gap of 3.3 eV (3.0–3.3 eV[136, 192]) because DFT with (semi) local XC functionals is well known to severely underestimate the solid band gap. To better estimate this important quantity, using the HSE06 hybrid XC functional[193] which is a standard way but at a tremendously higher computational cost. The band gaps of MoO_{3-x} were calculated using this scheme. Figure 3.11 demonstrates the calculated density of states (DOS), band gaps and the corresponding structures for MoO_{3-x} with $x = 0.0$, 0.17, and 0.33. The actual calculated band gap was 3.2201 eV for $x = 0.0$ and 2.8786 eV for $x = 0.17$. Interestingly, a metallic behavior with a band gap of 0.0 eV was calculated for $x = 0.33$.

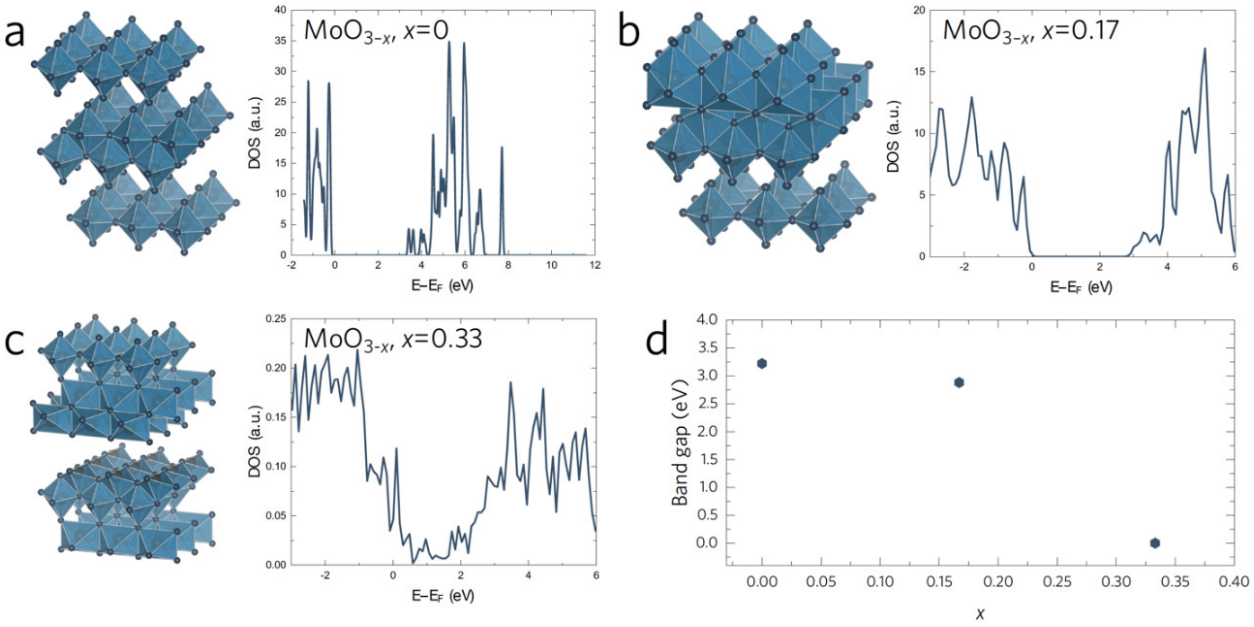

Figure 3.11. *Ab initio* electronic density of states and band gap of MoO_{3-x}. Calculated DOS using the optB88-vdW exchange correlation functional for (a) $x = 0.0$, (b) $x = 0.17$, and (c) $x = 0.33$. (d) Electronic band gaps for different oxygen vacancy concentrations calculated using the HSE06 hybrid XC functional.

In a previous study, Borgschulte *et al.* [194] reported the reduction of a 10 nm-thick MoO_3 thin film deposited on a Pd membrane using thermal evaporation by H_2 intercalation at room temperature. In order to investigate whether the H_2-containing gas treatment at room temperature induces considerable reduction in bulk scale powder MoO_3, 200 mg of Alfa Aesar No. 12930 (denoted as Ref.-MoO_3) was kept under (5% H_2/95% Ar) at room temperature for 12 hours. The XRD patterns of the sample before the treatment and after the treatment are shown in Figure 3.12 in the supporting information. As can be observed, both patterns are assigned to MoO_3 orthorhombic phase indicating that no reduction in the bulk of the material has occurred due the room-temperature treatment.

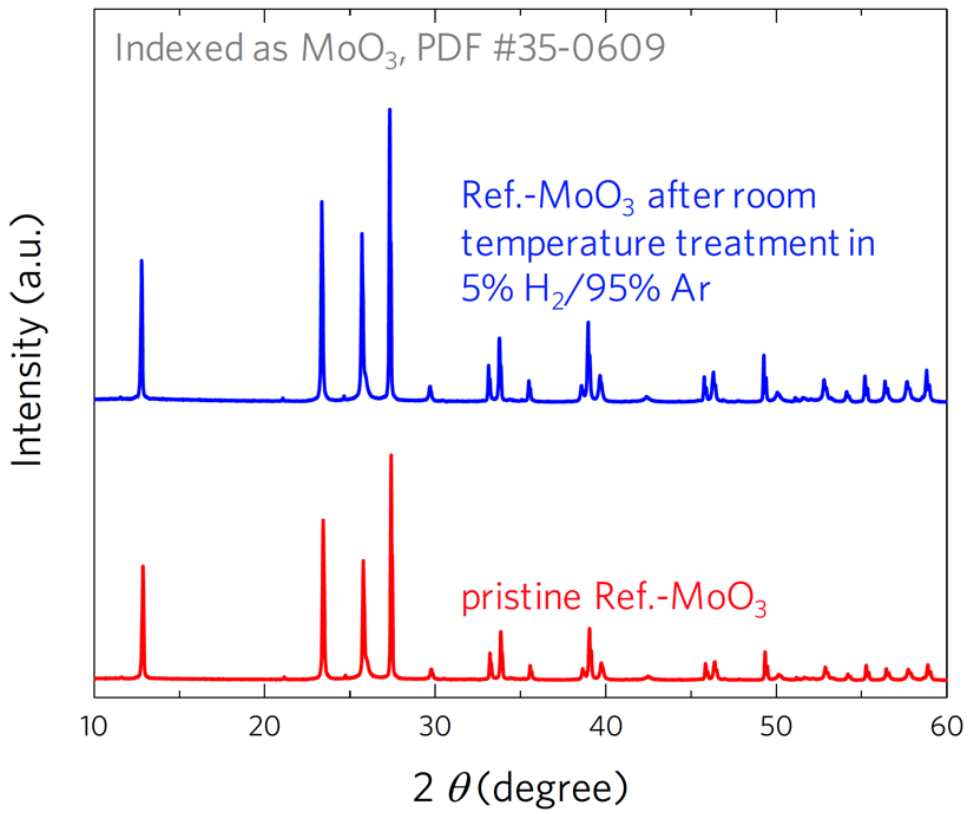

Figure 3.12. XRD patterns of bulk MoO_3 (Alfa Aesar No. 12930, denoted as Ref.-MoO_3). XRD patterns of the Ref.-MoO_3 pristine sample compared with those of Ref.-MoO_3 kept under 5%H_2/95%Ar gas at room temperature for 12 h. No reduction of MoO_3 is observed with room temperature H_2 treatment.

Calculations based on the TGA analysis of the treated sample show a very small $x = 0.036$ even after heating to 600°C during the TGA analysis (Figure 3.13). This negligible vacancy concentration seems to be from the vacancy initially present in the pristine Alfa Aesar No. 12930 sample by comparing the TGA results to that of the sample annealed under Ar with $x = 0.035$ as shown in Figure 3.13a. In addition, we investigated the effects of annealing time and PDDA concentration on the sub-stoichiometry of MoO_{3-x}. Based on the performed TGA analysis for Ref.-

MoO_{3-x} samples, increasing the annealing time under Ar resulted in a large sub-stoichiometry parameter $x = 0.86$ (Figure 3.13c). In contrast, by increasing the PDDA concentration by 10 times from 100 to 1000 µl, $x = 0.42$ was obtained (Figure 3.13d). Thus, sub-stoichiometry appears to be more dependent on the annealing time compared to the polyelectrolyte concentration.

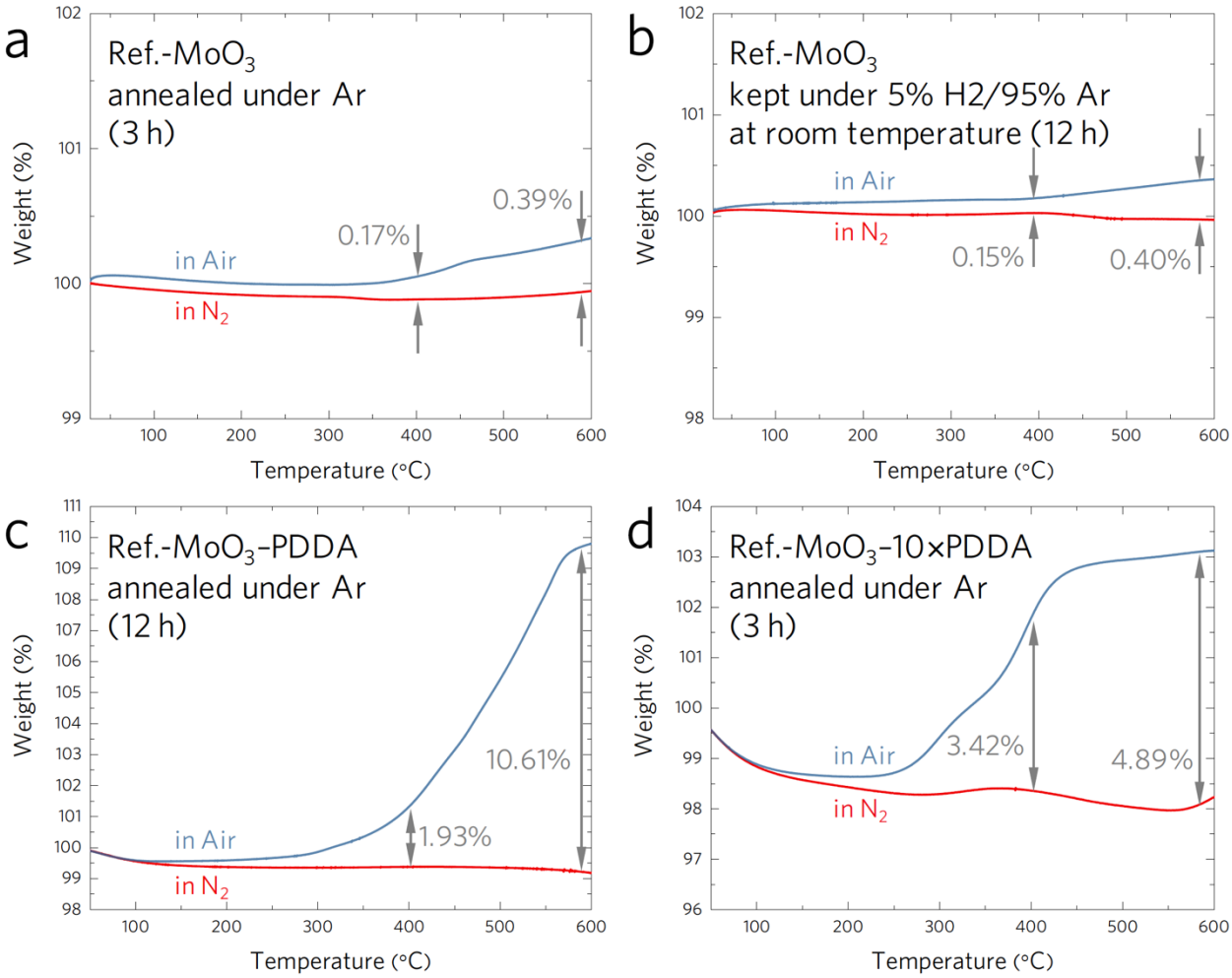

Figure 3.13. Thermogravimetric analysis (TGA) indicating the effects of annealing temperature, time, and PDDA concentration on reduction of MoO_3. Air and nitrogen TGA analysis of: (a) Ref.-MoO_3 (Alfa Aesar No. 12930, without PDDA) annealed under Ar at 600°C for 3 h, (b) Ref.-MoO_3 kept under 5% H_2 in Ar at room temperature for 12 h, (c) Ref.-MoO_3–PDDA (Alfa Aesar No. 12930, with PDDA) annealed under Ar at 600°C for 12 h, and (d) Ref.-MoO_3–

10×PDDA [Alfa Aesar No. 12930, with 10 times more vol.% PDDA than in (c)], annealed under Ar at 600°C for 3 h. The obtained results indicate the sub-stoichiometry concentration seems to be more dependent on annealing time compared to PDDA concentration.

3.7 Oxygen reduction reaction*

3.7.1 Chemical and structural analyses

Possessing a high surface area can guarantee the access of oxygen to the catalyst while also favoring formation of more vacancy sites on the surface. Mesoporous molybdenum oxide-graphene composites were synthesized using the method described in the experimental section. In the first step, mesoporous MoO_3 was synthesized via a nanocasting technique where SBA-15 and KIT-6 mesoporous silica were used to template cylindrical and gyroidal structures, respectively. After synthesis of mesoporous SBA-15 and KIT-6, phosphomolybdic acid (PMA, $H_3PMo_{12}O_{40}$) was used as the molybdenum precursor, and was impregnated inside the porous structure of mesoporous silica templates. The choice of precursor in this technique is of the utmost importance; PMA provides required hydrogen-bond interactions with silica templates and it has both a high molybdenum content and high solubility in ethanol, which was used as the solvent. After solvent evaporation, composites of PMA@SBA-15 and PMA@KIT-6 were calcined at 550°C to decompose the PMA into crystalline MoO_3 inside the channels of SBA-15 or KIT-6 templates. The silica templates were removed by etching in a 4% hydrogen fluoride (HF) aqueous solution.

* Reproduced in part with permission from Raana Kashfi-Sadabad†, Sajad Yazdani†, Tran Doan Huan, Zhao Cai and Michael Thompson Pettes, "Role of Oxygen Vacancy Defects in the Electrocatalytic Activity of Substoichiometric Molybdenum Oxide" *J. Phys. Chem. C, Accepted Manuscript*, https://doi.org/10.1021/acs.jpcc.8b03536 . Copyright 2018 American Chemical Society. (†These authors contributed equally)

Figure 3.14 shows the low-angle X-ray diffraction (XRD) patterns the SBA-15 and KIT-6 derived mesoporous molybdenum oxide samples. For the SBA-15-based samples (Figure 3.14a), four distinct peaks are observed which can be assigned to the (100), (110), (200), and (210) Bragg reflections of the P6mm hexagonal structure as per ref. [173]. The low-angle XRD of KIT-6 (Figure 1b) shows peaks attributed to the (211), (220), and (321) Bragg reflections of the bicontinuous cubic gyroidal Ia3d structure (Figure 3.14b), indicating highly ordered mesostructures as per ref. [173]. The low-angle XRD patterns of the mesoporous MoO_3@KIT-6 and MoO_3@SBA-15 prepared at 550°C show one intense peak at $2\theta = 1.0°$, corresponding to the poorly resolved (211) and (100) diffraction peaks of SBA-15 and KIT-6, respectively. After removing the template by HF, three well-resolved diffraction peaks were observed from the low-angle XRD pattern of MoO_3–SBA-15, which can be indexed to (100), (110), and (200) diffraction planes of a highly ordered 2D hexagonal structure. This, in turn, indicated that the MoO_3 crystal nanoarrays replicated the ordered mesostructure of their host silica template. In comparison, after removal of silica with HF, the MoO_3–KIT-6 sample only exhibited one intense peak at $2\theta = 0.9°$ [assigned to (211)], indicating lower structural regularity (see Figure 3.14b). Further details on the low-angle diffraction patterns of the samples is discussed in the supporting information. As shown in Figure 3.15, peaks in the high-angle XRD patterns of the mesoporous sample after removing SBA-15 and KIT-6, denoted as MoO_3−SBA15 and MoO_3−KIT−6 respectively, were assigned to orthorhombic MoO_3 (powder diffraction file #05-0508).

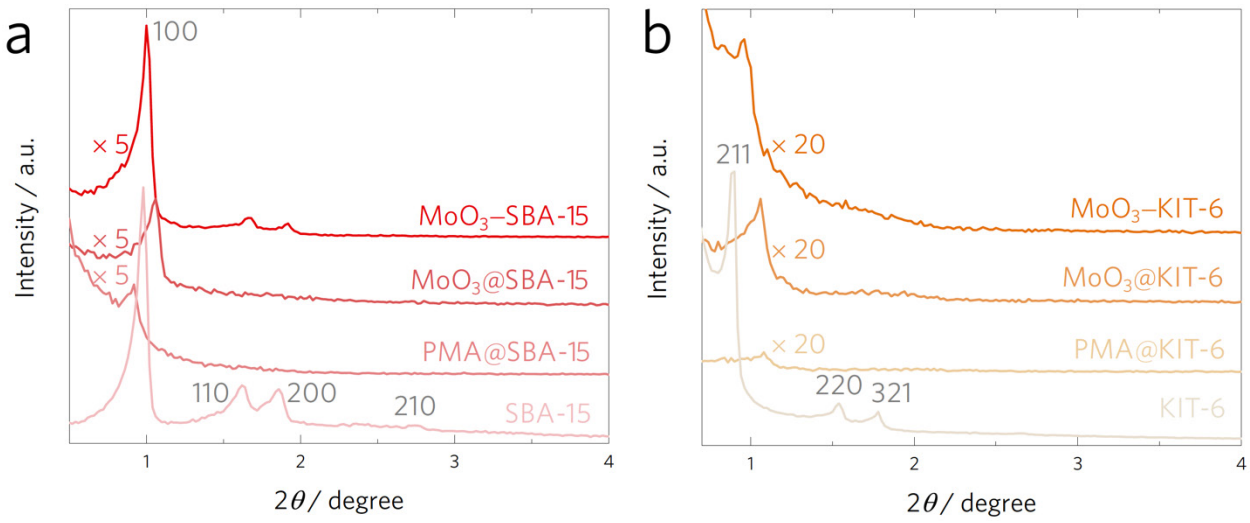

Figure 3.14. X-ray diffraction (XRD) analysis of the molybdenum oxide hard templating process. (a) Low-angle powder XRD of the mesoporous silica KIT-6 hard template, the mesostructured composite of phosphomolybdic acid (Mo precursor) impregnated into the SBA-15 mesochannels (PMA@SBA-15), the mesostructured MoO_3@SBA-15 composite prepared via high-temperature calcination of PMA@SBA-15 in air at 600°C, and the final product of mesoporous MoO_3 after removal of the SBA-15 hard template by hydrofluoric acid (MoO_3–SBA-15). (b) Low-angle powder XRD of KIT-6, PMA@KIT-6, MoO_3@KIT-6, and the mesoporous MoO_3–KIT-6 sample after removing the template.

In order to boost the electrical conductivity of our MoO_3, the mesoporous samples were wrapped by graphene oxide sheets. PDDA polyelectrolyte was added during the synthesis to provide strong electrostatic interaction between the GO support and mesoporous catalysts. In order to reduce GO to reduced graphene oxide (rGO), the samples were annealed at temperatures of 400 and 600°C under an argon atmosphere. Figure 3.15 illustrates the XRD patterns of the MoO_3–SBA15 sample composited with both polymer and rGO and annealed at 400 and 600°C,

denoted as rGMS-400 and rGMS-600 respectively. Unexpectedly, the XRD patterns indicated that the annealed samples were a mixed phase of partially reduced MoO_3 and a monoclinic phase of MoO_2 (powder diffraction file #73-1807).

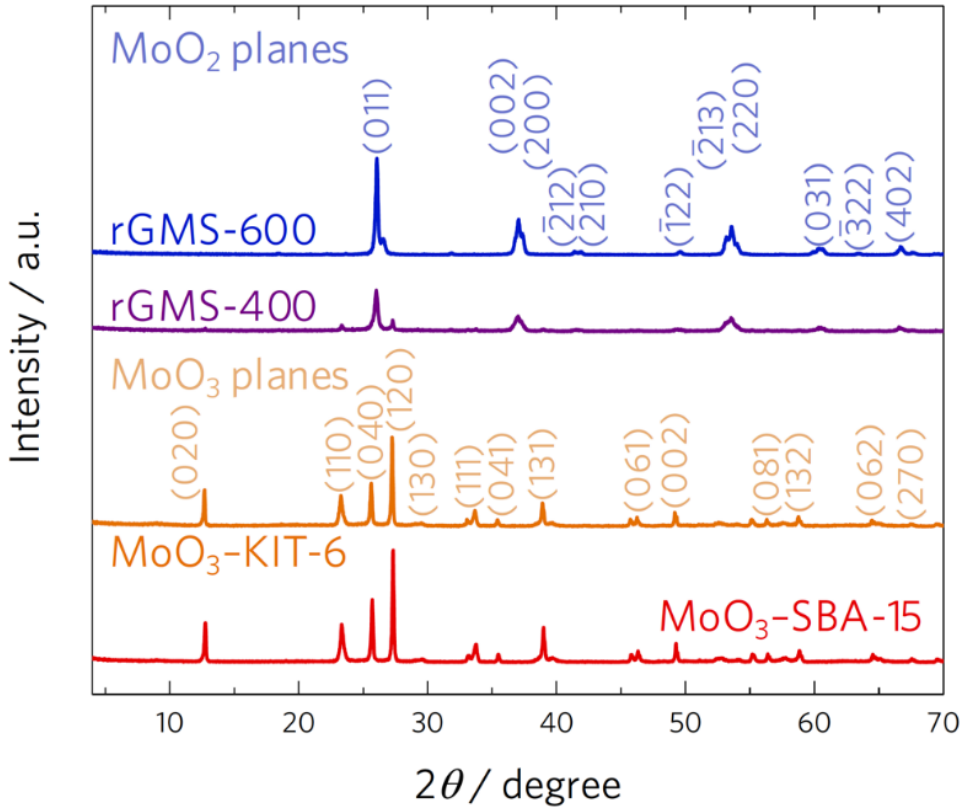

Figure 3.15. High-angle powder XRD patterns of the mesoporous MoO_3–SBA-15 and MoO_3–KIT-6 samples. The patterns are assigned to an orthorhombic phase of MoO_3 (powder diffraction file #5-0508). High-angle powder XRD patterns of the composites with MoO_3–SBA-15, PDDA polyectrolyte, and rGO annealed at 400 and 600°C under argon, denoted as rGMS-400 and rGMS-600 respectively. The patterns are assigned to the monoclinic phase of MoO_2 (powder diffraction file #73-1807).

Compared to the XRD patterns obtained for KIT-6 and SBA-15, a slight shift to higher angles was detected in the low-angle diffraction peaks of mesoporous MoO_3@KIT-6 and MoO_3@SBA-15, which indicated a small shrinkage of the mesostructure[12]. In the MoO_3@SBA-15 composite, the precursor has been decomposed inside the pores of the silica template by annealing at the crystallization temperature, thus the sample consists of MoO_3 confined inside the template pores. However, the filling of the pores of the template is not expected to be fully complete in most cases[12], otherwise there should not be any low angle diffraction peak observed. We propose that the low-angle diffraction in MoO_3@SBA-15 originates from the unfilled or partially filled pores of the silica templates where the shrinkage due to calcination possibly leads to the small observed shift in 2θ. For MoO_3–SBA-15 where the silica template has been removed, the entire template including the unfilled parts are etched away and the low angle peak originates from the sample, which expectedly shows slightly higher angle due to pore shrinkage during the synthesis. Shifts from 2θ = 1.62 to 1.86° along (110) and from 1.66° to 1.92° along (200) were measured for the replica (MoO_3–SBA-15) compared to the original template (SBA-15). Similar behavior was observed for KIT-6 based samples. In KIT-6 templated samples, (100) diffraction peaks show a similar trend as for SBA-15 based samples, 2θ= 0.88, 1.06 and 0.96° for the template (KIT-6), the filled template (MoO_3@KIT-6) and the replica (MoO_3–KIT-6), respectively.

Transmission electron microscopy (TEM) analysis revealed that samples preserve the regularity of the template mesostructures (Figure 3.16). We observe the MoO_3 products have a highly ordered mesostructure throughout the whole domain consisting of hexagonally aligned nanowires and gyroid-porous structures for MoO_3–SBA-15 and MoO_3–KIT-6, respectively, reflecting true replication of the hard templates and a high yield of MoO_3 incorporation into the template channels. N_2 adsorption−desorption isotherms was obtained to examine the textural

properties of the catalysts. The prominent hysteresis loops indicate the mesoporous nature of MoO_3–SBA-15 and MoO_3–KIT-6 samples (Figure 3.16d,e). The Brunauer−Emmett−Teller (BET) surface areas of these catalysts were 50 m^2/g for MoO_3–SBA-15 and 63 m^2/g for MoO_3–KIT-6, all of which were much lower than that for the SBA-15 (529 m^2/g) and KIT-6 (851 m^2/g) templates (see Figure 3.17 and Table 3.3).

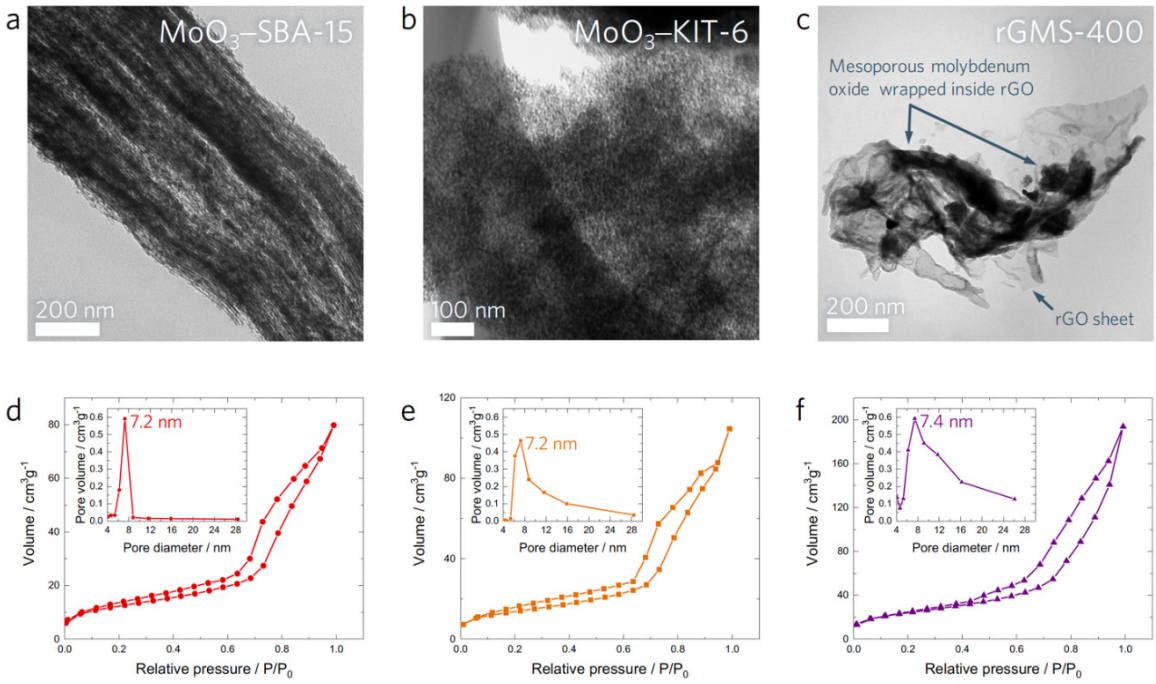

Figure 3.16. Transmission electron microscopy (TEM) analysis of mesoporous MoO_3 and composite catalysts. TEM images of (a) MoO_3–SBA-15, (b) MoO_3–KIT-6, and (c) rGMS-400. (d−f) Corresponding N_2 adsorption isotherm curves for the three mesoporous MoO_3 catalysts shown in panels (a–c). Insets show the calculated Barrett−Joyner−Halenda pore size distributions.

The Barrett−Joyner−Halenda (BJH) pore size distributions of MoO_3–SBA-15 and MoO_3–KIT-6 catalysts were centered at 7.2 nm. In the case of MoO_3–SBA-15, the peak at 7.2 nm is in

agreement with that of the original SBA-15 (5.4 nm) and is evidence of well controlled template replication.

Table 3.3. Structural properties of mesoporous silica and nanocast composites.

Sample	BET surface area (m^2/g)	BJH desorption pore volume (cm^3/g)	BJH desorption pore diameter (nm)
KIT-6	851	0.95	5.4
SBA-15	529	0.88	5.4
MoO_3@KIT-6	43.7	0.059	5.2
MoO_3@SBA-15	41.5	0.089	7.2
MoO_3–KIT-6	63	0.162	7.2
MoO_3–SBA-15	50	0.123	7.2
rGMS-400 [a]	122	0.313	7.4
rGMS-600 [a]	53	0.089	7.4

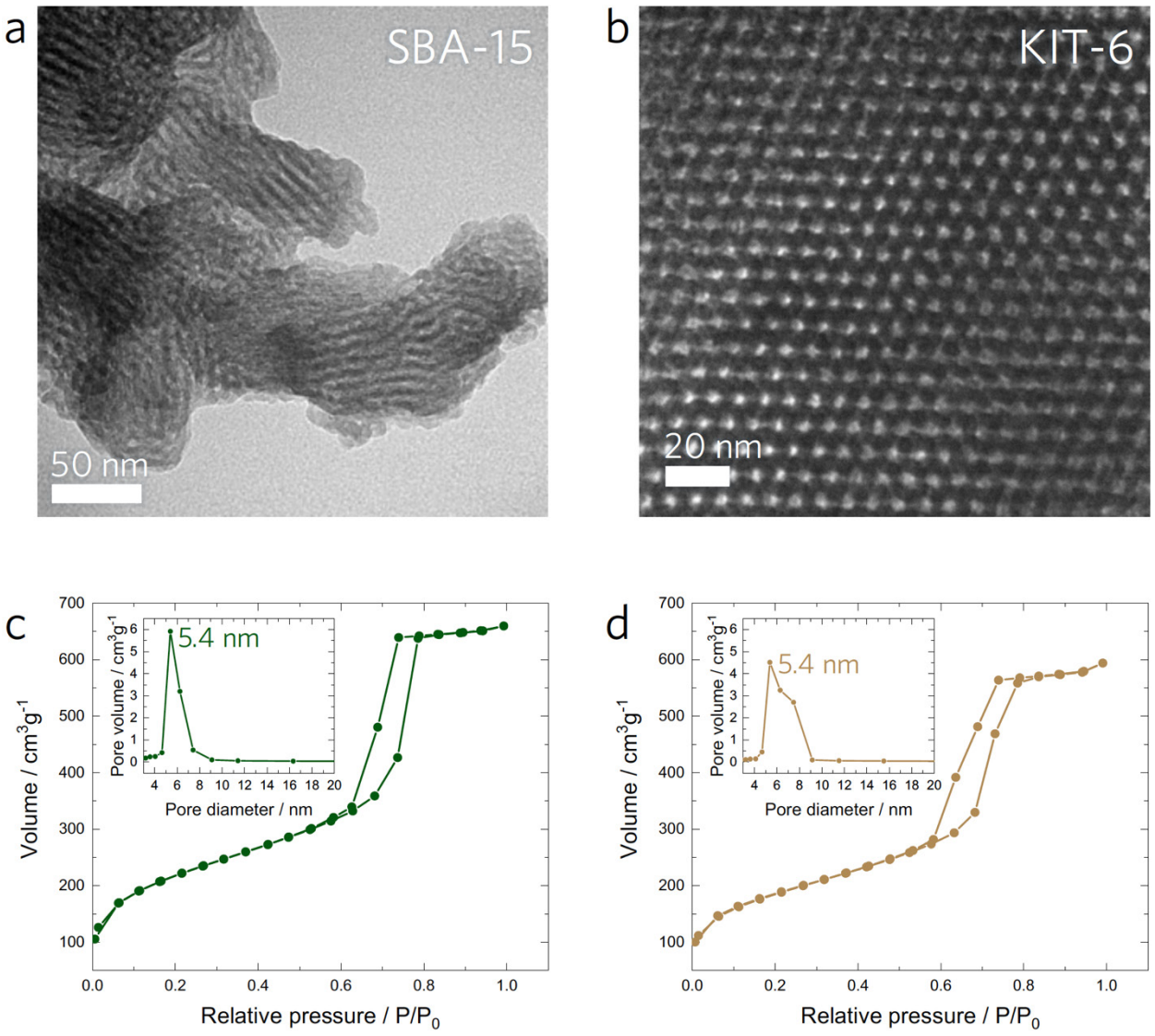

Figure 3.17. TEM images of mesoporous (a) SBA-15 and (b) KIT-6 templates. (c−d) N_2 sorption isotherms of SBA-15 and KIT-6, respectively. Insets show the BJH pore size distribution.

The nitrogen sorption isotherms of KIT-6 and SBA-15 templates shown in Figure 3.17 appear to have type IV isotherms whose capillary condensations occur at a relative pressure ranging from 0.7 to 0.8 P/P_0, indicating orderly mesoporosity[195]. Both silica templates exhibit narrow BJH pore size distributions peaked at 5.4 nm obtained by looking at their respective

adsorption branches. These values are slightly below what one would observe from the TEM images as a result of the existence of nanobridges. Both templates are good candidates for the nanocasting process of mesoporous MoO_3 in cylindrical and gyroidal forms due to well-ordered structure, large surface area, and uniform pore size (Table 3.3).

The physical properties reported in Table 3.3 for both unfilled and filled mesoporous silica templates indicate a significantly higher suppression of N_2 adsorption for the filled composites (MoO_3@KIT-6 and MoO_3@SBA-15) compared to the unfilled silica templates (SBA-15 and KIT-6). This suggests that the phosphomolybdic acid was adequately incorporated into the channels of the latter. The pore volumes of KIT-6 and SBA-15 are reduced by a factor of ~10 compared to those of MoO_3@KIT-6 and MoO_3@SBA-15 composites. After removing the silica templates with HF, type-IV isotherms were observed in the mesoporous MoO_3 samples with a noticeable condensation plateau at a relative pressure (P/P_0) range of 0.5–0.7 (see Figure 3.16d), indicating uniform mesopores.

Additionally, TEM analysis of rGMS-400 shown in Figure 3.16c confirmed that thin layers of graphene were attached to the MoO_{3-x} likely as a result of electrostatic interaction. This encapsulation of the mesoporous structure can significantly facilitate the transport of electrons through the highly conductive graphene-based scaffold. Moreover, the conventional (0002) peak expected for graphite at $2\theta = 26.68°$ was not resolved in XRD, which suggests a homogeneous dispersion of the graphene sheets over the surface of the MoO_x samples[196]. The porosity of the rGMS-400 and rGMS-600 composites was quantified using nitrogen adsorption–desorption isotherm measurements (Figure 3.16f and Table 3.3). According to the BJH equation, the centered pore diameter in rGMS-400 was 7.4 nm, which confirms a relatively uniform pore size distribution. The BET specific surface areas of rGMS-400 and rGMS-600 were 122 and 53 m^2/g, respectively.

The higher specific surface area of rGMS-400 compared to MoO_3–SBA-15 (50 m^2/g) is due to the porosity of the replicate MoO_3 and the secondary pores between the MoO_3 and the graphene sheets[197]. The lower surface area of rGMS-600, on the other hand, results from a partial collapse of the mesoporous structure after high temperature reduction at 600°C. TEM and HAADF-STEM images of rGMS-600 (Figure 3.18) and rGMS-400 (Figure 3.19) catalysts confirm the attachment of mesoporous particles to the rGO. TEM also reveals partial collapse of the porous structures indicated by BET data.

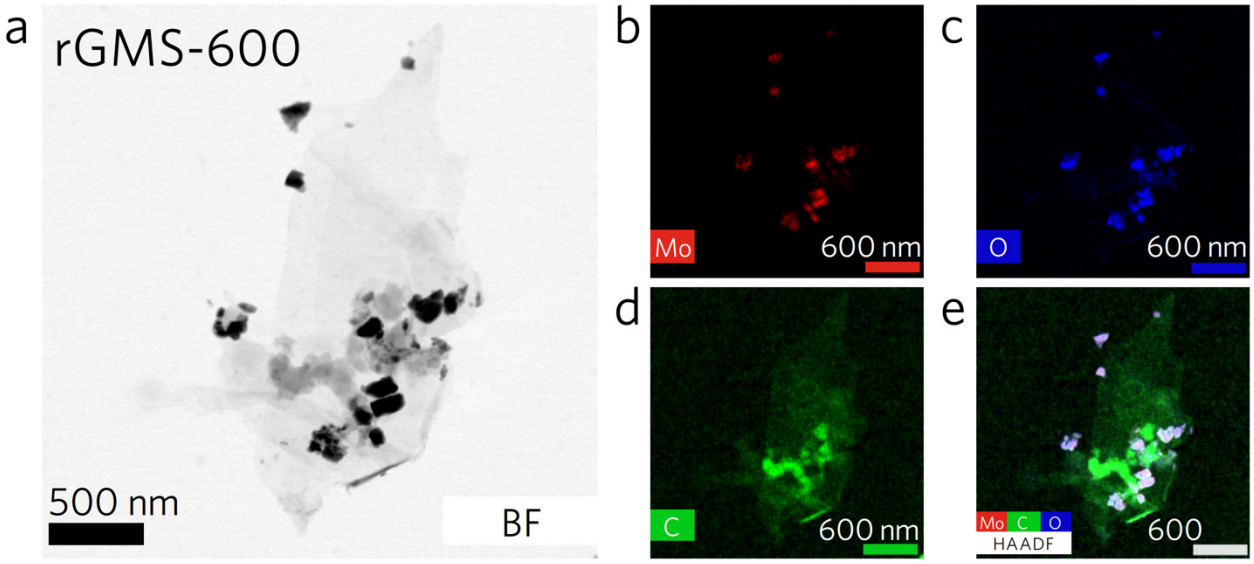

Figure 3.18. Scanning transmission electron microscopy (STEM) confirms wrapping of MoO_{3-x} catalysts by rGO. (a) Bright field STEM and (b-e) scanning energy dispersive X-ray spectroscopy (EDS) and high angle annular dark field (HAADF) micrographs of rGMS-600.

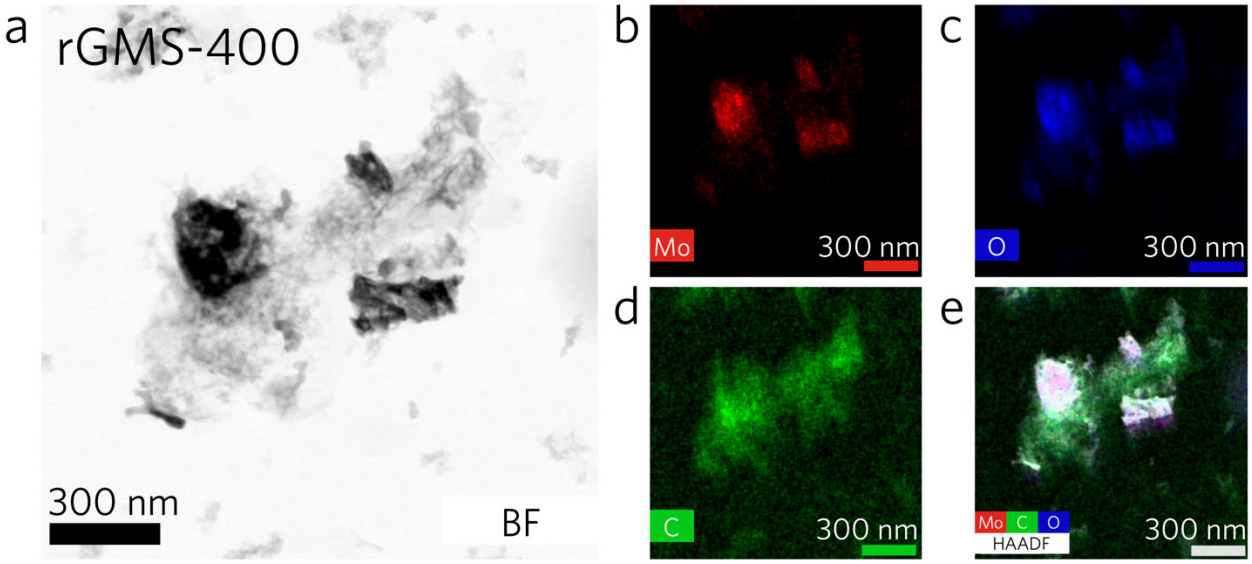

Figure 3.19. (a) Brightfield scanning transmission electron micrograph (BF-STEM) and (b-e) high-angle annular dark-field (HAADF) and scanning energy dispersive x-ray spectroscopy (EDS) of rGMS-400.

Raman spectra of mesoporous MoO_3–SBA-15 powders and rGMS-400 and rGMS-600 composites is shown in Figure 3.20. Similar to MoO_3–SBA-15, Raman spectrum of the rGMS-400 composite displayed characteristic orthorhombic MoO_3 vibrational frequencies whereas rGMS-600 peaks are ascribed to Raman bands of monoclinic MoO_2[198] consistent with the XRD analysis. In the MoO_3 spectra, various bending modes were found responsible for the peaks below 400 cm^{-1}, while the three peaks at 663, 820, and 993 cm^{-1} were traced to the various stretching frequencies of molybdenum and oxygen[199]. Raman bands detected at 743, 571, 493, 364, 345 and 229 cm^{-1} in the rGMS-600 sample are the evidence of reduction of MoO_3 to MoO_2[198]. The Raman spectra of the rGMS-400 and rGMS-600 composites in the range of 1200 to 3000 cm^{-1} exhibit the characteristic peaks of rGO. The D and G graphitic bands observed at 1360 and 1594 cm^{-1} for rGMS-400, respectively, and at 1359 and 1583 cm^{-1} for rGMS-600, respectively, confirm the

existence of defects in the sp^2-bonded carbon in the composite[200]. The removal of oxygen-containing groups in rGMS-400 and rGMS-600 was monitored by Raman spectroscopy in the range of 1200 to 3000 cm^{-1}. The major oxygen functional groups in GO include epoxide (–O–) and hydroxyl (–OH) groups, which are located on the basal plane of GO, while minor functional groups include carbonyl (–C=O) and carboxyl (–COOH) groups located at the edges[201-205]. GO by itself is known to be electrically insulating due to presence these oxygen groups[206]. Thermal or chemical reduction can remove these groups and restore the electrical properties depending on the degree of reduction, layer disorder, and structural defects[205-207]. The appearance of the defect-induced D-band in the Raman spectra of rGMS-400 at 1360 cm^{-1} as well as a rather broad G-band at 1594 cm^{-1} and unresolved second-order 2D peak (expected ~2700 cm^{-1}) indicated that a high degree of oxidation and disorder[208] was still present in rGMS-400 even though it had been reduced at 400°C (Figure 3.20b). For rGMS-600, the D-peak shifted to 1359 cm^{-1} and a narrower G-peak at 1583 cm^{-1} was observed. The I_D/I_G ratio decreased from 0.86 for rGMS-400 to 0.19 for rGMS-600 which indicated that reduction was improved as the annealing temperature was elevated to 600°C.

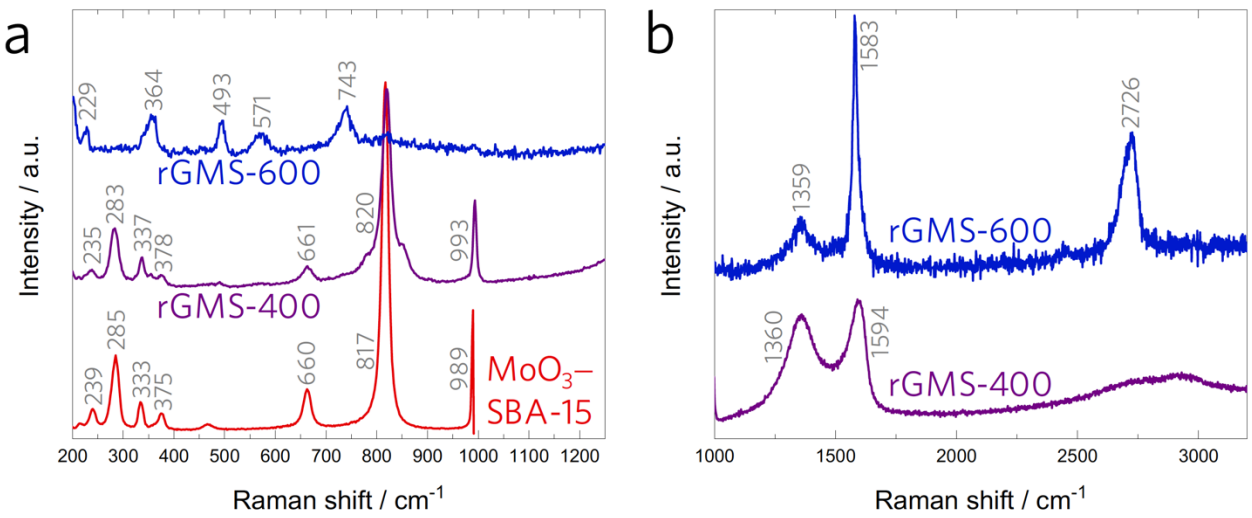

Figure 3.20. (a) Raman spectra of rGMS-400 and rGMS-600 composites shown in comparison with that of mesoporous MoO_3–SBA-15. (b) Raman spectra of the rGO-related peaks of rGMS-400 and rGMS-600 samples.

Further reduction of oxygen functional groups in GO by raising the thermal reduction temperature from 400 to 600°C was verified by the high-resolution C 1s spectra acquired from X-ray photoelectron spectroscopy (XPS, shown in Figure 3.21). The C 1s spectra of the GMS-400 and GMS-600 composites were deconvolved into four peaks corresponding to carbon atoms with different oxygen-containing functional groups[209]: (1) non-oxygenated C sp^2 and sp^3 at 284.6 and 285.8 eV, respectively, (2) carbon in C–O at 287.4 eV, (3) carbonyl carbon (C=O) at 287.9 eV, and (4) carboxylate carbon (O–C=O) at 289.0 eV. Increasing the intensity of the sp^2 carbon peak relative to the peaks of sp^3 carbon and carbon binding to oxygen indicates a higher degree of reduction by increasing the annealing temperature.

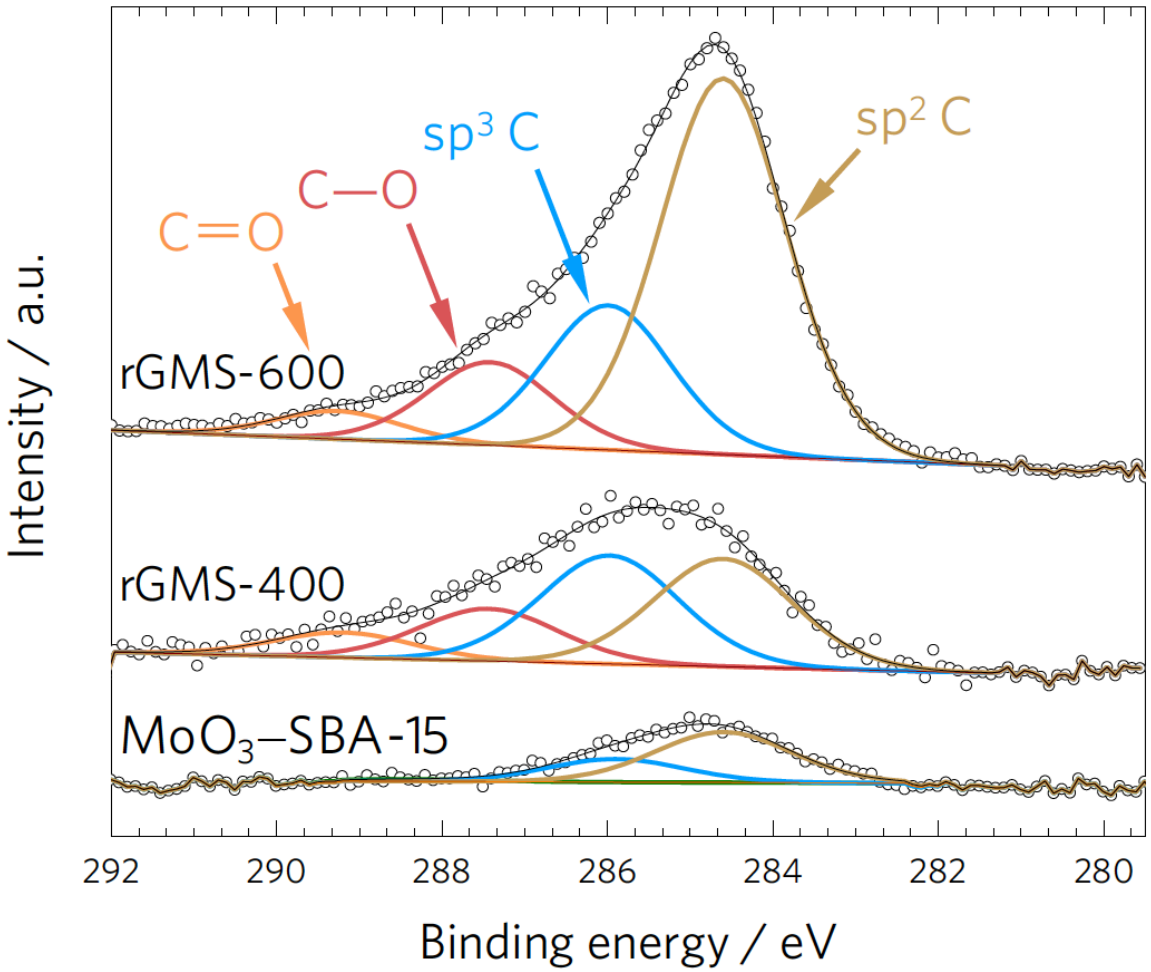

Figure 3.21. Deconvoluted XPS carbon 1s peak of MoO_3–SBA-15 and the rGMS-400 and rGMS-600 composites.

3.7.2 Role of defects in the electrocatalytic reduction of oxygen

The ORR electrocatalytic activity of mesoporous MoO_3–SBA-15, rGMS-400, and rGMS-600 composites were characterized by linear sweep voltammetric (LSV) measurements in 0.1 M KOH and are shown in Figure 3.22. The activity for MoO_3–KIT-6 is shown in Figure 3.23, supporting information. The ORR onset potentials of mesoporous MoO_3–SBA-15 and MoO_3–KIT-6 were 0.78 and 0.79 V versus reversible hydrogen electrode (RHE). The improved

performance of MoO_3–KIT-6 compared to MoO_3–SBA-15 is assigned to the higher surface area and abundance of three-dimensional channels in the gyroidal structure improving oxygen diffusion on the catalyst surface. Compared with MoO_3–SBA-15, the rGMS-400 and rGMS-600 electrodes showed an even greater positive shift in the onset potential, 0.82 and 0.86 V (vs. RHE), respectively, with a more notable increase in the current density as shown in Figure 3.22a. The improved ORR activity of rGMS-400 and rGMS-600 can be explained by following factors. PDDA can functionalize GO through the reduction process and a possible synergic effect between rGO, PDDA, and catalyst plays an important role in high ORR activity of rGMS-400 and rGMS-600. This happens through the physical adsorption of polyelectrolyte chains that contain positively charged nitrogen moieties on rGO where intermolecular charges created a net positive charge on the carbon atoms. This can change the electronic properties of rGO causing the electrons to be attracted more from the anode to the cathode and facilitating oxygen desorption as well as the ORR process[172, 210]. The integration of MoO_3–SBA-15 with PDDA-rGO helps overcome the slow electron conduction in MoO_3–SBA-15 and the interface between them plays a key role in increasing the overall catalytic performance.

Moreover, although the surface area of rGMS-600 (53 m^2/g) was lower than that of rGMS-400 (122 m^2/g), its onset potential (vs. RHE) was 40 mV higher than rGMS-400 at the same mass loading. This higher ORR activity, in spite of having lower surface area, can be attributed to the higher degree of oxygen vacancies on the surface of the active material in the rGMS-600 catalyst due to reduction of orthorhombic MoO_3 to monoclinic MoO_2 by increasing the reduction temperature from 400 to 600 °C accompanied by a higher degree of reduction of GO as confirmed by XPS and Raman spectroscopy.

Electrochemical impedance spectroscopy (EIS) of the catalysts showed smaller diameter of the Nyquist plot curves for rGMS-400, and rGMS-600 compared to MoO_3–SBA-15 (Figure 3.22b). This is an indication of lower electrical resistance of rGMS-400, and rGMS-600 due to wrapping with more electrically conductive rGO sheets in theses samples. The smaller diameter of the rGMS-600 curve compared to rGMS-400 is due to a combination of the higher oxygen vacancy concentration and a higher degree of reduction of rGO as well as the reduction of the bulk of rGMS-600 from orthorhombic α-MoO_3 to nearly monoclinic MoO_2. Although outside the scope of the current work, the effects of oxygen vacancy concentrations on conductivity can be studied by a set of controlled experiments where the oxygen vacancy concentration is kept as the only variable in the investigation, most appropriate for single crystalline samples so that the intrinsic contribution of oxygen vacancies to the conductivity can be determined.

Because of its strong orbital overlap[211], MoO_2 has a relatively low, metallic electrical resistivity (8.8×10^{-5} Ω-cm) [212] which can significantly facilitate the electron transfer through the core of catalyst. Accordingly, a comparison between the RDE polarization curves of MoO_3–SBA-15 and rGMS-600 indicates improved the ORR kinetic of rGMS-600 due to this promoted electron conduction the catalyst (Figure 3.22c,d). The integration of MoO_3 with PDDA-rGO also helps overcome the slow electron conduction in MoO_3–SBA-15.

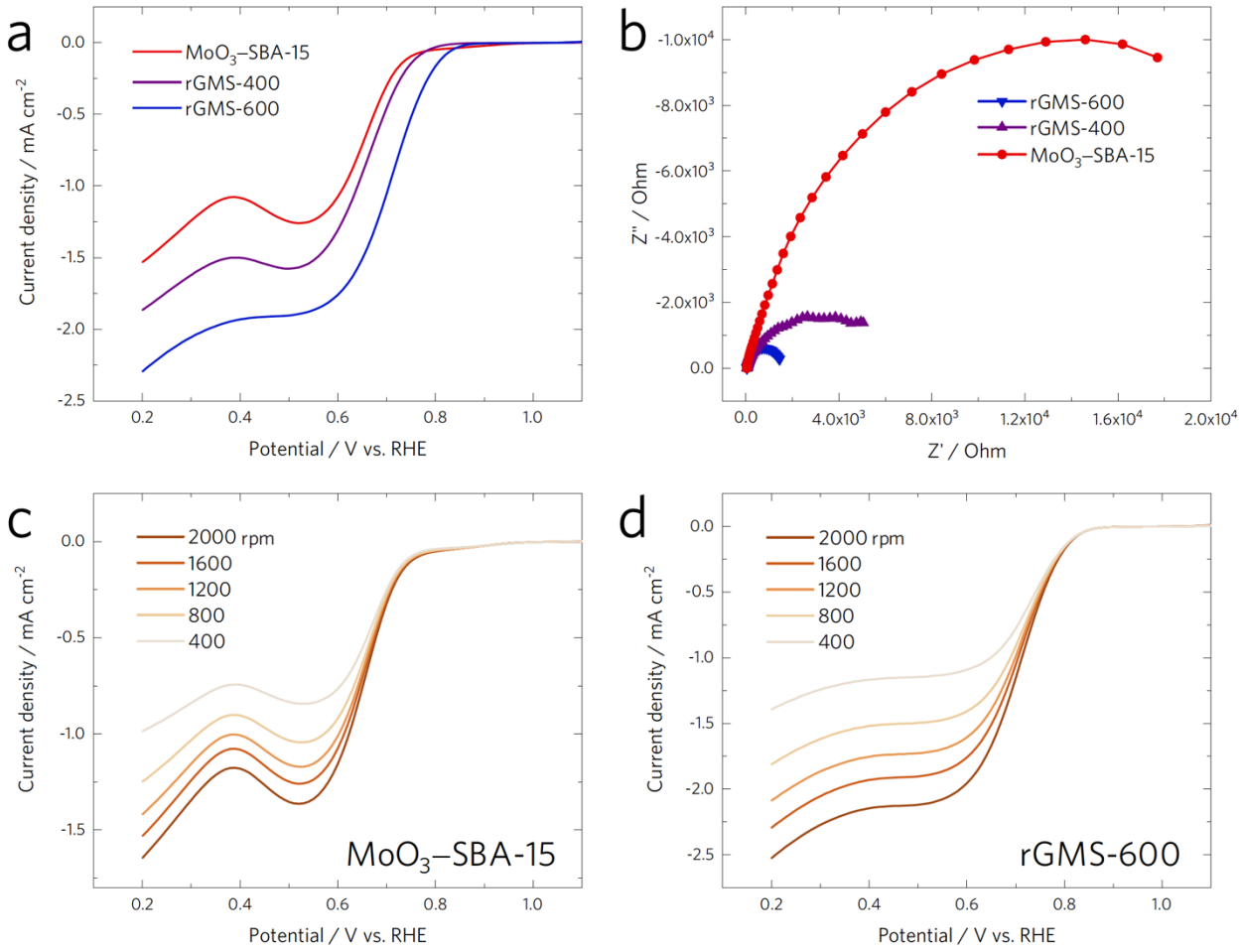

Figure 3.22. Oxygen reduction activity is increased through a composite electrode with less defective rGO and more highly reduced MoO_{3-x}, demonstrating the importance of PDDA and thermal treatment at 600°C. (a) Linear sweep voltammetry polarization curves obtained in O_2-saturated 0.1 M KOH and (b) Nyquist plots for MoO_3–SBA-15, rGMS-400, and rGMS-600 catalysts. Rotating-disk voltammograms of the catalysts: (c) MoO_3–SBA-15 and (d) rGMS-600 in O_2-saturated 0.1 M KOH with a sweep rate of 5 mVs^{-1}.

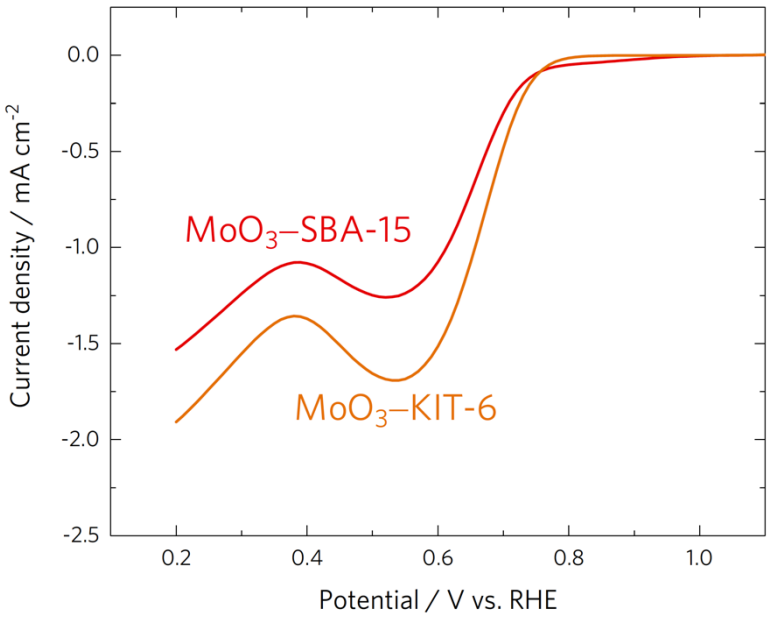

Figure 3.23. Linear sweep voltammetric (LSV) measurements of mesoporous MoO_3–SBA-15 and MoO_3–KIT-6 catalysts.

In order to model the ORR of MoO_{3-x}, the following mechanism is employed for alkaline solutions[213]

$$M^{m+}\text{—}O^{2-} + H_2O + e^- \rightarrow M^{(m-1)+}\text{—}OH^- + OH^- \quad (3.2)$$

$$O_2 + e^- \rightarrow O_{2,ads}^- \quad (3.3)$$

$$M^{(m-1)+}\text{—}OH^- + O_{2,ads}^- \rightarrow M^{m+}\text{—}O\text{—}O^{2-} + OH^- \quad (3.4)$$

$$M^{m+}\text{—}O\text{—}O^{2-} + H_2O + e^- \rightarrow M^{(m-1)+}\text{—}O\text{—}OH^- + OH^- \quad (3.5)$$

$$M^{(m-1)+}\text{—}O\text{—}OH^- + e^- \rightarrow M^{m+}\text{—}O^{2-} + OH^- \quad (3.6)$$

where M represents the transition metal Mo, *m* denotes the oxidation state, and the subscript "ads" stands for adsorption. In order to identify the ORR active site, DFT calculations based on the

reaction (3.2) were performed. According to Kim and Dunn *et al.* [15], Mo^{5+} bipolarons and Mo^{4+} polarons at oxygen terminal sites (O_t) are the most favorable defect configurations with formation enthalpies of 1.32 and 1.51 eV, respectively. The results of our DFT calculations based on a Mo^{4+} polaron at an O_t site indicated that the presence of this particular defect structure significantly reduces the reaction energy barriers (Figure 3.24). We found that the energy barrier against the reaction (3.2) decreased from 3.0 eV for the MoO_3 catalyst to -0.55 eV for the MoO_{3-x} catalyst with a $v_O^{\cdot\cdot}$ oxygen vacancy site. Our calculated results are consistent with the performed experimental observations as the rGMS-600 catalyst with the highest degree of metal oxide reduction exhibited the highest ORR activity.

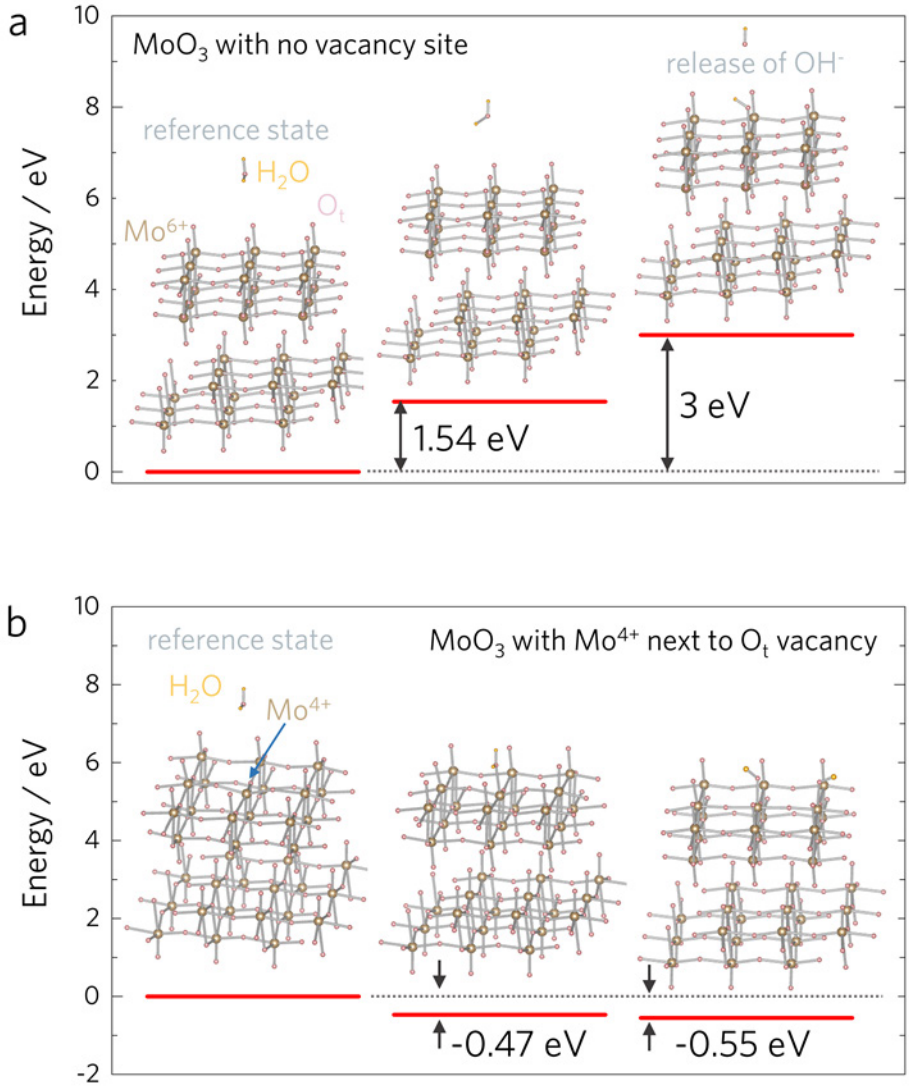

Figure 3.24. Surface oxygen vacancies are required to accelerate the ORR reaction. DFT calculated energy barriers for the oxygen reduction reaction (ORR) for MoO_3 catalyst based on the reaction (3.2) (a) without vacancies and (b) with the presence of a Mo^{4+} next to the oxygen vacancy site. This result proposes that the energy barriers of the reaction kinetics are significantly reduced due the presence of the surface oxygen vacancy. In these calculations, the products and reactants are conserved, which is required to enable direct comparison between the different states.

Since durability is a major concern of today's fuel cell industry, the stability of MoO_3–SBA-15 and Pt/C catalysts during ORR were assessed through chronoamperometric measurements at -0.5 V. As shown in Figure 3.25, a relative current of 91% still persisted after 16.7 h on the MoO_3–SBA-15 catalyst, which is likely related to the carbon constituent in the composite electrode. In contrast, Pt/C showed a gradual decrease to 60.0% relative current after only 5.6 h. The measured Pt/C stability can be compared with reports from previous investigations. Singh *et al.*[214] reported 36% current loss after 2.78 h for a Pt/C electrode in a 0.1 M KOH electrolyte at 0.6 V versus RHE. Sun *et al.*[215] reported a Pt/C current stability to decrease to ~ 82, 69 and 51.7% after 5.6, 20 and 80 h, respectively for a 0.1 M KOH electrolyte at -0.3 V versus Ag/AgCl. The obtained results indicate the superior stability of the mesoporous MoO_3–SBA-15 catalyst compared to the Pt/C catalyst in an alkaline solution popular in the development of alkaline fuel cells. On the one hand, Pt-based catalysts gradually degrade over time (especially in alkaline electrolytes) because of surface oxidation, particle dissolution, and particle aggregation. On the other hand, existing ORR catalysts that show improved stability over Pt (such as Ag) still lack the needed activity and are not durable enough for practical purposes[216]. The excellent stability and durability of our mesoporous molybdenum oxide even in the absence of rGO protection makes it a promising candidate as a catalyst for ORR.

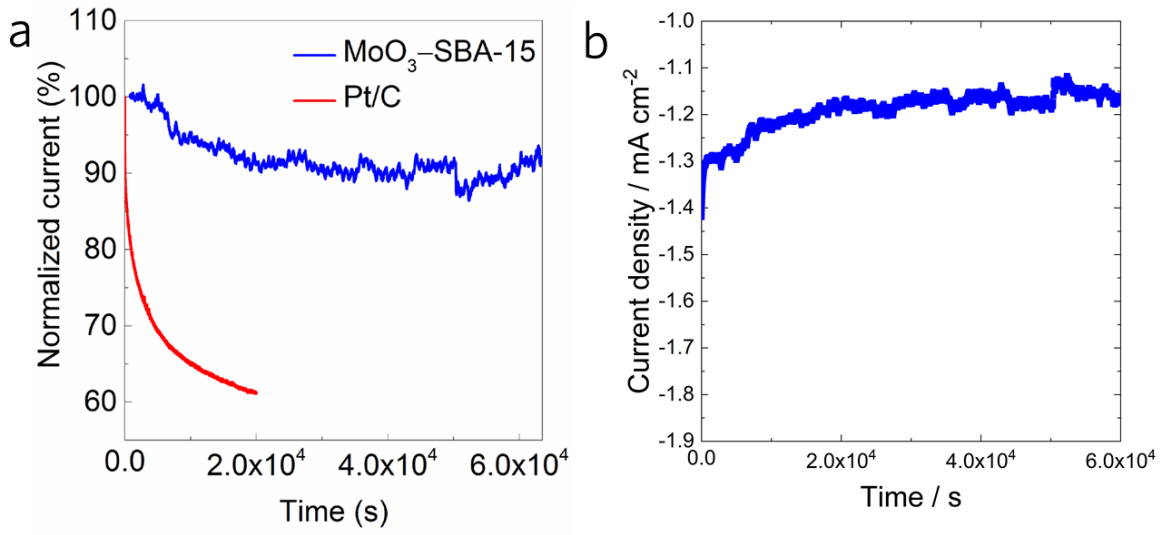

Figure 3.25. (a) Chronoamperometric response at a potential of -0.5 V vs. SCE (0.55 V vs. RHE) for mesoporous MoO_3–SBA-15 and Pt/C indicates the improved stability of the mesoporous catalyst. (b) Current density stability of MoO_3–SBA-15 at -0.5 V vs. SCE.

3.8. Conclusion

The thermochemical reaction mechanism between a PDDA polyelectrolyte and an α-MoO_3 metal oxide was determined by a combined experimental and theoretical investigation. Our experiments indicated that if the fully oxidized MoO_3 is annealed at 400 and 600°C under Ar for 3 h, α-MoO_3 is negligibly reduced to MoO_{3-x} with $x = 0.01$, 0.03, respectively. In contrast, if the fully oxidized α-MoO_3 is treated with PDDA polyelectrolyte, significant vacancy concentrations form allowing transformation to MoO_{3-x}, where $x = 0.14$ ($MoO_{2.86}$) and 0.36 ($MoO_{2.64}$) were obtained for annealing temperatures of 400 and 600°C, respectively at the same conditions. Similar reduction behavior was observed under 5% H_2/95% Ar as the sub-stoichiometry x was increased from 0.62 to 0.98 by using the PDDA treatment. This phenomenon was explained by absorption

of O_t upon decomposition of PDDA, where our DFT calculations suggested that O_t atoms were absorbed into the pentagonal ring of PDDA as ionic O^- and neutral O^{2-} creating Mo^{5+}-$v_O^{\cdot}$ and Mo^{4+}-$v_O^{\cdot\cdot}$ vacancy complexes on the metal oxide surface. Due to crucial role of oxygen vacancy concentration in determining physical or chemical properties of materials, the study of similar interactions of oxide materials with PDDA or other polymers in the polyelectrolyte family is suggested for future investigations.

Reduced graphene oxide-wrapped mesoporous molybdenum oxides were synthesized via a two-step procedure, utilizing nanocasting and a self-assembly/thermal reduction approach, then used as an electrocatalyst in ORR. The obtained products replicated the mesostructure of both KIT-6 and SBA-15 silica templates and exhibited large surfaces areas (up to 80 m^2/g), and narrow pore size distributions (~3 nm full width at half maximum). The obtained mesoporous MoO_3 material exhibited improved ORR activity, which was associated with the well-defined mesoporous structure. Experimental results indicated that using PDDA for wrapping mesoporous α-MoO_{3-x} with rGO followed with thermal annealing created catalyst surfaces with qualitatively high degree of vacancy densities. Theoretical results have demonstrated that these surface vacancy sites are crucial in the electrochemical activity of catalysts by being the origin of ORR activity in α-MoO_{3-x} based materials for the first time. Finally, we emphasize that the synthesis approach presented here can be readily extended to the preparation of other mesoporous metal oxide–graphene composite materials, with broad applications in various critical energy conversion areas[217].

CHAPTER 4: The Role of Highly Charged Interface Trap States in the Electro-Thermal Transport Properties of PbS_{1-x}

4.1 Background

A polycrystalline material is composed of crystallite domains joined by grain boundaries. In crystallites, atoms are ordered and arranged similar to a small single crystalline material[218]. In contrast, the structure of grain boundaries can be quite complicated as it usually consists of few layers of disordered atoms. These atomic layers con be considered as transitions between various orientations of crystalline domains. Due to the disordered nature, a high concentration of defects can be formed at the deficient atomic bonding[218]. It has been suggested that these defects can act as trapping states by trapping and immobilizing charge carriers[218-220]. Therefore, the number of available carriers for conduction decreases and mobile carrier concentration can be much lower than that of the doping concentration[218]. In addition, the trapped carriers cause the grain boundaries to be electrically charged. These electrically charged interfaces act as potential barriers at the grain boundaries and can obstruct the charge transfer, thereby decreasing the mobility[218]. This model explains the much smaller carrier concentration and mobility of polycrystalline materials compared to those of single crystals for the same doping concentrations measured by using Hall method for polycrystalline silicon[218, 220]. Moreover, when these grain boundaries are electrically charged, the charged layer is balanced by two layers of the opposite charges on both sides of the interface[219]. This causes formation of a dipole layer whose width is correlated with the potential barrier strength[221]. According to the model by Seto[218], the barrier height can be estimated using $\sigma \propto T^{-1/2} \exp\left(-E_B / k_B T\right)$ (for $NL > Q_t$), where σ, T, k_B, E_B, N, L, and Q_t are electrical conductivity,

temperature, Boltzmann constant, barrier height, doping concentration, crystallite size and trapping states density, respectively.

The existence of a potential barrier against charge transport can induce a non-linear current-voltage behavior in materials. This non-linear behavior has been technologically exploited in voltage-dependent-resistors (VDRs), known as varistors[221]. This behavior is only observed in polycrystalline materials and can be regarded as having Schottky barriers at grain boundaries[221]. A varistor has a high electrical resistivity at low voltages, and as the voltage increases, the electrical resistivity of the varistor decreases. Another major application of such a non-linear behavior is in dye-sensitized solar cells (DSSCs). Unlike the prior text book definition of solar cells which is based on high purity, defect and interface-free semiconductors, DSSCs are functional based on interface-rich materials synthesized by simple methods suitable for large-scale economical applications[222]. In general, a DSSC is a photoelectrochemical system consisting of a mesoporous TiO_2 anode covered with a molecular light-absorbance dye, an electrolyte and a cathode. In contrast to electron transport by diffusion, it was observed that the electron transport depends on the intensity of the incident light and becomes faster by increasing the intensity[222, 223]. This light-intensity dependent phenomenon was explained by a multiple trapping model[224-227]. According to this model, most electrons are locally trapped in states below the conduction band at the interfaces and can escape and contribute in the transport through thermal activation[226]. The presence of traps is crucial because the electron lifetime in TiO_2 nanoparticles is related to the trapping state density[222], and similar to other photovoltaic systems[222, 228, 229], the efficiency of DSSCs is dependent on the recombination of electrons with acceptors known as the electron lifetime. Other investigations have emphasized the importance of the trap states at the grain boundaries by reporting that no light-intensity dependence was found in DSSCs fabricated by single crystalline

ZnO nanorods without grain boundaries compared to DSSCs based on interface-rich ZnO nanoparticle[230]. For an extensive review of the fundamentals and applications of DSSCs, readers are referred to ref.[222].

Another important application of grain boundary-rich polycrystalline materials is in the field of thermoelectric energy conversion. Current manufacturing processes display major energy losses as most of energy being used is wasted as heat. One way to combat the increasing global energy demand is by capturing the waste heat and recycling it into useful electricity through the use of thermoelectric materials. A great advantage of a thermoelectric system is that it has no moving part or noise during operation. Thus, improving thermoelectric energy conversion is highly beneficial in order to promote sustainability and efficiency in the long-term use of current industrial methods. The performance of thermoelectric materials is limited by low values of their figure of merit which is defined by the equation $zT = \sigma S^2 T/\kappa$ where S, and κ are Seebeck coefficient and thermal conductivity, respectively. Thermal conductivity is composed of lattice and electronic contributions. Having a high density of grain boundaries in solution-processed materials can be very appealing. Grain boundaries of the appropriate size can effectively suppress thermal conductivity by scattering the majority of phonons. First principle calculations of thermal conductivity accumulation have predicted that nanostructures of ~ than 10 nm can be used to effectively reduce the thermal conductivity for PbSe, PbTe, SnS, and SnSe (80% and 90% for PbSe and PbTe, respectively at 300 K)[231-233]. The advancements in solution-processed syntheses of nanocrystals have made achieving such size ranges possible[234].

Thermoelectric devices operate at both low and high temperatures. High temperature thermal-to-electrical energy conversion materials, such as PbS, are very attractive for waste heat recovery from a thermodynamic stand point. Recently, there has been a number of promising

reporting high *zT*s, by using bottom-up methods in PbS-based materials[21, 28]. These encouraging improvements on PbS, emphasize the potential implications of using bottom-up material preparation methods for high performance thermoelectric applications. However, it is often reported that chemistry-processed materials exhibit lower electrical conductivities when compared to conventional top-down (solid-state) materials due to presence of defects as well as remaining organic species introduced during synthesis. In order to remove any of the insulating ligands or organic species, most of these thermoelectrics are annealed at high temperatures under vacuum or an inert gas environment[21-23, 235]. This exposure to high temperatures, can cause vacancy sites formations in the materials. Sulfur losses have been reported during the material preperation[26, 236] or can be caused by surface evaporation of sulfur upon cycling during operations at high temperatures[237, 238]. The presence of vacancies and defects can significantly alter the electronic properties of materials and dominate Seebeck coefficient and electrical conductivity. While bulk Bi_2Te_3 is known to be p-type for stoichiometry and Bi-rich cases, Mehta *et al.* [26] reported a major majority carrier reversal in solution-processed Bi_2Te_3 pellets showing n-type behavior due to presence of point-defects. Additionally, defects can interact with dopants present in a thermoelectric[239]. Dopant–defect interactions have not been fully understood and can potentially be used for power factor enhancement[26].

In solution-processed materials with polycrystalline nature and high densities of grain boundaries, the effects of defects or vacancies can be even more substantial because presence of impurities and vacancies can charge interfaces and dominate electronic properties. In the current work, the effects of highly charged interface trap-states on the electro-thermal properties of PbS_{1-x} is investigated. The formation of sulfur vacancy ($v_S^{\cdot\cdot}$) is studied and modeled by density functional

theory (DFT) calculations. The experimental observations are modeled by DFT and Seto's[218] formulation for charge transport over potential barriers.

4.2 Experimental section

4.2.1 Characterizations

Powder X-ray diffraction (XRD) analysis was carried out using a Bruker D2 Phaser with Cu Kα radiation (λ =1.54184 Å) at an operating voltage of 30 kV and current of 10 mA. Transmission electron microscopy (TEM) analysis was performed on a FEI Talos F200X TEM/STEM at an accelerating voltage of 200 kV. Chemical analyses were conducted using STEM and energy dispersive X-ray spectroscopy (EDS) with HAADAF/BF detectors. Raman spectroscopy was operated on a Renishaw System 2000 with a wavelength of 514 nm laser. SPS densification was performed via a SPS, Dr. Sinter Lab, SPS-515S. The power factor measurements were conducted on an Ulvac-Riko ZEM-3 (300−800 K). Thermal diffusivity measurements were conducted using a Netzsch LFA-457 Microflash by taking an average of three data points at each temperature. A differential scanning calorimeter, Netzsch DSC 404 C, was employed for the heat capacity measurements. All the transport property measurements of each sample as well as ICP-OES analysis were conducted on the same pellets.

4.2.2 Synthesis

Lead (II) acetate trihydrate, $Pb(CH_3CO_2)_2\times3H_2O$ (467863, Sigma-Aldrich), thiourea NH_2CSNH_2 (T8656, Sigma-Aldrich) were used as the Pb and S sources, respectively. Glycerol $HOCH_2CH(OH)CH_2OH$ (G9012, Sigma-Aldrich) was used as the solvent. In a typical synthesis, 0.02 mol of the Pb precursor was stirred in 50 ml glycerol on a hotplate at 90°C for 45 minutes

until dissolved. Then, 0.02 mol of S precursor was added to the solution and mixed for 10 minutes. At this point, the reaction was removed from the hotplate and is poured into a 125 ml autoclave (PTFE#A305AC, Parr Instrument Co.). The autoclave was placed in an oven at 160°C for 3 hours. Afterwards, the autoclave was removed from the oven and, when it was cooled back to room temperature, a viscous solution with black precipitates at the bottom was obtained. In order to remove the solvent, 50 ml of ethanol was added to the solution and left for 24 hours. Then, a black powder was obtained by washing with ethanol through a three-time centrifugation at 5000 rpm. The obtained powder was dried under vacuum at room temperature.

4.2.3 High temperature Ar annealing

The dried powders were placed in an alumina combustion boat (Z561746, Sigma-Aldrich) and annealed in a horizontal tube furnace under Ar at 600°C for 3 hours with a ramp 1 °C min^{-1}.

4.2.4 Sulfur post-synthesis treatments

2.9 g of the synthesized PbS sample was placed in the middle of the furnace. An alumina combustion boat containing 1 g of S powder was placed in the upstream. A long heating tape was wrapped around the quartz tube where the S boat was placed as shown in Figure 4.1d. A carrier gas mixture of 20 sccm of hydrogen and 100 sccm of argon was used. For each treatment, the tape was rapidly heated to 150°C when the furnace temperature reached 120°C. The furnace was heated to 600°C and kept at for 3 hours with a ramp of 1 °C min^{-1}. The heating tape was turned off when the temperature of the furnace cooled down to 150°C.

4.2.5 Sample preparations for the measurements of transport properties

Spark plasma sintering (SPS) was conducted on the dried powders at the desired temperatures for 8-10 minutes under the same current pulse pattern on/off ratio. 1.2–1.3 g of the powders was loaded into a graphite die with an internal diameter of 12.7 mm. Each side, top and bottom, was covered by three layers of graphite foils. The SPS pellets were prepared under an axial pressure of 4 kN. After the SPS, both sides were polished in order to completely remove the graphite foils. The removal of the graphite foils was assured by XRD. For the thermopower measurements using ZEM-3, rectangular uniform bars were cut using a diamond saw. For the cold-press samples, the powders were converted to a dense pellet by using a hydraulic the powders under 10^4 lbf in a 12.7 mm die.

4.2.6 Density functional theory calculations[*]

First-principles computations at the level of density functional theory (DFT) as implemented in the Vienna *Ab initio* Simulation Package (VASP) [240, 241] were employed to simulate crystalline PbS. Within this computational scheme, the Perdew-Burke-Ernzerhof (PBE) functional[179] was used for the exchange-correlation energies while the plane-wave cutoff was chosen to be 500 eV. For energy and force calculations, a dense *k*-point mesh of 9×9×9 was employed to sample the Brilouin zone --- this setup typically leads to an energy convergence of less than 1 meV/atom.

While the energies, the atomic forces, and the electronic structure of PbS can be obtained with VASP, the estimations of the thermal conductivity, electrical conductivity, conductivity

[*] Density functional theory calculations (DFT) were performed by Dr. Huan Tran at the University of Connecticut.

electron effective mass, and Seebeck coefficient require some additional tools. The electronic contributions to the thermal conductivity, the electrical conductivity, and the Seebeck coefficient were estimated using BoltzTraP[242]. For this work, the electronic bands of PbS were calculated at a very dense *k*-point mesh (we used 45×45×45 herein). From this data, smoothed Fourier interpolation of the bands was obtained with BoltzTraP, allowing for transport coefficient calculations[243, 244]. The *average* electron effective mass m^* was defined[245, 246] to approximately capture the nonparabolicity and the anisotropy of the bands, and the competitions of pockets throughout the Brillouin zone in the transport. The carrier concentration n was then computed from the chemical potential μ as

$$n(\mu) = \int \sum_b \delta\left(\mu - \varepsilon_{b,\mathbf{\kappa}}\right) \frac{d\mathbf{k}}{8\pi^3} \tag{4.1}$$

where the subscript b runs over the electronic bands computed using DFT, and $\mathbf{k}$ the wave vector. The aforementioned (electronic) transport properties were collected and processed with the help of PYMATGEN[247] by using the obtained BoltzTraP data. On the other hand, the lattice contribution to the thermal conductivity was estimated using PHONO3PY[248]. This step involves accurately computing a large number of displaced structures of PbS for obtaining the required third-order force constants. The lattice thermal conductivity is then computed from the group velocity, the mode-dependent heat capacity, and the single-mode relaxation time[248], all of them are accessible from the computed force constants via lattice dynamics. Within this formalism, the single-mode relaxation time is assumed to be equal to the phonon life time, which can be computed as the reciprocal of the imaginary part of the self-energy, obtained from three-phonon interaction strength via an analogous form of the Fermi's golden rule[248].

It is worth mentioning that the state-of-the-art computational methods/techniques used in this work have some well-known deficiencies. Although the electronic dispersions can be computed reasonably, the electronic band gap may not be highly correct. In fact, we obtained E_g = 0.36 eV, being consistent the experimentally reported band gap of PbS, 0.37 eV[249]. With BoltzTraP, the semi-classical transport coefficients are calculated within the relaxation time approximation, leaving the relaxation time τ an unknown parameter (we used $\tau = 10^{-14}$ s[250]). In the formalism used to estimate the lattice thermal conductivity, only the lowest-order (3rd) anharmonic terms of the energy can be considered. Because this approach may fail at high temperatures, our transport property calculations were carried out at the room temperature (300 K), where the validity of the approach is assumed.*

4.3 Results and discussions

Solvothermal reaction, high temperature annealing and spark plasma sintering (SPS) were the steps used for the material preparations. High-temperature annealing can potentially enhance vacancy and defects density and SPS is essential in order to sinter the grain boundaries and obtain high density solid materials needed for thermoelectric energy conversion. Figure 4.1 illustrates the synthesis procedure. Thiourea, lead (II) acetate trihydrate were used as the sulfur and lead precursors and glycerol was used as the solvent. The solvothermal reaction occurred in a Teflon lid autoclave reactor. The obtained sample, denoted as PbS-Solvo was annealed under H_2/Ar at 600°C.

* BoltzTraP calculations were performed by Dr. Huan Tran, University of Connecticut.

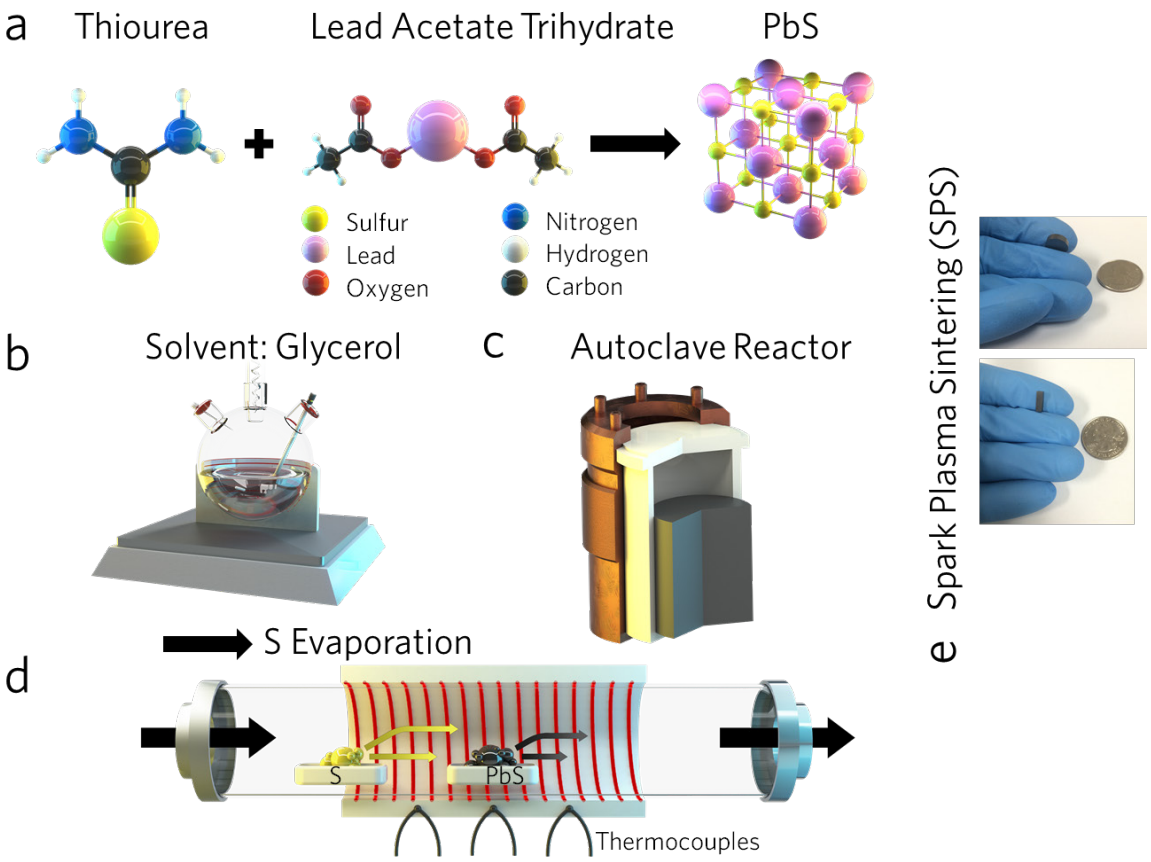

Figure 4.1. Illustration of the synthesis steps (a) the reaction scheme (b-c) pyrolysis and autoclave reactions (d) annealing process under H_2/Ar. For sulfurization, the sulfur powder was placed in an upstream location. The powder was evaporated by using a heating tape set at a temperature of 150°C providing a constant flow of sulfur over the sample (e) dense pellet and rectangular bar obtained after SPS for electro-thermal measurements.

In addition, other samples were prepared by annealing under a sulfur-rich environment in order to obtain a stoichiometry sample with no sulfur vacancy. During annealing, a constant flow of sulfur was provided by evaporating sulfur powders placed in an alumina boat located in the upstream with H_2/Ar carrier gas (Figure 4.1d).

The sulfurized samples were denoted as PbS-S and PbS-S–SPS referring to the obtained products after sulfurization and SPS, respectively. For comparison, the annealing and SPS steps were also conducted on a sample from Sigma-Aldrich (#372595) with a different morphology denoted as PbS-ref.–SPS. After SPS, the obtained pellets were used for laser flash thermal diffusivity measurements. For the electrical and Seebeck coefficient measurements, the pellets were cut into rectangular bars from the same pellet used for diffusivity measurements (Figure 4.1e). The details of the sample treatments have been listed in Table 4.1. The synthesis steps and sample treatments were intentionally designed in order to answer the following questions: (i). At which synthesis step of solvothermal reaction, high-temperature annealing or SPS, $v_S^{\cdot}$ sites are formed? (ii). Can sulfurization process prevent formation of $v_S^{\cdot}$? (iv). How does the presence of interfaces affect electro-thermal transport properties in a sulfide material with or without $v_S^{\cdot}$? (v). how does a different morphology and grain boundary concentration (PbS-ref.–SPS versus the synthesized samples) affect the electro-thermal transport properties?

Figure 4.2 demonstrates TEM, STEM/EDS and SEM analysis of the samples after each synthesis steps. The sample after the high-temperature Ar annealing (PbS) exhibited a dendrite morphology with high concentrations of grain boundaries (Figure 4.2a and 4.2c).

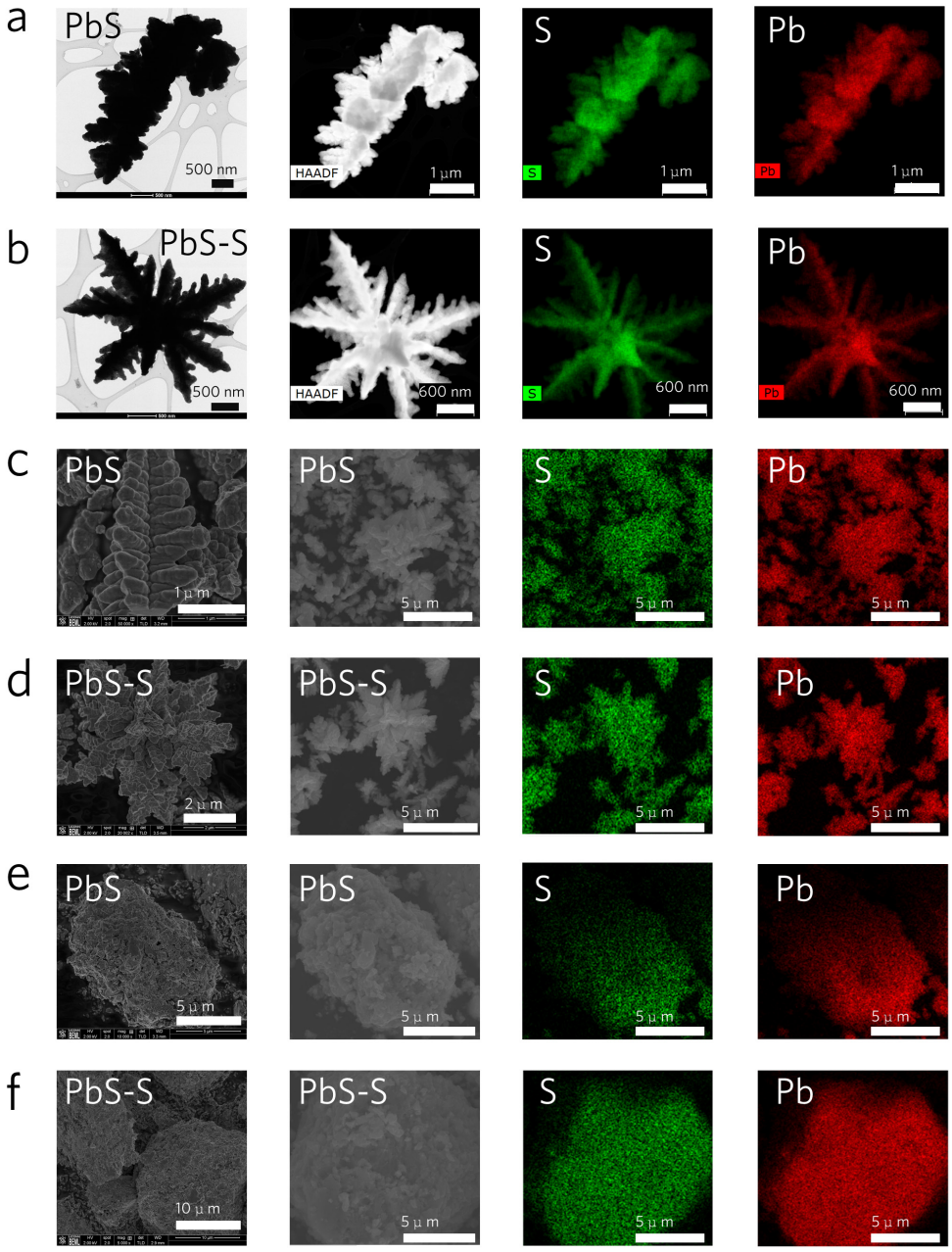

Figure 4.2. TEM and HAADF-STEM images of the PbS sample are shown (a) after the Ar treatment (PbS) and (b) after sulfur treatment (PbS-S). SEM and EDS images for sample (c) PbS and (d) PbS-S are shown for comparison. TEM and HAADF-STEM images of the PbS sample are shown (e) after SPS (PbS-SPS) and (f) after SPS (PbS-S–SPS). The elemental mappings are based on S K series and Pb M series.

The dendrite morphology was preserved after the sulfur treatment as it can be seen for PbS-S sample in Figures 4.2b,d. Sintering of the grain boundaries and densification can be observed after the SPS as shown in Figures 4.2e–f. All samples demonstrated a uniform dispersion of Pb and S elements. X-ray diffraction patterns of all samples were assigned to the cubic phase of PbS (Figure 4.3a). The analysis of the sulfur treated sample, PbS-S–SPS reveals crystal growths along [111] and [220] planes compared to those of the untreated sample (Table 4.2). The crystallite size of the reference samples PbS-ref.–SPS showed a larger Sherrer crystal size of 310 nm compared to those of the PbS-SPS (199 nm) and PbS-S–SPS (206 nm) (Table 4.2). TGA analysis of the solvothermal product indicated three major weight loss peaks (Figure 4.3d). The goal of the performed TGA analysis was to identify a temperature range at which any possible S-loss occurred where $v_S^{\cdot\cdot}$ vacancy sites were formed. The first peak at 166°C was attributed to removal of chemisorb water and solvents. The peak at 244°C was assigned to the removal of the remaining glycerol (see Figure 4.3b for the TGA analysis of Glycerol). Assuming the third peak at 266.4°C with a weight loss of 1.97 % is due to the sulfur loss from the sample, a vacancy degree of $x = 0.17$ is obtained based on PbS_{1-x}. This calculation was based on a mass-balance equation assuming the initial sample was stoichiometry (these assumptions are later verified by using ICP-OES analysis)

$$M_w(\mathrm{PbS}) = (1 + [\,(\%\ mass\ loss\ in\ N_2)\,/100)\,] \times M_w(\mathrm{PbS}_{1-x})\,. \qquad (4.2)$$

After this major peak loss, only 0.3% weight loss is obtained in a temperature range from 226.3 to 600°C. Figure 4.3c, shows the red-shift of the endothermic peaks from 970.7 to 1052.5°C after SPS being an indication of grain boundary sintering by SPS.

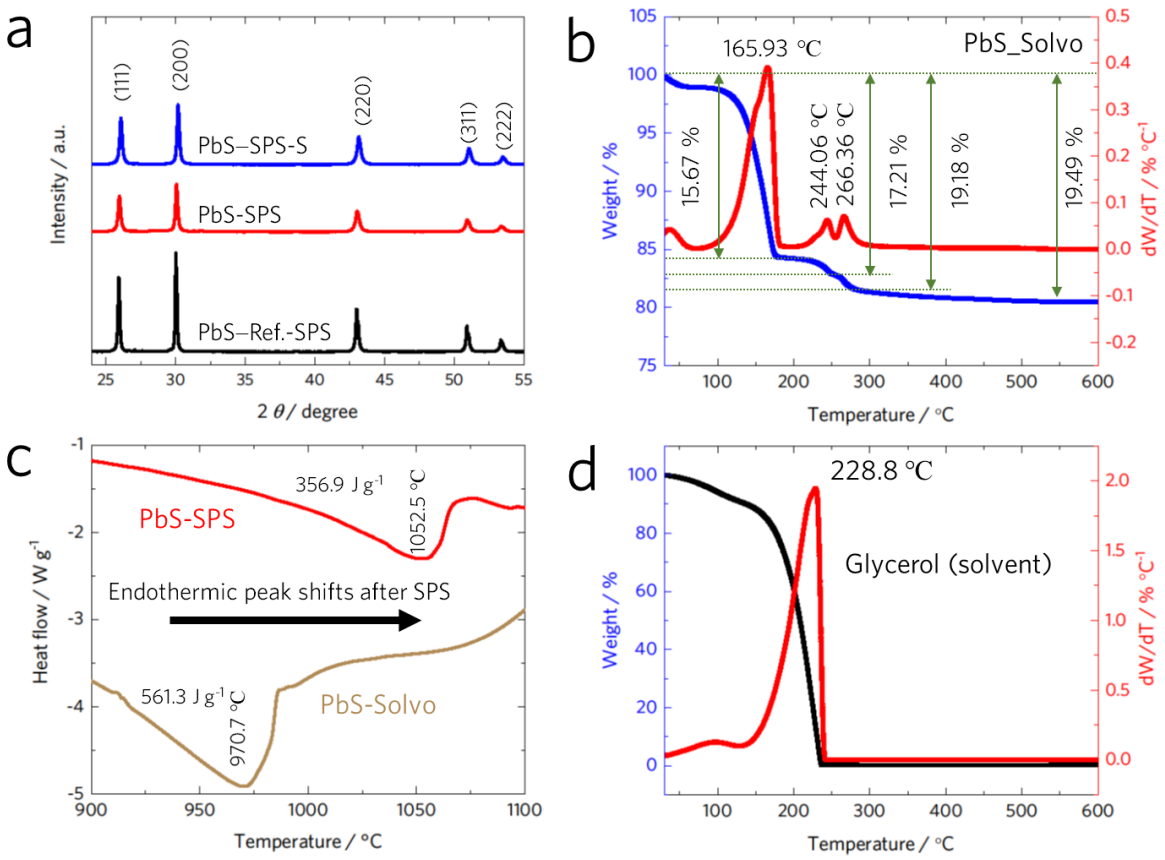

Figure 4.3. (a) X-ray diffraction patterns of PbS samples after spark plasma sintering (SPS) at 600°C. The peaks are assigned to the cubic PbS with space group Fm3m(225) according to powder diffraction file #05-0592. (b) TGA analysis of glycerol, identifying the glycerol removal temperature range. (c) DSC analysis of the samples before and after SPS. (d) TGA analysis of the solvothermal product identifying the sulfur loss temperature range.

ICP-OES analysis of the solvothermally synthesized sample (PbS-Solvo) revealed that the atomic ratio of S was 0.46% higher than that of the Pb which indicated that the product of the solvothermal process did have any sulfur deficiency (Table 4.1). Having no initial vacancy verified our prior assumption for the calculation of x based on TGA. Interestingly, the H_2/Ar annealing at 600°C, induced sulfur under-stoichiometry $x = 0.16$ sulfur vacancies based on PbS_{1-x}. This value

is very close the value calculated based on the TGA analysis ($x = 0.17$) indicating the sulfur loss temperature range was identified properly. The SPS process at the same temperature enhanced the sub-stoichiometry parameter to $x = 0.19$ (PbS-SPS sample). The analysis of the sulfur treated sample, PbS-S indicated that the performed sulfurization indeed prevented sulfur deficiency in the sample. A value of $x = -0.06$ was obtained for PbS-S, in which the negative sign indicated the presence of excess sulfur. SPS removed some of the excess sulfur and $x = -0.03$ was obtained for PbS-S–SPS. $x = 0.04$ was obtained for the reference sample (PbS-ref.–SPS.) after SPS at 600°C (Table 4.1).

Table 4.1. Sample descriptions, ICP-OES analysis results, sulfur under-stoichiometry degree, estimated the lower and upper limits of carrier concentrations, the density of trapping states and barrier heights.

sample	sample description	measured ICP-OES (atom%)		x, PbS_{1-x}	carrier concentration at $T = 300$ K				barrier height (eV) Scherrer crystallite size (nm)
		Pb	S		mobile carriers n/p (cm^{-3})	trap states density Q_t (cm^{-2})	N_{ICP}/P_{ICP} (cm^{-3})	trap states density Q_t (cm^{-2})	
PbS-Solvo	after the solvothermal reaction	49.77	50.23	-0.01	--	--	--	--	--
PbS	after argon annealing at 600°C	54.38	45.62	0.16	--	--	--	--	--
PbS-SPS	after SPS at 600°C	55.40	44.6	0.19	3.72×10^{19}	1.44×10^{13}	7.40×10^{21}	2.04×10^{14}	0.352 198.9
PbS-S	after sulfur treatment at 600°C	48.51	51.49	-0.06	--	--	--	--	--
PbS-S–SPS	after SPS at 600°C	49.18	50.82	-0.03	1.8×10^{18}	1.16×10^{12}	1.17×10^{21}	2.92×10^{13}	0.046 206.1
PbS-ref.–SPS	after SPS at 600°C	50.98	49.02	0.04	1.7×10^{18}	2.02×10^{12}	1.56×10^{21}	6.12×10^{13}	0.151 308.8

Table 4.2. XRD analysis of the SPS sintered samples.

sample	sample description	measured values from the XRD analysis				
		$d_{[111]}$ (Å)	$d_{[200]}$ (Å)	$I_{[200]}/I_{[111]}$	$I_{[200]}/I_{[220]}$	crystallite size (nm)*
PbS-SPS	after SPS at 600°C	3.43	2.97	1.33	2.27	198.9
PbS-S–SPS	after SPS at 600°C	3.41	2.96	1.28	2.13	206.1
PbS-ref.–SPS	after SPS at 600°C	3.43	2.97	1.35	2.33	309.8

*The crystallite sizes are calculated based on the Scherrer equation[237] using the integral breadth of the XRD peak areas with a Scherrer Constant of 0.89.

The performed TGA and ICP-OES analyses revealed several important observations: (i). the sulfur loss occurred during the high-temperature annealing, not the solvothermal process. (ii). sulfur loss peak centered at the temperature of 266.4°C. (iii) sulfurization prevented the sulfur deficiency. However, another observation is still un-explained. Sulfur loss was a major event happening at 266.4°C, and above this temperature only limited evaporation occurred with no clear peak. This is consistent with the observation that SPS at 600°C only added small values to the sulfur under-stoichiometry degree x caused by H_2/Ar annealing at the same temperature. In order to gain a deeper insight, DFT calculations of $v_S^{\cdot}$ formation energy was performed on the surface as well as the bulk of the materials (Figure 4.4). The PbS crystal with no vacancy was assumed as the ground state. Then on sulfur atoms in a 9-step process was removed from the surface and the bulk. The calculation suggested a major energy obstacle against the S removal from the bulk of the material being 1.72 times higher than that of the surface. These calculations suggest that $v_S^{\cdot}$ sites are first created on layers close to the surface. Creation of $v_S^{\cdot}$ in the deeper layers faces larger

barrier energies. This can explain the sulfur loss being a major event at 266.4°C. The small concentration of sulfur under-stoichiometry addition after SPS can also be explained by having a smaller outer surface by pelletization of the powders under SPS pressing conditions. In addition, the major $v_S^{\cdot\cdot}$ sites were formed prior to SPS during the H_2/Ar thermal annealing of the powders removing sulfur from the layers closer to the surface.

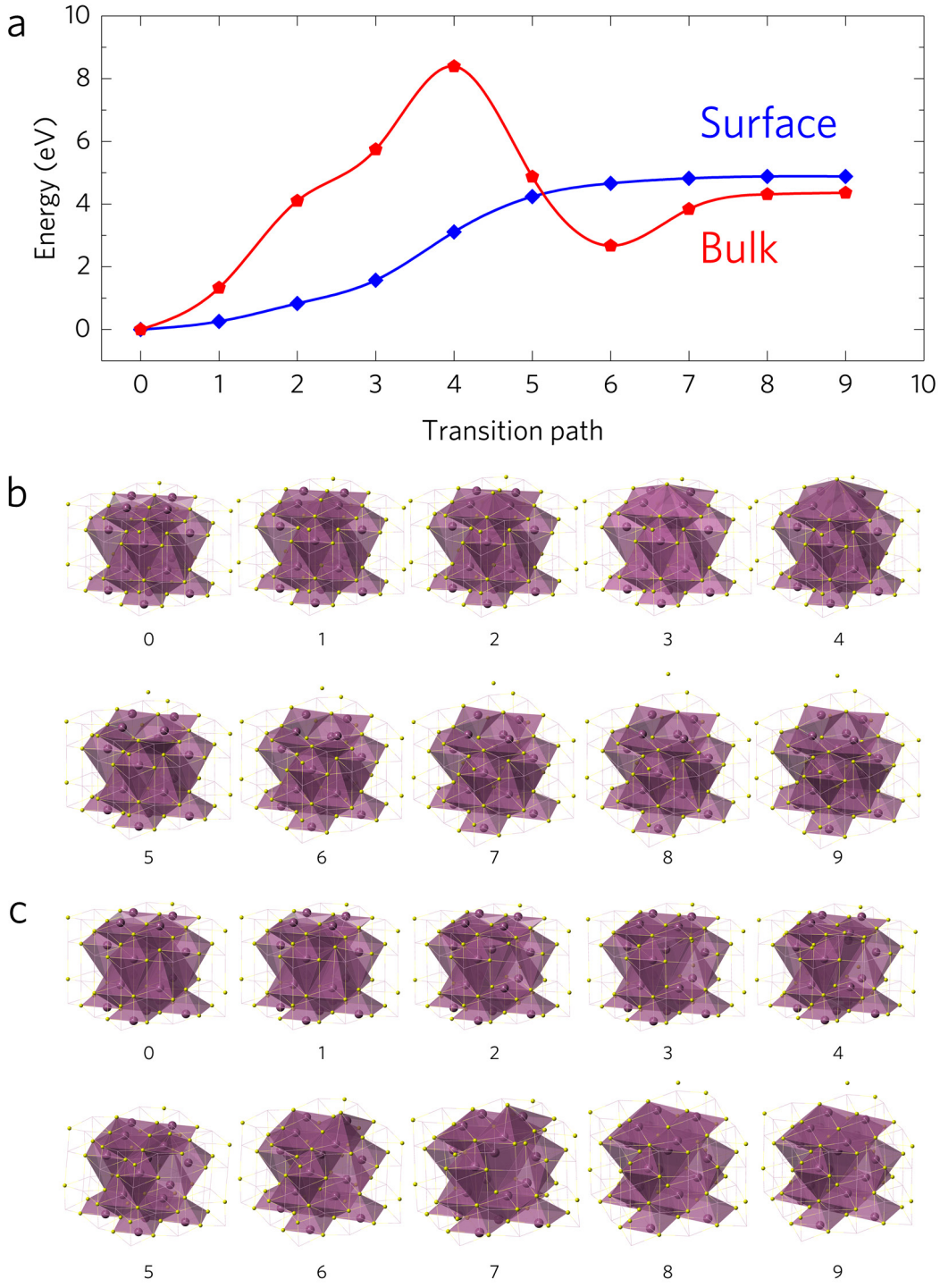

Figure 4.4. DFT calculations of $v_S^{\cdot}$ vacancy formation energy values for the bulk and surface of the PbS in a 9-step S removal: (a). The corresponding atomic arrangements in the 9-step S removal process from the PbS: (b) surface and (d) bulk.

4.3.1. Electro-thermal transport property measurements

The temperature-dependent electrical conductivity data of the samples are shown in Figure 4.5a. The electrical conductivity of PbS-SPS sample with $x = 0.19$ (the sample with the highest concentration of $v_S^{\cdot}$) exhibited a small decrease from 20.6 to 14.3 S cm^{-1} as the temperature is increased from 302.3 to 416.7 K. From 464.2 to 609.7 K, the electrical conductivity showed a rapid increase to 71.7 S cm^{-1}. Above this range, the electrical conductivity remains fairly constant. Such behavior can be caused by solid-state chemical reactions upon cycling as has been previously reported[251]. However, repeated TGA analysis at a high-temperature of 600°C did not confirm occurrence of such reactions. The other reason for such trend in the electrical conductivity can be due to a change in the majority of carriers due to increasing carrier concentration by thermal activation[23]. In such cases, a sign inversion in Seebeck coefficient measurements is expected. However, PbS-SPS sample demonstrates an *n*-type behavior over the entire temperature range with no sign inversion (Figure 4.5b). Another, explanation can be due to existence of potential barriers in the sample. As the temperature increases, some of the charge carries gain enough energy to jump over the barrier caused by the charged grain boundaries according to the model proposed by Seto[218]. The sulfurized sample, (PbS-S–SPS with $x = -0.03$), exhibited a steady enhancement of the electrical conductivity as temperature increases (Figure 4.5a). A maximum value of 14.4 S cm^{-1} is measured at a temperature of 854.8 K. Interestingly, the Seebeck coefficient measurements showed a *p*-type behavior over the entire temperature range with a maximum of $S = 373$ μVK^{-1} at a temperature of 465.4 K. The *p*-type behavior suggests the existence of excess sulfur with no $v_S^{\cdot}$, which is consistent with the performed ICP-OES analysis. The slope in logarithm of electrical conductivity versus $1/k_BT$ curves in the linear region was taken in order to estimate the barrier heights (Figure 4.5c). In contrast to PbS-SPS and PbS-S–SPS, the reference sample (PbS-

ref.–SPS) shows a trend that is expected for electrical conduction dominated by phonon-electron scattering known as metallic behavior (decreasing *vs.* temperature) (Figure 4.5a, d). However, at temperatures above 600 K, the behavior changes as the electrical conductivity increases from 12 to 16.3 S cm^{-1} at temperatures of 661 and 885.5 K, respectively (Figure 4.5c,d). The Seebeck coefficient of the reference sample shows an *n*-type behavior with a maximum $S = -453.5\ \mu VK^{-1}$ at $T = 564.4$ K (Figure 4.5b).

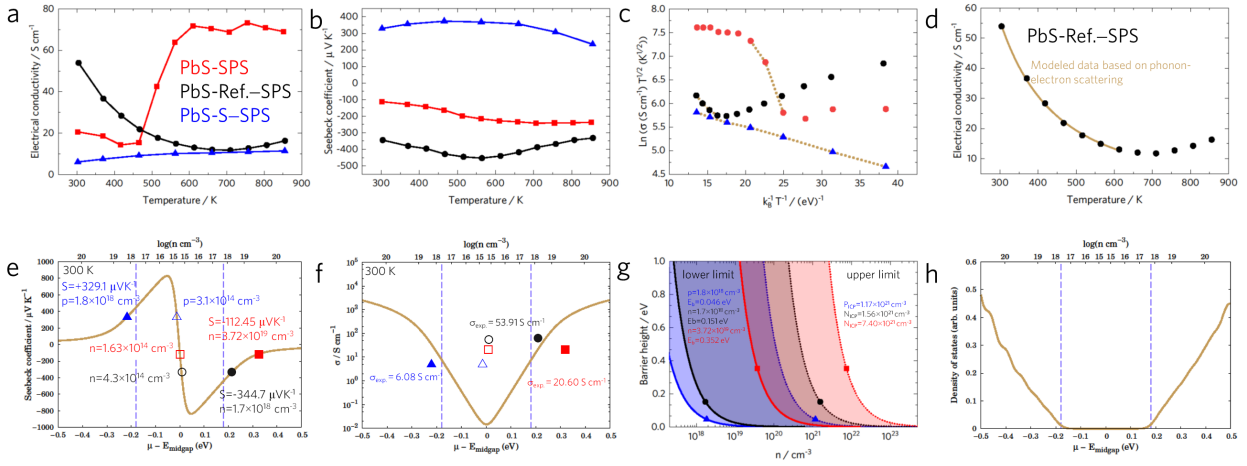

Figure 4.5. (a) Temperature dependent electrical conductivity measurements. (b) Temperature-dependent Seebeck coefficient measurements. (c) Logarithm of electrical conductivity versus $1/k_BT$ in order to calculate the barrier height according to Seto modeling[218], (d) Modelling of the electrical conductivity of PbS-ref.–SPS sample based on the phonon-electron scattering. (e) The carrier concentration can be estimated from the room temperature experimental data and DFT/BoltzTraP calculated values of Seebeck coefficients. Degenerate regime carrier concentrations are indicated by solid symbols and the values closer to the intrinsic regimes are shown by open symbols. (f) A comparison between the experimentally measured electrical conductivity values for the synthesized polycrystalline samples with those from the DFT/BoltzTraP calculations representing the expected single crystalline defect-free values at 300

K. (g) Calculated barrier height versus carrier concentrations. The estimated carrier concentration values based on DFT were considered as the lower limit (n) and the carrier concentrations obtained based on the ICP-OES analysis were considered as the upper limit (N). (h) DFT calculation of PbS electronic density of states (DOS).

According to the trapping states model[218], the doping concentration N can be larger than mobile carrier concentration n as a portion of the carriers are immobilized in the trap states at the interface. The mobile carrier concentration can be measured by the Hall method. In the current work, n is estimated by a comparison between the measured the Seebeck coefficients with those obtained from the BoltzTraP calculations at 300 K. For the measured Seebeck coefficient, there are two possibilities for corresponding carrier concentrations as shown by solid and open symbols in Figure 4.5e. Using the electrical conductivity data and those from DFT calculations (Figure 4.5f), the solid symbols were considered to estimate carrier concentrations n for the samples as the values obtained by open symbols are very far from the measured electrical conductivities. Using Seto's formulations[218], the barrier height *vs.* the carrier concentrations is plotted in Figure 4.5g for each sample. The lower limits of carrier concentration n were estimated from experimental Seebeck measurements and DFT calculations and the upper limit N were based on the performed ICP-OES analysis (Table 4.1). Based on the Seto's formulations, in the range $NL > Q_t$, the height of the barrier decreases as the carrier concentrations increases ($E_B \propto 1/N$) (Figure 4.5g). For the PbS-SPS ($x = 0.19$), PbS-S–SPS ($x = -0.03$), and PbS-ref.–SPS ($x = 0.04$), the density of trap states and barrier heights of $Q_t = 2.04\times10^{14}$, 2.92×10^{13}, 6.12×10^{13} cm^{-2} and $E_B = 0.352$, 0.151, 0.046 eV were calculated, respectively (Table 4.1 and Figure 4.5g). For PbS-ref.–SPS sample, the barrier height was calculated only in temperatures above 600 K in the linear region of the logarithmic

curve shown in Figure 4.5c. Because the grain boundaries and morphologies of the PbS-SPS and PbS-S–SPS seemed to be similar by using TEM and SEM analysis, the much higher barrier height of the former compared to the latter (sulfurized sample with no $v_S^{\cdot}$) is attributed to the high concentrations $v_S^{\cdot}$ vacancies. Each $v_S^{\cdot}$ can introduce two negative charge which can essentially be trapped in the interfaces creating a highly charged barriers against electrons/holes transport. The different temperature-dependent electrical conductivity of the reference sample compared to solvothermally synthesized samples can be due to its much lower grain boundary density as shown in Figure 4.6.

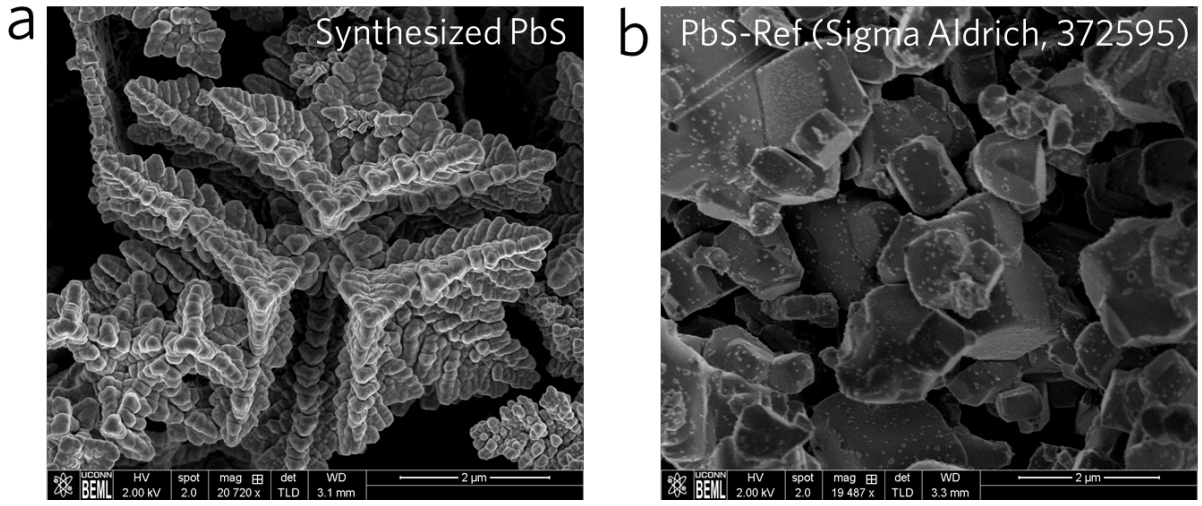

Figure 4.6. A compression of the morphology and grain boundary concentration of the solvothermal synthesized sample with those of the reference sample.

Temperature-dependent total and lattice thermal conductivity of the samples are shown in Figure 4.7a,b. In order to extract lattice thermal conductivities, the Lorenz numbers were calculated based on the measured Seebeck coefficients according to Kim and Snyder *et al.*, [252]. PbS-SPS and PbS-S–SPS exhibited lower lattice thermal conductivities compared to those of PbS-

ref.–SPS. The porosity-corrected thermal conductivity of PbS-ref.–SPS decreased more rapidly as the temperature increased approaching those of the other samples. Porosity corrected values of the 1.081, 1.28 and 1.23 $Wm^{-1}K^{-1}$ was measured for PbS-SPS and PbS-S–SPS and PbS-ref.–SPS, at a temperature of 873 K, respectively. The porosity correction calculation was based on the measured density compared to that of the theoretical value according to the Eucken[253, 254] and Russel[255] models. DFT calculations estimated the lattice thermal conductivity to be 0.833 $Wm^{-1}K^{-1}$ at 870 K. The DFT calculated total thermal conductivity, as well as lattice and electronic contributions were shown in Figure 4.7c. The calculated effective mass values have been demonstrated in Figure 4.7d.

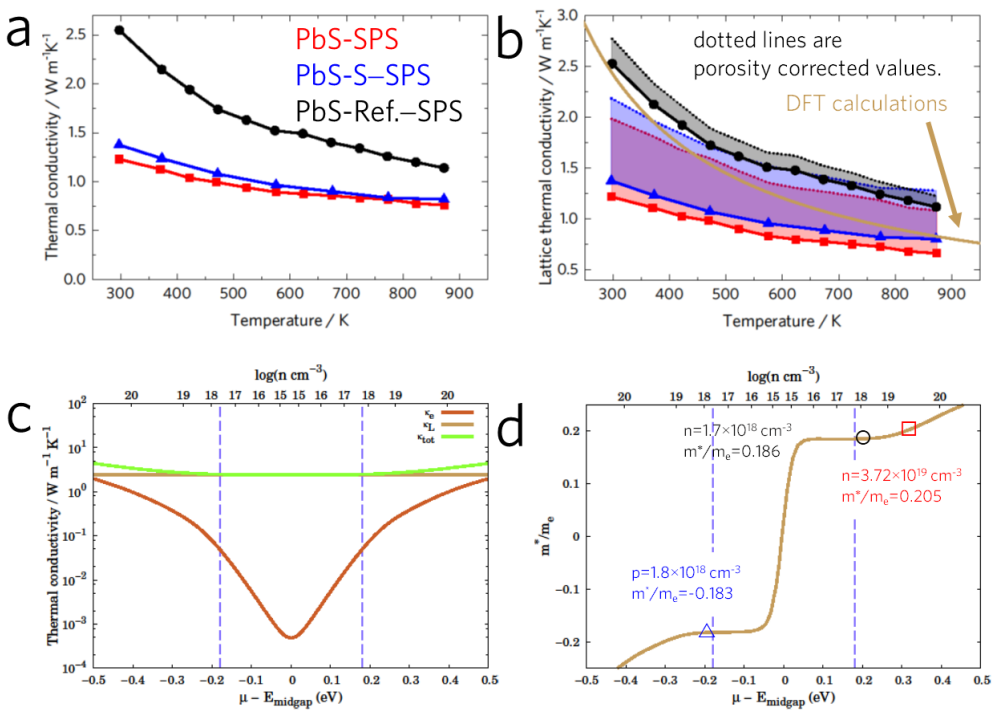

Figure 4.7. (a) Measured temperature-dependent total thermal conductivity values. (b) Lattice thermal conductivity of the samples without (symbols, solid lines) and with (dashed lines)

porosity corrections. (c) DFT calculated total, lattice, and electronic thermal conductivity of PbS at 300 K. (e) DFT calculated effective mass for PbS at 300 K.

Prior to thermal diffusivity measurements using LFA-457 Microflash, NETZSCH, pyrex 7740 and pyroceram 9606 reference samples were measured and the obtained data was compared with those provided from NETZSCH Group. An excellent agreement was observed as shown in Figure 4.8.

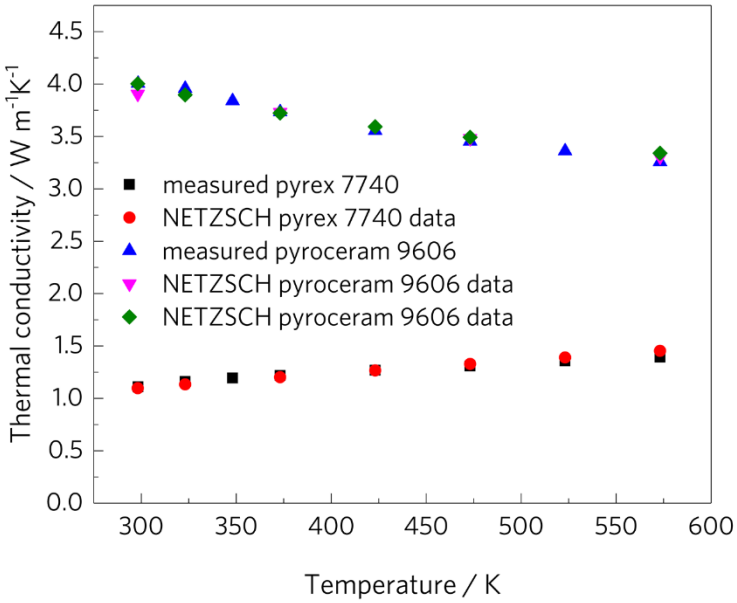

Figure 4.8. A comparison between the measured thermal conductivity values with those provided by NETZSCH for the same reference samples of pyrex 7740 and pyroceram 9606.

Multiple runs of the electrical conductivity, Seebeck coefficient and thermal conductivity measurements have been plotted in Figure 4.9. First the thermal diffusivity measurements were conducted on the pellets obtained from SPS at 600 and 700 °C (Figure 4.9a,b). Figure 4.9a

indicates a good agreement between the first and the second run thermal conductivity measurements of the pellet with SPS at 600°C. A good reproducibility is also observed for the data collected while heating and while cooling back to room temperature for the sample with SPS at 700°C, as shown in Figure 4.9b. After the thermal diffusivity measurements, the samples were cut into rectangular bars, and the surfaces were re-polished for the electrical conductivity and Seebeck coefficient using ZEM-3 instrument. Figure 4.9c compares the 1st and 2nd electrical measurement runs for a PbS rectangular bar obtained from a pellet with SPS at 600 °C. Interestingly, in the second run, the sample exhibited higher values of electrical conductivity at temperatures below 800 K (e.g. 44.5 S cm^{-1} compared to 14.9 S cm^{-1} at room temperature for the 2nd and first runs, respectively). However, the electrical conductivity values for both runs approached 71.3 S cm^{-1} at a temperature of 806 K. This behavior can be explained by using the barrier height versus carrier concentration plot shown in Figure 4.5g. After each run at the temperature range up to 600°C, the carrier concentration increases due to sulfur evaporation. By increasing the carrier concentration, the barrier height decreases, thereby improving the electrical conductivity. At the high temperature of 800 K, all the carriers have gain enough thermal energy to jump over the barrier causing the electrical conductivities to approach the same value. The Seebeck coefficient values remain relatively close within the range of the Seebeck measurement uncertainty despite sulfur evaporation (Figure 4.9d). This is due to the carrier concentration being in the degenerate region where Seebeck coefficient change versus carrier concentration remains fairly small (solid square symbol in Figure 4.9e). In contrast, the barrier height changes rapidly versus the carrier concentration (based on $E_B \propto 1/n$, See Figure 4.5g). This means that even a slight S evaporation can alter the barrier height. Similar trend was seen between the first and second run of the sample made from a pellet with SPS at a higher temperature of 700°C (Figure 4.9e,f). The 2nd run of this

sample exhibited a phonon-electron scattering similar to that of the reference sample which was attributed to the more effective sintering of the grain boundaries by SPS at 700°C. The density of this sample was measured as 6.65 g cm^{-1} compared to those of the sample with SPS at 600°C and the reference sample being 6.28 and 7.34 g cm^{-1}, respectively.

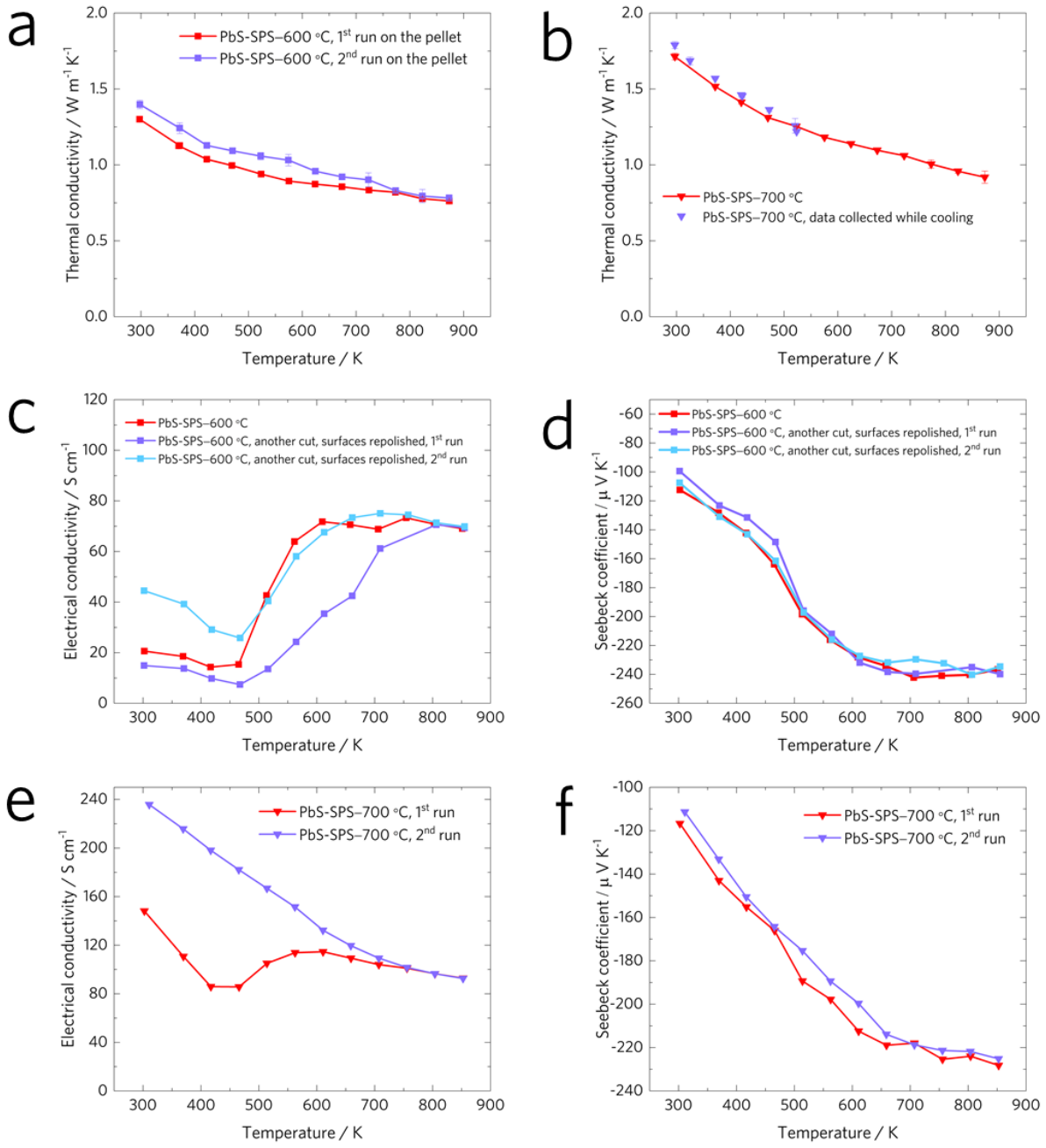

Figure 4.9. Thermal conductivity measurements of the samples (a) after SPS at 600°C, 1st (red) and 2nd (purple) runs on the same pellet, and (b) after SPS at 700°C during heating to 600°C (red) and cooling back to room temperature (purple). Temperature-dependent measurements of PbS samples from two rectangular cuts of the same pellet after SPS at 600°C: (c) electrical conductivity measurements, (d) Seebeck coefficient measurements. 1st and 2nd measurement runs of the PbS sample after SPS at 700°C: (e) electrical conductivity measurements, (f) Seebeck coefficient measurements.

A good agreement between the first and second run thermal conductivity measurements of the reference sample is shown in Figure 4.10a. The electrical conductivity and Seebeck coefficient measurements of two rectangular bars from the same pellet have been shown in Figure 4.10b,c indicating the sintered pellet being homogenous.

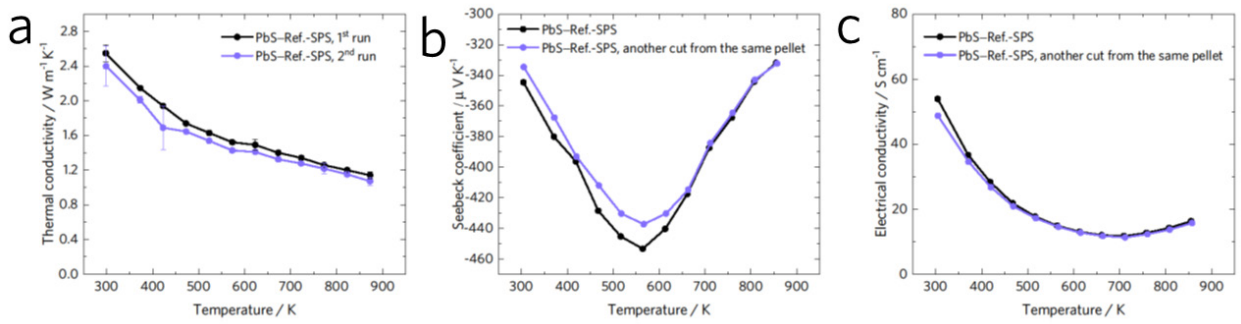

Figure 4.10. (a) Thermal conductivity, (b) electrical conductivity, and (c) Seebeck coefficient measurements of the reference PbS sample. The thermal conductivity measurements were conducted on the same pellet. The electrical conductivity and Seebeck coefficient measurements were performed on two different rectangular bars from the same pellet.

4.4. Conclusion

The effects of highly charged interfaces on the electro-thermal transport properties of Pb_{1-x} was studied. High concentrations of grain boundaries were observed for the samples synthesized using solvothermal method with dendrite structures compared to the reference sample. Sulfur vacancy was formed during the annealing process with a major loss at the temperature of 266.4 °C. DFT calculations suggested that this major loss was attributed to the regions close to the surface as the $v_S^{\cdot}$ surface formation energy was 1.72 times less than that of the bulk. The sulfurization process prevented $v_S^{\cdot}$ vacancy formations creating *p*-type samples. The electrical conductivity behavior of the PbS-SPS (x = 0.19) and PbS-S–SPS (x = -0.03) was dominated by thermionic transport through charged interface barriers. The electrical conductivity behavior of PbS-ref.–SPS was dominated by phonon-electron scattering at temperatures below 600 K due to lower concentration of grain boundaries. Barrier heights of E_B = 0.352, 0.151 and 0.046 eV were estimated for PbS-SPS, PbS-S–SPS, and PbS-ref.–SPS. The much larger barrier height of PbS-SPS was due to high density of $v_S^{\cdot}$ vacancies charging the interfaces, and thus, raising the barrier potential.

CHAPTER 5: An Instrument Design for Consecutive and Accurate Measurements of Seebeck Coefficient, Thermal Conductivity, Electrical Conductivity and Ionic Conductivity

5.1. Background: Cold-finger effect

Thermoelectric energy conversion holds the potential to convert unused streams of thermal energy, offering improved reliability with no moving parts, smaller size, longer operational lifetime on the order of decades, and thermal efficiencies on the order of 5–10%. It should be noted however that the laws of nature do not dictate an upper limit on the performance metric of thermoelectric materials, and thus this technology is capable of achieving one third of the Carnot efficiency, deemed the definition of a practical system[18]. Many promising material systems may lead to breakthroughs in efficiency including mesoporous materials[27, 256, 257], new phases of solid-state synthesized materials[30, 32, 258], and possibly topologically insulating materials[259]. However, experimental observations are rare and controversial as there is a wide degree of uncertainty arising from the current use of disparate measurement techniques on different samples which erodes confidence and obfuscates material design efforts[260-262].

There are 3 material properties that figure into the device efficiency[263]: (1) electrical conductivity, σ, (2) thermopower (Seebeck coefficient), S, and (3) thermal conductivity, $\kappa = \kappa_{electronic} + \kappa_{lattice}$ which is comprised of electronic and lattice contributions. Commercial technology utilizes materials with a dimensionless thermoelectric figure of merit on the order of unity, defined as $zT \equiv (S^2\sigma/\kappa)T$, where T is the absolute temperature. Measurement of the Seebeck coefficient is an important way to conduct high throughput screening studies used for experimental validation of computationally designed materials to increase efficiency. Therefore, the accuracy of this particular measurement is of critical importance to demonstrate an acceptable level of

experimental confidence. The most widely accepted techniques to measure Seebeck coefficient are the Ulvac ZEM-3 instrument for a bar of material longer than 6 mm in height, or the Snyder[264, 265] technique where thermocouples are applied axially to minimize errors at high temperature (Figure 5.1). An ideal design for Seebeck coefficient requires measurements of temperature and voltage difference to be conducted at well-defined locations. Thus, thermocouples are used to serve both as probes for temperature measurements and as voltage leads. However, one major source of uncertainty is that the temperature measurement is obtained at the thermocouple junction, which is not necessarily the same point as the voltage measurement due to finite sizes of the thermocouples leads[264]. This uncertainty can be intensified by increasing the temperature gradient across the thermocouple lead if the thermocouple act as a fin and removes heat from the sample. This is phenomenon is known as cold-finger effect which can dominate the error and overestimate the Seebeck coefficient by 13% at 917°C for a silicon germanium thermoelectric sample in a ZEM-3 instrument[266]. This arises from long thermocouples with large junctions touching the side surface of the sample and drawing non-negligible heat fluxes. Snyder[265] developed a new design by embedding axial thermocouples at the center of the heat spreaders in order to reduce the temperature gradient across thermocouple junctions, thereby suppressing the cold-finger effect. Moreover, very fine wires of two different materials (niobium and chromel) were used in a crossed-wire geometry connected via mechanical force applied at the junction.

Although a detailed estimation of uncertainty for the ZEM-3 instrument has been performed[266], to the best of our knowledge computational thermal analysis of the Synder *et al.*[264, 265] axial thermocouple design is not available. Herein, uncertainty in the method used by Iwanaga and Snyder *et al.*[264] for Seebeck coefficient measurements is quantified using finite-element analysis, which confirms this method's reduction of error caused by the cold finger effects.

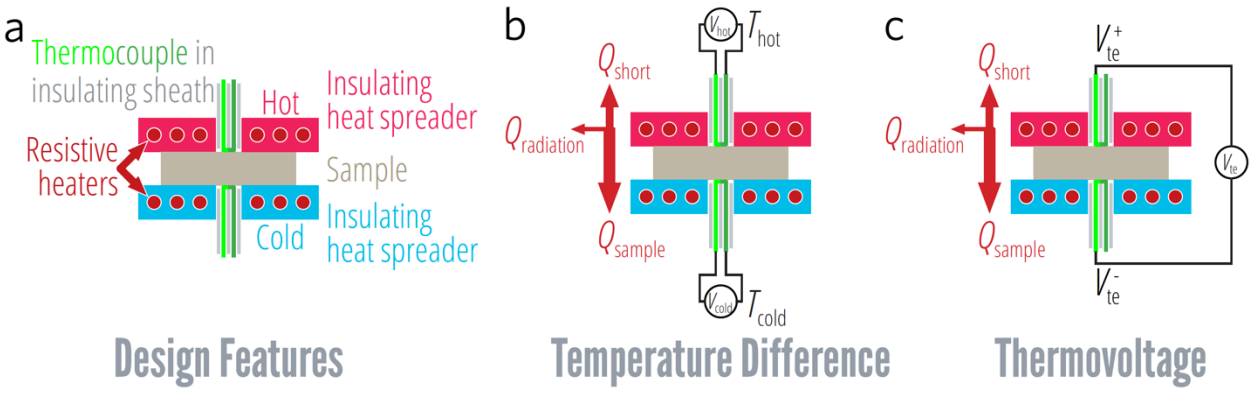

Figure 5.1. (a) Overview of the experimental methodology modeled in this work. The Seebeck coefficient is obtained by measurement of the (b) temperature difference and (c) thermovoltage through the relationship $S=-(V^{+}-V^{-})/(T_{hot}-T_{cold})$. (This figure was prepared by Dr. Michael Pettes).

5.2 Finite element analysis of the Seebeck measurement apparatus of Snyder *et al.*[264]

In order to analyze the uniaxial four-point geometry and its cold finger effects, we have produced the geometry given in ref. [264]. Figure 5.2 illustrates the physical geometry of the measurement setup used in the modeling. A 25 mm-diameter, 2 mm-thick pellet sample was used for the modeling. Two boron nitride heat spreaders were placed at the top and the bottom of the sample, with diameters of 60 mm and height of 35 mm each, with a 0.2 mm-thick sheet of grafoil® in between, matching the sample diameter. Cylinders 8 mm in diameter and 25.4 mm in height were used in place of cartridge heaters, with six heaters embedded into each of the heat spreaders symmetric about the center axis. Two 2.197 mm-diameter mullite tubes were inserted through the center of the heat spreaders and onto the surfaces of the grafoil® sheets at the top and bottom of the sample. Two 0.1 mm-thick leads of chromel and niobium were then threaded through the mullite tubing and embedded into the grafoil® sheets. Three equally spaced equi-radial thin-walled cylinders of Inconel® with 13.52 mm diameter, 127 mm in height and 0.71 mm thickness were

placed onto both the top and the bottom heat spreaders. Copper wires 1.87 mm in diameter were attached to the outer surface of each of the cartridge heaters, while a 1.6 mm-diameter thermocouple probe was embedded into each of the heat spreaders. All of the wires, probes, mullite tubing, niobium and chromel leads, and Inconel cylinders were made to terminate 200 mm from the top and the bottom edges of the heat spreaders. The entire model was constructed with a bilateral symmetry, and the system was bisected vertically to reduce the computational cost.

A thermal boundary condition was set up so that the terminating ends were at room temperature. All outer surfaces were assumed to be perfectly enclosed in a radiation shield set at temperatures of 300, 500, 700, and 900°C. The sample sides were also set to undergo radiation with the overhanging surfaces of the heat spreaders. The cartridge heaters in the top and bottom heat spreader were set as internal heat generation with values adjusted to produce a temperature difference of approximately 0, 5 and 10°C across the sample with a cold side temperature set at 900°C (Table 5.1). The entire system was placed at a high vacuum condition with no convective heat transfer, and contact resistances were not included. An open-circuit condition was assumed in order to neglect thermoelectric modeling. Thermal conductivities and emissivity for the boron nitride, mullite, niobium, and chromel were estimated using the Thermophysical Properties of Matter handbooks[267]. Pyroceram 9606 was chosen as the sample as the thermal conductivity is known accurately and used as a calibration standard (see Table 5.2 for thermal conductivity provided by the Netzsch Group). The thermal conductivities of the grafoil® and Inconel® were estimated using product specifications given by Graftech Inc.[268] and the Special Metals Corporation[23], respectively. The entire model was discretized into 1,340,789 elements, and the Mechanical ANSYS Parametric Design Language (MAPDL) non-linear iterative solver was used.

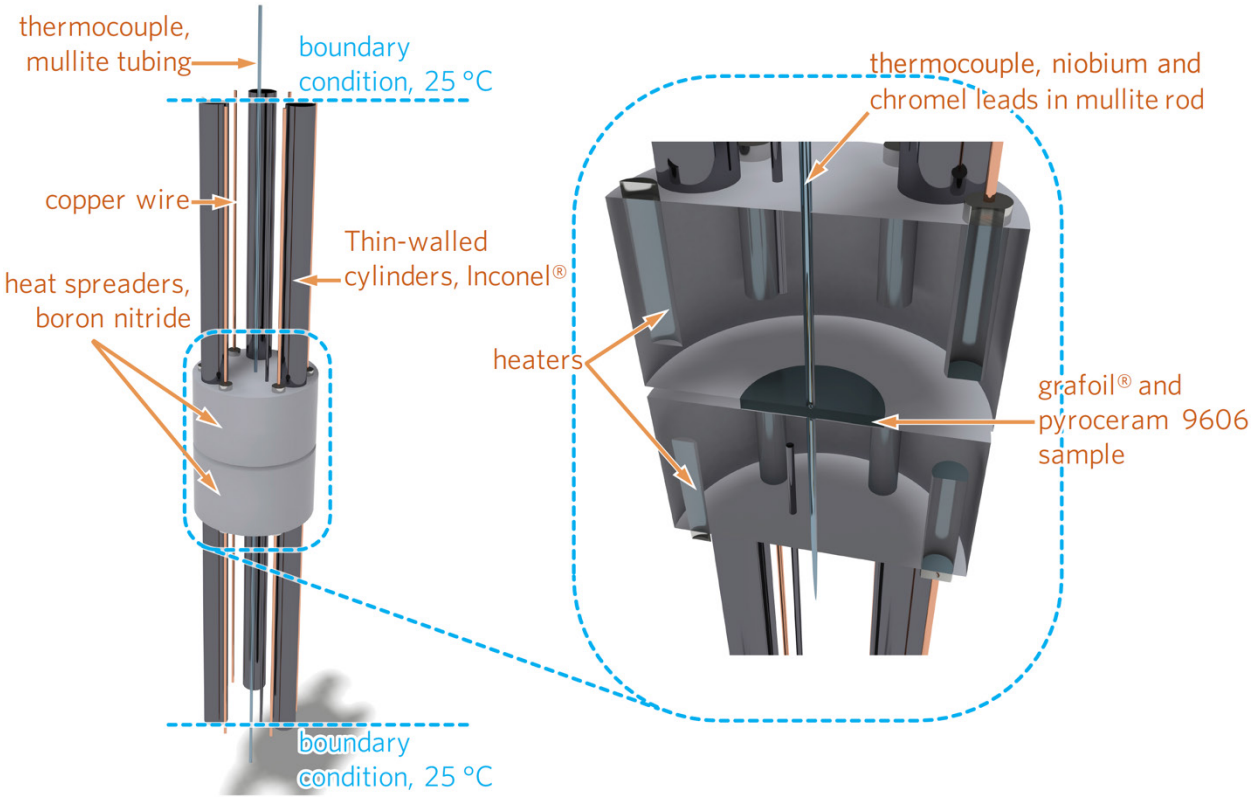

Figure 5.2. Physical geometry of the computational model. The heat spreaders are made of boron nitride. The six thin-walled support cylinders are made of Inconel®. The thermocouple configuration includes mullite tubing with niobium and chromel in a crossed-wire geometry based on the design of Snyder *et al.* [264]

Table 5.1. Heater power inputs required in the model at different set-point temperatures. Six cartridge heaters were used inside each heat spreader, with each having a volume of 8.04398×10^{-7} m^3.

Cold side center temperature(°C)	$\Delta T = T_{hot} - T_{cold}$ (°C)	Radiation shield condition	Hot side heater power (Wm^{-3})	Cold side heater power (Wm^{-3})
300	0	--	14,554,000	14,554,000
	5	--	16,230,000	13,390,000
	10	--	18,000,000	12,190,000
900	0	--	204,200,000	204,200,000
	5	--	209,850,000	201,870,000
	10	--	215,500,000	199,550,000
900	0	not heated	58,580,000	58,580,000
	5	not heated	60,570,000	57,410,000
	10	not heated	62,789,000	56,125,000
900	0	heated	3,189,000	3,189,000
	5	heated	5,323,500	1,984,700
	10	heated	7,458,000	780,400

Table 5.2. Thermal conductivity of pyroceram 9606 measured experimentally by Netzsch Group.

Temperature (°C)	Thermal conductivity ($Wm^{-1}K^{-1}$)
25	3.904
100	3.729
200	3.481
300	3.305
400	3.154
500	3.043
600	2.966
700	2.883
900	2.815
1000	2.770

5.3 Finite element analysis of the cold-finger effect

The temperature distribution across the sample diameter at the top and bottom surfaces can be seen in Figure 5.3, as a variation from the sample center temperature. Since the surrounding heat spreaders have much lower resistance, more heat flows through the sides, causing higher temperatures on the hot side and lower temperatures on the cold side. While the grafoil® sheet reduces this effect and creates a more uniform temperature distribution, a non-negligible amount of variation remains. The upper surface temperature distribution changes appreciably with the measurement temperature, which can be attributed to competition between radiation losses at the

sample sides and increased thermal resistance through the heat spreaders arising from the temperature dependence of the thermal conductivity, resulting in reduced temperature variation at high temperatures. In order to estimate the effect of the surrounding radiation effective emissivities were calculated based on[269]

$$\varepsilon_{eff} = \frac{1}{\frac{1}{\varepsilon_{surface}} + \frac{r_i}{r_o}\left(\frac{1}{\varepsilon_{shield}} - 1\right)}, \tag{5.1}$$

where we have set the ratio of the tungsten shield (r_o) and heat spreader (r_i) radii to 1.87. Figure 5.3 illustrates temperature variations across the hot and cold sides of the sample at 900°C for the cases with no radiation shield, room temperature radiation shield, as well as radiation shield kept at the same temperature as that of the center of the cold side i.e. 900°C. All cases were modeled for ΔT = 0, 5 and 10°C, where ΔT is defined by the difference between the center temperature at the upper and lower surface of the sample. It can be observed that the temperature variations on both surfaces are dominated by the three heat fluxes: heat generation from the top and bottom heaters transferred through the heat spreader and the grafoil® sheets, thermal conduction through the central thermocouples (cold-finger effect) and radiation from the sample circumference side. The thermal transport through the central thermocouples causes a minimum at the center of the sample. Sharp slopes at the sides of the sample are due to parasitic radiation. The maximum temperature variation increases by increasing the temperature drop across the sample, ΔT. For the cases with no radiation shield and with a room-temperature shield, the maximum of the temperature variation occurs at locations between the center and the side of the sample. In contrast, in the case with heated radiation shields (at 900°C), a minimum for the hot side and a maximum for the cold side occur at center of the sample for ΔT = 5 and 10°C which is due to suppressing

thermal radiation by the heated shield (Figure 5.4). In this case, the radiation is transferred to the sample as opposed to prior cases because the shield temperature (900°C) is greater than that of the circumference side. For the $\Delta T = 0$ the radiation contribution is negligible. Standard deviations of all cases can be found in Table 5.3.

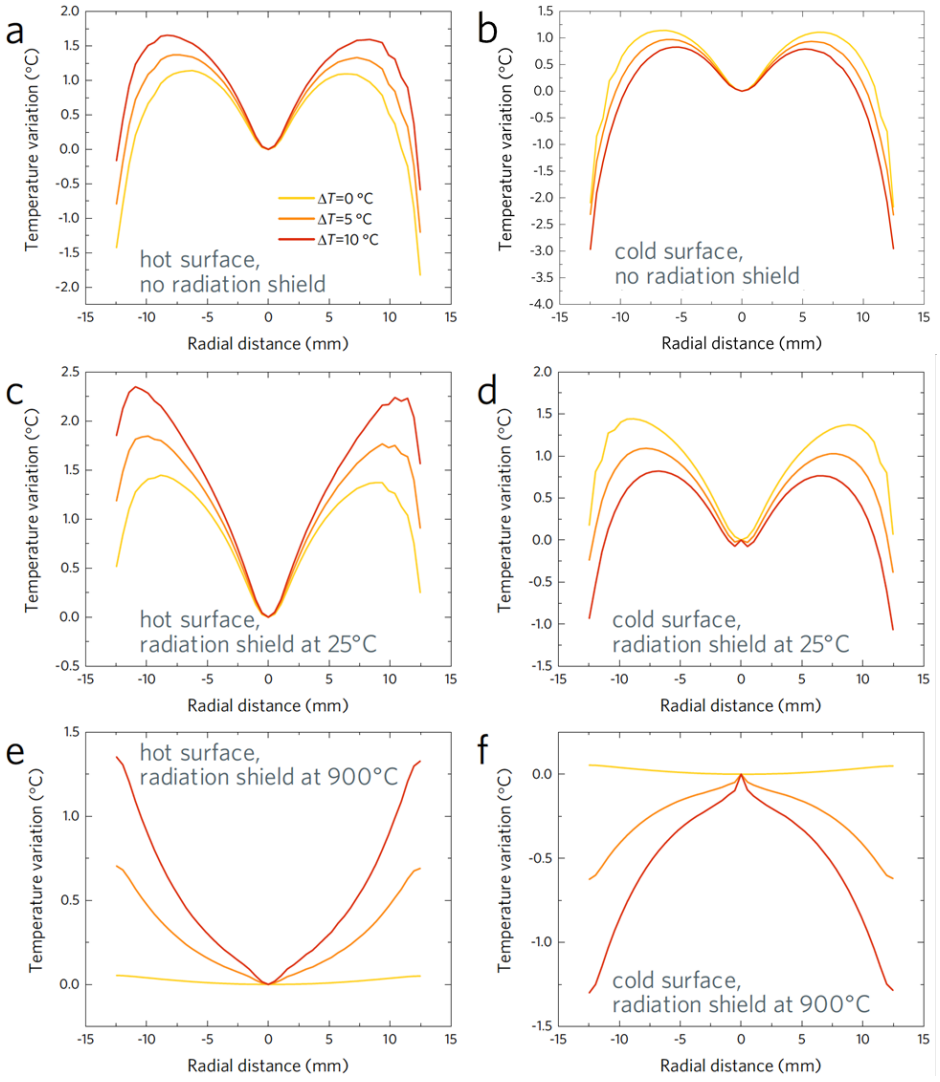

Figure 5.3. Temperature distribution on the hot surface (left panels) and on the cold surface (right panels) with (a,b) no radiation shield, (c,d) a radiation shield set at 25°C, and (e, f) a radiation

shield set at 900°C. ΔT represents the temperature difference between the centers of the hot and cold sample surfaces.

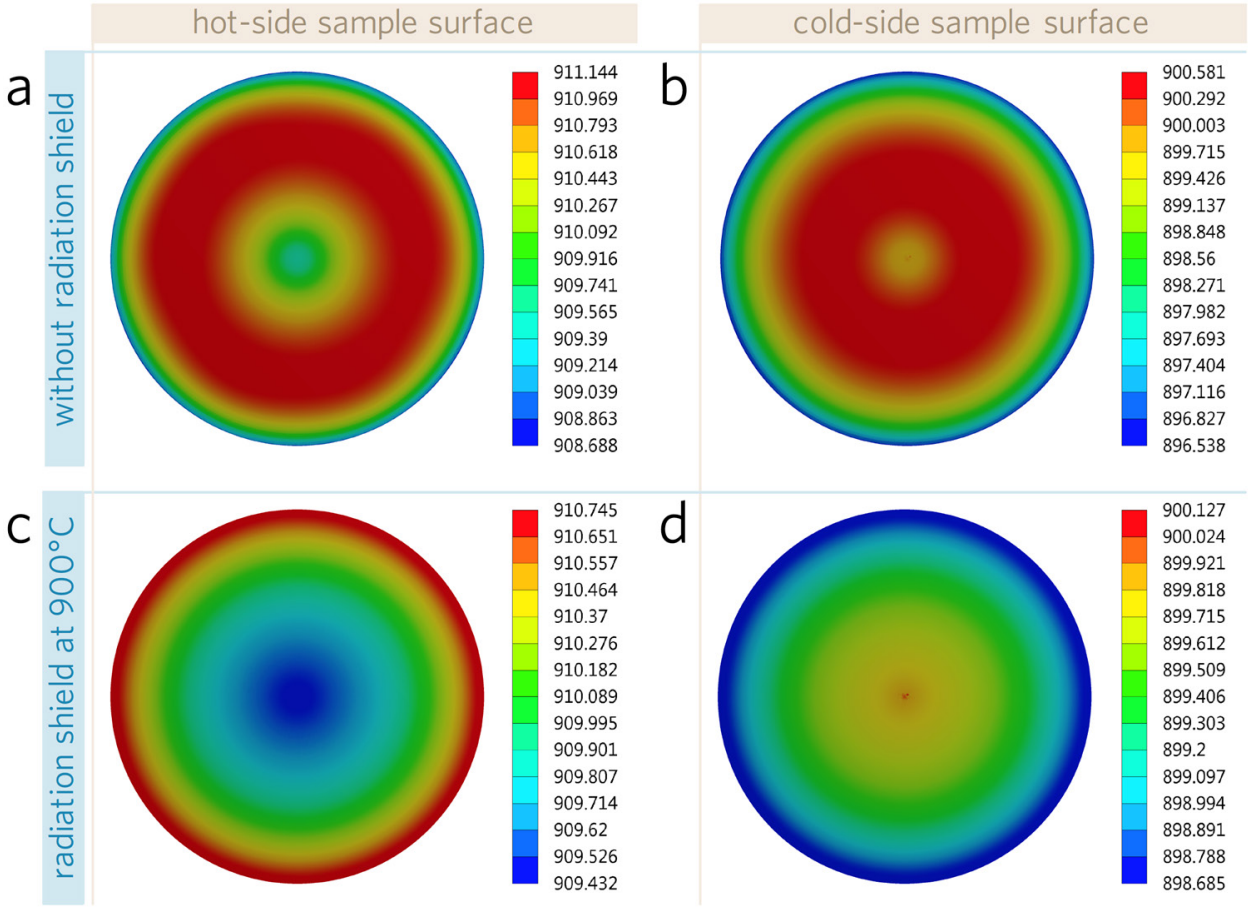

Figure 5.4. Spatial temperature distribution across hot and cold sides of the sample at 900°C with $\Delta T = T_{hot} - T_{cold} = 10°C$: (a,b) without the use of a radiation shield, (c,d) with a radiation shield set at 900°C.

Table 5.3. Standard deviation in the sample temperature distribution on the cold and hot sides at different radiation shield conditions for the bottom center (cold-side, center) of the sample being held at a temperature of 900°C with a temperature difference of ΔT across the sample. ΔT describes the temperature difference between the top (hot) center and the bottom (cold) center.

Sample surface	Radiation shield temperature (°C)	Standard deviation of $T_{surface}$ (°C)		
		ΔT= 0°C	ΔT= 5°C	ΔT= 10°C
Hot	--	0.67	0.60	0.58
Cold	--	0.65	0.88	1.03
Hot	25	0.45	0.57	0.73
Cold	25	0.46	0.41	0.46
Hot	900	0.02	0.21	0.41
Cold	900	0.02	0.18	0.37

Temperature distribution across the measurement apparatus, top and bottom thermocouples as well as the niobium-chromel crossed-wire junctions are shown in Figure 5.5. It can be seen that sinking the thermocouples in the heat spreader is indeed effective in reducing the temperature gradient in areas close to the measurement contact leads. As a result, only small variations are observed on the cross-wire leads calculated as maximum variations 0.219, 0.216 and 0.056°C on the cold side for the case with no shield, shield at 25°C, and shield at 900°C respectively. Thus, by heating the tungsten radiation shield, the temperature gradient across the thermocouple lengths is effectively reduced, thereby, decreasing the cold-finger effect. However, it should be noted that temperature distribution across the crossed-wire leads is related to the contact thermal resistance

between the leads, grafoil®, as well as the sample. These contact resistances can be the dominant factors as the leads are in contact only via mechanical force.

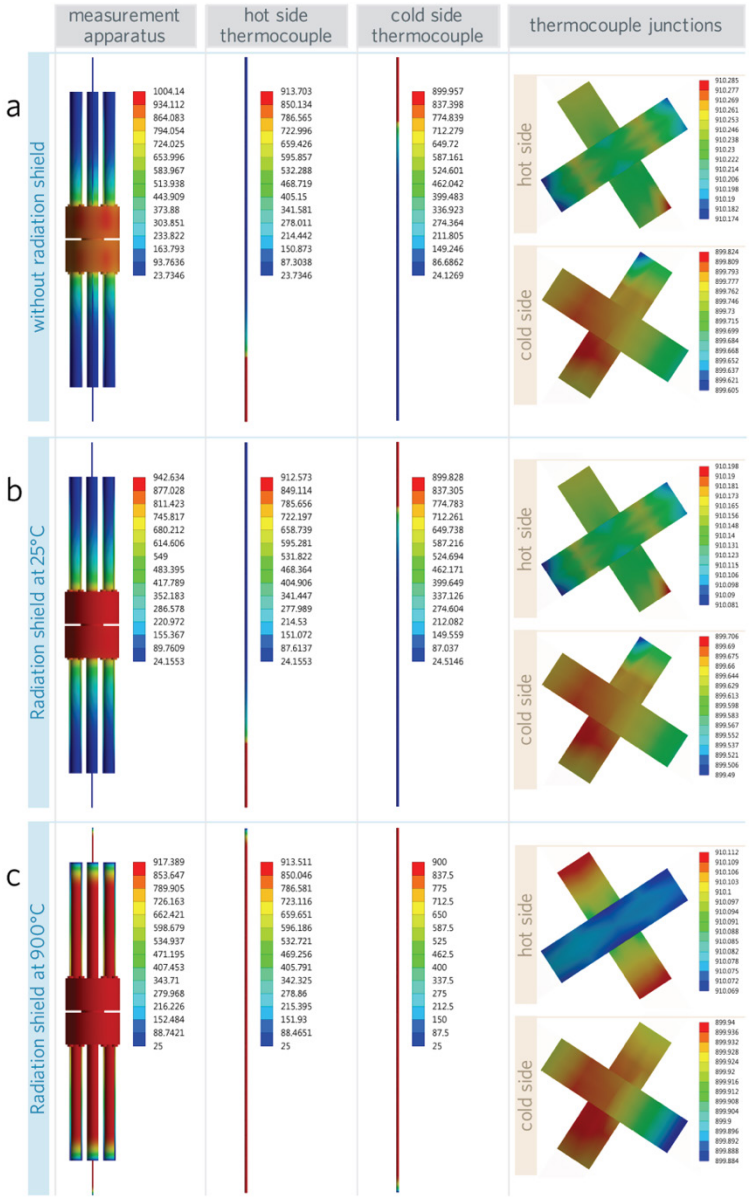

Figure 5.5. The temperature distribution of the entire measurement apparatus, top and bottom thermocouples, and crossed-wire thermocouple junctions of the niobium and chromel leads at 900°C with $\Delta T = 10$°C across the sample. Distributions are shown for the cases of (a) no radiation shield present, (b) a tungsten radiation shield at 25°C, and (c) a tungsten radiation shield set at

900°C. Embedding the thermocouples inside the heat spreaders suppresses the temperature gradient along the thermocouples, mitigating the cold-finger effect.

Table 5.4 lists the uncertainty analysis of the Snyder's[265] design. Two types of uncertainties were taken into account. The uncertainty due to non-uniform temperature distribution on the top and bottom surfaces of the sample where the temperatures are measured by the axial thermocouples and the uncertainty due to the cold-finger effect. The former is caused by thermal resistances and the radiation heat loss from the outer surface of the sample. It is noted that the results are calculated for a pyroceram sample assuming the isotropic thermal conductivity with values specified in Table 5.2 and emissivity values obtained from Thermophysical Properties of Matter handbooks[267]. The uncertainty due to surface temperature distribution was calculated based on:

$$U_{T_{surface}} = \frac{(T_{h,average} - T_{c,average}) - (T_{h,measured} - T_{c,measured})}{(T_{h,measured} - T_{c,measured})}, \tag{5.2}$$

where $T_{h,average}$ *and* $T_{c,average}$ are the average of the top (hot) and bottom (cold) surfaces of the sample, respectively. $T_{h,measured}$ and $T_{c,measured}$ are the calculated temperatures of the sample center on the hot and cold surfaces, respectively, where the temperatures are measured by the axial thermocouples. The uncertainty due to the cold-finger effect was calculated according to:

$$U_{cold-finger} = \frac{(T_{j1_{hot},average} - T_{j1_{cold},average}) - (T_{j2_{hot},average} - T_{j2_{cold},average})}{(T_{j1_{hot},average} - T_{j1_{cold},average})}, \tag{5.3}$$

where $T_{j1hot,average}$, $T_{j2hot,average}$, $T_{j1cold,average}$ and $T_{j2cold,average}$ are the average temperature of the first and second cross-geometry thermocouple junctions on the hot and cold sides, respectively (see

Figure 5.5). The average values were calculated on the junction surfaces. The two niobium-chromel junctions are used for voltage and temperature measurements on each side.

The overall uncertainty was obtained by:

$$U_{total} = \sqrt{(U_{T_{surface}})^2 + (U_{cold-finger})^2}\,, \tag{5.4}$$

where $U_{Tsurface}$ and $U_{cold-finger}$ were calculated based on Equation (5.2) and Equation (5.3), respectively.

In order to identify the effects of the sample being in a different diameter than the heat spreader, the analysis was performed for $r_s/r_h = 0.42$ and 1 where r_s, and r_h refer to the radius of the sample and the heat-spreader, respectively. For the case $r_s/r_h = 1$, the results showed uncertainty values of 8.73% and 0.4% caused by a surface temperature non-uniformity and cold-finger effect, respectively for the hot side and cold side average surface temperatures of 905.8°C and 900.6°C. The overall uncertainty was calculated to be 8.74%. The calculated cold-finger uncertainty value of 0.4% shows the very effective suppression of the cold-finger effect by using the axial embedded thermocouples in the Snyder design[265] compared to a 13% cold-finger uncertainty value of ZEM-3 at a similar temperature of 917°C[266]. As the temperature of the hot side was raised to 912.7°C, the uncertainty values remained fairly constant. The analysis for the case $r_s/r_h = 0.42$ (sample smaller in diameter than the heat-spreaders), larger uncertainty values of 10.13, 0.97, and 10.18% were estimated for the surface temperature distribution, cold-finger, and overall uncertainty, respectively for a case with average sample surface temperatures of 905.89°C and 900.9°C.

Table 5. 4. The uncertainty analysis of the surface temperature distribution and cold-finger effect in Snyder's design. T_{hot} and T_{cold} are the top (hot) side and bottom (cold) side temperatures of the sample center, respectively with $\Delta T = T_{hot} - T_{cold}$ being the temperature drop. The temperature of the radiation shield was kept at 22°C. r_s and r_h refer to the radius of the sample and the heat spreader, respectively. The total average temperatures and standard deviations were obtained on the hot and cold surfaces. The uncertainty due to temperature non-uniformity was obtained according to Equation (5.2). The uncertainty due to cold-finger effect was obtained based on Equation (5.3). The overall uncertainty was calculated according to Equation (5.4).

Sample $T_{surface}$ (°C)			r_s/r_h	Total surface average (°C)		Standard deviation of $T_{surface}$ (°C)		Temperature uncertainty (%)		
T_{hot}	T_{cold}	ΔT		hot side	cold side	hot side	cold side	$U_{Tsurface}$	$U_{cold\text{-}finger}$	U_{total}
905.794	900.999	4.804	1	905.780	900.566	0.733	0.799	8.73	0.40	8.740
912.708	900.516	12.192	1	913.010	899.753	0.702	0.868	8.74	0.42	8.745
905.411	900.893	4.518	0.42	905.888	900.912	0.193	0.203	10.13	0.970	10.18
910.431	899.193	11.238	0.42	911.225	898.869	0.473	0.389	9.951	0.470	9.96

5.4 Design of a high temperature electro-thermal measurements apparatus*

5.4.1 Background

Obtaining accurate knowledge of temperature-dependent physical properties of manufactured materials has significantly broad implications in various industries as these properties are fundamental to many technologies. Measurements of thermal, electrical and ionic conductivity of materials are essential for practical use of newly developed materials and can affect the quality control aspects needed for the integrity of energy storage and conversion systems in particular. High-precision measurements become more critical at high temperatures (above 400°C) where obtaining accurate measurements of thermophysical properties, becomes more complicated and challenging. Combined measurements of electrical and thermal properties have focused on thermoelectric energy conversion for historical reasons where accuracy requirements are most stringent[260-262]. Thermal-to-electrical energy conversion holds the potential to convert unused streams of thermal energy, offering improved reliability with no moving parts, smaller size, longer operational lifetime on the order of decades, and thermal efficiencies on the order of 5–10% [270-272]. The laws of nature do not dictate an upper limit on the performance metric of thermoelectric materials, and thus this technology is capable of achieving one third of the Carnot efficiency, deemed the definition of a "practical system" by the U. S. Department of Energy[18]. However, the current conversion efficiencies, are too low for practical applications. Therefore, method of increasing this conversion efficiency are currently a topic of research, and measurement instruments have been devised to characterize the results. The efficiency is related to the dimensionless figure of merit zT[273]. There are three material properties that figure into zT: (1)

* The finite element modelling was performed in collaboration with Hyun-Young Kim at the University of Connecticut.

electrical conductivity, σ, (2) thermopower (Seebeck coefficient), *S*, and (3) thermal conductivity, κ. Currently, all three properties are measured in different instruments, at different times, and requiring different materials. The problem arises, however, if an instrument is inaccurate or has an excessive measurement error. A round-robin study of Seebeck coefficient measurements for un-doped Bi_2Te_3 and constantan found coefficients of variations of approximately 0.04 and 0.06 at 100°C, respectively[261]. A round-robin study of the Seebeck coefficient and electrical resistivity of Bi_2Te_3 and $Bi_{0.5}Sb_{1.5}Te_3$ revealed measurement errors of about 5.5 % for Seebeck coefficient and 12.5% for the electrical resistivity on the first round, and 4% for Seebeck coefficient and 5% to 9% for the electrical resistivity on the second round[262]. This indicates the level of uncertainty present in the currently used instruments. If an instrument's results vary too widely from these margins, or has an excessive measurement error, then its results may lose some significance. While the individual errors may remain within an acceptable range, when converted into the *zT* form the propagated error can become excessive. Indeed, a round-robin study for all thermoelectric properties revealed a variation in *zT* ranging from 11.5 to 16.4%, from temperature ranges of 300 to 773 K due to the large error in its component properties[274]. The problem is further exacerbated when different measurement instruments are used for each of the component properties, as this not only combines the errors in each of the instruments, but may also require different sample preparations, degradation of the samples, or use of multiple samples in general.

There are several problematic complications in existing experimental methods. The electrical conductivity of cylindrical pellet samples can be measured using the van der Pauw method [122]. This method, however, cannot be integrated with Seebeck or thermal conductivity measurements, as the voltage and current leads must be attached from the sides. During Seebeck and thermal conductivity measurements, this will introduce an additional parasitic heat loss that

will distort the temperature gradient. This cannot be mitigated by attaching the leads to a radiation shield, since the electrical contacts will be touching a non-uniform range of temperatures. Thus, van der Pauw methods must be performed in a separate portion of the instrument or using an outside instrument altogether. García-Cañadas and Min[275] arranged an apparatus for measuring electrical resistivity via Van der Pauw method as well as Seebeck coefficient at room temperatures. The Seebeck coefficient was measured by using only two probes directly in contact with the sample in order to read the voltage and temperature difference along the two points of contacts[275]. The presumption of using such configuration is that microstructure, temperature distribution and, therefore, Seebeck coefficient is highly homogenous across the sample[276]. Thus, using such methods is only appropriate for obtaining rough and quick evaluation of Seebeck coefficient at low temperatures. Another method involves running a current directly through a sample, using current leads embedded in the thermoelectric block. A square-wave alternating current is used to negate thermoelectric contributions to the measured voltage drop. Both heaters and the radiation shield are held at a desired temperature for measuring a desired property. The voltage fluctuation is then measured with a lead possessing a low Seebeck coefficient (niobium), and resistivity can be calculated as shown in ref. [277]. The major concern, however, is determining the effects that arise from non-uniform current distribution through the heat spreader and the electrical contact resistance. This is more concerning for instruments where thermocouples do not directly touch the sample. The most common scheme involves three separate measurements on three separate instruments: (i) electrical conductivity and thermopower are obtained by an Ulvac ZEM-3 instrument for a single rectangular bar or cylinder of material, (ii) thermal diffusivity is measured using a Netzsch Laser Flash Apparatus (LFA) for a single cylindrical pellet, and (iii) specific heat capacity is measured using a Netzsch Differential Scanning Calorimetry (DSC) instrument for a

single cylindrical pellet. As for existing commercial instruments for thermoelectric property measurements, the ULVAC ZEM-3 measures the Seebeck coefficient by setting a temperature gradient across two contact points along the height of a long rectangular or cylindrical sample, and the electrical conductivity by pulsing an electrical current through the sample. It then measures the voltage response using two thermocouples/voltage probes along the sample sides to extract S and σ. By measuring at the sample sides in a four-probe off-axis geometry, this avoids the additional contact resistances present in two-point geometries in which the probes are embedded in the contacts. A thermal finite element analysis by Mackey *et al.*[266] showed, however, that these parasitic conduction pathways resulted in an error of up to -13.1% at high temperature ranges for the Seebeck coefficient. A major contributor to this error was the cold-finger effect, in which the probes at sample sides leeched heat away from the sample and thus distort the temperature gradient. As a solution for this effect, Snyder *et al.*[264, 265] developed an instrument in which the probes were inserted axially through the contacts and onto the sample surface, thereby avoiding both the contact resistance and the cold finger effect. In their design, a crossed-wire thermocouple configuration composed of niobium and chromel wires were used at temperatures up to ~652°C. The thermocouple wires were threaded through a 4-bore ceramic tube, and the ceramic tube was in turn heat-sunk to the heaters, in order to minimize cold-finger effects. This axial arrangement of thermocouples minimizes errors at high temperatures[265], however this method lacks the capability to measure electrical or thermal properties. Configurations for different competing electrical and thermal property characterization methods are given in Figure 5.6. Thermal diffusivity measurements are conducted using transient flash diffusivity methods and specific heat is measured by using differential scanning calorimetry (DSC). A round-robin investigation of these measurements by Wang and co-workers[262] revealed that thermal conductivity measurements

contributed the greatest share in the overall uncertainty of the measured zT[262]. Two sets of round-robin investigations were conducted on *n*-type Bi_2Te_3 and *p*-type Bi_2Te_3-Sb_2Te_3 alloy by using Netzsch LFA447 and LFA457, TA Instrument/Anter Flashline5000 and XPlatform for themal diffusivity measurements and three types of Netzsch DSC, TA Instrument DSC and Quantum Design Physical Properties Measurement System (PPMS) for specific heat measurements. The thermal diffusivity measurements showed the largest scatters of ±6% to ±10% at a temperature ~ 502 K and ±15% to ±17% at 473 K, for the first and second round-robin investigations, respectively[262]. Interestingly, DSC measurements posed the biggest challenge with more than ±15% scatter in the combined data at temperatures up to 502 K. The nature of DSC measurements with three separate runs required to calculate the specific heat made the DSC measurements most difficult to reproduce[262]. One main challenge arises from the un-stable baselines changing from DSC to DSC equipment. The results showed more than ±15% scatter in the measured specific heat values in a temperature range from ~ 300 to 473 K[262]. The results from seven laboratories on 14 samples indicated that the DSC measurement is the most operator-dependent measurement and least likely to produce reliable data[262]. The data scatter for the figure of merit was ±6.8% near room temperature and ±17.1% at 475 K[262]. Lacking the capability for reliable and accurate measurements of the electro-thermal properties is even worse at higher temperatures above the investigated range of 300 to 500 K. On the other hand, the current steady state methods for direct thermal conductivity measurements are not rigorous enough to be employed for elevated temperatures. Thus, there is a critical need for new designs with improved capabilities.

In the present work, we propose a new design for an instrument for accurate and consecutive measurements of temperature-dependent thermal, electrical and ionic conductivities as well as Seebeck coefficient at high temperatures (1000 ℃ and above). The embedded axial

thermocouple configuration by Snyder's design[264, 265] is adopted and new modifications and arrangements are proposed for consecutive measurements of thermal conductivity, electrical conductivity and Seebeck coefficient in a single instrument. Additionally, a new configuration is analyzed with potential capabilities to provide reliable measurements even at an exotic temperature of 2500 °C. This is the first time, a new design at such temperature ranges is presented with capabilities to measure all the electro/electrochemical and thermal properties consecutively on the same sample without the need for breaking the vacuum or inert gas environment suitable for high-throughput measurements or quality-control processes.

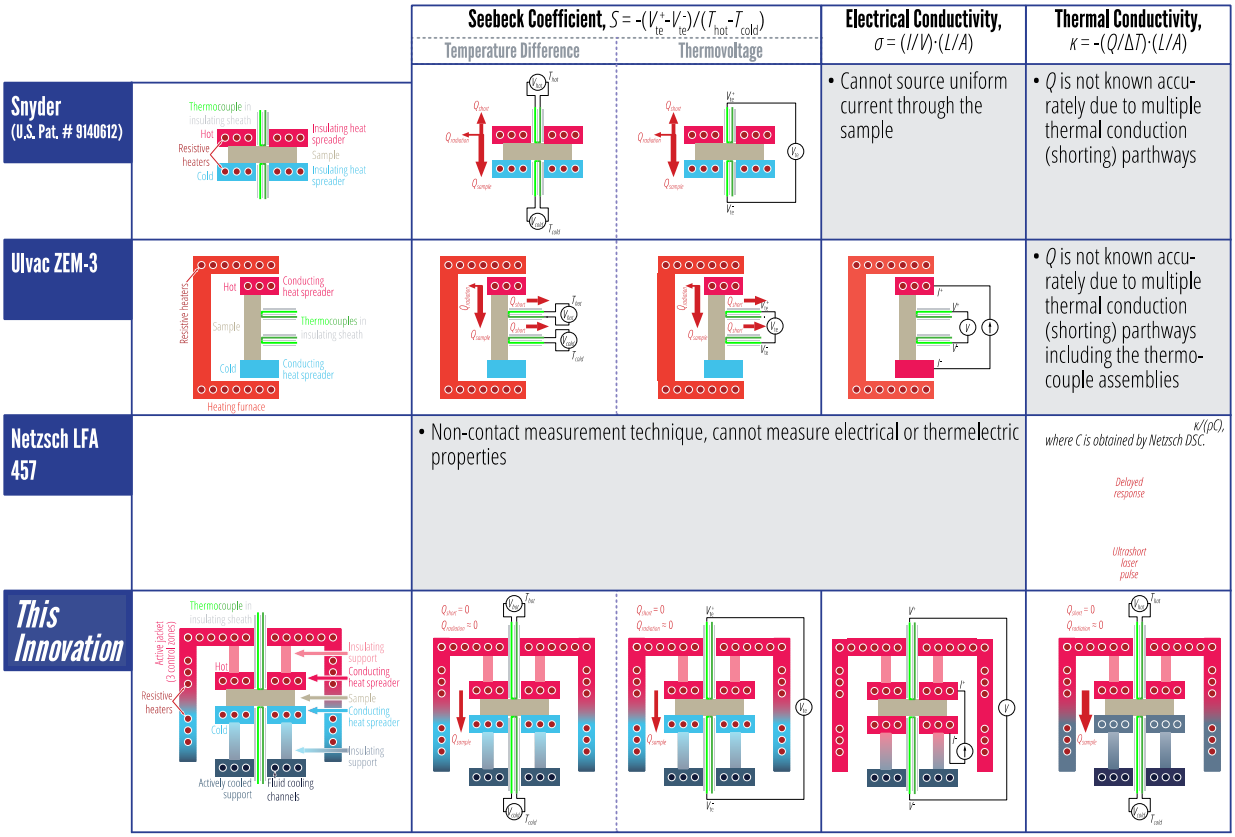

Figure 5.6. Overview of current electrothermal property characterization methods in comparison with the approach proposed here. The properties that must be obtained to quantify device efficiency are the electrical conductivity (σ), thermal conductivity (κ), and Seebeck coefficient (S). (This figure was prepared by Dr. Michael Pettes).

5.4.2. Instrument geometry description

In order to analyze the uncertainty in the electrothermal transport property measurements, a finite element model of the instrument was produced. A 12.7 mm-diameter, 5 mm-thick pellet sample was used for the modeling. Two tungsten heat spreaders were placed at the top and the bottom of the sample, with diameters of 12.7 mm and height of 40 mm each, with a 0.25 mm-thick sheet of grafoil® in between matching the sample diameter. Rectangular bars of 1.7 × 3 mm and 30 mm in height were used in place of cartridge heaters, with six heaters embedded into each of the heat spreaders symmetric about the center axis. Two 1.5875 mm-diameter and 65 mm in height alumina tubes were inserted through the center of the heat spreaders and onto the surfaces of the grafoil® sheets at the top and the bottom. Two 0.1 mm-thick leads of tungsten and niobium were then threaded through the alumina tubing and embedded into the grafoil® sheets. Three thin-walled cylinders of alumina with 3.175 mm diameter and 1.75 mm thickness were each placed axis-symmetrically on the top and the bottom heat spreaders. Tungsten wires of 0.2 mm in diameter were attached to the outer surface of each of the cartridge heaters, while a 1.6 mm-diameter thermocouple probe was embedded into each of the heat spreaders. All of the wires, probes, mullite tubing, niobium and chromel leads, and Inconel cylinders were made to terminate 25 mm from the top and the bottom edges of the heat spreaders. The entire model was setup with a bilateral symmetry. The simulation was run for base temperatures of 100, 300, 500, 800, 900 and 1000°C.

The support ends and wire ends for the hot side were set at 5°C higher than the base temperature assuming they were sunken into the second stage heating platform, while cold ends were set at 22°C. The bisected surfaces were assumed to be adiabatic due to symmetry. All other exposed surfaces were set with radiation with surrounding temperatures matching the hot-side temperature. Both below and above heaters were then adjusted to produce a desired temperature drop from the hot-side temperature to the base temperature at the center of the sample. It was assumed that the wires and supporting columns were electrically insulated enough for an open circuit condition, and therefore any thermoelectric effects were ignored. It was assumed that the entire system was placed in a vacuum condition with no convective heat transfer, and the contact were assumed to be with negligible resistances. An open-circuit condition was assumed in order to neglect thermoelectric modeling. Thermal conductivities and emissivity for the all the materials were estimated using the Thermophysical Properties of Matter handbooks[267]. The analyses were conducted on various sample materials of silicon dioxide, pyroceram 9606, boron nitride, and hafnia (HfO_2) with the same handbooks used for property values. Thermal conductivity values of pyroceram 9606 were adopted based on the data provided by NETZSCH group. The thermal conductivities of the grafoil® were estimated using product specifications from Graftech Inc. [268] and the Special Metals Corporation[20]. The entire model was discretized into 1,038,273 elements, and the Mechanical APDL non-linear iterative solver was used. The outside perspective of the modeled apparatus and a detailed view of the inside arrangement are illustrated in Figure 5.7.

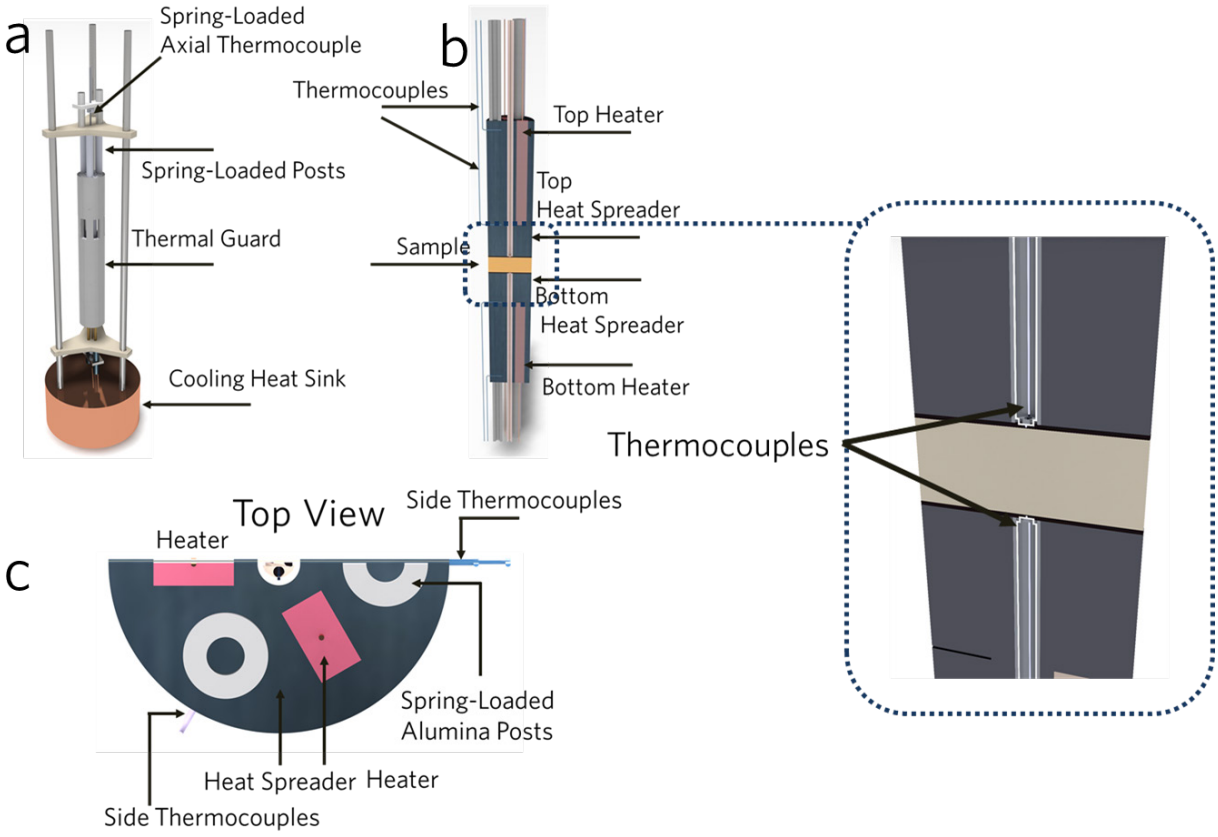

Figure 5.7. (a) Schematic of the high temperature electrothermal characterization apparatus showing axial thermocouples, radiation shield and actively cooled heat sink. (b) Detail of the enabling design components. (c) A detailed top view of the instrument design component.

5.4.3 Finite element analysis of thermal conductivity measurement

A flowchart algorithm of the performed steps in the ANSYS Steady-State Thermal program is shown in Figure 5.8.

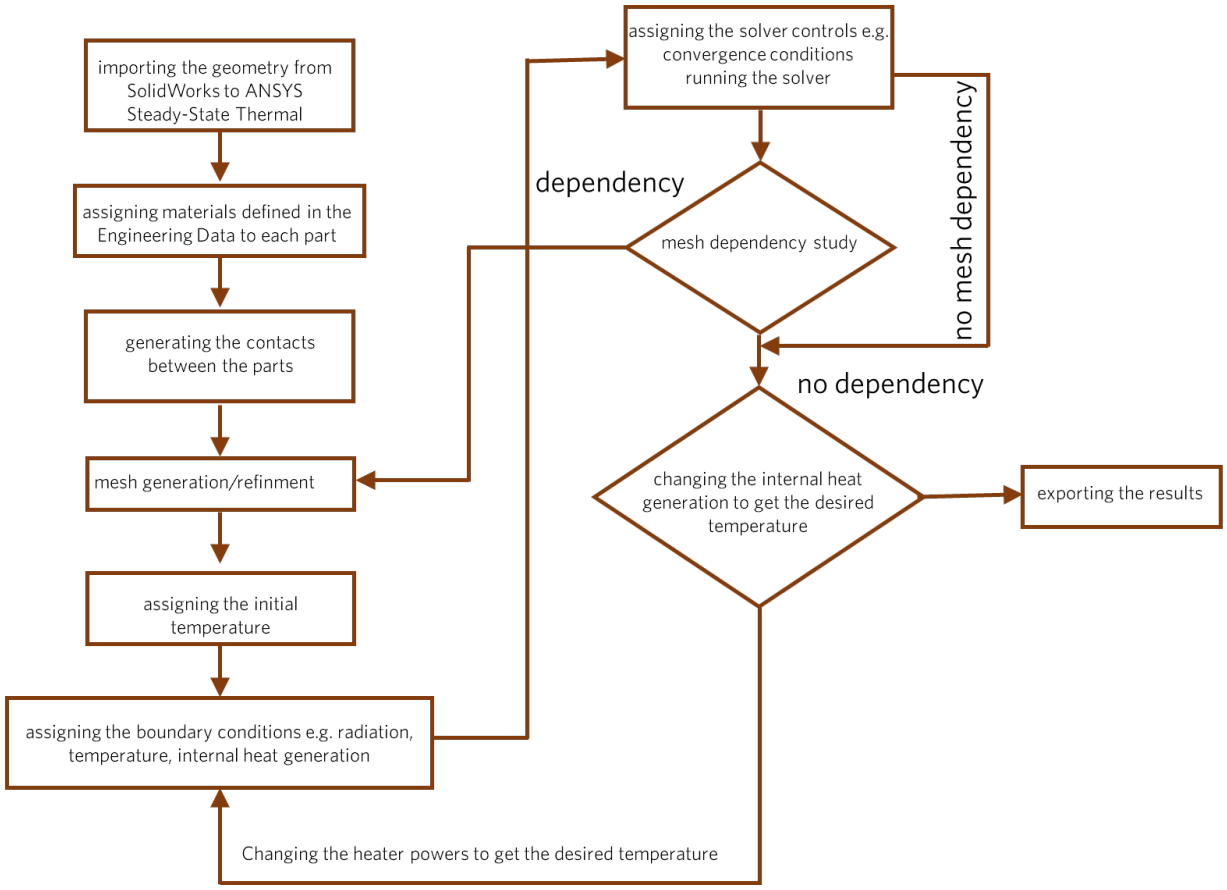

Figure 5.8. A flowchart of the performed finite element analysis showing the steps from importing the geometry to controlling the solution process in the ANSYS Steady-State Thermal program.

By keeping track of the amount of heat flowing through the sample, q_{sample}, the same setup can also be used to measure thermal conductivity using the equation[278]

$$k = -\frac{q_{sample} L_{sample}}{\Delta T A_{cross-sectional}}. \tag{5.5}$$

In a regular thermal guard design for a direct measurement of thermal conductivity, due to the large heat losses in the instrument itself, the power input to the heaters will vary wildly from the

actual heat flow through the sample, and therefore be unsuitable for thermal conductivity measurements. This is particularly relevant at higher temperatures, where the heat losses are magnified by the fourth-power term present in radiative losses. It is, however, possible to minimize the heat losses from one side of the instrument in order to estimate the amount of sample heat flux using the power supplied to the cartridge heaters. In order to minimize the conductive losses through the supporting columns and probes, using long and narrow geometry with low thermal conductivity materials is not enough, as the residual heat losses will directly contribute to the measurement error. Instead, a change can be implemented in which all columns and probes are sunk into a second heating stage with separately controlled heaters. This second stage can be set to the nominal temperature of the initial heating stage so that there will be a minimal temperature difference between the two stages. Combined with traditional usage of low cross-sectional areas, large lengths, and low thermal conductivity materials, this can help reduce the errors to acceptable degrees.

While convective losses are not an issue due to the common usage of vacuums, radiation losses can still cause large problems with thermal conductivity estimation even with radiation shields in place. This is a greater problem in high temperature measurements, due to the effects of the fourth-power terms for radiative heat transfer. Two steps can be taken to alleviate these errors: The radiation shield temperature can be set at the nominal temperature of the sample hot side, rather than being fixed at the average temperature or at approximately similar temperatures. This requires more accurate control of the radiation shield temperatures as well as the temperature changing with the hot side temperature as the temperature drop is increased for more measurements. It does, however, significantly reduce radiation losses from the hot side. This is due to the fact that even when the radiation shield is set at the nominal hot side temperature, there

will be some temperature variation, and therefore radiative losses. This can be further reduced by having the radiation shield be made of a low-emissivity material, for a passive shielding effect.

Emissivities were adjusted to estimate the emissivity of the surrounding radiation shield by using Equation 5.1. For this simulation, the ratio of radii was set at 0.7. The temperature of the top surfaces where set to be 5°C above the nominal temperatures. The heater output was compared to the averaged-heat flux down the sample presented in Table 5.5. As expected, there is a tendency for there to be some heat loss from the upper heaters, and therefore the heat flux will be overestimated from 2% at low temperatures and up to 7.6% at 1000°C. There is, however, a competing effect from the radiation on the sample itself which tends to increase the heat flux along the edges of the sample, especially in the lower half. This effect can be seen in Figures 5.9a, and 3b for both 300°C and 1000°C, respectively. Due to the fourth power present in radiative heat transfer, the effect is about an order of magnitude bigger in scale at the 1000°C limit. The heat flux, however, remains more stable at the centers of the sample. Instead, the steepest increases in the heat fluxes are mostly in the bottom edges, where they will have the lowest amount of impact on the measurement since it will have the least time to affect the temperature gradient, and the measurement is done at the center. Table 5.5 also includes an average over the top surface of the sample, before the radiation on the sample can take effect. This shows that, without the competing effect, the heat flux is overestimated from 2.1% at low temperatures to 12.8% at high temperatures. Since the heater losses are greater than the sample gains, higher emissivity samples as well as slightly larger temperature gradients should be tolerable without increasing the error.

Table 5.5. A comparison between the heater output and the average heat flux of the sample at various temperatures. The specified temperatures indicate the temperature of the sample center on the bottom (cold) surface. The center temperatures of the sample on the hot surface were kept 5°C above these values. The lower values of the top surface heat flux average, with no radiation from the sample, indicates the overestimation of the sample heat flux due to radiation.

Temperature (°C)	100	300	600	800	1000
Heater output ($W m^{-2}$)	1531.5	1721.5	1822.9	1973.2	2074.5
Full surface average ($W m^{-2}$)	1499.4	1693.0	1785.9	1888.0	1916.0
Top surface average ($W m^{-2}$)	1499.0	1689.0	1771.8	1834.0	1809.0

There is, however, a competing effect from the radiation on the sample itself which tends to increase the heat flux along the edges of the sample, especially in the lower half. This effect can be seen in Figure 5.9 for temperatures of 300°C and 1000°C. Due to the fourth power present in radiative heat transfer term, the effect is about an order of magnitude bigger in scale at the 1000°C limit. The heat flux remains more stable through the center of the sample. Instead, the steepest increases in the heat fluxes are mostly in the bottom edges, where they will have the lowest amount of impact on the measurement since it will have the least time to affect the temperature gradient, and the measurement is done at the center. Table 5.5 also includes an average over the top surface of the sample, before the radiation on the sample can take effect. This shows that, without the competing effect which we have included in our model, the heat flux would be overestimated from

2.1% at low temperatures to 12.8% at high temperatures. Since the heater losses are greater than the sample gains, higher emissivity samples as well as slightly larger temperature gradients should be tolerable without increasing the error.

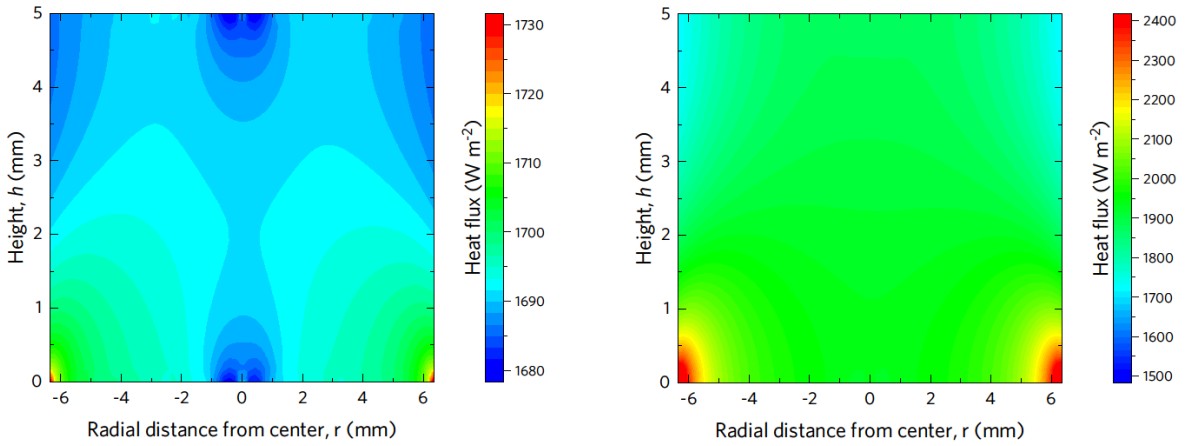

Figure 5.9. The heat flux across the sample for (a) $T = 300$°C and (b) $T = 1000$°C.

The thermal conductivity that would be measured in this case was calculated using Equation 5.5 and was compared with the input conductivity to obtain a relative error, as listed in Table 5.6. This was compared to the error propagated from the temperature probe error as well as the error between the input heat and the surface average. The two were found to be mostly in agreement, varying by at most 0.56% at 1000°C. The errors tended to overestimate the thermal conductivity, with minimum of 2.1% at 100°C and 8.22% at high temperature 1000°C. From the propagated error, it can be seen that the heat flux is the dominant error source in the system. The heat flux uncertainty values were calculated by:

$$U_{Heatflux} = \frac{q''_{fullsurface,average}}{q''_{heater,output}}, \tag{5.6}$$

where $q''_{fullsurface,average}$ and $q''_{heater,output}$ are the sample full surface average heat flux and the heater output, respectively obtained from Table 5.5 The temperature uncertainty was calculated based on:

$$U_T = \frac{(T_{h,\max} - T_{c,\min}) - (T_{h,measured} - T_{c,measured})}{(T_{h,measured} - T_{c,measured})}, \tag{5.7}$$

where $T_{h,max}$ *and* $T_{c,min}$ are the maximum and minimum temperatures on the top (hot) and bottom (cold) surfaces of the sample, respectively. $T_{h,measured}$ and $T_{c,measured}$ are the calculated temperatures of the sample center on the hot and cold surfaces, respectively, where the temperatures are measured by the axial thermocouples. The propagated thermal conductivity error was calculated based on:

$$U_{total} = \sqrt{(U_{Heatflux})^2 + (U_T)^2}\ , \tag{5.8}$$

where $U_{Heatflux}$ and U_T are the heat flux and temperature uncertainty values, respectively.

Table 5.6. The thermal conductivity error propagated from the temperature probe error, and as the error between the input and the surface average heat flux. The specified temperatures indicate the temperature of the sample center on the bottom (cold) surface. The center temperatures of the sample on the hot surface were kept 5°C above these values. The heat flux uncertainty was calculated based on Equation (5.6). The temperature uncertainty was obtained based on Equation (5.7). The propagated thermal conductivity error was calculated according to Equation (5.8). The direct thermal conductivity error was calculated based a comparison between the value obtained from Equation (5.5) and the input value in the program.

Temperature (°C)	100	300	600	800	1000
Temperature error (%)	0.21	0.26	0.30	0.41	0.65
Heat flux error (%)	2.09	1.66	2.03	4.31	7.64
Propagated conductivity error (%)	2.10	1.68	2.05	4.34	7.66
Direct conductivity error (%)	2.17	2.03	2.19	4.60	8.22

5.4.4 Analysis of thermal conductivity measurement (insulating top boundary condition versus constant temperature)

The effects of the top boundary conditions being insulating vs constant temperature is investigated. In reality, making an insulating surface at such high temperatures can be quite challenging. One solution to add a heating block in contact with the support ends and wire ends on the hot (top) side of the instrument. The role of this heating block is to keep the temperature gradient on support and wire ends at minimum, thereby suppressing the parasitic heat loss through conduction from the top side. The temperature of this heating block can be set by using thermocouples embedded in the block. Figure 5.10a,b demonstrates the temperature distribution across the instrument with a maximum temperature of 909°C with the radiation shield being kept at 909°C. The temperature distribution across the top heat spreader outer surface is shown in Figure 5.10c,d. The maximum temperature gradient across this surface was calculated to be 0.45°C even at the high temperature of 900°C. This temperature gradient plays an important role in the uncertainty of measured thermal conductivity and needs to be kept small. This is due the fact that

the radiation heat loss from the heat spreader is dominate compared to other surfaces on the top-half of the instrument. This emphasizes the importance of the temperature of the radiation shield being held at the nominal temperature of this surfaces.

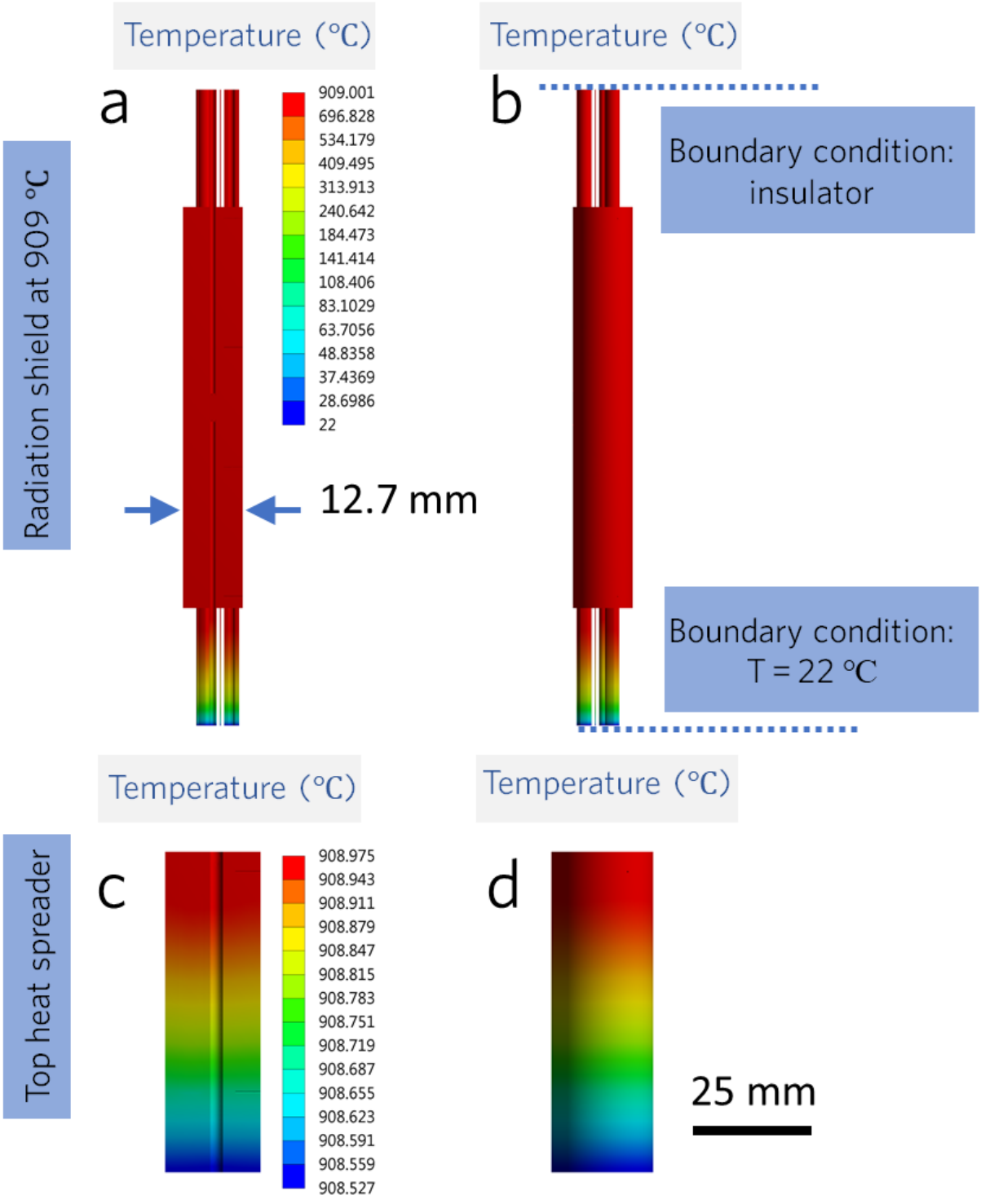

Figure 5.10. (a, b) Temperature distribution across the instrument. The top surface was assumed to be insulator and the bottom surface was kept at 22°C. (c, d) Temperature distribution

across the outer surface of the top heat spreader. The temperature gradient across this surface needs to be kept low in order to minimize the radiation heat flux between this surface and the shield contributing to the uncertainty of the thermal conductivity measurements.

Figure 5.11 demonstrates the temperature distribution across the sample for the top (hot) and bottom (cold) sides. On both sides, the outer surfaces have higher temperatures due to the inward radiation flux from the slightly hotter radiation shield. The variations at the center of the sample are due to the axial thermocouples and insulating alumina tubing. Figure 5.11d shows that the temperature variation on the sample is less than 0.012°C for both sides. Such a low temperature variation indicates the suppression of the cold finger effect based on the axial thermocouple configurations embedded in the heating block[264]. The results were obtained for a sample made of pyroceram 9606 with a relatively low thermal conductivity of ~2.9 $W\,m\,K^{-1}$ at 907°C. Keeping the sample temperature variation at minimum is essential for Seebeck coefficient and electrical resistivity measurements as the temperature variation contributes to the uncertainty, thereby contributing to the overall error for zT.

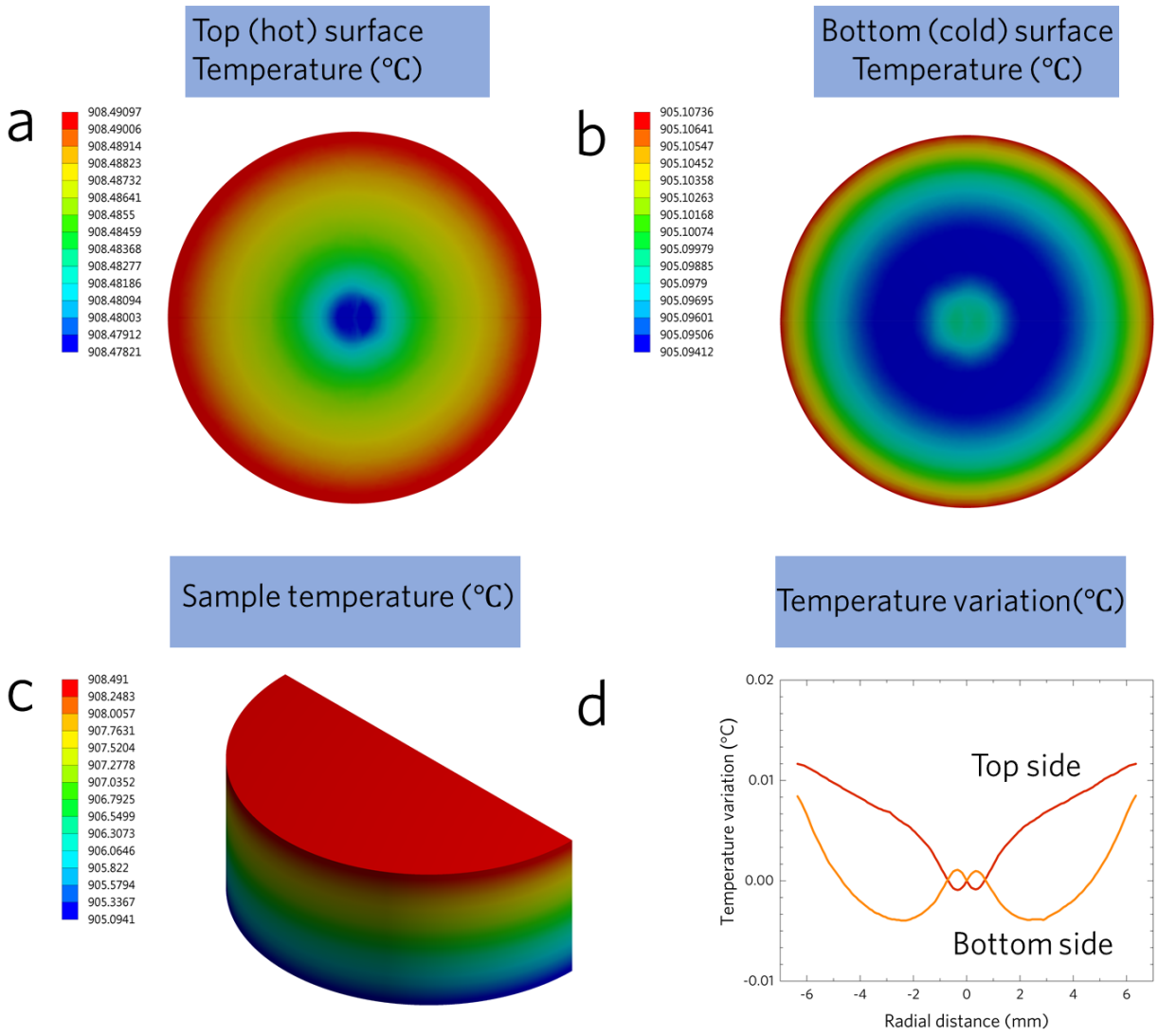

Figure 5.11. Temperature distribution for a pyroceram 9606 sample with a low thermal conductivity of ~2.9 W m K^{-1} at 907°C. (a) Hot side, (b) cold side, (c) isometric view, and (d) sample temperature variation along the radial direction with a maximum value less than 0.012°C above the center point temperature where the thermocouple contacts the sample.

Figure 5.12 shows the temperature distribution across the thermocouples consisting of tungsten-niobium wires. For the top side, the colder side of the thermocouple is in contact with the sample causing the center of the sample to be at a slightly lower temperature (Figures 5.11a, 5.12a)

which is the opposite of the bottom side (Figures 5.11b, 5.12b). Maximum temperature variations of 0.015 and 0.017 °C were obtained for the top and bottom thermocouple junctions. Such low variations highlight the elimination of the cold-finger effect by using axial thermocouples with cross-wire geometry introduced by Snyder[265].

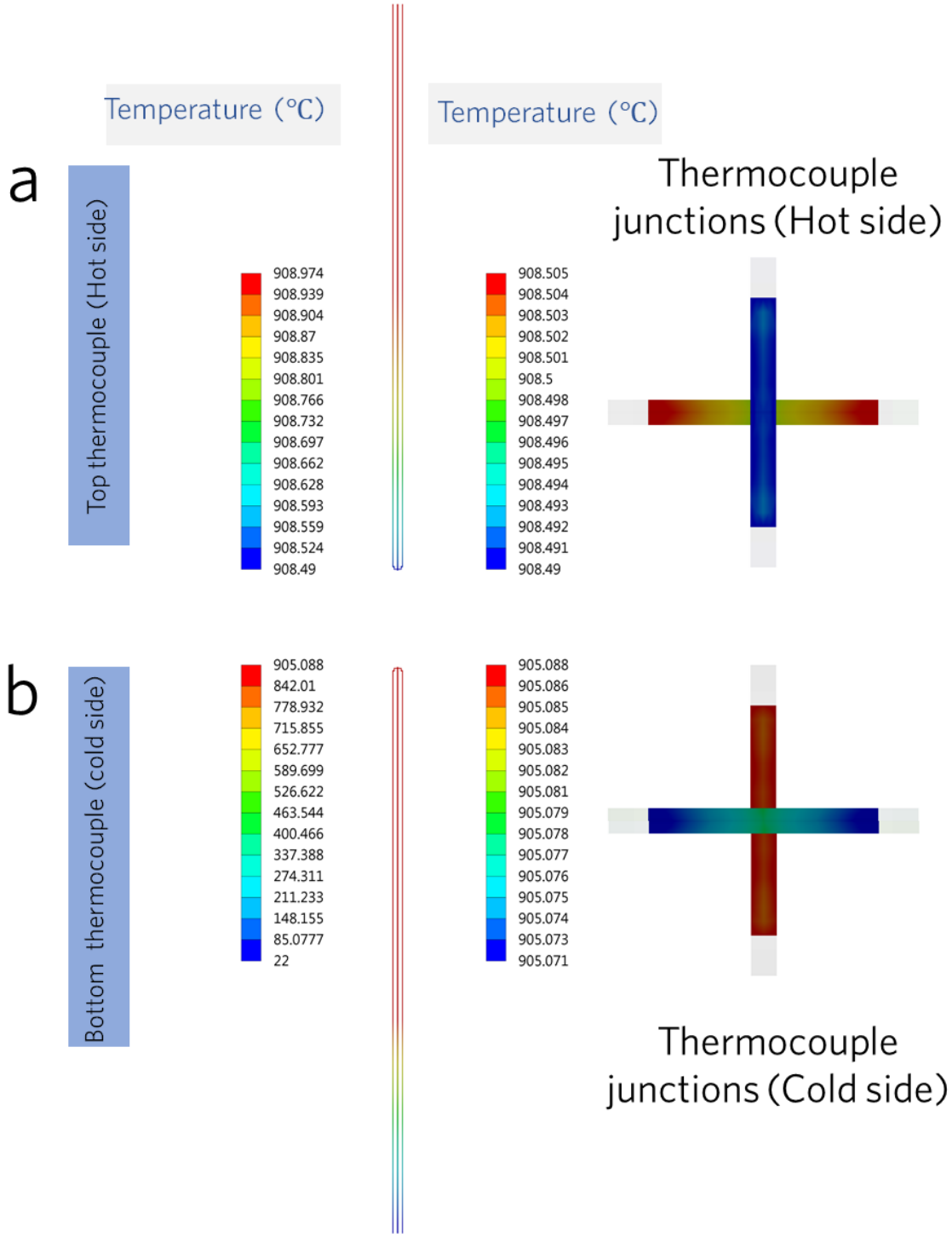

Figure 5.12. Temperature distribution across the (a) top thermocouple and (b) bottom thermocouple.

The uncertainty values for the thermal conductivity measurement of the pyroceram 9606 sample have been listed in Table 5.7. Errors of -7.7% and -8.6% were estimated for the insulating, and $T = 915$°C top boundary conditions, respectively. It can be seen that even when the boundary condition is set at $\sim\Delta T = 8$°C above the nominal sample temperature, the error increases only by 0.9% versus having a perfect insulating surface. $\Delta T = 8$°C is quite practical with the current temperature controller technologies. Thus, using an additional heating block contacting the support ends and wire ends is feasible replacement for an insulating boundary condition.

Table 5.7. The thermal conductivity error propagated from the temperature probe error, and as the error between the input and the surface average heat flux for the top surface set as an insulator as well as set at 915°C. The sample was assumed to be pyroceram 9606. The specified temperatures indicate the temperature of the sample center on the top (hot) and bottom (cold) surfaces. The heat flux uncertainty was calculated based on Equation (5.6). The temperature uncertainty was obtained based on Equation (5.7). The propagated thermal conductivity error was calculated according to Equation (5.8). The direct thermal conductivity error was calculated based a comparison between the value obtained from Equation (5.5) and the input value in the program.

Surface	Value
Top surface center temperature (℃) (Top boundary condition insulator)	908.47
Top surface center temperature (℃) (Top boundary condition kept at 915 ℃)	908.55
Bottom surface center temperature (℃) (Top boundary condition insulator)	905.10

Top surface center temperature (℃) (Top boundary condition kept at 915 ℃)	905.13
Temperature error (%)	0.46
Top surface average ($W\,m^{-2}$)	1867.6
Heater output ($W\,m^{-2}$)	1810.2
Heat flux error (%)	3.07
Propagated thermal conductivity error (%)	3.1
Direct thermal conductivity error (%) (Top surface insulator)	-7.7
Direct thermal conductivity error (%) (Top surface kept at 915 ℃)	-8.6

5.4.5 A Modified design for direct thermal conductivity measurement at an ultra-high temperature of 2500°C

The capability for direct thermal conductivity measurements at ultra-high temperature ranges above 1500°C and even 2000°C can be quite beneficiary from a quality-control technology stand point. A modified design for thermal conductivity measurement at 2500°C is analyzed. The tungsten-niobium thermocouple wires design is replaced with a tungsten-5% rhenium versus tungsten-26% rhenium combination. Such configuration is commercially available by OMEGA with the upper limit of 2760°C[24]. The alumina tubing (melting point ~2070°C) is replaced with hafnium oxide (HfO_2) with a melting temperature of ~2810°C. The heat spreaders and the radiation shield are assumed to be made of tungsten. Therefore, the only materials used in the proposed instruments design for ultra-high temperature applications are tungsten (melting point ~ 3380°C),

hafnium oxide (melting point ~2810°C) and tungsten-rhenium alloys (operating up-to 2760°C). The sample is assumed to be made of boron nitride (melting point 3000°C) with a dimension of 12.7 mm in diameter and 5 mm in height. All the materials properties were adopted from the Thermophysical Properties of Matter – The TPRC Data Series handbooks[267]. The first challenge in this case is to create a temperature gradient across the sample. Because the proportionality of the radiation heat flux with the fourth power of temperature difference, even a small temperature difference creates a considerable flux from/to the radiation shield making the temperature controlling challenging. To have a better control over the temperature gradient from the sample, the radiation shield is split into two sections, i.e. having a top and bottom shield with separate temperature control feedbacks. In practice, this can be made of two shields with embedded cartridge heaters each one covering half of the height of the instrument. Thermocouples need to be embedded in these shields for separate temperature controls. The temperature of the radiation shield for the bottom half and the bottom heater power are used in order to control the temperature gradient between the top and bottom surface of the sample. Table 5.8 lists the heater powers and the temperature set points for top and bottom radiation shield. A temperature gradient of 4.4°C between the hot and cold sides of the sample is calculated for the heater power values and radiation shield temperature setpoints listed in Table 5.8. The performed analysis reveals an error of -17.15% the thermal conductivity measurement of the sample at an average temperature of 2497.8°C.

Table 5.8. The thermal conductivity error propagated from the temperature probe error, and as the error between the input and the surface average heat flux for a boron nitride sample at ~2500°C The specified temperatures refer to the temperature of the sample center on the top (hot) and bottom (cold) surfaces. The heat flux uncertainty was calculated based on Equation (5.6). The temperature uncertainty was obtained based on Equation (5.7). The propagated thermal

conductivity error was calculated according to Equation (5.8). The direct thermal conductivity error was calculated based a comparison between the value obtained from Equation (5.5) and the input value in the program.

Surface	Value
Top heater power ($W m^{-3}$)	4,000,000
Bottom heater power ($W m^{-3}$)	1,000,000
Top surface temperature at the center (℃)	2500.042
Bottom surface temperature at the center (℃)	2495.628
Top radiation shield set temperature (℃)	2502
Bottom radiation shield set temperature (℃)	2490
Temperature error (%)	4.87
Top surface average ($W m^{-2}$)	14094.415
Heater output on the top surface ($W m^{-2}$)	14481.845
Heat flux error (%)	2.74
Propagated thermal conductivity error (%)	5.6
Direct thermal conductivity error (%)	-17.15

Figure 5.13a-c demonstrates the temperature distribution across the sample hot and cold sides. The maximum temperature variation was calculated to be less than 0.25°C. The temperature distribution of the instrument is shown in Figure 5.13d. An average heat flux of 8,946,149.2 W m^{-2} was calculated on the support ends and wire ends at the bottom (cooling side) of the instrument. This value determines the overall flux that is needed to be removed from the instrument. This value can be controlled by changing the temperature of the bottom shield as well as the bottom cartridge heaters.

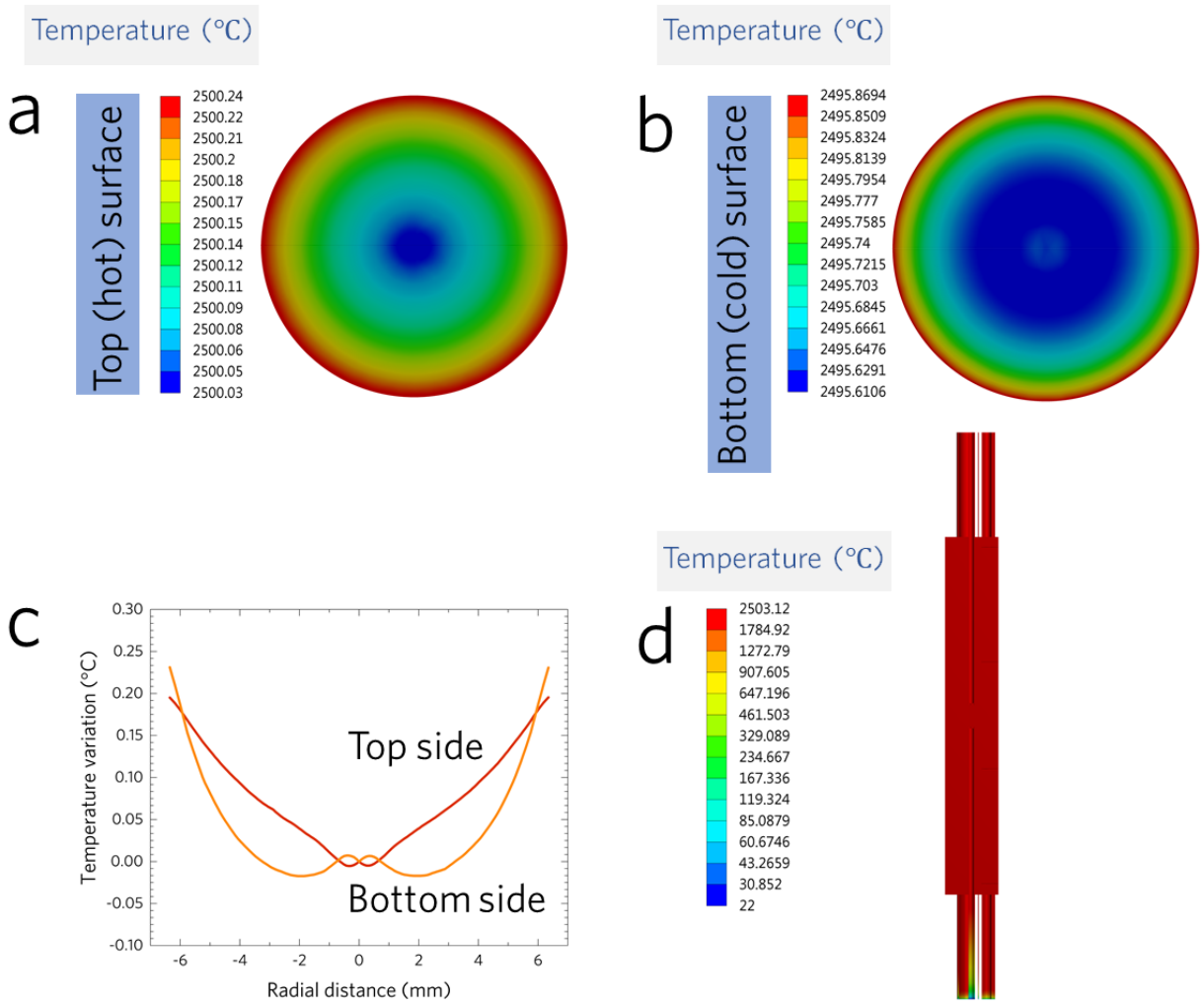

Figure 5.13. Temperature distribution across: (a) the hot sides of the sample, (b) the cold side of the sample. (c) Temperature variation across the radial direction on the sample for hot and cold sides. (d) Instrument temperature distribution.

Radiation loss from the top spreader to the top radiation shield has a major contribution in the uncertainty of the thermal conductivity measurements. The challenge is that, due to the thermal resistance across the top heat spreader, there exists a temperature gradient of ~2°C along the heat spreader. In such ultra-high temperature ranges, even, the smallest temperature difference between the top heat spreader and the top radiation shield can cause a major heat loss/gain. Thus, even though, the radiation shield is set at the average temperature of the heat spreader, the heat loss is still considerable due to the fact that the top heat spreader is not a constant temperature surface. Two solutions can be proposed in order to suppress such a heat loss: the first one is to use a material with a very high thermal conductivity for the heat spreader design. Having a high thermal conductivity material reduces the thermal resistance along the heat spreader, thereby the temperature gradient. There are, however, few machinable candidates suitable for such a high temperature ranges, and tungsten seems to be indeed a proper choice. The other solution is to design multi-stage top radiation shield. Figure 5.14 compares the temperature gradient along the top heat spreader for a single-stage radiation shield against a double-stage shield. For the single shield, the temperature was set to 2502°C (average temperature of the heat spreader). For the double-stage shield, the temperatures were set to 2502.1 and 2500.9°C for the first and second stage, respectively. The error analysis for the double-stage shield has been listed in Table 5.9. It can be seen that the thermal conductivity measurement error of -17.15% for a single-stage radiation shield can be reduced to -13.31% by using a double-stage shield. An ideal situation is to use

multiple stages depending on the height and temperature gradient of the heat spreader. A simpler alternative is to use a radiation shield with an optimum thickness in order to create a similar temperature gradient along the shield and the heat spreader as they both are made of the same material i.e. tungsten.

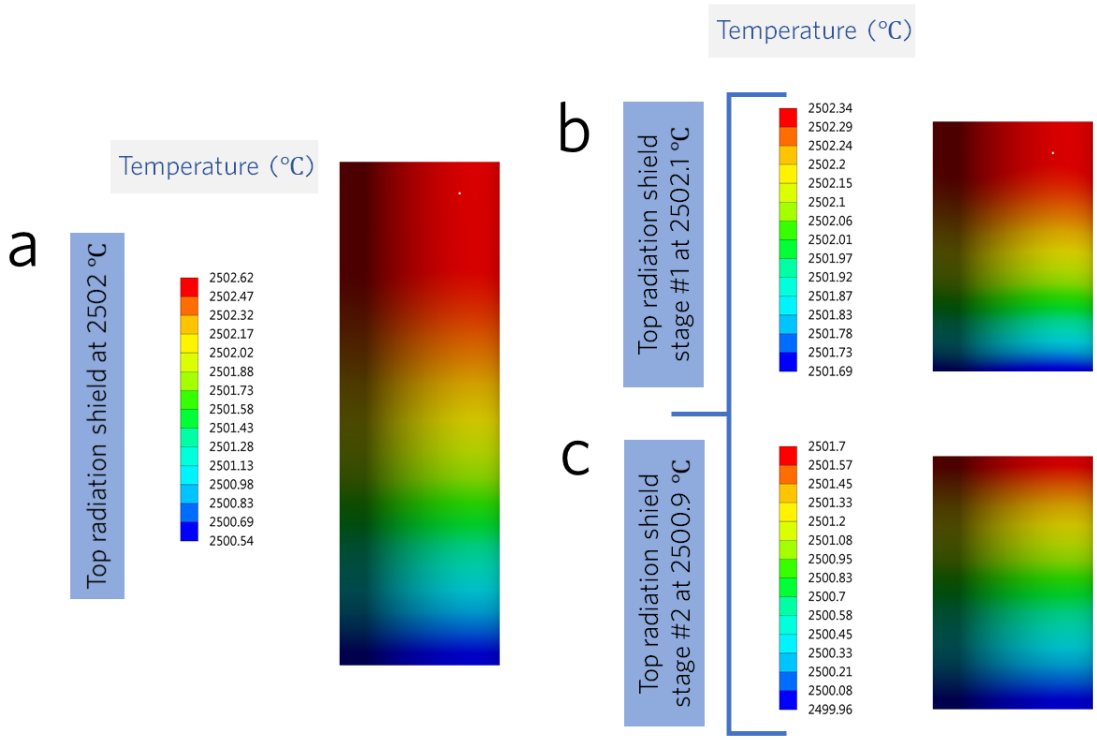

Figure 5.14. Temperature gradient along the top heat spreader at the temperature range ~2500°C. (a) the radiation loss is suppressed with a single-stage radiation shield (b) radiation loss is suppressed with a double-stage radiation shield.

Table 5.9. The thermal conductivity error propagated from the temperature probe error, and as the error between the input and the surface average heat flux for a boron nitride sample at ~ 2500°C with a two-stage top radiation shield. The specified temperatures refer to the temperature of the sample center on the top (hot) and bottom (cold) surfaces. The heat flux uncertainty was

calculated based on Equation (5.6). The temperature uncertainty was obtained based on Equation (5.7). The propagated thermal conductivity error was calculated according to Equation (5.8). The direct thermal conductivity error was calculated based a comparison between the value obtained from Equation (5.5) and the input value in the program.

Surface	Value
Top heater power ($W m^{-3}$)	4,000,000
Bottom heater power ($W m^{-3}$)	1,000,000
Top surface temperature at the center (℃)	2499.489
Bottom surface temperature at the center (℃)	2495.27
Top radiation shield stage #1 set temperature (℃)	2502.12
Top radiation shield stage #2 set temperature (℃)	
Bottom radiation shield set temperature (℃)	2490
Temperature error (%)	4.24
Top surface average ($W m^{-2}$)	13983.44
Heater output on the top surface ($W m^{-2}$)	14481.845
Heat flux error (%)	3.56
Propagated thermal conductivity error (%)	5.5
Direct thermal conductivity error (%)	-13.31

5.5 Conclusion

5.5.1 Analysis of the cold finger effects in Snyder's design summary

A finite element analysis was employed in order to calculate the cold-finger effect and temperature distribution across the sample in Snyder *et al.*[264, 265] at a high temperature of 900°C. The analysis indicated that the sample temperature distribution is dominated by the radiation, heat generation in the cartridge heaters, as well as cold-finger effects. Temperature variations (defined as one standard deviation) of 0.219, 0.216 and 0.056°C were calculated on the thermocouple cross-wires for the cases with no radiation shield, with a shield temperature set at 25°C, and with a shield set at 900°C, respectively. This demonstrated the effectiveness of the embedded axial thermocouple design provided that contact resistances to the sample are negligible. On the other hand, presence of a temperature minimum at the center of the sample surfaces showed that heat can still be drawn trough the thermocouples. Using a heated radiation shield was shown to be effective in suppressing the temperature gradient across the thermocouples and effectively mitigating the cold-finger effect. The performed analysis revealed that Snyder's design[265] was indeed effective in eliminating the cold-finger effect by reducing the uncertainty to a very small value of 0.4% for a sample with hot and cold average surface temperatures of 905.8 and 900.6 °C, respectively. The uncertainty due to non-uniform surface temperature distributions was dominate by being 8.73% leading to an overall uncertainty of 8.74%. By raising the temperature difference between the hot and cold surfaces to 12.2 °C, the uncertainty values remained almost the same. A mismatch between the diameter of the sample and that of the heat spreader enhanced the overall uncertainty to be 9.96% for a case with the ratio of the sample radius to that of the heat spreader to be 0.42. The average temperatures of the hot and cold surfaces were 911.2 and 898.9 °C, respectively. The increased error was due to the increased radiation fluxes between the heat

spreader and sample surfaces due to the mismatch causing a more non-uniform temperature distribution. The cold-finger uncertainty remained to be 0.47%.

5.5.2 Instrument design summary

A device for measuring a plurality of material properties was designed to include accurate sensors configured to obtain thermal conductivity, electrical conductivity, and Seebeck coefficient for a single sample consecutively while maintaining a vacuum or inert gas environment. Four major design factors were identified as the sample-heat spreader mismatch, the radiation losses, the parasitic losses, and the sample surface temperature variance. The system size was limited in order to prevent any sample-heat spreader mismatch error, which will result in a significant error if it is larger than ~1.5. The radiation shield temperature was set at the hot-side heat spreader temperature for more for practical purposes than to reduce the error, as the related errors were both small and similar for possible configurations of radiation shield temperatures. Unavoidable parasitic losses from the thermocouple were identified, although these can be reduced to manageable levels using an upper thermal guard. Finally, the temperature variation on the sample surface was reduced to 0.2°C by utilizing a thermally conduction interface material to help spread out the heat. For a typical system, this all resulted in an overall error of -1.32% and +7.80% at a temperature of 1000°C. Lower limits of -17.15 and -13.31% error in thermal conductivity measurements were estimated at an ultra-high temperature of ~2500°C for a single-stage and double-stage top radiation shield, respectively. Only tungsten, hafnium oxide and tungsten-rhenium (for thermocouple wires) materials were used in the modified design for such a temperature range. The major contribution to the error was due to the radiation heat loss from the top heat spreader. An ideal situation was to have a radiation shield and top heat spreader with the same temperature gradient. Such an ideal case can be approached by using a multi-stage radiation

shield. It is noted that this design is not limited to thermoelectric characterization and will enable measurement of ionic conductivity and surface temperatures of energy materials and high temperature materials under realistic operating conditions.

CHAPTER 6: Conclusion

In this thesis, thermal, electrical and electrochemical property measurements of various materials was investigated. Materials were synthesized by using bottom-up approaches. XRD, XPS, TEM, SEM, TGA, DSC, BET, and Raman analyses were employed in order to perform structural, physical and thermochemical analyses.

$Mn_{1-x}Co_xO$/MWCNTs ($0.0 \leq x \leq 1.0$) exhibited high capacity values for lithium ion battery anode applications. Controlled growth of nanoparticles on the outer walls of MWCNTs boosted the electrical conductivity by 8 orders of magnitude. The was a crucial step towards introducing Mn-based metal oxides for practical applications as MnO_x are very attractive due to being abundant. The results of present investigation showed that adding only 10% Co stabilized the MnO phase and consequently improved the cycling stability. This was a valuable observation as phase change in MnO_x was responsible for poor cyclability in the literature data. Such paradigm indicated that by using Co-alloying the phase transformation can be slowed resulting in more stable MnO-based anodes.

It was found that a thermochemical interaction between PDDA polyelectrolyte with α-MoO_3 induced large concentrations Mo^{5+}-$v_O^{\cdot}$ and Mo^{4+}-$v_O^{\cdot\cdot}$ oxygen vacancy bipolarons and polarons, respectively. The phenomenon was confirmed by XRD, XPS and TGA analyses. A new mechanism for such reaction was proposed based on DFT calculations. This was an important observation because presence oxygen vacancies greatly affect physical and electrochemical properties of metal oxides being even more interesting in the case of α-MoO_3 which is an important layered material. The presence of such vacancies, improved the electrochemical activity of MoO_{3-x} samples.

The effects of charged interfaces and grain boundaries on the electro-thermal transport properties of PbS_{1-x} were addressed in the present work. Interfaces have a crucial role in determining the transport properties in polycrystalline materials with abundance of grain boundaries. It was critical to investigate such effects as the majority of solution processed nanomaterials have a polycrystalline nature with high concentrations of grain boundaries. Solution -processed syntheses methods are appealing for large-scale productions due to simplicity and lower costs. It was found that upon heating PbS, a major sulfur-loss event occurred at a temperature at around 266.4 ℃ creating $v_S^{\cdot\cdot}$ sulfur vacancy sites. It was proposed that formation of $v_S^{\cdot\cdot}$ sulfur vacancy is more favorable on the layers close to the surface. Upon heating further to higher temperatures small and continuous weight loss was observed, attributed to the $v_S^{\cdot\cdot}$ sulfur vacancy formation at layers adjacent to the surface. Measurements of the electro-thermal transport properties revealed existence of potential barriers against charge transport. Defects at the interfaces acted as a trap for added charges due to sulfur vacancy formations, immobilizing them and creating charged interfaces.

Lastly, many of the uncertainty and error sources in the current thermal and electrical measurement methods were identified and analyzed by using the finite element analysis. Cold-finger effects in Seebeck coefficient and electrical conductivity measurements, a major source of uncertainty especially at high-temperatures, was analyzed in a design with an axial thermocouple (Snyder's design). Due to importance of accurate measurements a new design for consecutive measurements of thermal conductivity, electrical conductivity, ionic conductivity and Seebeck coefficient at high-temperatures were developed and analyzed.

REFERENCES

(1) Jiang, J., Li, Y., Liu, J., and Huang, X. Building one-dimensional oxide nanostructure arrays on conductive metal substrates for lithium-ion battery anodes, *Nanoscale* **2011**, *3*, 45-58. http://dx.doi.org/10.1039/C0NR00472C

(2) Green, M., Fielder, E., Scrosati, B., Wachtler, M., and Moreno, J. S. Structured silicon anodes for lithium battery applications, *Electrochem. Solid-State Lett.* **2003**, *6*, A75-A79. http://dx.doi.org/10.1149/1.1563094

(3) Reddy, M. V., Subba Rao, G. V., and Chowdari, B. V. R. Metal oxides and oxysalts as anode materials for Li ion batteries, *Chem. Rev.* **2013**, *113*, 5364–5457. http://dx.doi.org/10.1021/cr3001884

(4) Roy, P. and Srivastava, S. K. Nanostructured anode materials for lithium ion batteries, *J. Mater. Chem. A* **2015**, *3*, 2454–2484. http://dx.doi.org/10.1039/C4TA04980B

(5) G., B. P., Bruno, S., and Jean-Marie, T. Nanomaterials for rechargeable lithium batteries, *Angew. Chem., Int. Ed.* **2008**, *47*, 2930-2946. http://dx.doi.org/doi:10.1002/anie.200702505

(6) Wu, H. B., Chen, J. S., Hng, H. H., and Wen Lou, X. Nanostructured metal oxide-based materials as advanced anodes for lithium-ion batteries, *Nanoscale* **2012**, *4*, 2526-2542. http://dx.doi.org/10.1039/C2NR11966H

(7) Bhide, V. G. and Dani, R. H. Electrical conductivity in oxides of manganese and related compounds, *Physica* **1961**, *27*, 821–826. http://dx.doi.org/10.1016/0031-8914(61)90079-9

(8) Yazdani, S., Kashfi-Sadabad, R., Palmieri, A., Mustain, W. E., and Pettes, M. T. Effect of cobalt alloying on the electrochemical performance of manganese oxide nanoparticles nucleated on multiwalled carbon nanotubes, *Nanotechnology* **2017**, *28*, 155403. http://dx.doi.org/10.1088/1361-6528/aa6329

(9) Hu, X., Zhang, W., Liu, X., Mei, Y., and Huang, Y. Nanostructured Mo-based electrode materials for electrochemical energy storage, *Chem. Soc. Rev.* **2015**, *44*, 2376–2404. http://dx.doi.org/10.1039/C4CS00350K

(10) Yazdani, S., Kashfi-Sadabad, R., Huan, T. D., Morales-Acosta, M. D., and Pettes, M. T. Polyelectrolyte-assisted oxygen vacancies: A new route to defect engineering in molybdenum oxide, *Langmuir* **2018**, *34*, 6296–6306. http://dx.doi.org/10.1021/acs.langmuir.8b00539

(11) Chen, Z., Cummins, D., Reinecke, B. N., Clark, E., Sunkara, M. K., and Jaramillo, T. F. Core–shell MoO_3–MoS_2 nanowires for hydrogen evolution: A functional design for electrocatalytic materials, *Nano Lett.* **2011**, *11*, 4168–4175. http://dx.doi.org/10.1021/nl2020476

(12) Shi, Y., Guo, B., Corr, S. A., Shi, Q., Hu, Y.-S., Heier, K. R., Chen, L., Seshadri, R., and Stucky, G. D. Ordered mesoporous metallic MoO_2 materials with highly reversible lithium storage capacity, *Nano Lett.* **2009**, *9*, 4215–4220. http://dx.doi.org/10.1021/nl902423a

(13) Kashfi-Sadabad, R., Yazdani, S., Doan Huan, T., Cai, Z., and Pettes, M. T. Role of oxygen vacancy defects in the electrocatalytic activity of substoichiometric molybdenum oxide, *J. Phys. Chem. C* **2018**, *Accepted*. http://dx.doi.org/10.1021/acs.jpcc.8b03536

(14) Chandrasekaran, S., Kim, E. J., Chung, J. S., Bowen, C. R., Rajagopalan, B., Adamaki, V., Misra, R. D. K., and Hur, S. H. High performance bifunctional electrocatalytic activity of a reduced graphene oxide-molybdenum oxide hybrid catalyst, *J. Mater. Chem. A* **2016**, *4*, 13271–13279. http://dx.doi.org/10.1039/C6TA05043C

(15) Kim, H.-S., Cook, J. B., Lin, H., Ko, J. S., Tolbert, S. H., Ozolins, V., and Dunn, B. Oxygen vacancies enhance pseudocapacitive charge storage properties of MoO_{3-x}, *Nat. Mater.* **2017**, *16*, 454–460. http://dx.doi.org/10.1038/nmat4810

(16) Dieterle, M., Weinberg, G., and Mestl, G. Raman spectroscopy of molybdenum oxides Part I. Structural characterization of oxygen defects in MoO_{3-x} by DR UV/VIS, Raman spectroscopy and X-ray diffraction, *Phys. Chem. Chem. Phys.* **2002**, *4*, 812–821. http://dx.doi.org/10.1039/B107012F

(17) Biswas, K., He, J., Blum, I. D., Wu, C.-I., Hogan, T. P., Seidman, D. N., Dravid, V. P., and Kanatzidis, M. G. High-performance bulk thermoelectrics with all-scale hierarchical architectures, *Nature* **2012**, *489*, 414-418. http://dx.doi.org/10.1038/nature11439

(18) Elson, A., Tidball, R., and Hampson, A. Waste Heat to Power Market Assessment. ICF International: Fairfax, Virginia, **2015**. http://info.ornl.gov/sites/publications/Files/Pub52953.pdf

(19) Heikes, R. R. and Ure, R. W. Thermoelectricity: Science and Engineering. Interscience Publishers, Inc.: New York, **1961**.

(20) Kim, H. S., Liu, W., Chen, G., Chu, C.-W., and Ren, Z. Relationship between thermoelectric figure of merit and energy conversion efficiency, *Proc. Natl. Acad. Sci. U. S. A.* **2015**, *112*, 8205–8210. http://dx.doi.org/10.1073/pnas.1510231112

(21) Ibáñez, M., Luo, Z., Genç, A., Piveteau, L., Ortega, S., Cadavid, D., Dobrozhan, O., Liu, Y., Nachtegaal, M., Zebarjadi, M., Arbiol, J., Kovalenko, M. V., and Cabot, A. High-performance thermoelectric nanocomposites from nanocrystal building blocks, *Nat. Commun.* **2016**, *7*, 10766. http://dx.doi.org/10.1038/ncomms10766

(22) Ibáñez, M., Zamani, R., Gorsse, S., Fan, J., Ortega, S., Cadavid, D., Morante, J. R., Arbiol, J., and Cabot, A. Core–shell nanoparticles as building blocks for the bottom-up production of functional nanocomposites: PbTe–PbS thermoelectric properties, *ACS Nano* **2013**, *7*, 2573–2586. http://dx.doi.org/10.1021/nn305971v

(23) Ibáñez, M., Korkosz, R. J., Luo, Z., Riba, P., Cadavid, D., Ortega, S., Cabot, A., and Kanatzidis, M. G. Electron doping in bottom-up engineered thermoelectric nanomaterials through HCl-mediated ligand displacement, *J. Am. Chem. Soc.* **2015**, *137*, 4046–4049. http://dx.doi.org/10.1021/jacs.5b00091

(24) Varghese, T., Hollar, C., Richardson, J., Kempf, N., Han, C., Gamarachchi, P., Estrada, D., Mehta, R. J., and Zhang, Y. High-performance and flexible thermoelectric films by screen printing solution-processed nanoplate crystals, *Sci. Rep.* **2016**, *6*, 33135. http://dx.doi.org/10.1038/srep33135

(25) Zhang, C., Ng, H., Li, Z., Khor, K. A., and Xiong, Q. Minority carrier blocking to enhance the thermoelectric performance of solution-processed $Bi_xSb_{2-x}Te_3$ nanocomposites via a liquid-phase sintering process, *ACS Appl. Mater. Interfaces* **2017**, *9*, 12501-12510. http://dx.doi.org/10.1021/acsami.7b01473

(26) Mehta, R. J., Zhang, Y., Karthik, C., Singh, B., Siegel, R. W., Borca-Tasciuc, T., and Ramanath, G. A new class of doped nanobulk high-figure-of-merit thermoelectrics by scalable bottom-up assembly, *Nat. Mater.* **2012**, *11*, 233–240. http://dx.doi.org/10.1038/nmat3213

(27) Zhang, Y., Day, T., Snedaker, M. L., Wang, H., Krämer, S., Birkel, C. S., Ji, X., Liu, D., Snyder, G. J., and Stucky, G. D. A mesoporous anisotropic n-Type Bi_2Te_3 monolith with low thermal conductivity as an efficient thermoelectric material, *Adv. Mater.* **2012**, *24*, 5065-5070. http://dx.doi.org/doi:10.1002/adma.201201974

(28) Xu, B., Feng, T., Li, Z., Pantelides, S. T., and Wu, Y. Constructing highly porous thermoelectric monoliths with high-performance and improved portability from solution-synthesized shape-controlled nanocrystals, *Nano Lett.* **2018**, *18*, 4034-4039. http://dx.doi.org/10.1021/acs.nanolett.8b01691

(29) Liu, Y., Zhang, Y., Ortega, S., Ibáñez, M., Lim, K. H., Grau-Carbonell, A., Martí-Sánchez, S., Ng, K. M., Arbiol, J., Kovalenko, M. V., Cadavid, D., and Cabot, A. Crystallographically textured nanomaterials produced from the liquid phase sintering of $Bi_xSb_{2-x}Te_3$ nanocrystal building blocks, *Nano Lett.* **2018**, *18*, 2557-2563. http://dx.doi.org/10.1021/acs.nanolett.8b00263

(30) Biswas, K., He, J., Blum, I. D., Wu, C.-I., Hogan, T. P., Seidman, D. N., Dravid, V. P., and Kanatzidis, M. G. High-performance bulk thermoelectrics with all-scale hierarchical architectures, *Nature* **2012**, *489*, 414-418. http://dx.doi.org/10.1038/nature11439

(31) Wu, H. J., Zhao, L. D., Zheng, F. S., Wu, D., Pei, Y. L., Tong, X., Kanatzidis, M. G., and He, J. Q. Broad temperature plateau for thermoelectric figure of merit ZT>2 in phase-separated $PbTe_{0.7}S_{0.3}$, *Nat. Commun.* **2014**, *5*, 4515-1−8. http://dx.doi.org/10.1038/ncomms5515

(32) Zhao, L.-D., Lo, S.-H., Zhang, Y., Sun, H., Tan, G., Uher, C., Wolverton, C., Dravid, V. P., and Kanatzidis, M. G. Ultralow thermal conductivity and high thermoelectric figure of merit in SnSe crystals, *Nature* **2014**, *508*, 373-377. http://dx.doi.org/10.1038/nature13184

(33) Zhao, L.-D., Tan, G., Hao, S., He, J., Pei, Y., Chi, H., Wang, H., Gong, S., Xu, H., Dravid, V. P., Uher, C., Snyder, G. J., Wolverton, C., and Kanatzidis, M. G. Ultrahigh power factor and thermoelectric performance in hole-doped single-crystal SnSe, *Science* **2016**, *351*, 141–144. http://dx.doi.org/10.1126/science.aad3749

(34) Rowe, D. M. CRC Handbook of Thermoelectrics: Macro to Nano CRC Press/Taylor & Francis: New York, **2006**. ISBN: 9781420038903, https://www.crcpress.com/Thermoelectrics-Handbook-Macro-to-Nano/Rowe/9780849322648

(35) Zhu, T., Hu, L., Zhao, X., and He, J. New insights into intrinsic point defects in V_2VI_3 thermoelectric materials, *Adv. Sci.* **2016**, *3*, 1600004-1−16. http://dx.doi.org/10.1002/advs.201600004

(36) Satyavani, T. V. S. L., Srinivas Kumar, A., and Subba Rao, P. S. V. Methods of synthesis and performance improvement of lithium iron phosphate for high rate Li-ion batteries: A review, *Eng. Sci. Technol. Int. J.* **2016**, *19*, 178−188. http://dx.doi.org/10.1016/j.jestch.2015.06.002

(37) Kou, T., Yao, B., Liu, T., and Li, Y. Recent advances in chemical methods for activating carbon and metal oxide based electrodes for supercapacitors, *J. Mater. Chem. A* **2017**, *5*, 17151−17173. http://dx.doi.org/10.1039/C7TA05003H

(38) Freitas, J. N., Goncalves, A. S., and Nogueira, A. F. A comprehensive review of the application of chalcogenide nanoparticles in polymer solar cells, *Nanoscale* **2014**, *6*, 6371−6397. http://dx.doi.org/10.1039/C4NR00868E

(39) Ummartyotin, S. and Infahsaeng, Y. A comprehensive review on ZnS: From synthesis to an approach on solar cell, *Renew. Sust. Energ. Rev.* **2016**, *55*, 17−24. http://dx.doi.org/10.1016/j.rser.2015.10.120

(40) Yusoff, A. R. b. M. and Nazeeruddin, M. K. Low-dimensional perovskites: From synthesis to stability in perovskite solar cells, *Adv. Energy Mater.* **2017**, 1702073-1−16. http://dx.doi.org/10.1002/aenm.201702073

(41) Anantharaj, S., Ede, S. R., Sakthikumar, K., Karthick, K., Mishra, S., and Kundu, S. Recent trends and perspectives in electrochemical water splitting with an emphasis on sulfide, selenide, and phosphide catalysts of Fe, Co, and Ni: A review, *ACS Catal.* **2016**, *6*, 8069−8097. http://dx.doi.org/10.1021/acscatal.6b02479

(42) Min, Y., Moon, G. D., Kim, C.-E., Lee, J.-H., Yang, H., Soon, A., and Jeong, U. Solution-based synthesis of anisotropic metal chalcogenide nanocrystals and their applications, *J. Mater. Chem. C* **2014**, *2*, 6222–6248. http://dx.doi.org/10.1039/C4TC00586D

(43) Kovalenko, M. V., Manna, L., Cabot, A., Hens, Z., Talapin, D. V., Kagan, C. R., Klimov, V. I., Rogach, A. L., Reiss, P., Milliron, D. J., Guyot-Sionnnest, P., Konstantatos, G., Parak, W. J., Hyeon, T., Korgel, B. A., Murray, C. B., and Heiss, W. Prospects of nanoscience with nanocrystals, *ACS Nano* **2015**, *9*, 1012–1057. http://dx.doi.org/10.1021/nn506223h

(44) Varma, A., Mukasyan, A. S., Rogachev, A. S., and Manukyan, K. V. Solution combustion synthesis of nanoscale materials, *Chem. Rev.* **2016**, *116*, 14493–14586. http://dx.doi.org/10.1021/acs.chemrev.6b00279

(45) Yin, Y. and Alivisatos, A. P. Colloidal nanocrystal synthesis and the organic-inorganic interface, *Nature* **2005**, *437*, 664–670. http://dx.doi.org/10.1038/nature04165

(46) Kumar, S. and Nann, T. Shape control of II–VI semiconductor nanomaterials, *Small* **2006**, *2*, 316–329. http://dx.doi.org/10.1002/smll.200500357

(47) Xia, Y., Xiong, Y., Lim, B., and Skrabalak, S. E. Shape-Controlled Synthesis of Metal Nanocrystals: Simple Chemistry Meets Complex Physics?, *Angew. Chem. Int. Edit.* **2009**, *48*, 60–103. http://dx.doi.org/10.1002/anie.200802248

(48) Nasilowski, M., Mahler, B., Lhuillier, E., Ithurria, S., and Dubertret, B. Two-dimensional colloidal nanocrystals, *Chem. Rev.* **2016**, *116*, 10934–10982. http://dx.doi.org/10.1021/acs.chemrev.6b00164

(49) Boles, M. A., Ling, D., Hyeon, T., and Talapin, D. V. The surface science of nanocrystals, *Nat. Mater.* **2016**, *15*, 141–153. http://dx.doi.org/10.1038/nmat4526

(50) Ji, X., Zhang, B., Tritt, T. M., Kolis, J. W., and Kumbhar, A. Solution-chemical syntheses of nano-structured Bi_2Te_3 and PbTe thermoelectric materials, *J. Electron. Mater.* **2007**, *36*, 721–726. http://dx.doi.org/10.1007/s11664-007-0156-y

(51) Zhao, X. B., Ji, X. H., Zhang, Y. H., Zhu, T. J., Tu, J. P., and Zhang, X. B. Bismuth telluride nanotubes and the effects on the thermoelectric properties of nanotube-containing nanocomposites, *Appl. Phys. Lett.* **2005**, *86*, 062111-1–3. http://dx.doi.org/10.1063/1.1863440

(52) Ji, X., He, J., Su, Z., Gothard, N., and Tritt, T. M. Improved thermoelectric performance in polycrystalline *p*-type Bi_2Te_3 via an alkali metal salt hydrothermal nanocoating treatment approach, *J. Appl. Phys.* **2008**, *104*, 034907-1–6. http://dx.doi.org/10.1063/1.2963706

(53) Fan, X. A., Yang, J. Y., Xie, Z., Li, K., Zhu, W., Duan, X. K., Xiao, C. J., and Zhang, Q. Q. Bi_2Te_3 hexagonal nanoplates and thermoelectric properties of n-type Bi_2Te_3 nanocomposites, *J. Phys. D.: Appl. Phys.* **2007**, *40*, 5975–5979. http://dx.doi.org/10.1088/0022-3727/40/19/029

(54) Fu, J., Song, S., Zhang, X., Cao, F., Zhou, L., Li, X., and Zhang, H. Bi_2Te_3 nanoplates and nanoflowers: Synthesized by hydrothermal process and their enhanced thermoelectric properties, *CrystEngComm* **2012**, *14*, 2159–2165. http://dx.doi.org/10.1039/C2CE06348D

(55) Zhang, Y. H., Zhu, T. J., Tu, J. P., and Zhao, X. B. Flower-like nanostructure and thermoelectric properties of hydrothermally synthesized La-containing Bi_2Te_3 based alloys, *Mater. Chem. Phys.* **2007**, *103*, 484–488. http://dx.doi.org/10.1016/j.matchemphys.2007.02.059

(56) Mi, J. L., Zhu, T. J., Zhao, X. B., and Ma, J. Nanostructuring and thermoelectric properties of bulk skutterudite compound $CoSb_3$, *J. Appl. Phys.* **2007**, *101*, 054314-1–6. http://dx.doi.org/10.1063/1.2436927

(57) Tai, G. a., Zhou, B., and Guo, W. Structural characterization and thermoelectric transport properties of uniform single-crystalline lead telluride nanowires, *J. Phys. Chem. C* **2008**, *112*, 11314–11318. http://dx.doi.org/10.1021/jp8041318

(58) Wang, W. Z., Poudel, B., Wang, D. Z., and Ren, Z. F. Synthesis of PbTe nanoboxes using a solvothermal technique, *Adv. Mater.* **2005**, *17*, 2110–2114. http://dx.doi.org/10.1002/adma.200500514

(59) Zhou, J., Chen, Z., and Sun, Z. Hydrothermal synthesis and thermoelectric transport properties of PbTe nanocubes, *Mater. Res. Bull* **2015**, *61*, 404–408. http://dx.doi.org/10.1016/j.materresbull.2014.10.056

(60) Shi, W., Zhou, L., Song, S., Yang, J., and Zhang, H. Hydrothermal synthesis and thermoelectric transport properties of impurity-free antimony telluride hexagonal nanoplates, *Adv. Mater.* **2008**, *20*, 1892–1897. http://dx.doi.org/10.1002/adma.200702003

(61) Jin, R., Chen, G., Pei, J., Xu, H., and Lv, Z. S. Solvothermal synthesis and growth mechanism of ultrathin Sb_2Te_3 hexagonal nanoplates with thermoelectric transport properties, *RSC Adv.* **2012**, *2*, 1450–1456. http://dx.doi.org/10.1039/C1RA00642H

(62) Sun, S., Peng, J., Jin, R., Song, S., Zhu, P., and Xing, Y. Template-free solvothermal synthesis and enhanced thermoelectric performance of Sb_2Te_3 nanosheets, *J. Alloy. Compd.* **2013**, *558*, 6–10. http://dx.doi.org/10.1016/j.jallcom.2013.01.017

(63) Zhou, N., Chen, G., Zhang, X.-S., Xu, Y.-C., Xu, B.-R., and Li, M.-Q. Size-controlled synthesis and transport properties of Sb_2Te_3 nanoplates, *RSC Adv.* **2014**, *4*, 2427–2432. http://dx.doi.org/10.1039/C3RA44172E

(64) Shi, W., Yu, S., Liu, P., and Fan, W. Hydrothermal synthesis and thermoelectric transport properties of Sb_2Te_3-Te heterogeneous nanostructures, *CrystEngComm* **2013**, *15*, 2978–2985. http://dx.doi.org/10.1039/C3CE27010F

(65) Feng, H., Wu, C., Zhang, P., Mi, J., and Dong, M. Facile hydrothermal synthesis and formation mechanisms of Bi_2Te_3, Sb_2Te_3 and Bi_2Te_3-Sb_2Te_3 nanowires, *RSC Adv.* **2015**, *5*, 100309–100315. http://dx.doi.org/10.1039/C5RA20014H

(66) Zhou, W., Zhao, W., Lu, Z., Zhu, J., Fan, S., Ma, J., Hng, H. H., and Yan, Q. Preparation and thermoelectric properties of sulfur doped Ag_2Te nanoparticles via solvothermal methods, *Nanoscale* **2012**, *4*, 3926–3931. http://dx.doi.org/10.1039/C2NR30469D

(67) Yang, H. Q., Miao, L., Liu, C. Y., Wang, X. Y., Peng, Y., Zhang, A. J., Zhou, X. Y., Wang, G. Y., Li, C., and Huang, R. Solvothermal synthesis of wire-like $Sn_xSb_2Te_{3+x}$ with an enhanced thermoelectric performance, *Dalton T.* **2016**, *45*, 7483–7491. http://dx.doi.org/10.1039/C6DT00974C

(68) Zheng, W., Bi, P., Kang, H., Wei, W., Liu, F., Shi, J., Peng, L., Wang, Z., and Xiong, R. Low thermal conductivity and high thermoelectric figure of merit in *p*-type Sb_2Te_3/poly(3,4-ethylenedioxythiophene) thermoelectric composites, *Appl. Phys. Lett.* **2014**, *105*, 023901-1–4. http://dx.doi.org/10.1063/1.4887504

(69) Wei, W., Cui, X., Chen, W., and Ivey, D. G. Manganese oxide-based materials as electrochemical supercapacitor electrodes, *Chem. Soc. Rev.* **2011**, *40*, 1697–1721. http://dx.doi.org/10.1039/C0CS00127A

(70) Nitta, N. and Yushin, G. High-capacity anode materials for lithium-ion batteries: Choice of elements and structures for active particles, *Part. Part. Syst. Charact.* **2014**, *31*, 317–336. http://dx.doi.org/10.1002/ppsc.201300231

(71) Poizot, P., Laruelle, S., Grugeon, S., and Tarascon, J.-M. Rationalization of the low-potential reactivity of 3d-metal-based inorganic compounds toward Li, *J. Electrochem. Soc.* **2002**, *149*, A1212–A1217. http://dx.doi.org/10.1149/1.1497981

(72) Aragón, M. J., Pérez-Vicente, C., and Tirado, J. L. Submicronic particles of manganese carbonate prepared in reverse micelles: A new electrode material for lithium-ion batteries, *Electrochem. Commun.* **2007**, *9*, 1744–1748. http://dx.doi.org/10.1016/j.elecom.2007.03.031

(73) Ji, L., Medford, A. J., and Zhang, X. Porous carbon nanofibers loaded with manganese oxide particles: Formation mechanism and electrochemical performance as energy-storage materials, *J. Mater. Chem.* **2009**, *19*, 5593–5601. http://dx.doi.org/10.1039/B905755B

(74) Liu, J. and Pan, Q. MnO/C nanocomposites as high capacity anode materials for Li-ion batteries, *Electrochem. Solid State Lett.* **2010**, *13*, A139–A142. http://dx.doi.org/10.1149/1.3465312

(75) Zhong, K., Xia, X., Zhang, B., Li, H., Wang, Z., and Chen, L. MnO powder as anode active materials for lithium ion batteries, *J. Power Sources* **2010**, *195*, 3300–3308. http://dx.doi.org/10.1016/j.jpowsour.2009.11.133

(76) Deng, Y., Wan, L., Xie, Y., Qin, X., and Chen, G. Recent advances in Mn-based oxides as anode materials for lithium ion batteries, *RSC Adv.* **2014**, *4*, 23914–23935. http://dx.doi.org/10.1039/C4RA02686A

(77) Kokubu, T., Oaki, Y., Hosono, E., Zhou, H., and Imai, H. Biomimetic solid-solution precursors of metal carbonate for nanostructured metal oxides: MnO/Co and MnO-CoO nanostructures and their electrochemical properties, *Adv. Funct. Mater.* **2011**, *21*, 3673–3680. http://dx.doi.org/10.1002/adfm.201101138

(78) Xiao, Y. and Cao, M. Carbon-anchored MnO nanosheets as an anode for high-rate and long-life lithium-ion batteries, *ACS Appl. Mater. Interfaces* **2015**, *7*, 12840–12849. http://dx.doi.org/10.1021/acsami.5b02171

(79) Liu, D.-H., Lu, H.-Y., Wu, X.-L., Hou, B.-H., Wan, F., Bao, S.-D., Yan, Q., Xie, H.-M., and Wang, R.-S. Constructing the optimal conductive network in MnO-based nanohybrids as high-rate and long-life anode materials for lithium-ion batteries, *J. Mater. Chem. A* **2015**, *3*, 19738–19746. http://dx.doi.org/10.1039/C5TA03556B

(80) Wang, J.-G., Zhang, C., Jin, D., Xie, K., and Wei, B. Synthesis of ultralong MnO/C coaxial nanowires as freestanding anodes for high-performance lithium ion batteries, *J. Mater. Chem. A* **2015**, *3*, 13699–13705. http://dx.doi.org/10.1039/C5TA02440D

(81) Luo, W., Hu, X., Sun, Y., and Huang, Y. Controlled synthesis of mesoporous MnO/C networks by microwave irradiation and their enhanced lithium-storage properties, *ACS Appl. Mater. Interfaces* **2013**, *5*, 1997–2003. http://dx.doi.org/10.1021/am302813d

(82) Xia, P., Lin, H. B., Tu, W. Q., Chen, X. Q., Cai, X., Zheng, X. W., Xu, M. Q., and Li, W. S. A novel fabrication for manganese monoxide/reduced graphene oxide nanocomposite as high performance anode of lithium ion battery, *Electrochim. Acta* **2016**, *198*, 66–76. http://dx.doi.org/10.1016/j.electacta.2016.03.077

(83) Gu, X., Yue, J., Chen, L., Liu, S., Xu, H., Yang, J., Qian, Y., and Zhao, X. Coaxial MnO/N-doped carbon nanorods for advanced lithium-ion battery anodes, *J. Mater. Chem. A* **2015**, *3*, 1037–1041. http://dx.doi.org/10.1039/C4TA05622A

(84) Zang, J., Qian, H., Wei, Z., Cao, Y., Zheng, M., and Dong, Q. Reduced graphene oxide supported MnO nanoparticles with excellent lithium storage performance, *Electrochim. Acta* **2014**, *118*, 112–117. http://dx.doi.org/10.1016/j.electacta.2013.12.016

(85) Qiu, D., Ma, L., Zheng, M., Lin, Z., Zhao, B., Wen, Z., Hu, Z., Pu, L., and Shi, Y. MnO nanoparticles anchored on graphene nanosheets via in situ carbothermal reduction as high-

performance anode materials for lithium-ion batteries, *Mater. Lett.* **2012**, *84*, 9–12. http://dx.doi.org/10.1016/j.matlet.2012.06.045

(86) Zhang, K., Han, P., Gu, L., Zhang, L., Liu, Z., Kong, Q., Zhang, C., Dong, S., Zhang, Z., Yao, J., Xu, H., Cui, G., and Chen, L. Synthesis of nitrogen-doped MnO/graphene nanosheets hybrid material for lithium ion batteries, *ACS Appl. Mater. Interfaces* **2012**, *4*, 658–664. http://dx.doi.org/10.1021/am201173z

(87) Lu, G., Qiu, S., Lv, H., Fu, Y., Liu, J., Li, X., and Bai, Y.-J. Li-ion storage performance of MnO nanoparticles coated with nitrogen-doped carbon derived from different carbon sources, *Electrochim. Acta* **2014**, *146*, 249–256. http://dx.doi.org/10.1016/j.electacta.2014.08.142

(88) Su, K., Wang, C., Nie, H., Guan, Y., Liu, F., and Chen, J. Facile template-free synthesis of 3D porous MnO/C microspheres with controllable pore size for high-performance lithium-ion battery anodes, *J. Mater. Chem. A* **2014**, *2*, 10000-10006. http://dx.doi.org/10.1039/C4TA01587H

(89) Guo, J., Liu, Q., Wang, C., and Zachariah, M. R. Interdispersed amorphous MnO_x–carbon nanocomposites with superior electrochemical performance as lithium-storage material, *Adv. Funct. Mater.* **2012**, *22*, 803–811. http://dx.doi.org/10.1002/adfm.201102137

(90) Poizot, P., Laruelle, S., Grugeon, S., Dupont, L., and Tarascon, J. M. Nano-sized transition-metal oxides as negative-electrode materials for lithium-ion batteries, *Nature* **2000**, *407*, 496–499. http://dx.doi.org/10.1038/35035045

(91) Mai, Y. J., Zhang, D., Qiao, Y. Q., Gu, C. D., Wang, X. L., and Tu, J. P. MnO/reduced graphene oxide sheet hybrid as an anode for Li-ion batteries with enhanced lithium storage performance, *J. Power Sources* **2012**, *216*, 201–207. http://dx.doi.org/10.1016/j.jpowsour.2012.05.084

(92) Zhu, W., Huang, H., Zhang, W., Tao, X., Gan, Y., Xia, Y., Yang, H., and Guo, X. Synthesis of MnO/C composites derived from pollen template for advanced lithium-ion batteries, *Electrochim. Acta* **2015**, *152*, 286–293. http://dx.doi.org/10.1016/j.electacta.2014.11.092

(93) Wang, T., Peng, Z., Wang, Y., Tang, J., and Zheng, G. MnO nanoparticle@mesoporous carbon composites grown on conducting substrates featuring high-performance lithium-ion battery, supercapacitor and sensor, *Sci. Rep.* **2013**, *3*, 2693-1–9. http://dx.doi.org/10.1038/srep02693

(94) Qiu, T., Wang, J., Lu, Y., and Yang, W. Facile fabrication of Chinese lantern-like MnO@N-C: A high-performance anode material for lithium-ion batteries, *RSC Adv.* **2014**, *4*, 23027–23035. http://dx.doi.org/10.1039/C4RA01285B

(95) Xia, Y., Xiao, Z., Dou, X., Huang, H., Lu, X., Yan, R., Gan, Y., Zhu, W., Tu, J., Zhang, W., and Tao, X. Green and facile fabrication of hollow porous MnO/C microspheres from microalgaes for lithium-ion batteries, *ACS Nano* **2013**, *7*, 7083–7092. http://dx.doi.org/10.1021/nn4023894

(96) Jiang, H., Hu, Y., Guo, S., Yan, C., Lee, P. S., and Li, C. Rational design of MnO/carbon nanopeapods with internal void space for high-rate and long-life Li-ion batteries, *ACS Nano* **2014**, *8*, 6038–6046. http://dx.doi.org/10.1021/nn501310n

(97) Lu, K., Xu, J., Zhang, J., Song, B., and Ma, H. General Preparation of Three-Dimensional Porous Metal Oxide Foams Coated with Nitrogen-Doped Carbon for Enhanced Lithium Storage, *ACS Appl. Mater. Interfaces* **2016**, *8*, 17402-17408. http://dx.doi.org/10.1021/acsami.6b04587

(98) Sun, Y., Hu, X., Luo, W., and Huang, Y. Porous carbon-modified MnO disks prepared by a microwave-polyol process and their superior lithium-ion storage properties, *J. Mater. Chem.* **2012**, *22*, 19190–19195. http://dx.doi.org/10.1039/C2JM32036C

(99) Sun, Y., Hu, X., Luo, W., Xia, F., and Huang, Y. Reconstruction of conformal nanoscale MnO on graphene as a high-capacity and long-life anode material for lithium ion batteries, *Adv. Funct. Mater.* **2013**, *23*, 2436–2444. http://dx.doi.org/10.1002/adfm.201202623

(100) Tang, X., Sui, G., Cai, Q., Zhong, W., and Yang, X. Novel MnO/carbon composite anode material with multi-modal pore structure for high performance lithium-ion batteries, *J. Mater. Chem. A* **2016**, *4*, 2082–2088. http://dx.doi.org/10.1039/C5TA10073A

(101) Liang, Y., Wang, H., Diao, P., Chang, W., Hong, G., Li, Y., Gong, M., Xie, L., Zhou, J., Wang, J., Regier, T. Z., Wei, F., and Dai, H. Oxygen reduction electrocatalyst based on strongly coupled cobalt oxide nanocrystals and carbon nanotubes, *J. Am. Chem. Soc.* **2012**, *134*, 15849–15857. http://dx.doi.org/10.1021/ja305623m

(102) Hummers, W. S. and Offeman, R. E. Preparation of graphitic oxide, *J. Am. Chem. Soc.* **1958**, *80*, 1339–1339. http://dx.doi.org/10.1021/ja01539a017

(103) Palmieri, A., Kashfi-Sadabad, R., Yazdani, S., Pettes, M., and Mustain, W. E. High performance bi-metallic manganese cobalt oxide/carbon nanotube Li-ion battery anodes, *Electrochim. Acta* **2016**, *213*, 620–625. http://dx.doi.org/10.1016/j.electacta.2016.07.147

(104) Vegard, L. Die konstitution der mischkristalle und die raumfüllung der atome, *Z. Phys.* **1921**, *5*, 17–26. http://dx.doi.org/10.1007/BF01349680

(105) Rao, A. M., Jorio, A., Pimenta, M. A., Dantas, M. S. S., Saito, R., Dresselhaus, G., and Dresselhaus, M. S. Polarized Raman study of aligned multiwalled carbon nanotubes, *Phys. Rev. Lett.* **2000**, *84*, 1820–1823. http://dx.doi.org/10.1103/PhysRevLett.84.1820

(106) Dresselhaus, M. S., Dresselhaus, G., Saito, R., and Jorio, A. Raman spectroscopy of carbon nanotubes, *Phys. Rep.* **2005**, *409*, 47–99. http://dx.doi.org/10.1016/j.physrep.2004.10.006

(107) Ramesh, K., Chen, L., Chen, F., Liu, Y., Wang, Z., and Han, Y.-F. Re-investigating the CO oxidation mechanism over unsupported MnO, Mn_2O_3 and MnO_2 catalysts, *Catal. Today* **2008**, *131*, 477–482. http://dx.doi.org/j.cattod.2007.10.061

(108) Liao, Q., Li, N., Cui, H., and Wang, C. Vertically-aligned graphene@MnO nanosheets as binder-free high-performance electrochemical pseudocapacitor electrodes, *J. Mater. Chem. A* **2013**, *1*, 13715–13720. http://dx.doi.org/10.1039/C3TA13102E

(109) He, X., Song, X., Qiao, W., Li, Z., Zhang, X., Yan, S., Zhong, W., and Du, Y. Phase- and size-dependent optical and magnetic properties of CoO nanoparticles, *J. Phys. Chem. C* **2015**, *119*, 9550–9559. http://dx.doi.org/10.1021/jp5127909

(110) Li, Y., Zhou, W., Wang, H., Xie, L., Liang, Y., Wei, F., Idrobo, J.-C., Pennycook, S. J., and Dai, H. An oxygen reduction electrocatalyst based on carbon nanotube-graphene complexes, *Nat. Nanotechnol.* **2012**, *7*, 394–400. http://dx.doi.org/10.1038/nnano.2012.72

(111) Moulder, J., Stickle, W., Sobol, P., and Bomben, K. Handbook of X-ray Photoelectron Spectroscopy. Perkin-Elmer Corporation: Eden Prairie, Minnesota, **1992**. https://www.phi.com/support/reference-material/handbook.html

(112) Tan, B. J., Klabunde, K. J., and Sherwood, P. M. A. XPS studies of solvated metal atom dispersed (SMAD) catalysts. Evidence for layered cobalt-manganese particles on alumina and silica, *J. Am. Chem. Soc.* **1991**, *113*, 855–861. http://dx.doi.org/10.1021/ja00003a019

(113) Shen, Z. X., Allen, J. W., Lindberg, P. A. P., Dessau, D. S., Wells, B. O., Borg, A., Ellis, W., Kang, J. S., Oh, S. J., Lindau, I., and Spicer, W. E. Photoemission study of CoO, *Phys. Rev. B* **1990**, *42*, 1817–1828. http://dx.doi.org/10.1103/PhysRevB.42.1817

(114) Langell, M. A., Anderson, M. D., Carson, G. A., Peng, L., and Smith, S. Valence-band electronic structure of Co_3O_4 epitaxy on CoO(100), *Phys. Rev. B* **1999**, *59*, 4791–4798. http://dx.doi.org/10.1103/PhysRevB.59.4791

(115) McIntyre, N. S. and Cook, M. G. X-ray photoelectron studies on some oxides and hydroxides of cobalt, nickel, and copper, *Anal. Chem.* **1975**, *47*, 2208–2213. http://dx.doi.org/10.1021/ac60363a034

(116) Frost, D. C., McDowell, C. A., and Woolsey, I. S. Evidence for multiplet splitting of 2p photoelectron lines of transition metal complexes, *Chem. Phys. Lett.* **1972**, *17*, 320–323. http://dx.doi.org/10.1016/0009-2614(72)87086-6

(117) Langell, M. A., Gevrey, F., and Nydegger, M. W. Surface composition of $Mn_xCo_{1-x}O$ solid solutions by X-ray photoelectron and Auger spectroscopies, *Appl. Surf. Sci.* **2000**, *153*, 114-127. http://dx.doi.org/10.1016/S0169-4332(99)00361-X

(118) Wang, F., Zhang, S., Bai, D., Zhang, F., and Xu, S. Graphene-supported binary active $Mn_{0.25}Co_{0.75}O$ solid solution derived from a CoMn-layered double hydroxide precursor for highly improved lithium storage, *RSC Adv.* **2016**, *6*, 19716-19722. http://dx.doi.org/10.1039/C6RA01500J

(119) Bergman, B. and Ågren, J. Thermodynamic Assessment of the System CoO-MnO, *J. Am. Ceram. Soc.* **1986**, *69*, 877-881. http://dx.doi.org/10.1111/j.1151-2916.1986.tb07387.x

(120) Wang, H., Cui, L.-F., Yang, Y., Sanchez Casalongue, H., Robinson, J. T., Liang, Y., Cui, Y., and Dai, H. Mn_3O_4−graphene hybrid as a high-capacity anode material for lithium ion batteries, *J. Am. Chem. Soc.* **2010**, *132*, 13978–13980. http://dx.doi.org/10.1021/ja105296a

(121) Yu, Y., Chen, C.-H., Shui, J.-L., and Xie, S. Nickel-foam-supported reticular CoO–Li_2O composite anode materials for lithium ion batteries, *Angew. Chem. Int. Ed.* **2005**, *44*, 7085-7089. http://dx.doi.org/10.1002/anie.200501905

(122) Van der Pauw, L. J. A method of measuring the resistivity and Hall coefficient on lamellae of arbitrary shape, *Philips Tech. Rev.* **1958**, *20*, 220–224.

(123) Thurber, W. R. Resistivity and Hall Measurements, *National Institute of Standards and Technology* **2010**. http://dx.doi.org/http://www.nist.gov/pml/div683/hall_resistivity.cfm#resistivity

(124) Sharma, P. K., Moore, G. J., Zhang, F., Zavalij, P., and Whittingham, M. S. Electrical properties of the layered manganese dioxides $M_xMn_{1-y}Co_yO_2$, M = Na, K *Electrochem. Solid-State Lett.* **1999**, *2*, 494-496. http://dx.doi.org/10.1149/1.1390881

(125) Kim, J. H., Park, C. W., and Sun, Y. K. Synthesis and electrochemical behavior of $Li[Li_{0.1}Ni_{0.35-x/2}Co_xMn_{0.55-x/2}]O_2$ cathode materials, *Solid State Ion.* **2003**, *164*, 43-49. http://dx.doi.org/10.1016/j.ssi.2003.08.003

(126) Ngala, J. K., Chernova, N. A., Ma, M., Mamak, M., Zavalij, P. Y., and Whittingham, M. S. The synthesis, characterization and electrochemical behavior of the layered $LiNi_{0.4}Mn_{0.4}Co_{0.2}O_2$ compound, *J. Mater. Chem.* **2004**, *14*, 214-220. http://dx.doi.org/10.1039/B309834F

(127) Nakayama, M., Suzuki, K., Okamura, K., Inoue, R., Athouël, L., Crosnier, O., and Brousse, T. Doping of cobalt into multilayered manganese oxide for improved pseudocapacitive properties, *J. Electrochem. Soc.* **2010**, *157*, A1067-A1072. http://dx.doi.org/10.1149/1.3467865

(128) Liu, R., Jin, D., and Yue, L. Synthesis and electrochemical properties of Co doped MnO_2 framework with nanofibrous structure, *Int. J. Appl. Ceram. Technol.* **2015**, *12*, E59-E64. http://dx.doi.org/10.1111/ijac.12226

(129) Kim, B. C., Justin Raj, C., Cho, W.-J., Lee, W.-G., Jeong, H. T., and Yu, K. H. Enhanced electrochemical properties of cobalt doped manganese dioxide nanowires, *J. Alloys Compd.* **2014**, *617*, 491-497. http://dx.doi.org/10.1016/j.jallcom.2014.08.018

(130) Li, H., Wang, Z., Chen, L., and Huang, X. Research on advanced materials for Li-ion batteries, *Adv. Mater.* **2009**, *21*, 4593–4607. http://dx.doi.org/10.1002/adma.200901710

(131) Palmieri, A., Yazdani, S., Kashfi-Sadabad, R., Karakalos, S. G., Pettes, M. T., and Mustain, W. E. Cobalt doping as a pathway to stabilize the solid-state conversion chemistry of manganese oxide anodes in Li-ion batteries, *J. Phys. Chem. C* **2018**, *122*, 7120-7127. http://dx.doi.org/10.1021/acs.jpcc.8b00403

(132) Alessandro, P., Sajad, Y., Raana, K.-S., G., K. S., Benjamin, N., Alexandra, O., Xiong, P., T., P. M., and E., M. W. Improved capacity retention of metal oxide anodes in Li-ion batteries: Increasing intraparticle electronic conductivity through Na inclusion in Mn_3O_4, *ChemElectroChem*, *0*. http://dx.doi.org/10.1002/celc.201800358

(133) Greenwood, N. N. and Earnshaw, A. Chemistry of the Elements. 2nd ed.; Butterworth-Heinemann: New York, **1997**. ISBN: 978-0-7506-3365-9

(134) Xie, Q., Zheng, X., Wu, D., Chen, X., Shi, J., Han, X., Zhang, X., Peng, G., Gao, Y., and Huang, H. High electrical conductivity of individual epitaxially grown MoO_2 nanorods, *Appl. Phys. Lett.* **2017**, *111*, 093505-1–5. http://dx.doi.org/10.1063/1.5001183

(135) Mendoza-Sánchez, B., Brousse, T., Ramirez-Castro, C., Nicolosi, V., and Grant, P. S. An investigation of nanostructured thin film α-MoO_3 based supercapacitor electrodes in an aqueous electrolyte, *Electrochim. Acta* **2013**, *91*, 253–260. http://dx.doi.org/10.1016/j.electacta.2012.11.127

(136) Guo, Y. and Robertson, J. Origin of the high work function and high conductivity of MoO_3, *Appl. Phys. Lett.* **2014**, *105*, 222110-1–4. http://dx.doi.org/10.1063/1.4903538

(137) Meyer, J., Khalandovsky, R., Görrn, P., and Kahn, A. MoO_3 films spin-coated from a nanoparticle suspension for efficient hole-injection in organic electronics, *Adv. Mater.* **2011**, *23*, 70–73. http://dx.doi.org/10.1002/adma.201003065

(138) Greiner, M. T., Helander, M. G., Tang, W.-M., Wang, Z.-B., Qiu, J., and Lu, Z.-H. Universal energy-level alignment of molecules on metal oxides, *Nat. Mater.* **2011**, *11*, 76–81. http://dx.doi.org/10.1038/nmat3159

(139) Chen, Z., Santoso, I., Wang, R., Xie, L. F., Mao, H. Y., Huang, H., Wang, Y. Z., Gao, X. Y., Chen, Z. K., Ma, D., Wee, A. T. S., and Chen, W. Surface transfer hole doping of epitaxial graphene using MoO_3 thin film, *Appl. Phys. Lett.* **2010**, *96*, 213104-1–3. http://dx.doi.org/10.1063/1.3441263

(140) Meyer, J., Kidambi, P. R., Bayer, B. C., Weijtens, C., Kuhn, A., Centeno, A., Pesquera, A., Zurutuza, A., Robertson, J., and Hofmann, S. Metal oxide induced charge transfer doping and band alignment of graphene electrodes for efficient organic light emitting diodes, *Sci. Rep.* **2014**, *4*, 5380-1–7. http://dx.doi.org/10.1038/srep05380

(141) Be, Ge, Mo, Si, Ti, W, Zn. In Encyclopedia of Electrochemistry of the Elements, Bard, A. J., Ed. Marcel Dekker Inc.: New York, **1973**; Vol. 5. ISBN: 0824725050

(142) Anbananthan, N., Nagaraja Rao, K., and Venkatesan, V. K. Cyclic voltammetric investigations of the reduction of Mo(VI) to Mo(IV) in 1 M sulphuric acid, *J. Electroanal. Chem.* **1994**, *374*, 207–214. http://dx.doi.org/10.1016/0022-0728(94)03356-0

(143) Anbananthan, N., Nagaraja Rao, K., and Venkatesan, V. K. Electrochemical formation of oxygen-deficient molybdenum oxide, *Appl. Surf. Sci.* **1993**, *72*, 189–194. http://dx.doi.org/10.1016/0169-4332(93)90011-Y

(144) Tong, Y. and Lunsford, J. H. Mechanistic and kinetic studies of the reactions of gas-phase methyl radicals with metal oxides, *J. Am. Chem. Soc.* **1991**, *113*, 4741–4746. http://dx.doi.org/10.1021/ja00013a005

(145) Magnéli, A. The crystal structure of Mo_4O_{11} (γ-molybdenum oxide), *Acta Chem. Scand.* **1948**, *2*, 861–871. http://dx.doi.org/10.3891/acta.chem.scand.02-0861

(146) Spevack, P. A. and McIntyre, N. S. Thermal reduction of molybdenum trioxide, *J. Phys. Chem.* **1992**, *96*, 9029–9035. http://dx.doi.org/10.1021/j100201a062

(147) Inzani, K., Nematollahi, M., Selbach, S. M., Grande, T., and Vullum-Bruer, F. Progression of reduction of MoO_3 observed in powders and solution-processed films, *Thin Solid Films* **2017**, *626*, 94–103. http://dx.doi.org/10.1016/j.tsf.2017.02.029

(148) Dzhanelidze, R. B., Purtseladze, I. M., Khitarishvili, L. S., Chikovani, R. I., and Shkol'nik, A. L. Some optical and photoelectric properties of molybdenum oxide, *Sov. Phys. Solid State* **1966**, *7*, 2082–2083.

(149) Hu, X. K., Qian, Y. T., Song, Z. T., Huang, J. R., Cao, R., and Xiao, J. Q. Comparative study on MoO_3 and H_xMoO_3 nanobelts: Structure and electric transport, *Chem. Mater.* **2008**, *20*, 1527–1533. http://dx.doi.org/10.1021/cm702942y

(150) Balendhran, S., Deng, J., Ou, J. Z., Walia, S., Scott, J., Tang, J., Wang, K. L., Field, M. R., Russo, S., Zhuiykov, S., Strano, M. S., Medhekar, N., Sriram, S., Bhaskaran, M., and Kalantar-Zadeh, K. Enhanced charge carrier mobility in two-dimensional high dielectric molybdenum oxide, *Adv. Mater.* **2013**, *25*, 109–114. http://dx.doi.org/10.1002/adma.201203346

(151) Gruber, H. and Krautz, E. Untersuchungen der elektrischen leitfähigkeit und des magnetowiderstandes im system molybdän-sauerstoff, *Phys. Status Solidi A* **1980**, *62*, 615–624. http://dx.doi.org/10.1002/pssa.2210620233

(152) Mestl, G., Verbruggen, N. F. D., and Knoezinger, H. Mechanically activated MoO_3. 2. Characterization of defect structures, *Langmuir* **1995**, *11*, 3035–3041. http://dx.doi.org/10.1021/la00008a031

(153) Tilley, R. J. D. Defect crystal chemistry and its applications. Blackie & Son: London, **1987**. ISBN: 0412013312

(154) Porter, V. R., White, W. B., and Roy, R. Optical spectra of the intermediate oxides of titanium, vanadium, molybdenum, and tungsten, *J. Solid State Chem.* **1972**, *4*, 250–254. http://dx.doi.org/10.1016/0022-4596(72)90113-2

(155) Kihlborg, L. The structural chemistry of the higher molybdenum oxides, *Ark. Kemi.* **1963**, *21*, 357–364.

(156) Coquet, R. and Willock, D. J. The (010) surface of α-MoO_3, a DFT+U study, *Phys. Chem. Chem. Phys.* **2005**, *7*, 3819–3828. http://dx.doi.org/10.1039/B511044K

(157) Cora, F., Patel, A., Harrison, N. M., Roetti, C., and Richard A. Catlow, C. An *ab initio* Hartree-Fock study of α-MoO_3, *J. Mater. Chem.* **1997**, *7*, 959–967. http://dx.doi.org/10.1039/A607439A

(158) Chen, M., Waghmare, U. V., Friend, C. M., and Kaxiras, E. A density functional study of clean and hydrogen-covered α-MoO_3(010): Electronic structure and surface relaxation, *J. Chem. Phys.* **1998**, *109*, 6854–6860. http://dx.doi.org/10.1063/1.477252

(159) Smith, M. R. and Ozkan, U. S. The partial oxidation of methane to formaldehyde: Role of different crystal planes of MoO_3, *J. Catal.* **1993**, *141*, 124–139. http://dx.doi.org/10.1006/jcat.1993.1124

(160) Papakondylis, A. and Sautet, P. Ab *initio* study of the structure of the α-MoO_3 solid and study of the adsorption of H_2O and CO molecules on its (100) surface, *J. Phys. Chem.* **1996**, *100*, 10681–10688. http://dx.doi.org/10.1021/jp953727w

(161) Chen, M., Friend, C. M., and Kaxiras, E. The chemical nature of surface point defects on MoO_3(010): Adsorption of hydrogen and methyl, *J. Am. Chem. Soc.* **2001**, *123*, 2224–2230. http://dx.doi.org/10.1021/ja994376s

(162) Remediakis, I. N., Kaxiras, E., Chen, M., and Friend, C. M. Dinitrosyl formation as an intermediate stage of the reduction of NO in the presence of MoO_3, *J. Chem. Phys.* **2003**, *118*, 6046–6051. http://dx.doi.org/10.1063/1.1556846

(163) Wagner, F. T., Lakshmanan, B., and Mathias, M. F. Electrochemistry and the future of the automobile, *J. Phys. Chem. Lett.* **2010**, *1*, 2204–2219. http://dx.doi.org/10.1021/jz100553m

(164) Yu, W., Porosoff, M. D., and Chen, J. G. Review of Pt-based bimetallic catalysis: From model surfaces to supported catalysts, *Chem. Rev.* **2012**, *112*, 5780–5817. http://dx.doi.org/10.1021/cr300096b

(165) Nie, Y., Li, L., and Wei, Z. Recent advancements in Pt and Pt-free catalysts for oxygen reduction reaction, *Chem. Soc. Rev.* **2015**, *44*, 2168–2201. http://dx.doi.org/10.1039/C4CS00484A

(166) Gewirth, A. A. and Thorum, M. S. Electroreduction of dioxygen for fuel-cell applications: Materials and challenges, *Inorg. Chem.* **2010**, *49*, 3557–3566. http://dx.doi.org/10.1021/ic9022486

(167) Jaouen, F., Proietti, E., Lefèvre, M., Chenitz, R., Dodelet, J.-P., Wu, G., Chung, H. T., Johnston, C. M., and Zelenay, P. Recent advances in non-precious metal catalysis for oxygen-reduction reaction in polymer electrolyte fuel cells, *Energy Environ. Sci.* **2011**, *4*, 114–130. http://dx.doi.org/10.1039/C0EE00011F

(168) Liang, H.-W., Wei, W., Wu, Z.-S., Feng, X., and Müllen, K. Mesoporous metal–nitrogen-doped carbon electrocatalysts for highly efficient oxygen reduction reaction, *J. Am. Chem. Soc.* **2013**, *135*, 16002–16005. http://dx.doi.org/10.1021/ja407552k

(169) Guo, S. and Dong, S. Graphene nanosheet: Synthesis, molecular engineering, thin film, hybrids, and energy and analytical applications, *Chem. Soc. Rev.* **2011**, *40*, 2644–2672. http://dx.doi.org/10.1039/C0CS00079E

(170) Sgobba, V. and Guldi, D. M. Carbon nanotubes-electronic/electrochemical properties and application for nanoelectronics and photonics, *Chem. Soc. Rev.* **2009**, *38*, 165–184. http://dx.doi.org/10.1039/B802652C

(171) Eder, D. Carbon nanotube−inorganic hybrids, *Chem. Rev.* **2010**, *110*, 1348–1385. http://dx.doi.org/10.1021/cr800433k

(172) Wang, S., Yu, D., Dai, L., Chang, D. W., and Baek, J.-B. Polyelectrolyte-functionalized graphene as metal-free electrocatalysts for oxygen reduction, *ACS Nano* **2011**, *5*, 6202–6209. http://dx.doi.org/10.1021/nn200879h

(173) Zhao, D., Feng, J., Huo, Q., Melosh, N., Fredrickson, G. H., Chmelka, B. F., and Stucky, G. D. Triblock copolymer syntheses of mesoporous silica with periodic 50 to 300 angstrom pores, *Science* **1998**, *279*, 548–552. http://dx.doi.org/10.1126/science.279.5350.548

(174) Shi, Y., Wan, Y., Zhang, R., and Zhao, D. Synthesis of self-supported ordered mesoporous cobalt and chromium nitrides, *Adv. Funct. Mater.* **2008**, *18*, 2436–2443. http://dx.doi.org/10.1002/adfm.200800488

(175) Kim, T.-W., Kleitz, F., Paul, B., and Ryoo, R. MCM-48-like large mesoporous silicas with tailored pore structure: Facile synthesis domain in a ternary triblock copolymer−butanol−water system, *J. Am. Chem. Soc.* **2005**, *127*, 7601-7610. http://dx.doi.org/10.1021/ja042601m

(176) Dickinson, C., Zhou, W., Hodgkins, R. P., Shi, Y., Zhao, D., and He, H. Formation mechanism of porous single-crystal Cr_2O_3 and Co_3O_4 templated by mesoporous silica, *Chem. Mater.* **2006**, *18*, 3088–3095. http://dx.doi.org/10.1021/cm060014p

(177) Chang, J., Jin, M., Yao, F., Kim, T. H., Le, V. T., Yue, H., Gunes, F., Li, B., Ghosh, A., Xie, S., and Lee, Y. H. Asymmetric supercapacitors based on graphene/MnO_2 nanospheres and graphene/MoO_3 nanosheets with high energy density, *Adv. Funct. Mater.* **2013**, *23*, 5074-5083. http://dx.doi.org/10.1002/adfm201301851

(178) Kresse, G. and Furthmüller, J. Efficient iterative schemes for ab initio total-energy calculations using a plane-wave basis set, *Phys. Rev. B* **1996**, *54*, 11169–11186. http://dx.doi.org/10.1103/PhysRevB.54.11169

(179) Perdew, J. P., Burke, K., and Ernzerhof, M. Generalized gradient approximation made simple, *Phys. Rev. Lett.* **1996**, *77*, 3865–3868. http://dx.doi.org/10.1103/PhysRevLett.77.3865

(180) Dudarev, S. L., Botton, G. A., Savrasov, S. Y., Humphreys, C. J., and Sutton, A. P. Electron-energy-loss spectra and the structural stability of nickel oxide: An LSDA+U study, *Phys. Rev. B* **1998**, *57*, 1505–1509. http://dx.doi.org/10.1103/PhysRevB.57.1505

(181) Inzani, K., Grande, T., Vullum-Bruer, F., and Selbach, S. M. A van der Waals density functional study of MoO_3 and its oxygen vacancies, *J. Phys. Chem. C* **2016**, *120*, 8959–8968. http://dx.doi.org/10.1021/acs.jpcc.6b00585

(182) Lei, Y.-H. and Chen, Z.-X. DFT+U study of properties of MoO_3 and hydrogen adsorption on MoO_3(010), *J. Phys. Chem. C* **2012**, *116*, 25757–25764. http://dx.doi.org/10.1021/jp304122n

(183) Baldoni, M., Craco, L., Seifert, G., and Leoni, S. A two-electron mechanism of lithium insertion into layered α-MoO_3: A DFT and DFT+U study, *J. Mater. Chem. A* **2013**, *1*, 1778–1784. http://dx.doi.org/10.1039/C2TA00839D

(184) Ding, H., Ray, K. G., Ozolins, V., and Asta, M. Structural and vibrational properties of α-MoO_3 from van der Waals corrected density functional theory calculations, *Phys. Rev. B* **2012**, *85*, 012104-1–4. http://dx.doi.org/10.1103/PhysRevB.85.012104

(185) Huang, P.-R., He, Y., Cao, C., and Lu, Z.-H. Impact of lattice distortion and electron doping on α-MoO_3 electronic structure, *Sci. Rep.* **2014**, *4*, 7131-1–7. http://dx.doi.org/10.1038/srep07131

(186) Rozzi, C. A., Manghi, F., and Parmigiani, F. *Ab initio* Fermi surface and conduction-band calculations in oxygen-reduced MoO_3, *Phys. Rev. B* **2003**, *68*, 075106-1–6. http://dx.doi.org/10.1103/PhysRevB.68.075106

(187) Deskins, N. A. and Dupuis, M. Electron transport via polaron hopping in bulk TiO_2: A density functional theory characterization, *Phys. Rev. B* **2007**, *75*, 195212-1–10. http://dx.doi.org/10.1103/PhysRevB.75.195212

(188) Li, W., Liu, J., and Zhao, D. Mesoporous materials for energy conversion and storage devices, *Nat. Rev. Mater.* **2016**, *1*, 16023-1–17. http://dx.doi.org/10.1038/natrevmats.2016.23

(189) Inzani, K., Nematollahi, M., Vullum-Bruer, F., Grande, T., Reenaas, T. W., and Selbach, S. M. Electronic properties of reduced molybdenum oxides, *Phys. Chem. Chem. Phys.* **2017**, *19*, 9232–9245. http://dx.doi.org/10.1039/C7CP00644F

(190) Scanlon, D. O., Watson, G. W., Payne, D. J., Atkinson, G. R., Egdell, R. G., and Law, D. S. L. Theoretical and experimental study of the electronic structures of MoO_3 and MoO_2, *J. Phys. Chem. C* **2010**, *114*, 4636–4645. http://dx.doi.org/10.1021/jp9093172

(191) Ruiz Puigdollers, A., Schlexer, P., Tosoni, S., and Pacchioni, G. Increasing oxide reducibility: The role of metal/oxide interfaces in the formation of oxygen vacancies, *ACS Catal.* **2017**, *7*, 6493–6513. http://dx.doi.org/10.1021/acscatal.7b01913

(192) Kröger, M., Hamwi, S., Meyer, J., Riedl, T., Kowalsky, W., and Kahn, A. Role of the deep-lying electronic states of MoO_3 in the enhancement of hole-injection in organic thin films, *Appl. Phys. Lett.* **2009**, *95*, 123301-1–3. http://dx.doi.org/10.1063/1.3231928

(193) Heyd, J., Scuseria, G. E., and Ernzerhof, M. Erratum: "Hybrid functionals based on a screened Coulomb potential" [J. Chem. Phys. 118, 8207 (2003)], *J. Chem. Phys.* **2006**, *124*, 219906-1. http://dx.doi.org/10.1063/1.2204597

(194) Borgschulte, A., Sambalova, O., Delmelle, R., Jenatsch, S., Hany, R., and Nüesch, F. Hydrogen reduction of molybdenum oxide at room temperature, *Sci. Rep.* **2017**, *7*, 40761-1–9. http://dx.doi.org/10.1038/srep40761

(195) Roquerol, F., Rouquerol, J., and Sing, K. Adsorption by Powders and Porous Solids. Academic Press: San Diego, **1999**.

(196) Yang, S., Feng, X., Ivanovici, S., and Müllen, K. Fabrication of graphene-encapsulated oxide nanoparticles: Towards high-performance anode materials for lithium storage, *Angew. Chem. Int. Edit.* **2010**, *49*, 8408–8411. http://dx.doi.org/10.1002/anie.201003485

(197) Yang, X., Fan, K., Zhu, Y., Shen, J., Jiang, X., Zhao, P., and Li, C. Tailored graphene-encapsulated mesoporous Co_3O_4 composite microspheres for high-performance lithium ion batteries, *J. Mater. Chem.* **2012**, *22*, 17278–17283. http://dx.doi.org/10.1039/C2JM32571C

(198) Dieterle, M. and Mestl, G. Raman spectroscopy of molybdenum oxides Part II. Resonance Raman spectroscopic characterization of the molybdenum oxides Mo_4O_{11} and MoO_2, *Phys. Chem. Chem. Phys.* **2002**, *4*, 822–826. http://dx.doi.org/10.1039/B107046K

(199) Sun, Y., Wang, J., Zhao, B., Cai, R., Ran, R., and Shao, Z. Binder-free α-MoO_3 nanobelt electrode for lithium-ion batteries utilizing van der Waals forces for film formation and connection with current collector, *J. Mater. Chem. A* **2013**, *1*, 4736–4746. http://dx.doi.org/10.1039/C3TA01285A

(200) Thomsen, C. and Reich, S. Double resonant Raman scattering in graphite, *Phys. Rev. Lett.* **2000**, *85*, 5214–5217. http://dx.doi.org/10.1103/PhysRevLett.85.5214

(201) De La Cruz, F. A. and Cowley, J. M. Structure of graphitic oxide, *Nature* **1962**, *196*, 468–469. http://dx.doi.org/10.1038/196468a0

(202) Cai, W., Piner, R. D., Stadermann, F. J., Park, S., Shaibat, M. A., Ishii, Y., Yang, D., Velamakanni, A., An, S. J., Stoller, M., An, J., Chen, D., and Ruoff, R. S. Synthesis and solid-state NMR structural characterization of ^{13}C-labeled graphite oxide, *Science* **2008**, *321*, 1815–1817. http://dx.doi.org/10.1126/science.1162369

(203) Lerf, A., He, H., Riedl, T., Forster, M., and Klinowski, J. ^{13}C and ^{1}H MAS NMR studies of graphite oxide and its chemically modified derivatives, *Solid State Ion.* **1997**, *101–103*, 857–862. http://dx.doi.org/10.1016/S0167-2738(97)00319-6

(204) He, H., Klinowski, J., Forster, M., and Lerf, A. A new structural model for graphite oxide, *Chem. Phys. Lett.* **1998**, *287*, 53–56. http://dx.doi.org/10.1016/S0009-2614(98)00144-4

(205) Gao, X., Jang, J., and Nagase, S. Hydrazine and thermal reduction of graphene oxide: Reaction mechanisms, product structures, and reaction design, *J. Phys. Chem. C* **2010**, *114*, 832–842. http://dx.doi.org/10.1021/jp909284g

(206) Stankovich, S., Dikin, D. A., Piner, R. D., Kohlhaas, K. A., Kleinhammes, A., Jia, Y., Wu, Y., Nguyen, S. T., and Ruoff, R. S. Synthesis of graphene-based nanosheets via chemical reduction of exfoliated graphite oxide, *Carbon* **2007**, *45*, 1558–1565. http://dx.doi.org/10.1016/j.carbon.2007.02.034

(207) Mohan, V. B., Brown, R., Jayaraman, K., and Bhattacharyya, D. Characterisation of reduced graphene oxide: Effects of reduction variables on electrical conductivity, *Mater. Sci. Eng., B* **2015**, *193*, 49–60. http://dx.doi.org/10.1016/j.mseb.2014.11.002

(208) Tuinstra, F. and Koenig, J. L. Raman spectrum of graphite, *J. Chem. Phys.* **1970**, *53*, 1126–1130. http://dx.doi.org/10.1063/1.1674108

(209) Fan, Z.-J., Kai, W., Yan, J., Wei, T., Zhi, L.-J., Feng, J., Ren, Y.-m., Song, L.-P., and Wei, F. Facile synthesis of graphene nanosheets *via* Fe reduction of exfoliated graphite oxide, *ACS Nano* **2011**, *5*, 191–198. http://dx.doi.org/10.1021/nn102339t

(210) Wang, S., Yu, D., and Dai, L. Polyelectrolyte functionalized carbon nanotubes as efficient metal-free electrocatalysts for oxygen reduction, *J. Am. Chem. Soc.* **2011**, *133*, 5182-5185. http://dx.doi.org/10.1021/ja1112904

(211) Spevack, P. A. and McIntyre, N. S. A Raman and XPS investigation of supported molybdenum oxide thin films. 1. Calcination and reduction studies, *J. Phys. Chem.* **1993**, *97*, 11020–11030. http://dx.doi.org/10.1021/j100144a020

(212) Rogers, D. B., Shannon, R. D., Sleight, A. W., and Gillson, J. L. Crystal chemistry of metal dioxides with rutile-related structures, *Inorg. Chem.* **1969**, *8*, 841–849. http://dx.doi.org/10.1021/ic50074a029

(213) Goodenough, J. B. and Cushing, B. L. Handbook of fuel cells–fundamentals, technology and applications. John Wiley & Sons: New York, **2003**. ISBN: 0-471-49926-9.

(214) Singh, L., Azad, U. P., Singh, S. P., Ganesan, V., Rai, U. S., and Lee, Y. Yttrium copper titanate as a highly efficient electrocatalyst for oxygen reduction reaction in fuel cells, synthesized via ultrafast automatic flame technique, *Sci. Rep.* **2017**, *7*, 9407. http://dx.doi.org/10.1038/s41598-017-09661-9

(215) Sun, T., Wang, J., Qiu, C., Ling, X., Tian, B., Chen, W., and Su, C. B, N Codoped and defect-Rich nanocarbon material as a metal-free bifunctional electrocatalyst for oxygen reduction and evolution reactions, *Adv. Sci.*, *0*, 1800036. http://dx.doi.org/doi:10.1002/advs.201800036

(216) Bidault, F., Brett, D. J. L., Middleton, P. H., and Brandon, N. P. Review of gas diffusion cathodes for alkaline fuel cells, *J. Power Sources* **2009**, *187*, 39–48. http://dx.doi.org/10.1016/j.jpowsour.2008.10.106

(217) Gu, D. and Schuth, F. Synthesis of non-siliceous mesoporous oxides, *Chem. Soc. Rev.* **2014**, *43*, 313–344. http://dx.doi.org/10.1039/C3CS60155B

(218) Seto, J. Y. W. The electrical properties of polycrystalline silicon films, *J. Appl. Phys.* **1975**, *46*, 5247-5254. http://dx.doi.org/10.1063/1.321593

(219) Rai-Choudhury, P. and Hower, P. L. Growth and characterization of polycrystalline silicon, *J. Electrochem. Soc.* **1973**, *120*, 1761-1766. http://dx.doi.org/10.1149/1.2403359

(220) Kamins, T. I. Hall mobility in chemically deposited polycrystalline silicon, *J. Appl. Phys.* **1971**, *42*, 4357-4365. http://dx.doi.org/10.1063/1.1659780

(221) K., G. T. Application of zinc oxide varistors, *J. Am. Ceram. Soc.* **1990**, *73*, 1817-1840. http://dx.doi.org/10.1111/j.1151-2916.1990.tb05232.x

(222) Hagfeldt, A., Boschloo, G., Sun, L., Kloo, L., and Pettersson, H. Dye-sensitized solar cells, *Chem. Rev.* **2010**, *110*, 6595-6663. http://dx.doi.org/10.1021/cr900356p

(223) Cao, F., Oskam, G., Meyer, G. J., and Searson, P. C. Electron transport in porous nanocrystalline TiO_2 photoelectrochemical cells, *J. Phys. Chem.* **1996**, *100*, 17021-17027. http://dx.doi.org/10.1021/jp9616573

(224) Dloczik, L., Ileperuma, O., Lauermann, I., Peter, L. M., Ponomarev, E. A., Redmond, G., Shaw, N. J., and Uhlendorf, I. Dynamic response of dye-sensitized nanocrystalline solar cells: characterization by intensity-modulated photocurrent spectroscopy, *J. Phys. Chem. B* **1997**, *101*, 10281-10289. http://dx.doi.org/10.1021/jp972466i

(225) van de Lagemaat, J. and Frank, A. J. Effect of the surface-state distribution on electron transport in dye-sensitized TiO_2 solar cells: Nonlinear eectron-transport Kinetics, *J. Phys. Chem. B* **2000**, *104*, 4292-4294. http://dx.doi.org/10.1021/jp000836o

(226) Bisquert, J. and Vikhrenko, V. S. Interpretation of the time constants measured by kinetic techniques in nanostructured semiconductor electrodes and dye-sensitized solar cells, *J. Phys. Chem. B* **2004**, *108*, 2313-2322. http://dx.doi.org/10.1021/jp035395y

(227) Fisher, A. C., Peter, L. M., Ponomarev, E. A., Walker, A. B., and Wijayantha, K. G. U. Intensity dependence of the back reaction and transport of electrons in dye-sensitized nanocrystalline TiO_2 solar cells, *J. Phys. Chem. B* **2000**, *104*, 949-958. http://dx.doi.org/10.1021/jp993220b

(228) Santanu, P., Alexandros, S., Shuchi, G., Yu, B., Francesco, D. S., and Gerasimos, K. Trap-state suppression and improved charge transport in PbS quantum dot solar cells with synergistic mixed-ligand treatments, *Small* **2017**, *13*, 1700598. http://dx.doi.org/doi:10.1002/smll.201700598

(229) Bakulin, A. A., Neutzner, S., Bakker, H. J., Ottaviani, L., Barakel, D., and Chen, Z. Charge trapping dynamics in PbS colloidal quantum dot photovoltaic devices, *ACS Nano* **2013**, *7*, 8771-8779. http://dx.doi.org/10.1021/nn403190s

(230) Galoppini, E., Rochford, J., Chen, H., Saraf, G., Lu, Y., Hagfeldt, A., and Boschloo, G. Fast electron transport in metal organic vapor deposition grown dye-sensitized ZnO nanorod solar vells, *J. Phys. Chem. B* **2006**, *110*, 16159-16161. http://dx.doi.org/10.1021/jp062865q

(231) Guo, R., Wang, X., Kuang, Y., and Huang, B. First-principles study of anisotropic thermoelectric transport properties of IV-VI semiconductor compounds SnSe and SnS, *Phys. Rev. B* **2015**, *92*, 115202. http://dx.doi.org/10.1103/PhysRevB.92.115202

(232) Tian, Z., Garg, J., Esfarjani, K., Shiga, T., Shiomi, J., and Chen, G. Phonon conduction in PbSe, PbTe, and $PbTe_{1-x}Se_x$ from first-principles calculations, *Phys. Rev. B* **2012**, *85*, 184303. http://dx.doi.org/10.1103/PhysRevB.85.184303

(233) Tian, Z., Lee, S., and Chen, G. Heat transfer in thermoelectric materials and devices, *J. Heat Transfer* **2013**, *135*, 061605-061605. http://dx.doi.org/10.1115/1.4023585

(234) Carey, G. H., Abdelhady, A. L., Ning, Z., Thon, S. M., Bakr, O. M., and Sargent, E. H. Colloidal quantum dot solar cells, *Chem. Rev.* **2015**, *115*, 12732-12763. http://dx.doi.org/10.1021/acs.chemrev.5b00063

(235) Bux, S. K., Fleurial, J.-P., and Kaner, R. B. Nanostructured materials for thermoelectric applications, *Chem. Commun.* **2010**, *46*, 8311–8324. http://dx.doi.org/10.1039/C0CC02627A

(236) Li, J., Tan, Q., and Li, J.-F. Synthesis and property evaluation of $CuFeS_{2-x}$ as earth-abundant and environmentally-friendly thermoelectric materials, *J. Alloys Compd.* **2013**, *551*, 143-149. http://dx.doi.org/10.1016/j.jallcom.2012.09.067

(237) Johnsen, S., He, J., Androulakis, J., Dravid, V. P., Todorov, I., Chung, D. Y., and Kanatzidis, M. G. Nanostructures boost the thermoelectric performance of PbS, *J. Am. Chem. Soc.* **2011**, *133*, 3460-3470. http://dx.doi.org/10.1021/ja109138p

(238) Scanlon, W. W. Interpretation of Hall effect and resistivity data in PbS and similar binary compound semiconductors, *Phys. Rev.* **1953**, *92*, 1573-1575.

(239) Horák, J., Lošťák, P., Koudelka, L., and Novotný, R. Inversion of conductivity type in $Bi_2Te_{3-x}S_x$ crystals, *Solid State Commun.* **1985**, *55*, 1031-1034. http://dx.doi.org/10.1016/0038-1098(85)90583-6

(240) Kresse, G. and Hafner, J. Ab initio molecular dynamics for liquid metals, *Phys. Rev. B* **1993**, *47*, 558-561. http://dx.doi.org/10.1103/PhysRevB.47.558

(241) Kresse, G. and Furthmüller, J. Efficiency of ab-initio total energy calculations for metals and semiconductors using a plane-wave basis set, *Comput. Mater. Sci.* **1996**, *6*, 15-50. http://dx.doi.org/10.1016/0927-0256(96)00008-0

(242) Madsen, G. K. H. and Singh, D. J. BoltzTraP. A code for calculating band-structure dependent quantities, *Comput. Phys. Commun.* **2006**, *175*, 67-71. http://dx.doi.org/10.1016/j.cpc.2006.03.007

(243) Huan, T. D., Tuoc, V. N., Le, N. B., Minh, N. V., and Woods, L. M. High-pressure phases of Mg_2Si from first principles, *Phys. Rev. B* **2016**, *93*, 094109. http://dx.doi.org/10.1103/PhysRevB.93.094109

(244) Tuoc, V. N. and Huan, T. D. *J. Phys. Chem. C* **2018**, *in press*.

(245) Hautier, G., Miglio, A., Ceder, G., Rignanese, G.-M., and Gonze, X. Identification and design principles of low hole effective mass p-type transparent conducting oxides, *Nat. Commun.* **2013**, *4*, 2292. http://dx.doi.org/10.1038/ncomms3292

(246) Hautier, G., Miglio, A., Waroquiers, D., Rignanese, G.-M., and Gonze, X. How does chemistry influence electron effective mass in oxides? A high-throughput computational analysis, *Chem. Mater.* **2014**, *26*, 5447-5458. http://dx.doi.org/10.1021/cm404079a

(247) Ong, S. P., Richards, W. D., Jain, A., Hautier, G., Kocher, M., Cholia, S., Gunter, D., Chevrier, V. L., Persson, K. A., and Ceder, G. Python Materials Genomics (pymatgen): A robust, open-source python library for materials analysis, *Comput. Mater. Sci.* **2013**, *68*, 314-319. http://dx.doi.org/10.1016/j.commatsci.2012.10.028

(248) Togo, A., Chaput, L., and Tanaka, I. Distributions of phonon lifetimes in Brillouin zones, *Phys. Rev. B* **2015**, *91*, 094306. http://dx.doi.org/10.1103/PhysRevB.91.094306

(249) Streetman, B. G. and Banerjee, S. Solid state electronic devices. 5th ed.; Prentice Hall: Englewood Cliffs, NJ, **2000**.

(250) Ashcroft, N. W. and Mermin, N. D. Solid State Physics. Saunders College Publishing: Orlando, Florida, **1976**.

(251) Scheele, M., Oeschler, N., Veremchuk, I., Peters, S.-O., Littig, A., Kornowski, A., Klinke, C., and Weller, H. Thermoelectric properties of lead chalcogenide core–shell nanostructures, *ACS Nano* **2011**, *5*, 8541–8551. http://dx.doi.org/10.1021/nn2017183

(252) Kim, H.-S., Gibbs, Z. M., Tang, Y., Wang, H., and Snyder, G. J. Characterization of Lorenz number with Seebeck coefficient measurement, *APL Mater.* **2015**, *3*, 041506. http://dx.doi.org/10.1063/1.4908244

(253) Eucken, A. *Ceram. Abs.* **1932**, *11*, 576.

(254) Eucken, A. *Ceram. Abs.* **1933**, *12*, 231.

(255) Russell, H. W. Principles of heat flow in porous insulators, *J. Am. Ceram. Soc.* **1935**, *18*, 1–5. http://dx.doi.org/10.1111/j.1151-2916.1935.tb19340.x

(256) Fang, J., Kang, C. B., Huang, Y., Tolbert, S. H., and Pilon, L. Thermal conductivity of ordered mesoporous nanocrystalline silicon thin films made from magnesium reduction of polymer-templated silica, *J. Phys. Chem. C* **2012**, *116*, 12926–12933. http://dx.doi.org/10.1021/jp302531d

(257) Tang, J., Wang, H.-T., Lee, D. H., Fardy, M., Huo, Z., Russell, T. P., and Yang, P. Holey silicon as an efficient thermoelectric material, *Nano Lett.* **2010**, *10*, 4279-4283. http://dx.doi.org/10.1021/nl102931z

(258) Poudel, B., Hao, Q., Ma, Y., Lan, Y., Minnich, A., Yu, B., Yan, X., Wang, D., Muto, A., Vashaee, D., Chen, X., Liu, J., Dresselhaus, M. S., Chen, G., and Ren, Z. High-thermoelectric performance of nanostructured bismuth antimony telluride bulk alloys, *Science* **2008**, *320*, 634–638. http://dx.doi.org/10.1126/science.1156446

(259) Xu, Y., Gan, Z., and Zhang, S.-C. Enhanced thermoelectric performance and anomalous Seebeck effects in topological insulators, *Phys. Rev. Lett.* **2014**, *112*, 226801-1−5. http://dx.doi.org/10.1103/PhysRevLett.112.226801

(260) Wang, H., McCarty, R., Salvador, J. R., Yamamoto, A., and König, J. Determination of thermoelectric module efficiency: A survey, *J. Electron. Mater.* **2014**, *43*, 2274−2286. http://dx.doi.org/10.1007/s11664-014-3044-2

(261) Lowhorn, N. D., Wong-Ng, W., Zhang, W., Lu, Z. Q., Otani, M., Thomas, E., Green, M., Tran, T. N., Dilley, N., Ghamaty, S., Elsner, N., Hogan, T., Downey, A. D., Jie, Q., Li, Q., Obara, H., Sharp, J., Caylor, C., Venkatasubramanian, R., Willigan, R., Yang, J., Martin, J., Nolas, G.,

Edwards, B., and Tritt, T. Round-robin measurements of two candidate materials for a Seebeck coefficient Standard Reference Material™, *Appl. Phys. A* **2009**, *94*, 231−234. http://dx.doi.org/10.1007/s00339-008-4876-5

(262) Wang, H., Porter, W. D., Böttner, H., König, J., Chen, L., Bai, S., Tritt, T. M., Mayolet, A., Senawiratne, J., Smith, C., Harris, F., Gilbert, P., Sharp, J. W., Lo, J., Kleinke, H., and Kiss, L. Transport properties of bulk thermoelectrics—An international round-robin study, Part I: Seebeck coefficient and electrical resistivity, *J. Electron. Mater.* **2013**, *42*, 654−664. http://dx.doi.org/10.1007/s11664-012-2396-8

(263) Heikes, R. R. and Ure, R. W. Thermoelectricity: Science and Engineering. Interscience Publishers, Inc.: New York, **1961**.

(264) Iwanaga, S., Toberer, E. S., LaLonde, A., and Snyder, G. J. A high temperature apparatus for measurement of the Seebeck coefficient, *Rev. Sci. Instrum.* **2011**, *82*, 063905. http://dx.doi.org/10.1063/1.3601358

(265) Snyder, G. J. Measuring Seebeck Coefficient. 9,140,612 B2, **2015**. http://pdfpiw.uspto.gov/.piw?Docid=09140612

(266) Mackey, J., Dynys, F., and Sehirlioglu, A. Uncertainty analysis for common Seebeck and electrical resistivity measurement systems, *Rev. Sci. Instrum.* **2014**, *85*, 085119. http://dx.doi.org/10.1063/1.4893652

(267) Touloukian, Y. S. and Ho, C. Y. Thermophysical Properties of Matter. IFI/Plenum: New York, **1970**.

(268) Graftech engineering manual. http://www.graftech.com/

(269) Bergman, T. L., Lavine, A. S., Incropera, F. P., and Dewitt, D. P., 2011 Fundamentals of Heat and Mass Transfer. John Wiley & Sons: New York, **2011**.

(270) Snyder, G. J. and Toberer, E. S. Complex thermoelectric materials, *Nat. Mater.* **2008**, *7*, 105-114. http://dx.doi.org/10.1038/nmat2090

(271) Kraemer, D., Jie, Q., McEnaney, K., Cao, F., Liu, W., Weinstein, L. A., Loomis, J., Ren, Z., and Chen, G. Concentrating solar thermoelectric generators with a peak efficiency of 7.4%, *Nat. Energy* **2016**, *1*, 16153. http://dx.doi.org/10.1038/nenergy.2016.153

(272) Zhang, Q. H., Huang, X. Y., Bai, S. Q., Shi, X., Uher, C., and Chen, L. D. Thermoelectric devices for power generation: Recent progress and future challenges *Adv. Eng. Mater.* **2016**, *18*, 194-213. http://dx.doi.org/10.1002/adem.201500333

(273) Kim, H. S., Liu, W., Chen, G., Chu, C.-W., and Ren, Z. Relationship between thermoelectric figure of merit and energy conversion efficiency, *PNAS* **2015**, *112*, 8205-8210. http://dx.doi.org/10.1073/pnas.1510231112

(274) Wang, H., Bai, S., Chen, L., Cuenat, A., Joshi, G., Kleinke, H., König, J., Lee, H. W., Martin, J., Oh, M.-W., Porter, W. D., Ren, Z., Salvador, J., Sharp, J., Taylor, P., Thompson, A. J., and Tseng, Y. C. International round-robin study of the thermoelectric transport properties of an n-type half-Heusler compoundfrom 300 K to 773 K, *J. Electron. Mater.* **2015**, *44*, 4482-4491. http://dx.doi.org/10.1007/s11664-015-4006-z

(275) García-Cañadas, J. and Min, G. Multifunctional probes for high-throughput measurement of Seebeck coefficient and electrical conductivity at room temperature, *Rev. Sci. Instrum.* **2014**, *85*, 043906. http://dx.doi.org/10.1063/1.4871553

(276) He, X., Yang, J., Jiang, Q., Luo, Y., Zhang, D., Zhou, Z., Ren, Y., Li, X., Xin, J., and Hou, J. A new method for simultaneous measurement of Seebeck coefficient and resistivity, *Rev. Sci. Instrum.* **2016**, *87*, 124901. http://dx.doi.org/10.1063/1.4969056

(277) Kraemer, D. and Chen, G. High-accuracy direct ZT and intrinsic properties measurement of thermoelectric couple devices, *Rev. Sci. Instrum.* **2014**, *85*, 045107-1−9. http://dx.doi.org/10.1063/1.4870278

(278) Bergman, T. L., Lavine, A. S., Incropera, F. P., and P. DeWitt, D. Fundamentals of heat and mass transfer. 7 ed.; John Wiley & Sons,: **2015**.